中国科学技术大学

博士学位论文

ATLAS 谱仪上四轻子末态中希格斯玻色子产生截面与 ZZ 谱线的测量

作者姓名： 王融坤

学科专业： 粒子物理与原子核物理

导师姓名： 赵政国 教授　周冰 教授

完成时间： 二〇二〇年七月一日

University of Science and Technology of China

A dissertation for doctor's degree

Measurements of the Higgs cross section and inclusive ZZ lineshape using 4ℓ final state with the ATLAS experiment

Author: Rongkun Wang

Speciality: Experimental Particle Physics

Supervisors: Prof. Zhengguo Zhao, Prof. Bing Zhou

Finished time: July 1, 2020

中国科学技术大学学位论文原创性声明

本人声明所呈交的学位论文，是本人在导师指导下进行研究工作所取得的成果。除已特别加以标注和致谢的地方外，论文中不包含任何他人已经发表或撰写过的研究成果。与我一同工作的同志对本研究所做的贡献均已在论文中作了明确的说明。

作者签名：________________　　　　签字日期：________________

中国科学技术大学学位论文授权使用声明

作为申请学位的条件之一，学位论文著作权拥有者授权中国科学技术大学拥有学位论文的部分使用权，即：学校有权按有关规定向国家有关部门或机构送交论文的复印件和电子版，允许论文被查阅和借阅，可以将学位论文编入《中国学位论文全文数据库》等有关数据库进行检索，可以采用影印、缩印或扫描等复制手段保存、汇编学位论文。本人提交的电子文档的内容和纸质论文的内容相一致。

保密的学位论文在解密后也遵守此规定。

☑公开　□保密（____ 年）

作者签名：________________　　　　导师签名：________________

签字日期：________________　　　　签字日期：________________

摘　要

本篇论文介绍的分析利用了四轻子（轻子定义为电子或缪子）末态对希格斯粒子与 Z 玻色子的耦合常数，以及 ZZ 产生的谱线进行了测量。使用的数据是在大型强子对撞机上 ATLAS 实验采集的质心能量为 13TeV 的数据。

本文中的第一个数据分析是关于希格斯玻色子产生截面在四轻子末态中的测量。这一通道拥有本底小的特点，适合于对希格斯粒子的性质进行精确测量。该分析利用了 2015 到 2018 年采集的 139 fb^{-1} 的完整 Run 2 数据。根据简化模板截面框架 (STXS)，希格斯玻色子的产生模式和动力学变量被用于将事例在粒子阶段和重建阶段进行分类，以减少对理论误差的依赖性。在每一个希格斯质量窗的信号分类中，采用多变量分析进一步分离不同的希格斯产生模式和标准模型本底，输出的判别式被用于同步拟合的观测量。更进一步的，本文在质量边带中优化了若干个新的分类，以利用数据对标准模型的本底进行限制。总截面和各个粒子分类下的截面都得到了测量。在绝对快度小于 2.5 的区域，归一化的纵截面测量结果是 $(\sigma \cdot \mathcal{B})/(\sigma \cdot \mathcal{B})_{\mathrm{SM}} = 1.01 \pm 0.09$，标志着数据与理论估计存在着很好的一致性。

本文介绍的第二个分析是利用 2015 和 2016 年采集的 36 fb^{-1} Run 2 的 $\sqrt{s} =$ 13 TeV 的数据进行的四轻子不变质量谱线的测量。一维的不变质量的微分截面与二维的不变质量与第二变量的微分界面都分别进行了解谱分析，包括一个用于提取离壳希格斯粒子信号的基于矩阵元计算的判别式。各个谱线的采集面元都经过优化以以达到合适迁移率和提高纯度。本文通过伪实验的方法对解谱分析的进行了优化，在统计误差和残余偏差中建立了一个较好的平衡，并对解谱分析法进行了标准的一致性测试的验证。微分界面的测量与标准模型的估计符合，并被用于包括夸克对产生和胶子融和产生等四轻子产生模型的检验。胶子初态到 ZZ 过程的信号强度测量为 1.32 ± 0.45。这个结果基于的是 NLO QCD 的计算，它表明了我们需要更高阶的修正来理解四轻子的产生机制。该分析同时利用四轻子不变质量与矩阵元判别式的二维变量，将离壳希格斯粒子的信号强度的 95% 置信度上限利用 CLs 方法设为 6.5。在四轻子不变质量在 [80, 100] GeV 的区间下，Z 玻色子到四轻子的衰变分支比测量值为 4.70 ± 0.32 (统计误差) ± 0.21 (系统误差) ± 0.03 (理论误差）± 0.14 (亮度测量误差) * 10^{-6}。最后，本文用 CLs 方法给出了 95% 置信度下有效场理论中的改进的希格斯耦合参数 (Ct, Cg) 的排除轮廓线。

关键词：希格斯玻色子；ZZ；四轻子；大型强子对撞机；ATLAS；耦合常数；产

生截面；谱线；测量；STXS；

ABSTRACT

The physics analyses presented in this dissertation use four-lepton (4ℓ, $\ell = e, \mu$) final state to measure the Higgs boson to ZZ coupling, and the inclusive ZZ production lineshape with data collected by the ATLAS experiment in the proton-proton collisions of the Large Hadron Collider (LHC) at a center-of-mass energy of $\sqrt{s} = 13$ TeV.

The first analysis presented is the Higgs boson production cross section measurement in reaction of $H \rightarrow ZZ^* \rightarrow 4\ell$. The 4ℓ final state has the highest signal to background ratio compared to all other Higgs decay channels, thus it is ideal for precision measurement of the Higgs properties. The analysis uses the full Run 2 dataset, corresponding to an integrated luminosity of $139\,\text{fb}^{-1}$. The Higgs boson production mode and kinematic variables are used to categorize the selected Higgs events both at fiducial and the reconstructed level under the latest *Simplified Template Cross Section* (STXS) framework to reduce the dependence on uncertainties of theoretical modeling. In each of the signal category in the Higgs mass window with enough statistics, multivariate analysis is performed to further separate Higgs signal from different production modes and the Standard Model (SM) background. The output discriminant is used as the observable in the simultaneous fit to extract the Higgs boson production cross section. Furthermore, several new categories are optimized in the Higgs mass side-band region to constrain SM background from data. The inclusive cross section times branching ratio over the SM prediction in the Higgs production rapidity range, $|y_H| < 2.5$, is measured to be

$$(\sigma \cdot \mathcal{B})/(\sigma \cdot \mathcal{B})_{\text{SM}} = 1.01 \pm 0.09,$$

which marks a very good agreement between data and the SM prediction.

The second analysis presented is the lineshape measurement of invariant mass spectrum of four-lepton system using data collected during 2015 and 2016, corresponding to an integrated luminosity of $36\,\text{fb}^{-1}$. The differential distribution of $m_{4\ell}$ and several two-dimensional distributions of $m_{4\ell}$ vs secondary variables, including a Matrix Element discriminant “MELA” for the off-shell Higgs extraction, are measured with optimized binning for proper migration and high purity. The unfolding method used in the measurement is optimized with pseudo-experiments to make a balance between statistical uncertainty and residual bias. The unfolding process is validated with the standard unfolding closure test. The differential cross sections of the measurement are consistent with SM calculations. The results are then interpreted and tested against different 4ℓ production models, including the quark pair and the gluon-gluon fusion initial states. The $gg \rightarrow ZZ^*$, gluon-originated signal strength is measured to be $1.32^{+0.45}_{-0.45}$. This result is based on theoretical calculation of the $gg \rightarrow ZZ^*$ production with the QCD next-to-leading order (NLO) correction, and it indicates higher order correction in calculation is necessary to understand the source of the 4ℓ production mechanism. A 95% confidence level upper limit of 6.5 is set on the off-shell Higgs signal strength with the $m_{4\ell}$- MELA distribution using the CL_s statistical approach. The branching ratio of $Z \rightarrow 4\ell$ is measured in a phase space of $80 < m_{4\ell} < 100$ GeV and $m_{\ell\ell} > 4$ GeV as:

$$\mathcal{B}_{Z\rightarrow 4l} = (4.70 \pm 0.32(\text{stat.}) \pm 0.21(\text{sys.}) \pm 0.03(\text{theo.}) \pm 0.14(\text{lumi})) \times 10^{-6}.$$

Finally, a 95% confidence level CL_s exclusion contour is set on modified Higgs coupling parameters (c_t, c_g) in a Higgs effective field theory.

Acknowledgments

First and foremost, I would like to express my deepest gratitude to my supervisors Zhengguo Zhao from USTC and Bing Zhou from UM, Ann Arbor. You have provided me with a great platform to work at the frontier of high energy physics. Thank you for constantly challenging me with the physical questions and pushing me out of my comfortable zone to make me a better physicist. Without your encouragement and help I wouldn't have become who I am now. Your amazing stories in the past have set up a good model for me about physics and also life. You have always put the welfare of students at the foremost and it's really an honor to work with you.

I would like to thank Fabiola Gianotti and Peter Jenni for setting up the ATLAS PhD Grant that has offered great help supporting my stay at CERN.

Thank you Prof. Haibo Li, Prof. Lianliang Ma, Prof. Yanwen Liu, Prof. Qun Wang, and Prof. Yusheng Wu for serving as my defense committee. Thank you, my thesis review committee for spending long hours reading through my thesis. Your questions and comments have triggered more curiosity and reminded me I still have a long way to go. You will be my role models in science.

I'm grateful to be able to attend the wonderful lessons in USTC, here I thank for the teachers who diligently taught them: Prof. Daoneng Gao, Prof. Cheng Li, Prof. Shubin Liu, Prof. Jianxin Lu, Prof. Ziping Zhang, Prof. Renyou Zhang, Prof. Yang Zhang, and Prof. Jiejie Zhu.

I would also like to express my gratitude to the faculty at University of Michigan. You have always been sharp at physics, detector, and many other aspects. Thank you for all the questions and discussions, Claudio, Dan, Dante, Ed, Jianming, Junjie and Thomas.

Among all the people I have worked with, firstly I would like to thank you, Yusheng, with whom I have worked closely from the beginning. You have always been encouraging and patient, giving me the freedom to explore and allowing me to find the answers myself. Thank you for making work more enjoyable for me.

Lailin, thank you for providing endless help and timely discussion. Your attitude of work is the one I could only hope to hold a candle to. Your passion for physics and work has given me so much inspiration.

Jianbei, you have been the very first mentor in my high energy physics research and I'm thankful for all the guidance. I truly enjoyed your detector technology lesson

which is full of detailed knowledge and wisdom. I will never forget the discussions that happened almost like yesterday to me.

Thank you, Shuoxing, for the days working on WA105 together, you sowed a seed in my heart for the curiosity and interest in hardware that has driven me to walk down this path.

I want to thank all the nice people in the ATLAS collaboration. Thank you William Buttinger for being the first one to guide me with ATLAS analyses. Your skill in software has always left me in awe. You inspired me to become a better programmer and physicist, and I am glad to hear that you are back to ATLAS again. Thank you Loan, you have been very patient and kind to me. I am lucky to have you as a friend in this highly competitive environment. Thank you Andrea, Eleni and Roberto, for your questions, suggestions and trust. Your recognition has given me a lot of confidence and I truly appreciate it. I would like to thank HZZ group conveners RD, Gaetano, Giacomo, Will and colleagues Haider, Fabio, Maddie, Verena, Will, Bianca and Panagiotis, it is an honor to work with you and learn from you. Thank you, Max and Zara, for the joyful time tackling questions in ZZ4l analysis. Thank you Nan and Hongtao, your gave me a lot of help especially in understanding the statistics. Thank you, Tiesheng, Zhen, Philip and Karri. I am pleasant to have worked with you during the commissioning of BMG and you are my source of knowledge of the ATLAS muon detector. To the New Small Wheel community, I thank you so much for providing me with a chance to work on very diversified projects. Thank you Sun, Liang for the guidance and management. Without you the sTGC work would not be carried out smoothly. Thank you Xu, Xiong and Prachi, we made a good "team-C" at the building 180 on tackling the readout and trigger of sTGC with the FELIX system. To Stephanie, Cenk, Alex, Christos, Polyneikis, Brigitte, Emil, Henso, George, Gerardo, Larry and numerous people I have came across in this big community, you have been helpful and it's my pleasure to work with you towards a common goal. Finally, the more I work inside the ATLAS the more I feel that everyone is essentially, thank you all.

I have my heartfelt gratitude to all the friends at CERN, who made this PhD journey much more interesting than I expected. I will not forget all the parties we had together, they are joyful memories. Wen, Josh, Zirui, Yicheng and Hao, thank you for all the laughter and help you've brought to me. May the power of Old-Driver always go with you. Thank you, Xunwu and Yongbin, my friends at the other side of the experiment, it is very fun to be hanging out with you. Aaron, Ismet, Matt and Zhi, thank you for the help and pleasure you've given me. You constantly remind me that life is as important

as work. Cong Geng and Bing Li, thank you for all the guidance and help you provided me over the years. Heling, thanks for all the discussion, as they had made an impact to me. Diallo, Tom Cheng, Rachel Hyneman, Liqing Zhang, Jing Chen, Rustem Ospanov, Tairan Xu, Cheng Chen, Wenxiao Wang, Heng Li, Fudong He, Weitao Wang, Hanlin Xu, Kunlin Han and Jun Gao, thank you all for the companion. A special thank you to Xiangyu Xie, for being my defense secretariat under the extremely tight timeline and also all the help you offered.

Thank you Elise, Xiaotian, Man and Zhichen for being my first students, I hope I can live up to your expectation and bring you far on the track of particle physics.

I would like to thank my friends in from skiing and climbing: Margherita, Ors, Marco, Matteo, Roland, Tini and Enrico. You made my life so much more colorful.

I want to thank everyone who have taken care of me during my injury. It was a difficult period, without your help and accompany I cannot go past it alone.

I would like to thank my family for the love and support. Without you, I wouldn't have been where I am now.

Xin, you have always been by my side, even when you're physically away. You've helped me get past the hardest times. You brought me joy and gave me infinite amount of confidence and encouragement that I can not find elsewhere. Thank you for always being so patient and supportive. Thank you my love.

Contents

List of Figures

List of Tables

Notation

This is the list of Abbreviations

CERN	The European Organization for Nuclear Research
LHC	The Large Hadron Collider
ATLAS	A Toroidal LHC ApparatuS
SM	Standard Model
HZZ	the coupling of the Higgs boson with ZZ
ID	Inner Detector
SCT	Semiconductor Tracker, part of ID
TRT	Transition Radiation Tracker, part of the ID.
EM	Electromagnetic
MS	Muon Spectrometer
PMT	Photomultiplier
MIP	Minimum-ionizing particle
L1	first-level trigger
HLT	High-level trigger
ggF	gluon-gluon fusion: gg initiated Higgs production through quark loop
VBF	vector boson fusion: gauge boson radiated from quark scatter to produce Higgs
WH	quark-quark initiated Higgs production in association with a W boson
ZH	Higgs production in association with a Z boson, including ggZH processes
ggZH	gluon-gluon initiated Higgs production in association with a Z boson
VH	ZH + WH + ggZH
ttH	Higgs production in association with a top quark pair
bbH	Higgs production in association with a bottom quark pair
tH	tH+X where X is either j+b or W: Higgs production in association with a single top quark plus a jet and a b-quark, or with a W
qqZZ	Standard Model ZZ^*continuum produced from quark-quark annihilation

ggZZ	Standard Model ZZ^*continuum produced from gluon-gluon fusion
EWZZjj	Standard Model ZZ^*continuum produced from quark-quark in vector boson fusion style.
ttW	production of W in association with a top quark pair
ttZ	production of Z in association with a top quark pair
ttV	includes ttZ and ttW processes
tXX	includes mostly ttV and minor p rocesses: tWZ, $t\bar{t}W^+W^-$, $t\bar{t}W^{\pm}Z$, $t\bar{t}Z\gamma$, $t\bar{t}ZZ$, $t\bar{t}t$, $t\bar{t}t\bar{t}$ and tZ
$Z+$jets	Z boson production associated with jets
$t\bar{t}$	inclusive pair production of top and anti-top quarks
ΔR	The angular separation $\sqrt{(\Delta\eta)^2 + (\Delta\phi)^2}$.

Chapter 1 Introduction

The Standard Model (SM) is the theory representing our current understanding of the elementary particle physics. It has been successfully tested over the past 60 years in high energy physics experiments, including discoveries of new particles and physics processes predicted by the SM. The physical constants are measured with a very high precision and are in good agreement with the SM predictions.

The SM combines three of the four known fundamental interactions, the electromagnetic (EM) force, the weak force, and the strong force, with the former two unified as the electroweak force. The interactions happen between fermions, the building blocks of all known matters, through the exchange of spin-1 gauge bosons, the force carriers. The SM is a gauge quantum field theory. The interactions mentioned above are naturally introduced by the gauge invariant principle, i.e. under symmetry transformations the underlying physics laws are unchanged. The symmetry groups of the SM are $SU(3)_C \bigotimes SU(2)_L \bigotimes U(1)_Y$, where *C, L*, and *Y*, denote "color"; (the strong force charge), "left-handed", and "hyper-charge", respectively. The group $SU(3)_C$ gives rise to the strong interaction and the group $SU(2)_L \bigotimes U(1)_Y$ gives rise to the electroweak interaction. The gauge sector of the SM has been tested through coupling measurements with high precision in different experiments. However, gauge symmetry requires that the force carriers must be massless. This contradicts with experimental observations that weak force carriers, W and Z bosons, are massive. A big step in the development of the SM was to establish a mechanism to generate masses while keeping gauge invariance in the theory framework.

In 1962, Goldstone's theorem [1-3] showed that massless spin-zero bosons occur when global gauge symmetry is spontaneously broken in relativistic field theories. Such massless bosons were however excluded by experiments. Shortly afterwards, several studies [4-9] addressed the Goldstone theorem, stating that massless Goldstone bosons need not appear during a spontaneous breakdown of local gauge symmetries. The studies then formulated what later to be called the Englert–Brout–Higgs (EBH) mechanism. In the simplest case, EBH mechanism introduces an SU(2) complex scalar doublet field that has four degrees of freedom (DOF). During the electroweak symmetry breaking (EWSB), the scalar field generates three Goldstone bosons that couple to the vector fields, giving them longitudinal polarization and masses. The remaining DOF becomes a new massive scalar particle, the Higgs boson. Through this mechanism the Higgs boson is predicted to interact with vector boson pairs through the vertex HZZ and HWW. The fermions also acquire masses by interacting with the Higgs boson through Yukawa coupling. The interacting vertex is referred to as $Hf\bar{f}$. However, the theory did not predict the mass of the Higgs boson. The search for the Higgs boson was the highest priority in the past 50 years in high energy experiments.

Most of the fermions and gauge bosons predicted by the SM were discovered before the 21st century. On the 4th July 2012, both ATLAS ① and CMS ② experiments at the Large Hadron Collider (LHC) announced the observation of a SM-like Higgs boson [10-11] in data excess with 5σ significance over the background, completing the discovery of the last missing piece of the SM. The high energy physics research interest quickly switched to study the properties of the Higgs boson, in order to further our understanding of the EWSB and to find new physics beyond SM.

This dissertation focuses the study on the Higgs coupling measurement using the $H \to ZZ^* \to 4\ell$ ($\ell = e, \mu$) channel with the ATLAS experiment at the LHC. The four-lepton (4ℓ) channel has fully reconstructed final states and a small background. It is one of the golden channels for Higgs discovery and measurement (the other one being the di-photon channel). The channel plays a crucial role in Higgs physics in the LHC experiments. This thesis presents two analyses in this channel. The first analysis is the Higgs production cross section measurement based on the full Run 2 dataset collected in 2015-2018 corresponding to a total integrated luminosity of 139 fb^{-1} at the center-of-mass energy $\sqrt{s} = 13$ TeV. The second analysis is the lineshape measurement of the inclusive $ZZ \to 4\ell$ production with the Run 2 dataset of 36.1 fb^{-1} collected in 2015-2016, which includes an interpretation of the off-shell Higgs production signal strength. The results of these two analyses are published in Ref. [12] and Ref. [13], respectively.

An overview of physics analysis is illustrated in Figure 1.1. There are two chains of data and sample productions. The first one is Monte Carlo simulated data sample production, where events from the underlying physics studies are generated based on theoretical models. These events will further go through the detailed simulations of detector response, resulting in events in the same format as real data. The second one is real data produced in pp collisions of the LHC, and collected by the ATLAS experiments. Both MC and data will go through exactly the same process in physics objects and event reconstruction, and will be analyzed by physicists in parallel. Finally, data and MC predictions both in event rate and in kinematic distributions will be compared

① A Toroidal Lhc ApparatuS
② Compact Muon Spectrometer

with statistical analysis methods to extract the final physics results. These analysis procedures will be presented in this dissertation in detail.

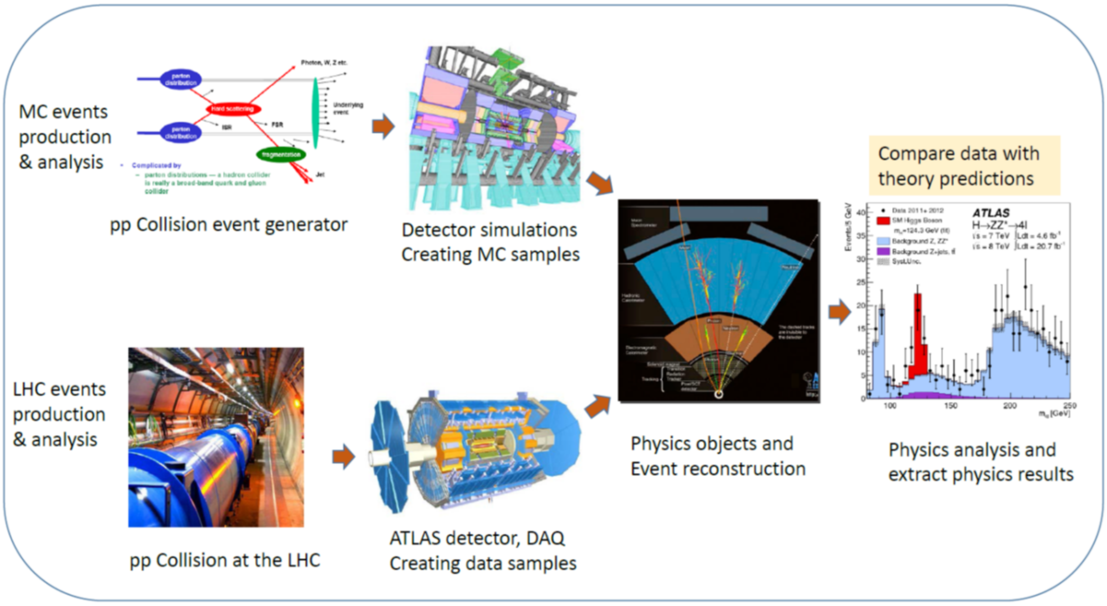

Fig. 1.1 Overview of physics analysis using Monte Carlo and real data samples. Production of MC simulated events is based on underlying physics modeling and our understanding of the detector responses for different particles created in pp collisions. Event reconstruction and analysis are treated exactly the same for MC and real data samples.

The thesis is organized as follows: Chapter 2 briefly reviews the Standard Model of particle physics; Chapter 3 introduces the phenomenology on LHC, with a focus on the Higgs and the ZZ^* decay channel; Chapter 4 provides an overview of the LHC and the ATLAS experiment; Chapter 5 describes the physics object reconstruction algorithms in ATLAS; Chapter 6 reports the Data and Monte Carlo samples used in the analyses; Chapter 7, the event selection for $H \to ZZ^* \to 4\ell$ event selection is presented. Chapter 8 summarizes the statistical modeling and procedures used in extracting the physics results. Chapter 9 presents the measurement of production cross section of the SM Higgs boson and Chapter 10 presents the inclusive ZZ^* production lineshape measurement. Chapter 11 provides a summary and a future aspect of the studies.

Additionally, as an experimental physicist the author of this thesis involved in the ATLAS Muon detector performance studies with high luminosity data during Run 2, and intensively worked on the new Small-Wheel integration and commissioning project for the ATLAS detector Phase I upgrade. Contributions to the hardware research projects are reported in the Appendix of this thesis as well.

Chapter 2 The Standard Model of Particle Physics

Following the successful establishment of the first gauge theory, Quantum Electrodynamics (QED) [14-19], another gauge theory of strong interactions, Quantum Chromodymanics (QCD) [15, 20-23], was also successfully developed. These gauge theories are fully consistent with all the experimental data. Following the same gauge theory framework and including all three fundamental interactions, the strong, weak and EM interactions, the SM of particle physics [24-25] based on $SU(3)_C \bigotimes SU(2)_L \bigotimes U(1)_Y$ symmetry groups was further developed in the second half of the twentieth century. It provides a unified description of the interactions between fermions and gauge bosons. It also introduces a scalar field, the Higgs field, in the theory, which spontaneously breaks the $SU(2)_L \bigotimes U(1)_Y$ symmetry and generates masses for all massive elementary particles through their interactions with the Higgs field. The fermions consist of three generations of spin $\frac{1}{2}$ quarks, (u, c, t and d, s, b) and leptons (e, μ, τ and ν_e, ν_μ, ν_τ). The gauge bosons consist of strong force carriers gluons (g), Electromagnetic (EM) force carrier photon (γ) and weak force carriers $W^\pm$ and Z. In addition there is a scalar Higgs boson, the quanta of the Higgs field. The summary of particles and their properties is shown in Figure 2.1.

This chapter will describe the two corner stones of the SM: the gauge field theory and the Higgs mechanism through spontaneous symmetry breaking.

2.1 Gauge field theory

The Quantum Field Theory (QFT), which successfully unifies quantum mechanics and special relativity, is the language on which all physics of SM is developed upon. Just as wave-particle duality is deeply embedded in quantum theory, each particle is described by a "field", $\psi(x)$, where $x = (t, \boldsymbol{x})$ is a 4-dimensional vector descriptive of time and space. Utilizing the formalism of classical mechanics, an action term can be constructed from time integral of Lagrangian L and then spacetime integral of Lagrangian density $\mathcal{L}(\psi, \partial_\mu \psi)$, the later being a function of the field and its spacetime derivative, the quantization of the momentum and energy:

$$\begin{aligned} S &= \int L dt \\ &= \int \mathcal{L}(\psi, \partial_\mu \psi) d^4 x. \end{aligned} \tag{2.1}$$

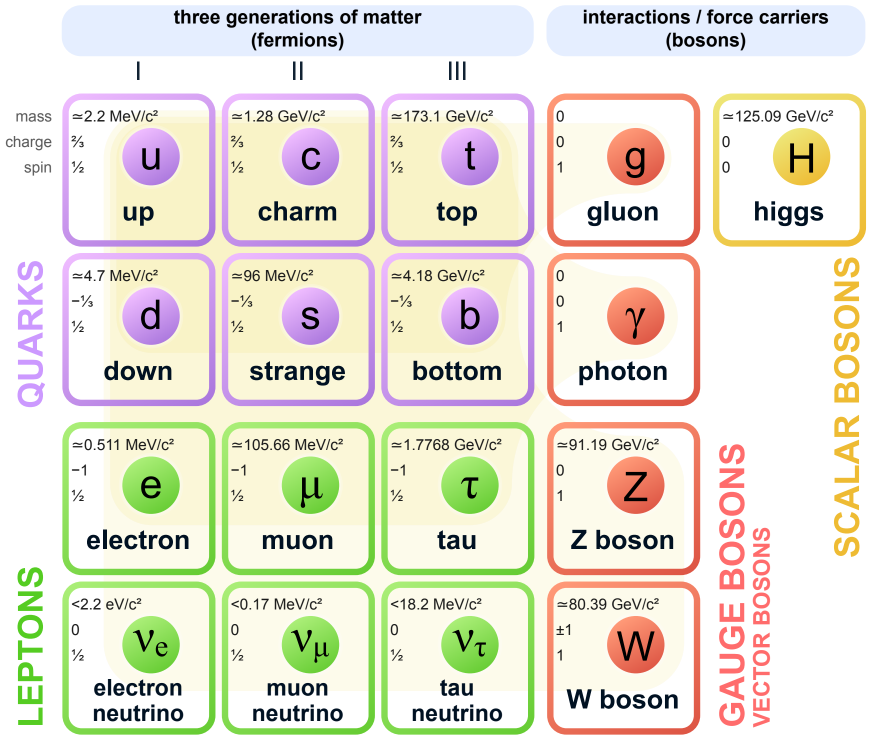

Fig. 2.1 Elementary particles in SM of particle physics [26]. The mass, charge and spin of particles are given in the boxes.

From the least action principle, the system evolves along a path where S is an extremum. Under a small perturbation of the field $\delta\psi$, the physics should be undisturbed:

$$0 = \delta S. \tag{2.2}$$

The the Euler-Lagrange equation can then be derived

$$\partial_\mu\left(\frac{\partial\mathcal{L}}{\partial(\partial_\mu\psi)}\right) - \frac{\partial\mathcal{L}}{\partial\psi} = 0 \tag{2.3}$$

for a particle field by requiring a constrained boundary of spacetime integration [14], which determines the motion of a field. Conversely, with the knowledge of the motion of a field, the Lagrangian density can be constructed. Thus the dynamics of a field is fully described by its Lagrangian density. In this thesis, it will be called Lagrangian for simplicity because only field theory is concerned.

If the physics law of equation of motion is invariant under a certain transformation, this kind of transformation is called symmetry. This allows the action term to change by a surface term.

2.1.1 Quantum electrodynamics

The Dirac equation [15] presented below describes a free-moving relativistic spin-1/2 fermion $\psi(x)$,

$$(i\gamma^{\mu}\partial_{\mu} - m)\psi(x) = 0, \tag{2.4}$$

where ψ is a Dirac spinor, and γ^{μ} is the Dirac matrix. The Lagrangian for the free Dirac field can be written down

$$\mathcal{L}_{Dirac} = \bar{\psi}(x)(i\gamma^{\mu}\partial_{\mu} - m)\psi(x) \tag{2.5}$$

where $\bar{\psi}(x) = \psi^{\dagger}\gamma_0$.

Consider a local $U(1)$ gauge transformation generated by a charge q

$$\psi(x) \to \psi'(x) = e^{iq\alpha(x)}\psi(x), \tag{2.6}$$

which also imply

$$\begin{aligned} \bar{\psi} &\to \bar{\psi'} = e^{-iq\alpha}\bar{\psi} \\ \partial_{\mu}\psi &\to \partial_{\mu}\psi' = e^{iq\alpha}[\partial_{\mu}\psi + iq(\partial_{\mu}\alpha)\psi]. \end{aligned} \tag{2.7}$$

Under such local phase transformation the Lagrangian will change as

$$\begin{aligned} \mathcal{L} \to \mathcal{L}' &= i\bar{\psi}\gamma^{\mu}(\partial_{\mu}\psi + iq(\partial_{\mu}\alpha)\psi) - mq\bar{\psi}\psi \\ &= \mathcal{L} - q(\partial_{\mu}\alpha)\bar{\psi}\gamma^{\mu}\psi, \end{aligned} \tag{2.8}$$

which violates the gauge invariance of the Lagrangian.

However, modifications can be made to keep the gauge invariance. If the derivative ∂_{μ} is replaced by the gauge covariance derivative with an introduced gauge field A_{μ}

$$\mathcal{D}_{\mu} \equiv \partial_{\mu} + iqA_{\mu}, \tag{2.9}$$

and the field $A_{\mu}(x)$ transforms under (2.6) as

$$A_{\mu}(x) \to A'_{\mu}(x) \equiv A_{\mu}(x) - \partial_{\mu}\alpha(x). \tag{2.10}$$

The transformation for gauge covariance derivative is

$$\mathcal{D}_{\mu}\psi(x) \to e^{iq\alpha(x)}\mathcal{D}_{\mu}\psi(x). \tag{2.11}$$

Consequently the Lagrangian remains gauge invariant and can be written as

$$\begin{aligned} \mathcal{L} &= \bar{\psi}(x)(i\gamma^{\mu}\partial_{\mu} - m)\psi(x) - q\bar{\psi}(x)\gamma^{\mu}A_{\mu}(x)\psi(x) \\ &= \mathcal{L}_{Dirac} - q\bar{\psi}(x)\gamma^{\mu}A_{\mu}(x)\psi(x). \end{aligned} \tag{2.12}$$

The transformation (2.10) required for the field $A_\mu(x)$ is precisely the gauge transformation in electrodynamics [15]. Thus the last term in (2.12) can be interpreted as the interaction between an electromagnetic current $J^\mu \equiv \bar{\psi}\gamma^\mu\psi$ and the photon field $A_\mu(x)$, with q identified as the electric charge of the fermion

The free EM field is then described by the Maxwell Lagrangian

$$\mathcal{L}_{Maxwell} = -\frac{1}{4}F^{\mu\nu}F_{\mu\nu}, \tag{2.13}$$

where $F_{\mu\nu} \equiv \partial_\mu A_\nu - \partial_\nu A_\mu$, is the electromagnetic field tensor. Any mass term $A^\mu A_\mu$ will break gauge invariance under the $U(1)$ local transformation (2.10), therefore the photon should be massless. The $U(1)$ is an abelian symmetry group and it does not have the photon self-interaction terms in the Lagrangian. Merging the three components from above, the QED Lagrangian has the form

$$\begin{aligned}\mathcal{L}_{QED} &= \mathcal{L}_{Dirac} + \mathcal{L}_{Maxwell} + \mathcal{L}_{int} \\ &= \bar{\psi}(x)(i\gamma^\mu\partial_\mu - m)\psi(x) - \frac{1}{4}F^{\mu\nu} - q\bar{\psi}(x)\gamma^\mu A_\mu(x)\psi(x).\end{aligned} \tag{2.14}$$

Precision tests of QED have been very successfully performed in low-energy atomic physics, high energy collider experiments and condensed matter system.

The gauge field theory is generalized by Yang-Mills theory [27] that by imposing symmetry under a local gauge transformation, massless gauge vector fields are therefore introduced.

2.1.2 Quantum chromodynamics

The strong interaction describes the behavior of quark fermions and gluon bosons. Since quarks are observed to be color triplets, the non-abelian $SU(3)$ symmetry group is needed to construct a strong interaction. Following the Yang-Mills theory, the Lagrangian can be written down as

$$\mathcal{L} = \bar{\psi}(i\gamma^\mu\mathcal{D}_\mu - m)\psi - \frac{1}{4}G_a^{\mu\nu}G_{\mu\nu}^a, \tag{2.15}$$

where the ψ is now a 3-dimensional color spinor that represents three colors of a quark field. The gauge covariance derivative is

$$\mathcal{D}_\mu = \partial_\mu + ig_s\frac{\lambda_a}{2}G_\mu^a, \tag{2.16}$$

where g_s is the strong interaction coupling constant, the G_μ^a are the gluon field with the Lorentz index μ and the color label a (=1, 2, ...8), and $\lambda^a/2$ are 3×3 matrices, the generators of SU(3). The gluon field-strength tensor is

$$G_{\mu\nu}^a = \partial_\mu G_\nu^a - \partial_\nu G_\mu^a - g_s f_{bc}^a G_\mu^b G_\nu^c, \tag{2.17}$$

where the constants f^{abc} are the structure constants of SU(3). The quantum chromodynamics (QCD) interaction term has the form

$$\mathcal{L}_{int} = -\frac{g_s}{2}\bar{\psi}\lambda_a \gamma^\mu G^a_\mu \psi \tag{2.18}$$

that describes how quark and anti-quark interact with a gluon. The non-abelian property of the field also leads to gluon self-interaction term from the free field Lagrangian. This shows precisely that strong interaction applies to particles with color charge, including gluons. Unlike photons are charge neutral, the fact that gluons carry color charge leads to the strange behavior that force between quarks increases as the distance between quarks is increased. This is similar to a spring that pulls harder and harder as it is stretched. At longer distance (lower energy) the interaction becomes stronger, and at some point the energy is large enough to create a pair of quarks out of the vacuum. Therefore when quarks are produced by particle accelerators, we never see the individual quarks in detectors, but instead jets of many color-neutral particles (mesons and baryons, the quark bound-states) clustered together. Such hadronization process is referred to as fragmentation. In fact, fragmentation is one of the least understood processes in particle physics. Since all the quarks are bounded inside hadrons by gluons, such as protons (uud bound state), neutrons (udd bound state), and pions (u and d quark and antiquark bound state), so the strong force is short-ranged (10^{-15} m) even though gluons are massless.

2.1.3 Electroweak Unification

The weak force is responsible for nuclear beta decays. Its effective force range is at subatomic distances (10^{-18} m). In the SM the weak force is unified with the electromagnetic force, called electroweak (EW) interactions.

In the EW theory the description of fermions are separated into chiral left-handed and right-handed field in the following form:

$$\begin{aligned} \psi_L &= \frac{1}{2}(1-\gamma^5)\psi \\ \psi_R &= \frac{1}{2}(1+\gamma^5)\psi. \end{aligned} \tag{2.19}$$

The left-handed fields form the weak-isospin doublet L_f which includes

$$\begin{pmatrix} \nu_e \\ e \end{pmatrix}, \begin{pmatrix} \nu_\mu \\ \mu \end{pmatrix}, \begin{pmatrix} \nu_\tau \\ \tau \end{pmatrix}, \begin{pmatrix} u \\ d \end{pmatrix}, \begin{pmatrix} c \\ s \end{pmatrix}, \begin{pmatrix} t \\ b \end{pmatrix}, \tag{2.20}$$

where the projection of isospin at z-direction, I_3, is $\frac{1}{2}$ and $-\frac{1}{2}$, respectively for two fields of the doublets. While the right-handed fields R_f (singlet) include

$$e_R, \mu_R, \tau_R, u_R, d_R, c_R, s_R, t_R, b_R. \tag{2.21}$$

Massless particles always have the same helicity and chirality and experiments observed only left-handed neutrino and right-handed antineutrino [28-29]. Therefore massless neutrinos do not have a right-handed field in the SM.

The hypercharge is defined as $Y = 2(Q - I_3)$ that relates isospin I_3 with the electric charge Q of the particle [30-31]. The symmetry group of transformation is generated by quantum numbers, I and Y, is $SU(2)_L \bigotimes U(1)_Y$. The corresponding gauge bosons are $b^1_\mu, b^2_\mu, b^3_\mu$ for $SU(2)_L$ and $\mathcal{A}_\mu$ for $U(1)_Y$.

The Lagrangian can then be written down in fermions and gauge fields terms:

$$\mathcal{L} = \mathcal{L}_{fermions} + \mathcal{L}_{gauge}. \tag{2.22}$$

The gauge term is

$$\mathcal{L}_{gauge} = -\frac{1}{4}\sum_{l=1}^{3} F^l_{\mu\nu}F^{l\mu\nu} - \frac{1}{4}f_{\mu\nu}f^{\mu\nu}, \tag{2.23}$$

where the field tensors are

$$\begin{aligned} F^l_{\mu\nu} &= \partial_\mu b^l_\nu - \partial_\nu b^l_\mu - g\sum_{j,k=1}^{3}\epsilon_{jkl}b^j_\mu b^k_\nu \\ f_{\mu\nu} &= \partial_\mu \mathcal{A}_\nu - \partial_\nu \mathcal{A}_\mu, \end{aligned} \tag{2.24}$$

where the ϵ_{jkl} is structure constants of SU(2). And the gauge covariance derivatives are

$$\mathcal{D}_{L,\mu} = \partial_\mu + ig'\frac{Y}{2}\mathcal{A}_\mu + ig\frac{\tau}{2}\cdot b_\mu \tag{2.25}$$

$$\mathcal{D}_{R,\mu} = \partial_\mu + ig'\frac{Y}{2}\mathcal{A}_\mu, \tag{2.26}$$

where g and g' are gauge coupling constants related to isospin and hypercharge respectively, and $\tau/2$ are 2×2 matrices as the $SU(2)$ generators. This construction is consistent with the fact that charged-current weak interaction only affect left-handed fermions. Also it would be difficult mathematically to incorporate 2-dimensional matrices with right-handed states where the neutrinos are missing.

With those above, the fermion Lagrangian in the gauge covariance derivative form is

$$\begin{aligned} \mathcal{L}_{fermions} &= \bar{L}i\gamma^\mu\mathcal{D}_{L,\mu}L + \bar{R}i\gamma^\mu\mathcal{D}_{R,\mu}R \\ &= \bar{L}i\gamma^\mu(\partial_\mu + ig'\frac{Y}{2}\mathcal{A}_\mu + ig\frac{\tau}{2}\cdot b_\mu)L + \bar{R}i\gamma^\mu(\partial_\mu + ig'\frac{Y}{2}\mathcal{A}_\mu)R, \end{aligned} \tag{2.27}$$

where the L and R are summed over all fermion fields concerned. As described in Section 2.1.1, the four gauge bosons in EW theory are massless. However, weak force mediators $W^\pm$ and Z bosons are massive. In addition, an explicit mass term for fermion

$\bar{\psi}\psi = \bar{\psi}_L\psi_R + \bar{\psi}_R\psi_L$ is also forbidden since the left- and right-handed fields transform differently and this breaks the gauge invariance. To solve these problems, the Higgs mechanism will be introduced in the Section 2.2 followed.

The four gauge fields $b^1_\mu, b^2_\mu, b^3_\mu$, and $\mathcal{A}_\mu$ introduced in the EW theory can be redefined to get the physical gauge bosons: W^+, W^-, Z and $A_\mu(\gamma)$ as below [15].

$$W^\pm_\mu = \frac{1}{\sqrt{2}}(b^1_\mu \mp i b^2_\mu) \tag{2.28}$$

$$Z_\mu = -\mathcal{A}_\mu sin\theta_W + b^3_\mu cos\theta_W \tag{2.29}$$

$$A_\mu = \mathcal{A}_\mu cos\theta_W + b^3_\mu sin\theta_W, \tag{2.30}$$

where the θ_W is the Weinberg weak-mixing angle satisfying

$$cos\theta_W = \frac{g}{\sqrt{g^2 + g'^2}}. \tag{2.31}$$

The weak-mixing angle describes the extent of mixing between weak and electromagnetic interactions, and the measured value satisfy $sin^2\theta_W = 0.231$ [26]. The EM interaction term can be rewritten as

$$\mathcal{L}_{EM-int} = \frac{gg'}{\sqrt{g^2 + g'^2}}\bar{\psi} i\gamma^\mu \psi A_\mu. \tag{2.32}$$

Therefore, the EM interaction coupling constant e is connected to the EW coupling constants in the form as

$$e = \frac{gg'}{\sqrt{g^2 + g'^2}} = g sin\theta_W = g' cos\theta_W. \tag{2.33}$$

At last, the Lagrangian (2.27) determines that the EW interaction only happens for particle with the same generation. However, strangeness-changing weak charged current is observed in experiments, indicating that the weak eigenstates are not exactly the same as the QCD eigenstates (or mass eigenstates) and there are mixing between the two. Without loss of generality in theory, by assuming there is no mixing of $I_3 = \frac{1}{2}$ quark states, the mixing of $I_3 = -\frac{1}{2}$ can be written down

$$\begin{pmatrix} d' \\ s' \\ b' \end{pmatrix} = V_{CKM} \begin{pmatrix} d \\ s \\ b \end{pmatrix} \equiv \begin{pmatrix} V_{ud} & V_{us} & V_{ub} \\ V_{cd} & V_{cs} & V_{cb} \\ V_{td} & V_{ts} & V_{tb} \end{pmatrix} \begin{pmatrix} d \\ s \\ b \end{pmatrix}, \tag{2.34}$$

where the V_{CKM} is the CKM ① matrix [32], measured to be [26]

$$V_{CKM} = \begin{pmatrix} 0.97446 \pm 0.00010 & 0.22452 \pm 0.00044 & 0.00365 \pm 0.00012 \\ 0.22438 \pm 0.00044 & 0.97359^{+0.00010}_{-0.00011} & 0.04214 \pm 0.00076 \\ 0.00896^{+0.00024}_{-0.00023} & 0.04133 \pm 0.00074 & 0.999105 \pm 0.000032 \end{pmatrix}. \tag{2.35}$$

①Cabibbo-Kobayashi–Maskawa

The coupling of quarks across generations through charged current $W^{\pm}$ are much smaller than that within generations. For bottom quarks, the decay to other quark is therefore suppressed. Since bottom quarks cannot decay to top quarks due to mass conservation, it has a long lifetime compared to all other quarks. From an experimental point of view, the relatively long lifetime can be utilized to tag the b-quarks.

2.2 Spontaneous Symmetry Breaking and the Higgs Mechanism

To tackle the mass problem of fermions and gauge bosons in the electroweak theory, the Englert–Brout–Higgs mechanism (EBH) [4-9] was introduced as a solution. It also addressed the unitarity problem in cross section calculation of longitudinally polarized W and Z bosons scattering [33]. This section covers the simplest Higgs model in the SM.

A complex doublet of spin-0 scalar Higgs field is introduced as follow:

$$\phi = \begin{pmatrix} \phi^+ \\ \phi^0 \end{pmatrix} = \frac{1}{\sqrt{2}} \begin{pmatrix} \phi^1 - i\phi^2 \\ \phi^3 - i\phi^4 \end{pmatrix}. \tag{2.36}$$

The Lagrangian of Higgs scalar field can be written down generally in the EW theory:

$$\mathcal{L}_H = (\mathcal{D}^{\mu}_{L}\phi)^{\dagger}(\mathcal{D}_{\mu,L}\phi) - V(\phi^{\dagger}\phi), \tag{2.37}$$

where the gauge covariance derivative is just the left-handed EW derivative defined in (2.25). The Higgs potential is parametrized as

$$\begin{aligned} V(\phi) &= \mu^2(\phi^{\dagger}\phi) + |\lambda|(\phi^{\dagger}\phi)^2 \\ &= \mu^2|\phi|^2 + |\lambda||\phi|^4, \end{aligned} \tag{2.38}$$

the two parameters introduced in the Higgs potential are λ and μ, which represents the strength of self-coupling term and mass of the scalar field, respectively.

The 2-dimensional shape of the Higgs potential is demonstrated in Figure 2.2 for two different sign of the μ^2 parameter. The ground state of the Higgs is determined by minimizing the potential $V(|\phi|)$. For $\mu^2 > 0$, the solution for $\frac{\partial V}{\partial|\phi|} = 0$ is at $|\phi| = 0$, which corresponds to the ground state of the vacuum with a $U(1)$ symmetry. However, for $\mu^2 < 0$, the minimum energy is not at the unstable state at $|\phi| = 0$, but at $|\phi| = \sqrt{-\mu^2/2|\lambda|} \equiv v/\sqrt{2}$ where v is the vacuum expectation value, and the $U(1)$ symmetry is "spontaneously broken". The ground state of the scalar field can be selected as

$$\langle\phi_0\rangle = \begin{pmatrix} 0 \\ \frac{v}{\sqrt{2}} \end{pmatrix}. \tag{2.39}$$

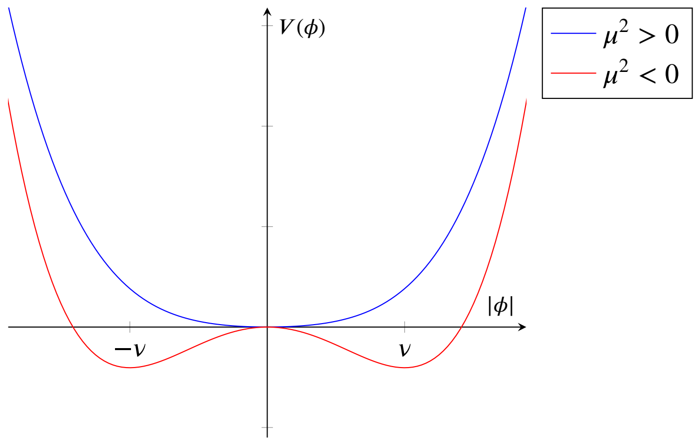

Fig. 2.2 Illustration of the shape of the Higgs potential $V(\phi)$.

It can be proved that the ground state breaks the $SU(2)_L$ and $U(1)_Y$ symmetries but preserves the $U(1)_{EM}$ electromagnetic symmetry [15]. The non-zero vacuum expectation implies that the Higgs field ϕ and its interactions with other fields do not vanish even in the absence of any excitation.

The Higgs field can be shifted and expanded around its minimum according to

$$\phi = exp(\frac{i\zeta \cdot \tau}{2v}) \begin{pmatrix} 0 \\ (v + H(x))/\sqrt{2} \end{pmatrix}, \tag{2.40}$$

where the exponential term absorbs the three degrees of freedom in (2.36). Here the $\zeta_i(x)$ (i = 1, 2, 3) represents massless Goldstone bosons [2] and the Higgs boson H(x) is the massive scalar boson, which will be derived below. The unitary gauge [15] can be selected without changing the underlying physics:

$$\phi \to \phi' = exp(-\frac{i\zeta \cdot \tau}{2v})\phi = \begin{pmatrix} 0 \\ (v + H(x))/\sqrt{2} \end{pmatrix}. \tag{2.41}$$

The dependence on ζ is removed and the term can be understood as being absorbed by gauge fields b_μ.

Applying the expansion (2.41) on the kinematic part of the Lagrangian (2.37) leads to

$$\frac{1}{2}\partial^\mu H \partial_\mu H + \frac{1}{8}g^2(v + H)^2|b^1_\mu + ib^2_\mu|^2 + \frac{1}{8}(v + H)^2|g' b^3_\mu - g\mathcal{A}_\mu|^2. \tag{2.42}$$

With the linear combination of the EW gauge fields to get the physical gauge bosons as shown in the previous section, the mass terms in the Lagrangian can be identified and written down as

$$M_W = \frac{gv}{2} \tag{2.43}$$

$$M_Z = \frac{\sqrt{g^2 + g'^2}}{2}v = \frac{M_W}{cos\theta_W}. \tag{2.44}$$

The measured values of gauge boson masses are $M_W = 80.379$ GeV and $M_Z = 91.1876$ GeV [26]. There is no mass term for A_μ, therefore γ remains massless. In addition to the gauge boson mass terms, there are also interaction terms between single Higgs and di-Higgs with the ZZ and WW boson pairs. Specifically, the HZZ interaction coupling is M_Z^2/v and the HWW coupling is $2M_W^2/v$. These interaction couplings are proportional to the vector boson mass-squared.

The same expansion on the Higgs potential (2.38) leads to

$$V(\phi) = -\frac{\mu^4}{4\lambda} - \mu^2 H^2 + \lambda v H^3 + \frac{\lambda}{4} H^4. \tag{2.45}$$

Clearly, the λ can be interpreted as the coupling strength of self-interaction of Higgs field, and the Higgs mass can be written down as

$$m_H = -\sqrt{2\mu^2} = \sqrt{2\lambda v^2}. \tag{2.46}$$

In summary, through the choice of the Higgs potential, $V(\phi)$, the symmetry is broken at the vacuum state. The massless Goldstone bosons are absorbed into the weak gauge bosons and give them masses. The EM interaction gauge boson, γ, remains massless. The symmetry breaking mechanism also predicted the existence of a massive scalar Higgs boson. There are two parameters related to the Higgs field: vacuum expectation value v measured to be around 246 GeV and the its self-interaction constant λ. With Higgs boson mass measured at the LHC as $125.09 \pm 0.21(\text{stat}) \pm 0.11(\text{syst})$ [34], λ is determined to be 0.13. Effectively the electroweak theory has two parameters: masses of W and Z bosons, which is connected by the weak mixing angle.

2.2.1 Masses of fermions

In the Lagrangian (2.37), it is possible to add interaction terms between fermions and Higgs field without breaking the $SU(2)_L \bigotimes U(1)_Y$ symmetry. The interaction terms take the following form:

$$\mathcal{L}_{Yukawa} = -\xi_f \bar{L}\phi R + h.c., \tag{2.47}$$

where ξ_f is the Yukawa coupling constant between the Higgs field and a specific fermion, and the $h.c.$ means Hermitian conjugate of the form terms. Substituting ϕ with the Higgs ground state term (2.41) after the symmetry breaking, the Lagrangian becomes

$$\begin{aligned}\mathcal{L}_{Yukawa} &= -\frac{\xi_f v}{\sqrt{2}}(\bar{\psi}_L\psi_R + \bar{\psi}_R\psi_L) - \frac{\xi_f}{\sqrt{2}}(\bar{\psi}_L\psi_R + \bar{\psi}_R\psi_L)H \\ &= -m_f\bar{\psi}\psi - \frac{m_f}{v}\bar{\psi}\psi H,\end{aligned} \tag{2.48}$$

where $m_f \equiv \xi_f v/\sqrt{2}$ is the mass of the fermion. There are 9 massive fermions in the SM theory, so there are 9 Yukawa Lagrangian terms in the form of (2.47), each with a different Yukawa constants that have to be determined by experiments.

Chapter 3 Phenomenology on the Large Hadron Collider

In the previous chapter, the SM Lagrangians and the Higgs mechanism are briefly introduced. This chapter makes a connection between theory and experimental measurements. It covers the calculation of physics properties for hadron accelerators, Monte Carlo event generation, and Higgs phenomenology at the LHC.

3.1 Cross Section and Luminosity

From an experimental point of view, the most important quantity for any physics process prediction is the rate of interesting physical events, or the number of scattering happening per unit time from particle collisions in colliding beams. It can be expressed as multiplication of two components, cross section σ and instantaneous luminosity $\mathcal{L}$:

$$R \equiv \frac{dN}{dt} = \sigma \cdot \mathcal{L}. \tag{3.1}$$

A cross section is defined as the effective scattering area of a bunch A for each particle in the other bunch B, i.e. assuming all particles from bunch B in the effective area scatter and the areas in bunch A doesn't overlap due to the particle density:

$$\begin{aligned} \sigma &\equiv \frac{\text{Number of interactions in one bunch crossing}}{N_A \cdot N_B/\mathcal{A}} \\ &= \frac{\text{Number of interactions per unit time}}{N_A N_B f/\mathcal{A}} \\ &\equiv \frac{R}{\mathcal{L}}, \end{aligned} \tag{3.2}$$

where N_A, N_B are the number of particles in bunch A and B, f is the frequency of collision and $\mathcal{A}$ is the cross-sectional area of the two bunches.

From a Lagrangian, the matrix element (ME) $M_{fi} \sim \langle f|H|i\rangle$ can be calculated. It is defined as the probability amplitude of a transition from initial state i to final state f, where those quantum states are usually momentum states of elementary particles. The cross section for a transition of two initial particles to final particles: $i \equiv a + b \rightarrow f_1 + f_2 ... f_n \equiv f$ is written as

$$\sigma_{i\rightarrow f} = \frac{1}{2s}\frac{1}{(2\pi)^{3n_f-4}} \int \Big(\prod_{f=1}^{n_f} \frac{d^3 p_f}{2E_f}\Big)\delta^4\Big(\sum_{f=1}^{n_f} p_f - p_a - p_b\Big)|\mathcal{M}_{fi}|^2. \tag{3.3}$$

The ME M_{fi} can be calculated perturbatively in theory:

$$|\mathcal{M}| = |M^0| + |M^1| + |M^2| \cdots, \tag{3.4}$$

where the $|M^0|$ is "leading-order" (LO) expansion, $|M^1|$ is "next-to-leading-order" (NLO) expansion, $|M^2|$ is "next-to-next-to-leading-order" (NNLO) expansion, and so forth. Many analyses carried out on the ATLAS experiment use proton-proton collisions data, therefore, all calculation of ME need to be done under the QCD theory. A non-physical parameter "renormalization scale" μ_R would need to be chosen in the QCD calculation to resolve the logarithmic divergences in loop diagrams. The dependence of ME on the scale is removed at infinite perturbation-order. In reality, the calculation of ME is up to a finite order, and the ME depends on the choice of μ_R. The impact of the change of scale is considered as a theoretical systematic uncertainty in the analysis. To reduce this uncertainty, the scale needs to be chosen at a reasonable value similar to the momentum transfer of the process. For $pp \to ZZ^* \to 4\ell$ processes, the scale is usually chosen to be half of invariant mass of four leptons $\frac{m_{4l}}{2}$.

Cross sections are purely determined by the underlying physics. They have the unit of area which is usually chosen to be "barn", or "b", which equals to $10^{-24}cm^2$.

Usually a detector cannot cover the full solid angle of 4π because it needs to leave space for beam pipe and there are usually gaps between sub-detectors. Besides, very soft particles cannot be efficiently detected and reconstructed in the LHC experiments. Therefore kinematic requirements are used to select sensitive phase space called fiducial region. The fiducial cross section, σ_{fid} is factorized by the acceptance "A" multiplied the total cross section σ_{tot}:

$$\sigma_{fid} = A \cdot \sigma_{tot} \tag{3.5}$$

3.1.1 Parton Distribution Function

A proton is not an elementary particle since it consists of valence quarks, sea quarks and gluons. According to the QCD factorization theorem [35], the calculation of inelastic hard scattering with a large momentum transfer Q^2 can be separated from soft processes. Hard scattering are the main interest on the hadron colliders because new particles can be generated, such as Higgs. Figure 3.1 shows the schematics for the process

$$A + B \to C + X, \tag{3.6}$$

where the X is the remnants of the incoming hadrons. The underlying partonic level process is

$$a + b \to c. \tag{3.7}$$

The X_1 and X_2 are defined as underlying events for the process.

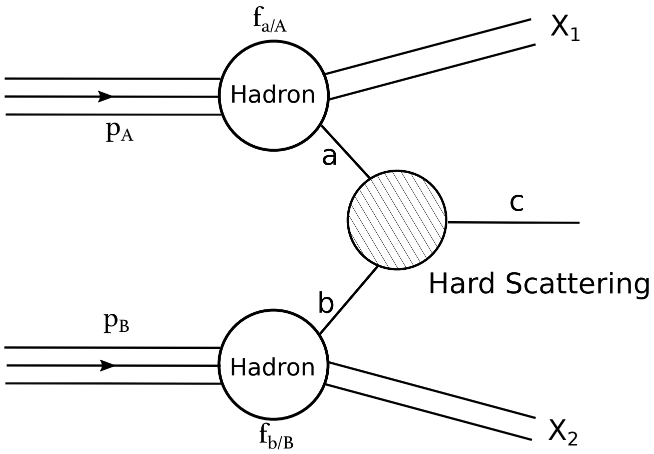

Fig. 3.1 Schematics of proton-proton collisions.

The total cross section can be calculated by integrating the cross section (3.3) over momentum and sum over all possible initial parton particles:

$$\sigma(A + B \to C + X) = \sum_{a,b} \int dx_a dx_b f_{a/A}(x_a, Q^2) f_{b/B}(x_a, Q^2) \sigma_{a+b\to c}, \tag{3.8}$$

where $f_{a/A}(x_a, Q^2)$ is the distribution of the momentum fraction x_a for parton a, at the momentum transfer Q^2, called parton distribution function (p.d.f.). The scale Q^2 here is called "factorization scale" μ_F, which is another non-physical parameter chosen to separate the hard and soft scattering. Similar to μ_R, the dependence of cross section on μ_F as a systematic uncertainty will also need to be taken into consideration.

Figure 3.2 is one of the p.d.f. set from PDF4LHC15 as a demonstration. In data analysis, when the theoretic models are used, such as to determine the signal acceptance and to estimate the background contributions, different p.d.f. set are selected to evaluate the impact on the result as a source of theoretical systematic uncertainty.

3.1.2 Luminosity

From (3.2), the definition of instantaneous luminosity in collision is already given implicitly:

$$\mathcal{L} = \frac{N_A N_B f}{\mathcal{A}}. \tag{3.9}$$

If the beam particle profile follows Gaussian distribution around the beam center with horizontal and vertical deviations σ_x and σ_y, the beam size $\mathcal{A}$ is given by

$$\mathcal{A} = 4\pi\sigma_x\sigma_y. \tag{3.10}$$

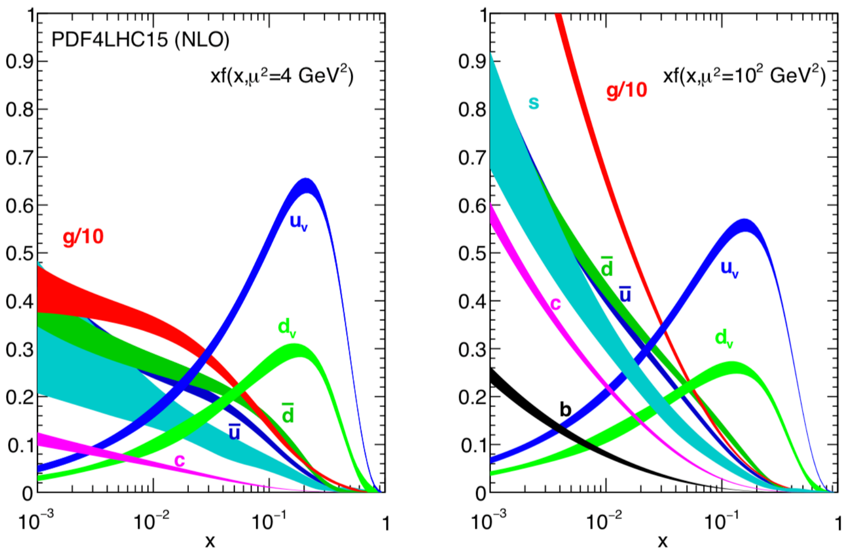

Fig. 3.2 PDF4LHC15 at scale $Q^2 = 4$ GeV^2 on the left and scale $Q^2 = 10^2$ GeV^2 on the right, as a function of x [36].

To predict the total number of events produced by the accelerator in a certain time interval, the calculation can be made as the following

$$N = \int R dt = \sigma \int \mathcal{L} dt \equiv \sigma L. \tag{3.11}$$

Luminosity is purely determined by the beam condition of the accelerator. Integrated luminosity has the unit of inverse area and at the LHC, we often use the unit of fb^{-1} (= $10^{-39} cm^{-2}$).

3.2 Simulated Event Generation at Hadron Colliders

In colliders, a collision of beam particles is called an event. In line with the non-determinism of each individual quantum system, each event would randomly have different final state particles and kinematic topology. However, the large data behavior of events forms a probability distribution functions, which can be studied against theory predictions. To simulate different physics processes, Monte Carlo (MC) generators programs are widely used to sample the probability distributions by producing weighted events, so that sampled spectra can match with what is predicted by theory as much as possible. The main aspects of the production is summarized below:

- Hard scattering: the main part of the event generation is to calculate the cross sections and to produce the event kinematic topology. The technique for calculating total cross section is described in section 3.1. Once the total cross section is calculated for the given process, based on the probability distribution, an event that contains different particles created in the pp collisions is generated with certain kinematics.

- Particle decay: models decay of unstable particles, such as W and Z, produced from hard scattering. They will decay almost promptly before reaching the detector. The particle decay modes for different final states are specified either by users of the generator or done on a probabilistic basis for inclusive decay mode. The lifetime parameters can be derived from coupling strength, or from measurements in previous experiments.
- Parton shower: softer gluons emitted due to QCD radiation, which is modeled on top of the hard scattering. They can further radiate in a chain reaction which forms showers. The emission is usually treated on a probabilistic basis, depending on underlying physics parameters. The choice of the parameters form a source of systematic uncertainty in theoretical models.
- Hadronization: as described in section 2.1.2, quarks and gluons need to go through "hadronization" process to form baryons and mesons. Those particles created in this process are appeared as "jets" in detectors. The hadronization process cannot be calculated non-perturbatively. It is described phenomenologically and need to be calibrated and tuned with measurements in experiments.
- ISR and FSR: initial state and final state particles with color or electric charge can radiate gluon or photon as initial state radiation (ISR) or final state radiation (FSR).
- Underlying events: the debris from the hard scattering hadrons can also take part in a soft interaction. Similarly, this kind of soft processes is modeled phenomenologically.
- Pile-up effect: as the beam luminosity increases and the number of particles inside the beam bunches increases, the chances of multiple inelastic collisions increase. Such multiple inelastic interactions within the beam bunch collision time interval is called pile-up. The average inelastic interaction per bunch crossing is denoted as $\langle \mu \rangle$ in MC simulations and in physics analysis.

The overall theoretical predictions are derived by summing up the calculations for all individual processes, treating them independently. In quantum field theory, when two processes have the same initial and final state, but with different intermediate states, the interference term needs to be considered by cross multiplication of two sets of Feynman diagrams. For practicality, if the interference contribution is very small, for example a very narrow Higgs resonance interfering with the SM continuum background process, two processes are simply summed up independently. But in case the interference cannot be ignored, its effect need to be taken into account in the generator calculations.

Once the theoretical calculations and simulations are performed at the particle level, simulated events need to pass the detector simulation and electronics digitization. More details on this topic related to this thesis work will be covered in section 4.2.6.

3.3 Higgs Physics at the LHC

The Higgs boson was discovered jointly by ATLAS and CMS in 2012 [10-11]. The Higgs boson production cross section and its decay branching ratios are closely related to its mass, therefore related to the vacuum expectation value. The mass is measured to be $125.09 \pm 0.21(\text{stat}) \pm 0.11(\text{syst})$ GeV in 2015 [34] and this value is used to calculate the cross sections and branching ratios used in this thesis.

The major Higgs boson production modes at the LHC are gluon-gluon fusion (ggF), vector boson fusion (VBF), associated production with a vector boson (VH), and associated production with a pair of top/antitop quarks (ttH), as shown in Fig 3.3 Feynman diagrams (a), (b), (c), (d), respectively. The gluon-gluon initiated associated production with a Z boson (ggZH) has a non-negligible contribution and is often included in the ZH process. The Feynman diagrams are shown in Figure 3.4. Produced in a similar Feynman diagram as ttH, bbH process has a smaller contribution since the bottom quark is much lighter than the top quark and the coupling with Higgs is smaller. The total cross sections for Higgs boson production with $m_H = 125.09$ GeV at center-of-mass energy of 13 TeV are summarized in Table 3.1.

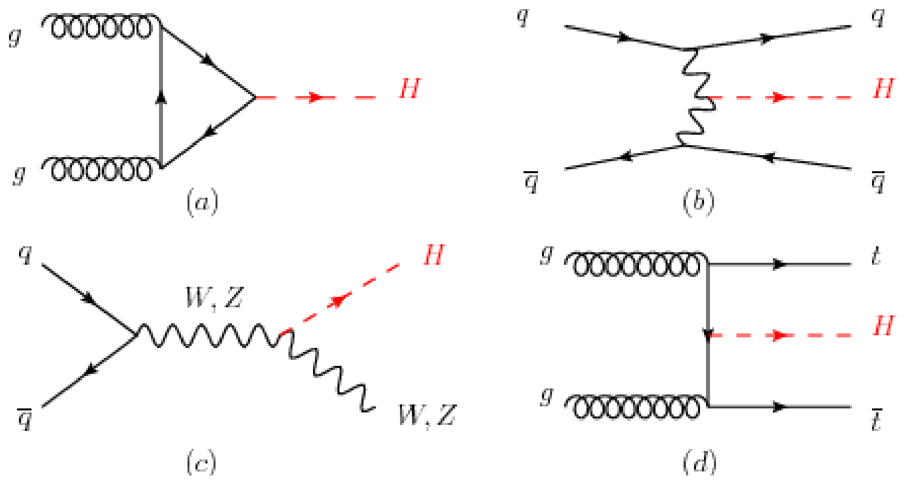

Fig. 3.3 Major production modes of the Higgs on the LHC: (a) gluon-gluon fusion; (b) vector boson fusion; (c) quark-initiated associated production with a vector boson (d) associated production with a pair of top/antitop quarks [37].

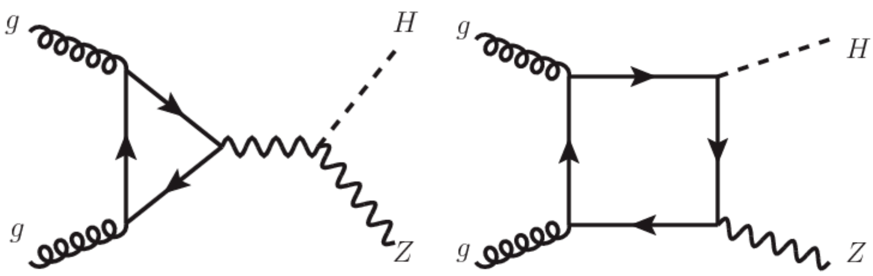

Fig. 3.4 Higgs production mode ggZH via a quark loop: the left plot is the production through gauge coupling and the right plot through Higgs mechanism and Yukawa coupling [38].

Table 3.1 Summary of Higgs production cross section for $m_H = 125.09$ GeV at $\sqrt{s} = 13$ TeV [39]. The uncertainty of the cross section is a combination of scale, p.d.f. and QCD coupling strength α_s uncertainties assuming no correlation. The cross section of ZH includes that of ggZH.

Production mode	Cross section (pb)	Precision
ggF	48.517 ±2.448	$\mathrm{N^3LO}$ QCD + NLO EW
VBF	3.779 ±0.081	NNLO QCD + NLO EW
WH	1.369 ±0.027	NNLO QCD + NLO EW
ZH	0.882 ±0.036	NNLO QCD + NLO EW
(ggZH)	0.1227 ±0.031	NLO QCD + NLO EW
ttH	0.507 ±0.050	NLO QCD + NLO EW
bbH	0.486 ±0.116	5FS NNLO QCD and 4FS NLO QCD

The Higgs decay branching ratio is summarized in Table 3.2. The total branching ratio for $H \to ZZ^* \to 4\ell$ is only 1.251×10^{-4} because it includes branching ratio of leptonic decays of both Z bosons, $Z \to \ell\ell$ ($\ell = e, \mu$). Even though the 4ℓ decay channel has very small branching fraction, it is the cleanest and most competitive Higgs boson decay channels at the LHC for Higgs physics studies.

The total decay width of the Higgs boson is predicted to be $\sim$ 4.1 MeV, which is much smaller than the detector resolution of about 2 GeV. Thus a direct measurement of the natural width of the Higgs boson is difficult. However, the Higgs boson can also be produced away from the resonant peak at high mass region, which is called off-shell region. The interference of off-shell Higgs with the SM continuum $gg \to ZZ^*$ production at the high mass region will cause a modification to the event rate, providing an indirect way to probe the natural width of the Higgs boson. This motivated the author of this thesis to measure the lineshape of inclusive $ZZ \to 4\ell$ production in a very broad

Table 3.2 Summary of Higgs decay branching ratio for $m_H = 125.09$ GeV [39], together with the theoretical uncertainty.

Decay mode	Branching ratio	Relative uncertainty (%)
bb	$5.809 \cdot 10^{-1}$	$^{+1.238}_{-1.263}$
WW^*	$2.152 \cdot 10^{-1}$	$^{+1.533}_{-1.525}$
gg	$8.180 \cdot 10^{-2}$	$^{+5.148}_{-5.081}$
$\tau\tau$	$6.256 \cdot 10^{-2}$	$^{+1.647}_{-1.633}$
cc	$2.884 \cdot 10^{-2}$	$^{+5.550}_{-1.971}$
ZZ^*	$2.641 \cdot 10^{-2}$	$^{+1.533}_{-1.525}$
$\gamma\gamma$	$2.270 \cdot 10^{-3}$	$^{+2.090}_{-2.053}$
$Z\gamma$	$1.541 \cdot 10^{-3}$	$^{+5.811}_{-5.832}$
$\mu\mu$	$2.171 \cdot 10^{-4}$	$^{+1.677}_{-1.704}$

mass region.

The on-shell and off-shell signal strength for gluon-gluon fusion process are given by [40]:

$$\mu_{\text{off-shell}} = \frac{\sigma^{gg\to H^*\to ZZ}_{\text{off-shell}}}{\sigma^{gg\to H^*\to ZZ}_{\text{off-shell,SM}}} = \kappa^2_{g,\text{off-shell}} \cdot \kappa^2_{Z,\text{off-shell}} \tag{3.12}$$

$$\mu_{\text{on-shell}} = \frac{\sigma^{gg\to H^*\to ZZ}_{\text{on-shell}}}{\sigma^{gg\to H^*\to ZZ}_{\text{on-shell,SM}}} = \frac{\kappa^2_{g,\text{on-shell}} \cdot \kappa^2_{Z,\text{on-shell}}}{\Gamma_H/\Gamma_H^{\text{SM}}}, \tag{3.13}$$

where κ are the corresponding coupling modifier. Assuming that off-shell and on-shell modifier are the same, the division of (3.12) and (3.13) provides the total width of the Higgs. A beyond the Standard Model (BSM) Higgs decay width is a hint for existence of exotic particles that interacts with the Higgs boson.

3.3.1 The SM Background in Four-lepton Final State

The main background for $H \to 4\ell$ channel is the SM ZZ production decaying into four leptons. The Feynman diagrams are shown in Figure 3.5. The largest contribution is from quark-induced t-channel process $q\bar{q} \to 4\ell$ 3.5(a). Those ZZ continuum background forms the largest background in the Higgs physics studies with four-lepton final state. In the on-shell Higgs production signal region, the SM ZZ production background contributes approximately one fourth of all the four-lepton events after the final Higgs event selection.

The lineshapes of various ZZ production processes can be seen in Figure 3.6. For $q\bar{q}/gg \to 4\ell$ continuum processes, there's a turn-on shoulder at $2m_Z$ due to both Z

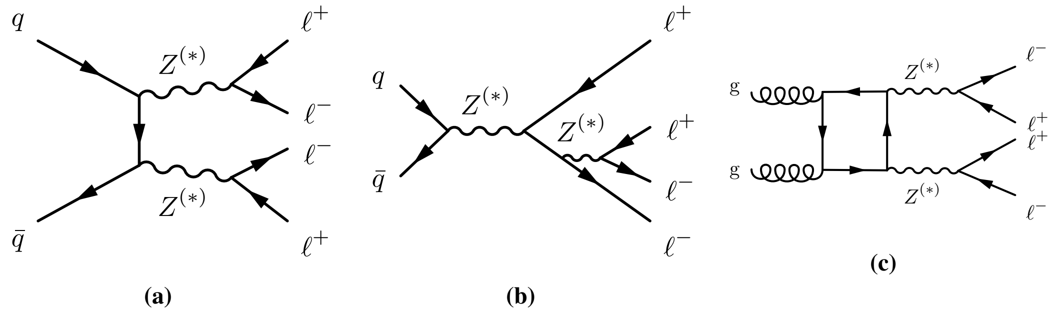

Fig. 3.5 The continuum SM ZZ production processes: (a) t-channel $q\bar{q} \to 4l$ (b) internal conversion in Z boson decays; (c) gluon-initiated $gg \to 4l$ production via a quark loop.

bosons becoming on-shell. The Z-mass peak comes from the contribution of the internal radioactive conversion process. For gluon-gluon fusion Higgs production, an off-shell contribution can be seen between 200 to 800 GeV in the plot (the blue dash line). This process have a non-negligible destructive interference with the gluon-initiated $gg \to 4l$ through a quark loop process (Figure 3.5(c)) in the off-shell region. The inclusion of the Higgs signal and its interference lead to an overall reduction of the continuum ZZ production rate. The so-called SBI process includes the off-shell Higgs signal (S), the SM gg continuum background (B) and their interference (I). The detailed effect in related differential cross section are shown in Figure 3.7.

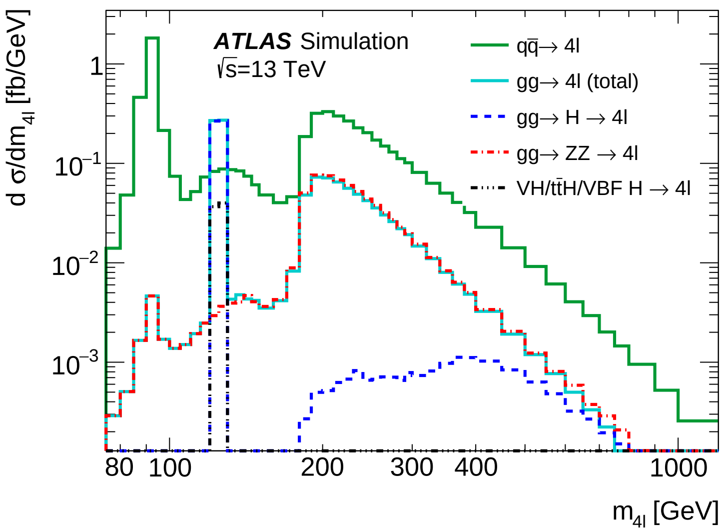

Fig. 3.6 Lineshapes of major $ZZ \to 4l$ production processes $q\bar{q} \to 4l$, $gg \to 4l(total)$(including interference effect), $gg \to H \to 4l$, $gg \to ZZ \to 4l$ and minor production mode of the Higgs [13].

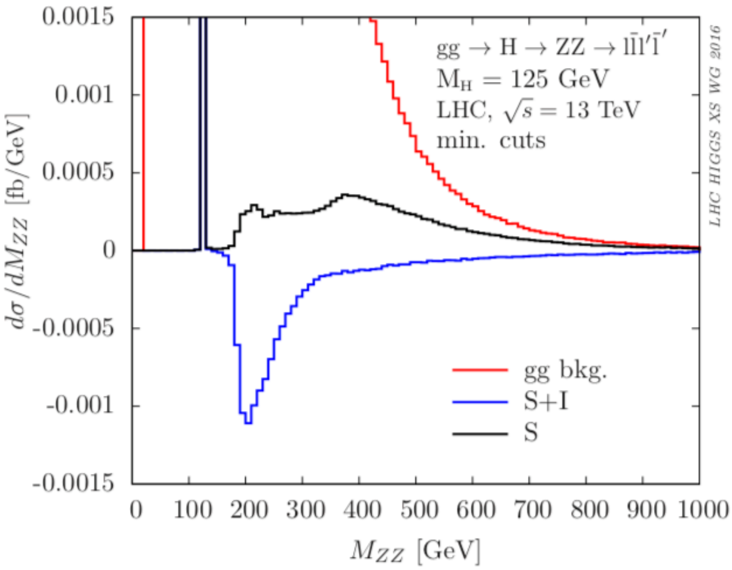

Fig. 3.7 The lineshapes of $gg \to 4l$ considering SM process, Higgs signal and signal plus interference process. The interference is destructive and have a negative contribution to inclusive $gg \to 4l$ process [39].

Chapter 4 Experimental Apparatus

4.1 The Large Hadron Collider

The Large Hadron Collider (LHC) [41] is currently the largest high energy experimental facility in the world. The main ring of LHC is a 26.7 kilometer-long double-ring circular superconducting accelerator at the European center for particle physics (CERN) located at Geneva, Switzerland. The LHC was built from 1998 to 2008 in the tunnel at around 100 meters underground, the tunnel is previously used by Large Electron Positron (LEP) collider. The LHC is designed to accelerate protons up to 7 TeV to reach a center-of-mass energy of $\sqrt{s} = 14$ TeV and an instantaneous luminosity of $1 \times 10^{34} cm^{-2} s^{-1}$ [42-44]. It is also capable of colliding high energy heavy ions. As can be seen in the schematics for the whole facility complex (Figure 4.1), the LHC hosts four main experiments among its eight collision points. Two general purpose detectors ATLAS [1] and CMS [2] are designed for high p_T new physics search like the Higgs boson and alternative schemes for the spontaneous symmetry-breaking mechanism. In addition, the search for BSM phenomena are conducted including Supersymmetry [26, 45], new gauge bosons, leptoquarks [46], graviton, and contact-interactions, which explore the fermion internal structures. The unbeatable high luminosity provided by the LHC will also allow the precision measurements of the electroweak production cross sections ever measured before and the properties of the heavy top quarks. The LHCb [3] experiment focuses on studies of the b-quark related properties including rare decays and CP violating decays of b-hadrons. The ALICE [4] experiment specializes in studying strong interaction through collisions of heavy ions, which includes proton structure, quark gluon plasma [47] and etc.

The basic principle of building the high energy physics research facility is that by using increasingly larger accelerators in series, the energy of protons are brought up efficiently. Such design is also budget friendly because existing accelerators facilities are reused. As shown in Figure 4.1 the protons are produced in bunches by stripping electrons away from hydrogen atoms with a strong electric field. The Linac 2 accelerates proton to 50 MeV with a series of radiofrequency (RF) cavities. Protons are then injected into Booster to be accelerated to 1.4 GeV. The following Proton Synchrotron

[1] A Toroidal LHC ApparatuS

[2] Compact Muon Spectrometer

[3] Large Hadron Collider beauty

[4] A Large Ion Collider Experiment

(PS) further accelerates protons up to 25 GeV. And the Super Proton Synchrotron (SPS) proceeds to accelerate protons before injecting to LHC at an energy of 450 GeV for the final acceleration and collisions at each experiment center. The whole acceleration process from initial filling to stable beams takes roughly 20 minutes. Once the beam is stable, collision will take place at interaction sites. After the beams have lost a considerable amount of protons, a new fill process will start, and one such data taking period is named as "run" with a unique run number. Each run is segmented into luminosity blocks where the operating conditions are assumed to be constant, especially the instantaneous luminosity [48]. The instantaneous luminosity of the LHC can be taken from (3.9) and

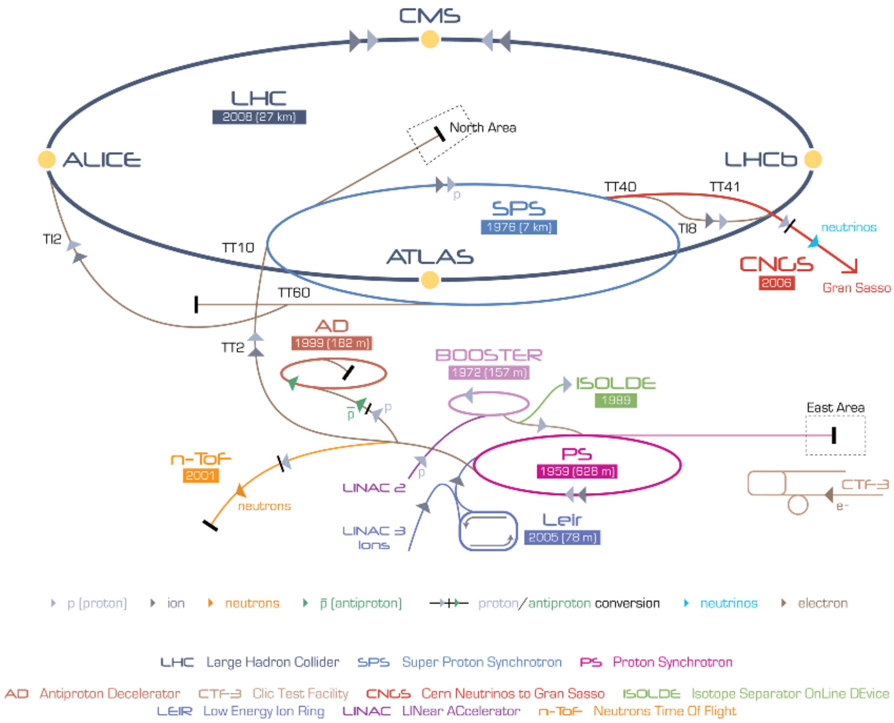

Fig. 4.1 Schematics of LHC and its injection chain including Linac 2, Booster, PS, SPS [49].

re-expressed [41]:

$$\mathcal{L} = \frac{N_A N_B f}{\mathcal{A}} = \frac{N_b^2 n_b f_{rev} \gamma}{4\pi \epsilon_n \beta^*} F, \tag{4.1}$$

where $N_b = N_A = N_B$ are number of particles per bunch. The frequency of collision $f = f_{rev} n_b$ is the multiplication of frequency of revolution and number of bunches in each beam. The remaining factors comes from the beam cross-section area parameters, including ϵ, the emittance of the beams, β^*, related to the transverse displacement of particles, F, the geometric reduction factor, and γ, the beam relativistic Lorentz factor. The designed parameters are summarized in Table 4.1.

During the first year of commissioning, the machine had an unfortunate incident in 2008 that damaged a number of superconducting magnets, delaying the LHC operation schedule and lowering the initial energy of the machine. During 2009 to 2012, the Run 1 data taking, the LHC energy was gradually brought to 8 TeV. The data collected led to the discovery of Higgs boson in 2012. In the Run 2 period between 2015 to 2018, the LHC operates at $\sqrt{s} = 13$ TeV with a luminosity peaked at $2.1 \times 10^{34} cm^{-2} s^{-1}$, exceeded its designed luminosity by a factor of two. The detailed operational parameters in the Run 2 are summarized in Table 4.1. The Run 2 was a very successful operation of the LHC that bring unprecedented luminosity for physics studies. As shown in Figure 4.2, the LHC delivered total 156 fb^{-1} data, and the ATLAS experiment collected total 147 fb^{-1} data, corresponding to an online data acquisition efficiency greater than 94%. It is planned that the LHC will reach its final designed energy of 14 TeV in Run 3, starting in 2022.

Table 4.1 Design and Run 2 operational parameters of the LHC [50].

Parameter	Design	2018	2017	2016	2015
Energy [TeV]	7.0	6.5	6.5	6.5	6.5
Number of bunches	2808	2556	2556-1868	2220	2244
Number of bunches per train	288	144	144-128	96	144
Max. energy per beam [MJ]	362	312	315	280	280
β^*	55	25-30	30-40	40	80
Protons per bunch [10^{11}] N_b	1.15	1.1	1.25	1.25	1.2
Normalized emittance ϵ_n	3.75	1.8-2.2	1.8-2.2	1.8-2	2.6-3.5
Peak luminosity [$10^{34}\mathrm{cm}^{-2}\mathrm{s}^{-1}$]	1.0	2.1	2	1.5	<0.6
Half crossing angle [μrad]	142.5	130-150	120-150	140-185	185

4.2 The ATLAS Detector

The ATLAS detector [52-53], shown in Figure 4.3, at the LHC is the largest particle detector ever built for high energy experiment. It has backward-forward structures with symmetric cylindrical geometry and covers nearly the entire solid angle around the collision point. It consists of an inner tracking detector surrounded by a thin superconducting solenoid with magnetic field strength of 2 T, high precision electromagnetic and hadronic calorimeters, and a standalone precision muon spectrometer incorporating three large superconducting toroidal magnets, a barrel plus two end-cap systems.

The design philosophy of the ATLAS detector is to have very robust and precision electron, photon and muon measurements, and a large coverage for hadronic jet

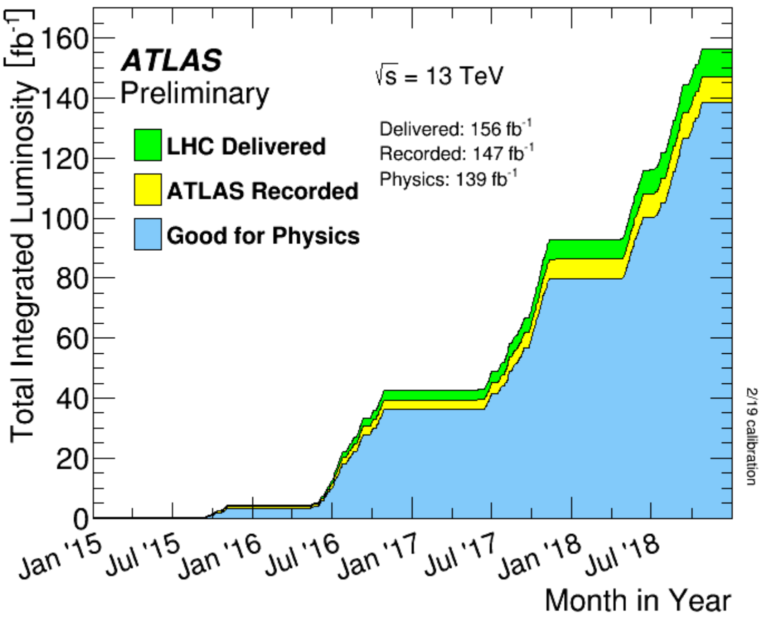

Fig. 4.2 Integrated luminosity versus time delivered to ATLAS (green), recorded by ATLAS (yellow) and certified to be good quality data (blue) during stable beams in Run 2 pp collision [51].

measurement with good energy resolution. In addition, the detector should be highly capable for precision event vertex measurement to separate the interaction vertex of the hard scattering event from the pile-up events, as well as to tag the b-hadrons with high efficiency from the secondary vertex of the b-decays. The general performance goal of the detector design is summarized in Table 4.2.

Table 4.2 General performance goals of the ATLAS detector [55]. Note that, for high-p_T muons, the muon-spectrometer performance is independent of the inner-detector system. The units for E and p_T are in GeV.

Detector component	Required resolution	η coverage	
		Measurement	Trigger
Tracking	$\sigma_{p_T}/p_T = 0.05\ \%\ p_T \bigoplus 1\ \%$	$\pm$ 2.5	
EM calorimetry	$\sigma_E/E = 10\ \%/\sqrt{E} \bigoplus 0.7\%$	± 3.2	± 2.5
Hadronic calorimetry (jets)			
barrel and end-cap	$\sigma_E/E = 50\ \%/\sqrt{E} \bigoplus 3\%$	± 3.2	
forward	$\sigma_E/E = 100\ \%/\sqrt{E} \bigoplus 10\%$	$3.1 < \lvert\eta\rvert < 4.9$	
Muon spectrometer	$\sigma_{p_T}/p_T = 10\ \%$ at $p_T = 1$ TeV	$\pm$ 2.7	$\pm$ 2.4

The ATLAS uses right-handed Cartesian coordinate system. The origin is at the interaction point (IP), the x axis points to the center of the LHC ring, the y axis points upwards, and the z axis lies along the beam pipe anticlockwise. In the transverse x-y

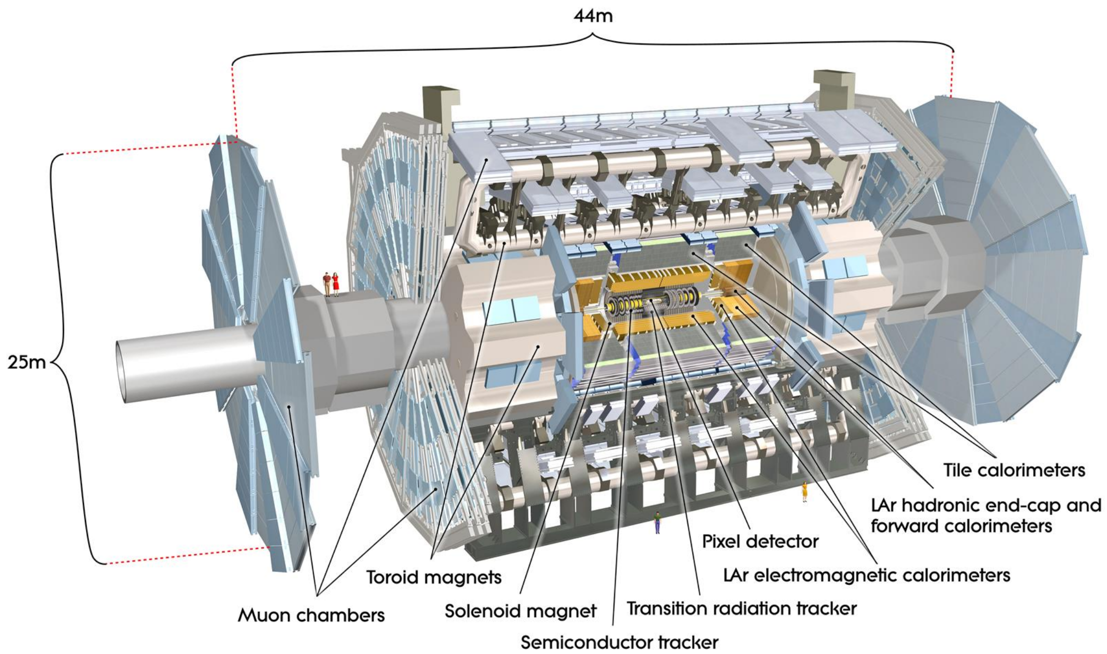

Fig. 4.3 Overview of the ATLAS detector [54].

plane, polar coordinates (r, ϕ) are used to describe detector geometry, and transverse momentum p_T and transverse energy E_T are usually used instead of total momentum and energy. The polar angle θ is defined as the angle with respect to the z axis. But pseudorapidity is used to instead to describe approximately massless particles, defined as η = -ln tan(θ/2) . For massive particles, rapidity $Y = \frac{1}{2}$ ln $[(E + p_z)/(E - p_z)]$ is used instead. The angular distance $\Delta R= \sqrt{\Delta\eta^2 + \Delta\phi^2}$ is used to describe the separation of particles.

The ATLAS sub-detector systems are briefly described in following sections.

4.2.1 Inner Tracker

The inner-detector (ID) system is immersed in a 2 T axial magnetic field and provides charged-particle tracking in the pseudorapidity range $|\eta| < 2.5$. The sketch of the ID is shown in Figure 4.4 The high-granularity silicon pixel detector covers the vertex region and typically provides four measurements per track, the first hit being normally in the insertable B-layer (IBL) installed before the start of Run 2 [56-57]. It is followed by the silicon microstrip Semiconductor Tracker (SCT) which usually provides eight measurements per track. These silicon detectors are complemented by the transition radiation tracker (TRT), which enables radially extended track reconstruction up to $|\eta|$ = 2.0. The TRT also provides electron identification information based on the fraction of hits (typically 30 in total) above a higher energy-deposit threshold corresponding to transition radiation. The Figure 4.5 shows the expected resolution of the ID as a function of $|\eta|$ of particles.

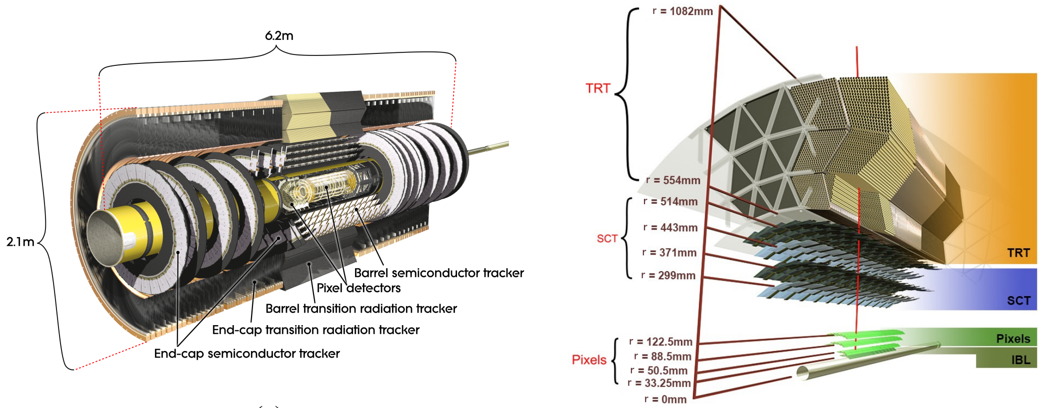

(a)

(b)

Fig. 4.4 (a) Cut-away view [58] and (b) sketch of a barrel module of the ATLAS Inner Detector [59].

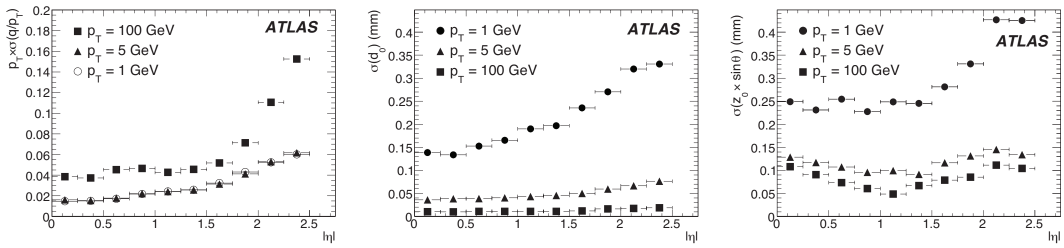

Fig. 4.5 Expected performance of momentum resolution (left), transverse impact parameter resolution (middle) and longitudinal impact parameter resolution (right) versus the η of particle for the ATLAS inner detector [58].

4.2.2 Calorimeters

ATLAS uses sampling type of calorimeter that provides a good granularity for spatial measurement. The calorimeter system covers the pseudorapidity range $|\eta| < 4.9$ and consist of the EM calorimeter which provides energy measurement for electrons, photons and the hadronic calorimeter which provides energy measurement for jets. Different materials and thickness is designed so that it provides a good containment of the EM and hadronic showers.

Within the region $|\eta| < 3.2$, electromagnetic calorimetry is provided by barrel ($|\eta| < 1.475$) and end-cap ($1.375 < |\eta| < 3.2$) high-granularity lead/liquid-argon (LAr) calorimeters, with an additional thin LAr presampler covering $|\eta| < 1.8$, to correct for energy loss in material upstream of the calorimeters. The cut-away view of the EM calorimeter is shown in Figure 4.6(a). The barrel consists of two identical half-barrels, separated by a small gap of 4 mm at z=0 and each end-cap consists of two coaxial wheels: an outer wheel covering the region $1.375 < |\eta| < 2$ and an inner wheel covering the region $2.5 < |\eta| < 3.2$. The total thickness of the EM calorimeter is > 22 radiation lengths (X_0) in the barrel and > 24 X_0 in the end-caps. This width is approximately the nuclear interaction length (λ) so that hadrons start interaction mostly after EM calorimeter. The layering of the calorimeter can be seen in Figure 4.6(b), in which the lead is the absorbing material that produces showering and LAr is the active material that will be ed by high energy electrons and photons to produce detector signal. The Figure 4.7 demonstrates the energy resolution of the EM calorimeter.

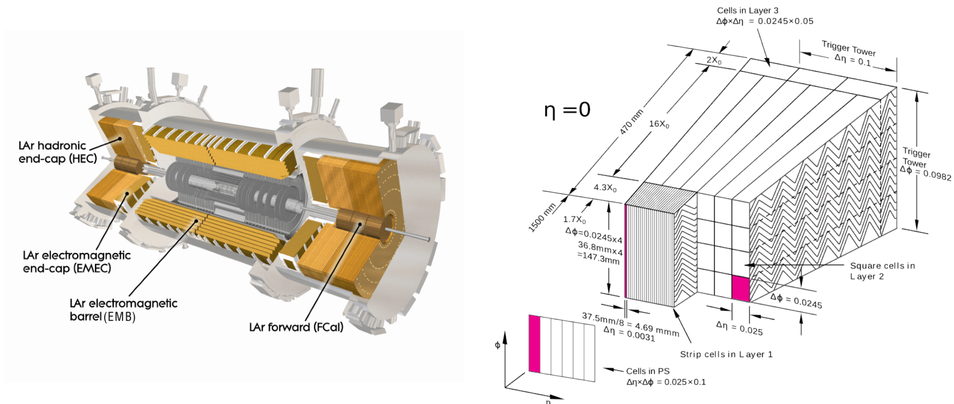

(a)

(b)

Fig. 4.6 (a) Cut-away view and (b) sketch of a barrel module of the ATLAS Liquid Argon calorimeter [60].

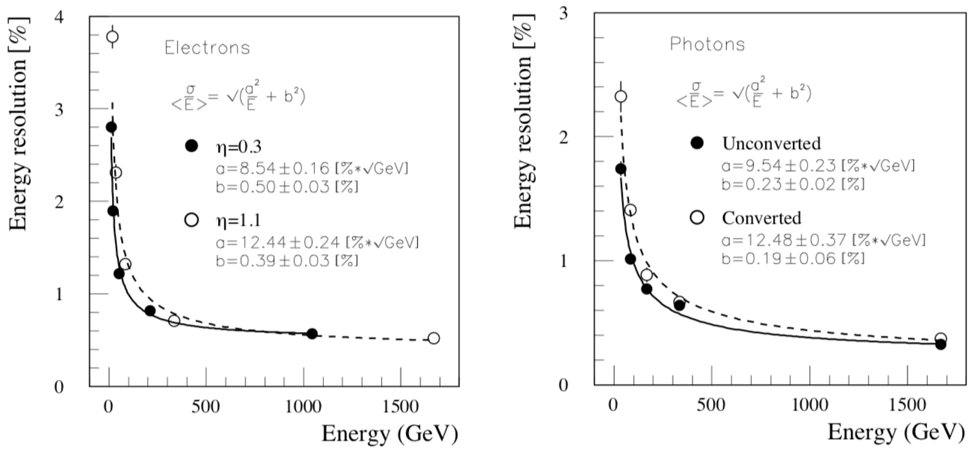

Fig. 4.7 Energy resolution for electrons (left) at $\eta = 0.3$ and $\eta = 1.1$ and photons (right) at $\eta = 1.1$, as a function of the energy [52].

Hadronic calorimetry is provided by the steel/scintillating-tile calorimeter(Figure 4.8(a)), segmented into three barrel structures within $\eta < 1.7$, and two copper/LAr hadronic end-cap calorimeters. The solid angle coverage is completed with forward copper/LAr and tungsten/LAr calorimeter modules optimized for electromagnetic and hadronic measurements respectively. The depth is between 7.4 to 9.7λ to allow showers to develop. The Figure 4.8(b) shows the energy resolution performance of the combined calorimetry.

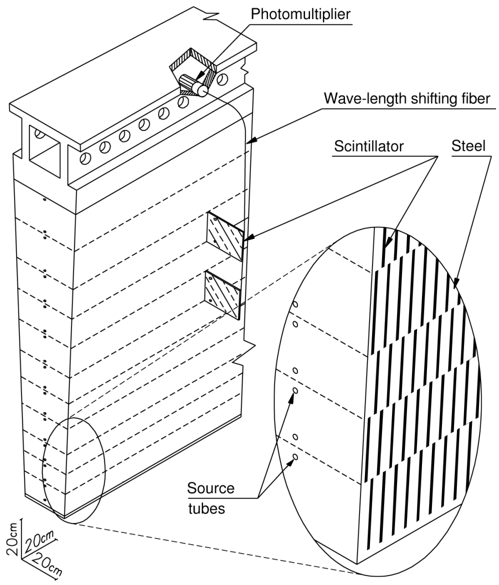

(a) Tile calorimeter wedge module.

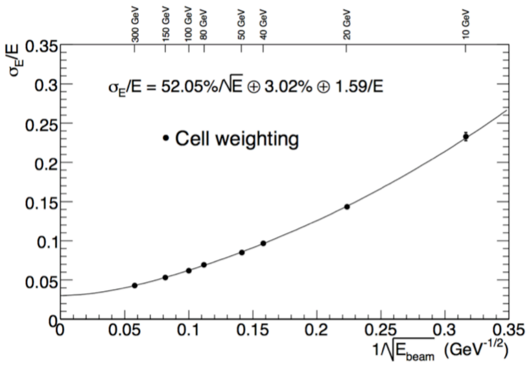

(b) Fractional energy resolution measured in pion test beam, for combined LAr electromagnetic and tile hadron calorimeter at $|\eta| = 0.25$.

Fig. 4.8 (a) Schematics and (b) energy resolution of the tile calorimeter [61].

4.2.3 Muon Spectrometer

The muon spectrometer comprises separate trigger and high-precision tracking chambers measuring the deflection of muons in a magnetic field generated by superconducting air-core toroids. The field integral of the toroids ranges between 2.0 and 6.0 Tm across most of the detector. The layout of the muon spectrometer and the toroidal magnetic system can be seen in Figure 4.9(a). There are three layers of detector chambers in the muon spectrometer, inner, middle and outer, for both the barrel and end-cap regions. A set of precision chambers covers the region $\eta < 2.7$ with three layers of monitored drift tubes (MDT), complemented by cathode-strip chambers (CSC) in the inner station of the forward region, where the background rate is the highest. The muon trigger system covers the range $|\eta| < 2.4$ with resistive-plate chambers (RPC) in the barrel, and thin-gap chambers (TGC) in the end-cap regions. The performance of the muon spectrometer is illustrated in the Figure 4.9(b).

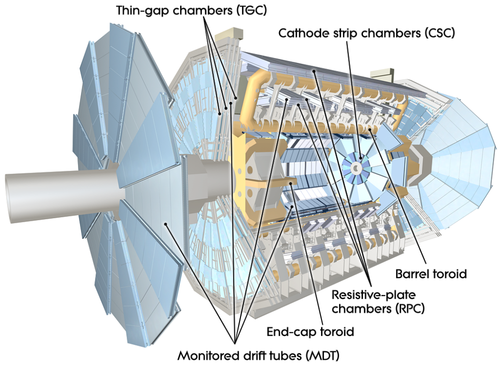

(a) Layout of the muon spectrometer [62].

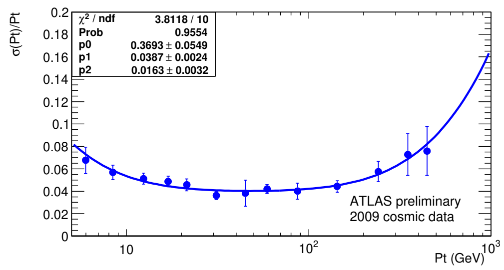

(b) Transverse momentum (p_T) resolution of stand-alone muons for small sectors, as a function of p_T [63].

Fig. 4.9 (a) Layout and (b) transverse momentum resolution of the MS.

4.2.4 Luminosity Measurement

The LUminosity Cherenkov Integrating Detector (LUCID-2) is used in Run 2 in ATLAS to provide luminosity measurement every 1-2 second [64-65]. The LUCID-2 consists of small Cherenkov detectors around the beam pipe, where Cherenkov light is produced with thin quartz windows of photo-multiplier tubes (PMT), coated with ^{207}Bi sources that provides constant calibration signal. Several luminosity algorithms are combined to convert measured raw hit counts into a visible interaction rate per bunch crossing, which is proportional to instantaneous luminosity, where the multiplying constant is calibrated using van der Meer method [66-67].

4.2.5 Trigger and data acquisition system

The LHC pp collisions have a rate at the level of 1 GHz but only a fraction of events are hard scattering events with interesting physics potential. A trigger and data acquisition system is designed to target interesting high p_T physics events can be recorded with . Interesting events are selected to be recorded by the first-level trigger (L1) system implemented in custom hardware. L1 triggers only use calorimeter and muon detector information and provides a coarse Region of Interest (ROI) for fast reconstruction and selection made by algorithms implemented in software in the high-level trigger (HLT) [68], which uses all sub-detectors information. The L1 trigger reduces the 40MHz bunch crossing rate to below 100 kHz, which the HLT further reduces in order to record events to disk at about 1 kHz. Some of the triggers are “prescaled”, meaning only a portion of the collisions that fires the trigger are processed are recorded. This can be due to the fact that trigger rate is too higher, or that a sub-sample of the events are enough for the analyses. The pipeline of triggers and the rate requirements are summarized in the left part of Figure 4.10.

The Data Acquisition (DAQ) system works in conjunction with the trigger system. The signal from the detectors are collected by custom front-end electronics and held in its buffers. Upon receiving of the L1 trigger, the event are sent to hardware-based custom Readout Driver (ROD), and held in buffers in Readout System (ROS). When the HLT computing farm send a trigger after processing the event information, ROS writes the corresponding event onto the disk for off-line analysis. The schematics of the ATLAS DAQ system can be seen in the right part of Figure 4.10.

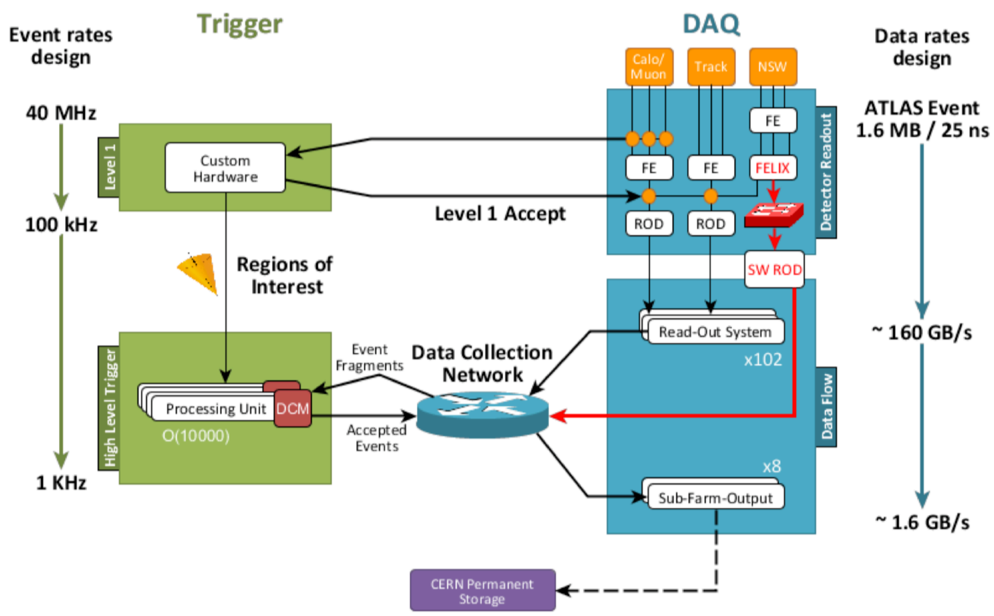

Fig. 4.10 Diagram of the ATLAS Trigger and Data Acquisition system planned for Run 3, including expected peak rate and bandwidths through each component.

4.2.6 ATLAS Detector Simulation

Monte Carlo (MC) simulations play an essential role in physics analysis, since the MC samples combine our understanding of the underlying physics and the detector performance. As already mentioned at the beginning of this thesis, MC event generators are used to simulate the signal and background events produced in the proton-proton collisions, and GEANT4 [69] is used for simulation of detector response. The detector geometry, material and high voltage information is utilized to model the interaction between detectors and particles passing through, including ionization, showering, Cherenkov light, transition radiation, etc. The simulated physical quantities like energy, charge and time are then converted to response of the front end electronics in the "digitization" process. The format of the events after digitization is the same as the real data recorded in experiments. Therefore MC simulated events, that represent our understanding of theory and detector, can be directly compared with data.

The full simulation is time-consuming due to the complex interaction inside the calorimeter. In some analyses the interest focuses on large number of MC events and a high level of precision is not necessary for objects like leptons. Fast simulation algorithm is used in those cases to improve the speed of simulation by parameterization and simplified methods of modeling detector material and responses [70-71].

These MC samples after simulation are used to optimize the analysis, evaluate systematic uncertainties, and parametrized to correct for the detector inefficiency and resolution in differential cross section measurements. Calibrations of MC simulations are done with well established data control samples. For example, the electron and muon energy and momentum scales and resolutions are calibrated with resonance productions of the Z boson, Υ and J/ψ, with their decays to lepton pairs: $Z/\Upsilon/J\psi \to \mu^+\mu^-, e^+e^-$.

Chapter 5 Physics Object Reconstruction

After particles leave experimental signals in the detector which is collected by the detector, the information need to be analyzed and converted back to particles in the offline computing process called reconstruction. The experimental signal features of different types of particles interacting with the detector can be seen in Figure 5.1. Muons usually leave tracks inside the ID and the MS, while a minimal energy due to ionization dE/dx energy loss is deposited in the calorimeters. Photons leave no tracks in the ID but generate electron pairs and therefore showers inside the EM calorimeter. Electrons acts similarly as photon inside the EM calorimeter, but they also leave tracks in the ID additionally. Hadrons usually start showering inside the hadronic calorimeter due to nuclear interactions, and the cluster can be matched to the tracks in the ID to determine the charge. Finally, neutrinos don't interact with the detector and therefore can only be detected passively by the transverse missing energy.

This chapter briefly introduces the reconstruction and identification algorithms of physical objects relevant to this thesis. The calibration processes to correct the differences of detector efficiency and responses between MC and data are not included in the description below. Readers can find more details in the references in the corresponding sections.

In the ATLAS reconstruction software framework different objects are reconstructed independently and it is possible that the same detector information is used to reconstruct more than one type of objects. It is usually determined at each analysis step which type of the objects are used over the other. For studies in this thesis, focusing on four-lepton event selection, the reconstructed leptons are selected with higher priority over the jet selection. We call this as "object-overlap remove" in analysis.

5.1 Inner Detector Tracks and Vertices

Charged particles produced at the IP leave tracks when they pass through the ID. A track can be fully described by five parameters:

- q/p_{T} the charged curvature, where q is the electric charge and p_{T} is the transverse momentum;
- ϕ, the azimuthal angle;
- θ, the polar angle;

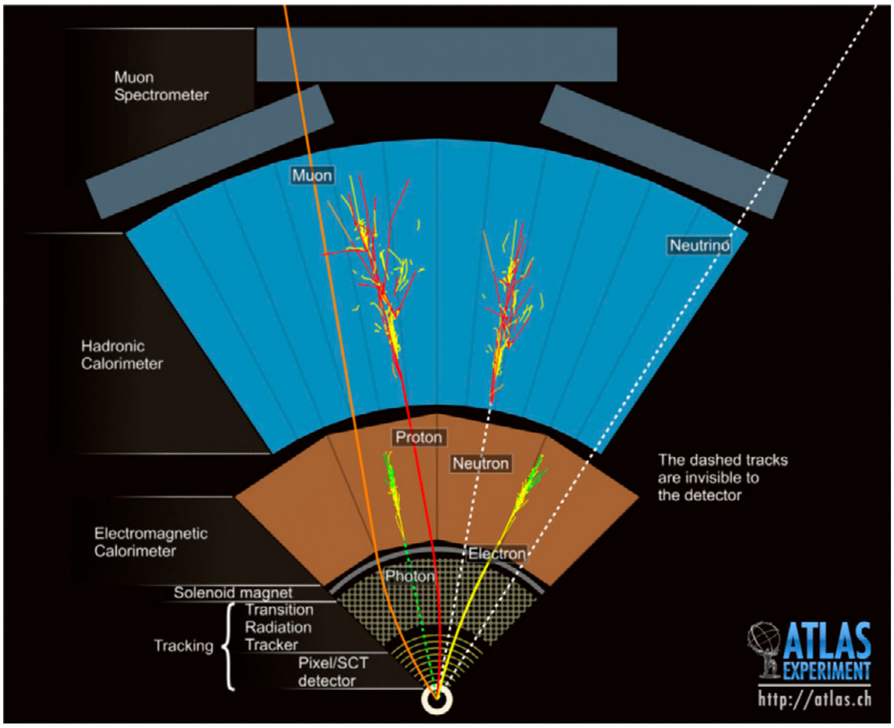

Fig. 5.1 Transverse view of particles interacting with the ATLAS detector. The particles from left to right are a muon, a photon, a proton, a neutron, an electron and a neutrino [72].

- d_0, the transverse impact parameter, the distance of the closest point of the track trajectory to associated primary vertex, in the x-y plane
- z_0, the longitudinal impact parameter, the same distance mentioned in the previous bullet point, along the z-direction.

A multi-staged algorithm is used to reconstruct these helical trajectories [73], and an overview is summarized below.

Clusters are first formed from the neighboring hits on pixel and SCT detector with deposited energy above certain threshold. The pixel clusters provides space-point in a straightforward way, while two SCT modules rotated by a stereo angle must be combined to reconstruct space-points.

Track seeds are formed from sets of three space-points from different layers of silicon detectors, which must follow certain impact parameters and momentum requirement depending on the type of detector they are from. A combinatorial Kalman filter [74] is then applied to incorporate additional space-points from pixel and SCT to build track candidates. Then the candidates must satisfy ambiguity solver requirements with track fitting to reject fakes tracks and resolve overlapping track segments. The cuts includes $p_T > 400$ MeV, $|\eta| < 2.5$, at least 7 silicon hits (12 expected) and some impact parameters requirement. More detailed cuts are described in [59]. The tracks are then extended to TRT detector and refitted as the last step of the inside-out track reconstruction.

A complementary outside-in algorithm is applied consecutively to recover the tracks that failed to be reconstructed by the inside-out algorithm. TRT segments are found first and then are extended inwards collecting silicon hits in the track candidates.

In order to cope with the efficiency loss with increasing multiplicity of tracks, an additional neural network utilizing information from hits as well as track candidates is used to further enhance the identification of merged clusters (Figure 5.2(b)) created by multiple particles.

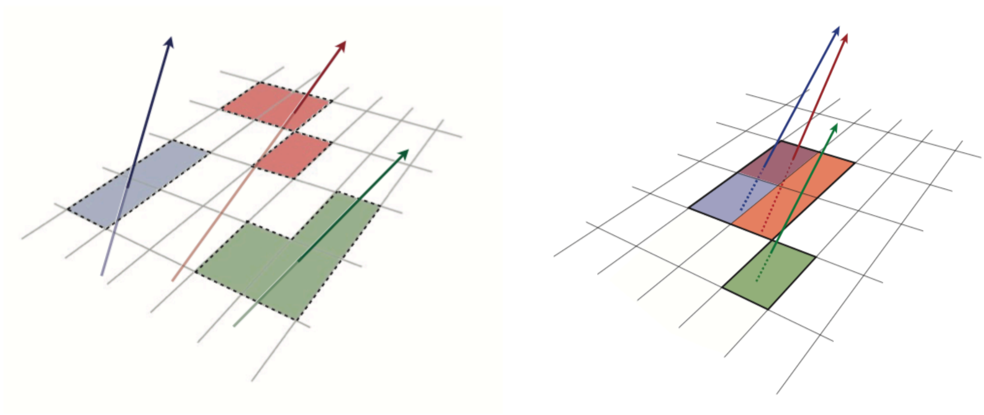

(a) Single-particle pixel clusters **(b) Merged pixel cluster**

Fig. 5.2 Illustration of (a) single-particle pixel clusters and (b) a merged pixel cluster [59].

5.1.1 Primary vertex

With the increasing luminosity, more inelastic pp interaction happens during each collision, creating multiple primary vertices (PVs). It is important to reconstruct and identify PVs from which the particles are originated, because usually only one PV produces an interesting physics event that is created through the hard scattering process during a time interval of the beam bunch collisions.

PVs are reconstructed with an iterative vertex finding algorithm, followed by vertex fitting. The vertex finding starts with selecting tracks that satisfy certain quality requirement [75]. At least two tracks are needed to form a vertex candidate. A seed position is selected for the first vertex, and a fit including the associated tracks is used to determine remove less compatible tracks. After the vertex position is recomputed and finalized, remaining tracks are used to reconstruct the next vertices repeatedly until there is not enough tracks left.

In analyses, the PV with the largest $\sum p_T^2$ of associated tracks is identified as the hard scattering PV and the remaining ones are considered as coming from pile-up interaction.

5.2 Muons

As MIP, muons signal are usually tracks inside ID and MS, and energy deposited in calorimetry. The muon reconstruction and identification procedures [76] of MS track reconstruction and matching to ID tracks and calorimeter hits are briefly describe in this section.

Muon construction begins with forming segments from hits inside muon chambers. MDT segments are fitted after hits in the bending plane are converted to straight lines by a Hough-transformed [77]. The trigger chambers RPC and TGC hits provides complementary measurement to MDT since they provide coordinate orthogonal to the bending plane. CSC chambers at end-cap uses a separate combinatorial search in the η and ϕ detector planes.

Muon tracks are formed by fitting the segments in different layers with a segment-seeded combinatorial search. The segments in the middle layers are used as the initial seed for more trigger hits and then search is extended into middle and outer layers. Certain requirements are used to select segments to form tracks. Finally the hits of the tracks are fitted with a global χ^2 fit and χ^2 also must satisfy a selection criteria.

The MS tracks are combined with ID and calorimeter information to form muons according to different algorithms:

- Combined (CB) muons: built from a global refit of hits from ID and MS tracks. MS hits may be removed or added from the track to improve the fit quality. An outside-in algorithm is used to reconstruct most of the muons, starting with MS tracks and extrapolate inward to match an ID track, complemented by an inside-out algorithm.
- Segment-tagged (ST) muons: an ID track is reconstructed as a muon if it can be extrapolated to at least one local segment in the MDT or CSC. The MS tracks in these cases are not reconstructed because they muons pass one layer in the MS. This is either because the muons have low p_{T} or they pass the region with reduced MS acceptance.
- Calorimeter-tagged (CT) muons: an ID track is reconstructed as a muon if can be matched to an energy deposit inside the calorimeter that has the property of a minimum-ionizing particle (MIP). This type of muon has the lowest purity but it recovers muons that fall into specific region of $|\eta| < 0.1$ and $15 < p_{\mathrm{T}} < 100$ GeV.

- Extrapolated (ME) muons: the muon is reconstructed based only on the MS track and are required loosely to be originating from the IP. This type of muons are majorly used to extend acceptance for $2.5 < |\eta| < 2.7$ region without ID coverage.

The first three types of muons are formed in the order defined, in parallel with ME muons. The overlap between ME muons and other muons are resolved by selecting tracks with better fit quality and larger number of hits.

5.2.1 Muon Identification

Muon identification algorithm is applied to suppress hadrons like pions and kaons faking muons. The algorithm uses the following variables for CB tracks:

- *q/p significance*, the absolute value of the difference between ratio of the charge and momentum of the muons measured in the ID and MS divided by the sum in quadrature of the corresponding uncertainties;
- ρ', the absolute value of the difference between the p_{T} measurements in the ID and MS divided by the p_{T} of the combined track;
- normalized χ^2 of the combined track fit.

Muons in this thesis are required to pass 'loose' identification criteria defined below. This working point is an ATLAS standard criteria designed to maximize reconstruction efficiency while keeping good-quality muon tracks. They are specifically optimized for Higgs to four-lepton final state.

For 'Loose' working point, CB tracks in the $|\eta| > 0.1$ region are required to have $\geqslant 3$ hits in at least two MDT layers. CB tracks in the $|\eta| < 0.1$ region are required to have at least one MDT layer but no more than one MDT hole layer. ME tracks are required to have at least three MDT/CSC layers, and only in $2.5 < |\eta| < 2.7$ regions. For both CB and ME tracks, to suppress the hadron mis-identification, they are required to have *q/p significance* < 7. CT and ST muons are restricted to the $|\eta| < 0.1$ region.

Under 'Loose' working point, in the region $|\eta| < 2.5$, about 97.5% of muons are combined muons, 1.5% are CT muons and the remaining 1% are ST muons.

5.3 Electrons

Electrons shower inside the EM calorimeter can usually be reconstructed as clusters because the shower particles are relatively collimated. If electron interacts with materials before the calorimeter, multiple tracks can be produced. The electron reconstruction including clustering of calorimeter hits, electron track reconstruction and cluster-track matching, as well as electron identification procedures [78] are briefly describe in this section.

A seed-cluster approach is used in 2015-16 data analyses. The EM calorimeter are divided into 200×256 towers in $\eta \times \phi$ regions, with three main layers and one presampler layer where available. The energy deposited in each tower among all layers are first summed up, then EM-energy cluster candidates are seeded from localized energy deposits using a sliding-window algorithm [79] of size 3×5 towers in $\eta \times \phi$ with a summed transverse energy larger than 2.5 GeV. The cluster with 10% more energy deposited or the central one with less than 10% higher energy is favored if two seed-clusters are overlapping within an area of $\Delta\eta \times \Delta\phi = 5 \times 9$. An improved supercluster approach [80] is used in full run 2 analyses. Proto-clusters are formed using both EM and hadronic calorimeters from cells that have energy deposited bigger above corresponding noise thresholds. The noise include electronic noise and an estimate of pile-up noise. Neighboring cells are added iteratively to the cluster following a so-called '4-2-0' topological cluster (topo-cluster) reconstruction. Only energy in the EM calorimeter is used except for in transition region of $1.37 < |\eta| < 1.63$.

The electron reconstruction uses standard tracks reconstructed in inner detector. In the cases where a track seed has $p_{\mathrm{T}} > 1$ GeV that cannot be matched to a full track with 7 silicon hits, a modified pattern recognition is used taking into account the bremsstrahlung energy loss. Track candidates are then fitted with the global χ^2 fitter [81], followed by re-fit on silicon hits that loosely matched to fixed-sized clusters using a Gaussian sum filter [73] with improved parametrization for energy loss.

The re-fitted tracks are then matched to the clusters with a stricter matching requirement. If multiple tracks are matched, an algorithm is used to resolves ambiguity which prefers tracks matched to clusters with smaller ΔR and with more hits in inner silicon detectors.

For the seed-cluster approach, the reconstructed electron clusters are formed around the seed-cluster with an extended window.

For the supercluster approach, final cluster reconstruction is separated into two stages: firstly, EM topo-clusters are tested to be used as seed cluster candidates; then EM topo-clusters that comes from bremsstrahlung radiation or topo-cluster splitting are added as satellite clusters, if they pass certain criteria. An ambiguity resolver runs on the superclusters to determine whether the supercluster belongs to an electron, a photon or "ambiguous" state where the decision can be made later in analyses.

5.3.1 Electron Identification

The electron identification is done with likelihood discriminant to distinguish prompt isolated electrons from converted photon, energy deposits from hadronic jets and electrons produced in heavy-flavor hadron decays. The variables include properties of primary electron track, the lateral and longitudinal development of the EM shower in the EM calorimeter, and the spatial compatibility between track and cluster. The likelihood is created by multiplying histograms of variables smoothed with adaptive kernel density estimator [82], evaluated separately in bins of E_{T} and $|\eta|$, and separately for signal and background. The signal and background likelihood are used to construct a discriminant on which a cut will be required to achieve an average electron efficiency of 93%, 88%, 80% for *Loose*, *Medium* and *Tight* working point correspondingly.

5.4 Jets

As discussed in previous chapters, quark and gluon form hadronic jets due to color confinement. Jets leave multiple tracks inside the trackers and shower inside calorimeters, which is used by the reconstruction algorithm briefly summarized in the following sections.

Calorimeter jets reconstruction are rather straightforward. The 'small-R' jets in ATLAS are reconstructed with topo-clusters (see section 5.3) with positive-energy grouped together using the anti-k_t algorithm [83] and radius parameter $R = 0.4$, implemented in the FastJet software package [84]. Similar algorithm is also used in fiducial level analysis for a similar property with the reconstruction-level analysis.

Particle flow jets [85] combines tracking and calorimetric information and does a cell-based energy subtraction to remove the overlap between them. The sketch of the flow chart of particle flow algorithm is shown in Figure 5.3. Certain criteria including $|\eta| < 2.5$ and $0.5 < p_{\mathrm{T}} < 40$ GeV are used to select the appropriate tracks that will improve the jet performance but not increase the processing time too much. Each track will be matched to a single topo-cluster by a reduced error-corrected angular separation and its energy-momentum compatibility. The expected deposited energy in the cluster is then calculated based on cluster position and track momentum using single-particle samples without pile-up effects. Then the expected energy can be used to determine whether more close-by topo-clusters need to be added to the track. The expected energy is then subtracted cell by cell from the set of matched clusters, starting from innermost to outermost. If the energy in the remaining sets of topo-clusters is small enough, they are considered as shower fluctuation and are removed. If the remnant energy is above the threshold, then the clusters are kept and treated as additional particles in the vicinity. Finally, anti-k_t algorithm with a radius parameter $R = 0.4$ takes the inputs from positive-energy topo-clusters surviving the energy subtraction and the selected tracks that are matched to the primary vertex.

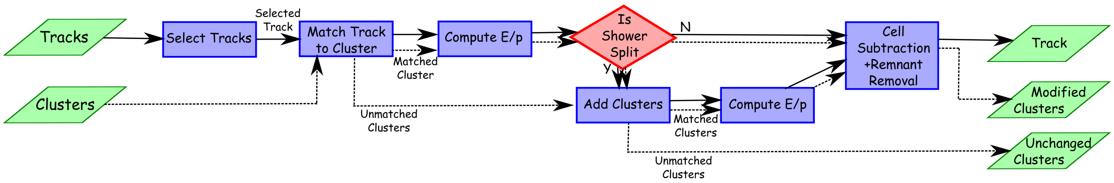

Fig. 5.3 The flow chart of how the particle flow algorithm proceeds.

5.4.1 b-tagging

As mentioned in section 2.1.3, the long lifetime (1.5 ps, or $c\tau \approx 450\mu m$) of bottom quarks can be utilized to identify them among jets. Such algorithms, called b-tagging [86], is important for increasing signal to background ratio in processes that include b quarks in the final state. For example, the ttH channel in the *coupling analysis* presented in this thesis include two b-hadrons that comes from prompt decay of the top quark pairs.

b-hadrons can travel a few mm in the tracker, therefore the tracks produced by b decay products have large impact parameters. A log-likelihood-ratio-based algorithm, IP3D, takes track impact parameters as input of pre-determined probability density functions to calculate weights for all tracks which are then combined as the score of the jet. SV1 algorithm attempts to reconstruct b-decay secondary vertices by doing vertex fit with tracks associated with the jet. SV1 then uses the vertex-related variables to create likelihood-based discriminant, similarly to IP3D. JetFitter [87] makes use of topological structure of weak b- and c-hadron to reconstruct the full decay chain with Kalman filter [74]. An artificial neural network is used to produce a discriminant from information of reconstructed vertices.

The final algorithm used in this thesis is MV2c10 [88-89], which combines the three algorithms describe above with boosted decision tree (BDT). The working points are defined by making cut on BDT score to achieve b-jet efficiencies of 85%, 77%, 70% and 60%.

5.5 Lepton Isolation

Leptons originating from the decay of heavy particles, such as Z and W bosons, are relatively isolated from other particles created in the same event, having a clean trajectories in its vicinity. This fact is used to suppress the contribution from hadronic faking-leptons with isolation requirements. Cuts are applied on isolation variables, defined as the sum of transverse momentum (track-based) or energy (calorimeter-based) contained within a cone around the direction of the lepton.

The track-based isolation variable, $p_{\mathrm{T}}^{varconeX}$, is defined as scalar sum of the transverse momenta of the tracks (excluding the muon track itself) with $p_{\mathrm{T}} > 1$ GeV in a cone of size $\Delta R = \min(10\ \mathrm{GeV}/p_{\mathrm{T}}, X/100)$ around the lepton of transverse momentum p_{T}. The 'varcone' in the isolation variable name indicates that the cone size is dependent on p_{T}, which reduces to improve the performance for high-p_{T} leptons. The tracks are required to pass the track-to-vertex-association (TTVA) requirement of $|z_0 sin\theta| < 3$mm [90] to make sure that they're from the vertex concerned.

The calorimeter-based isolation variable, $E_{\mathrm{T}}^{topoconeX}$, uses the topo-cluster mentioned in the electron reconstruction section. It is defined as the sum of transverse energy of topo-clusters in a cone of size $\Delta R = X/100$ around the lepton, excluding the energy deposited by the lepton itself and corrected for pile-up effects.

Recently, ATLAS has developed new isolation variables to deal with the efficiency loss under increasing pile-up condition. For track-based variables, pt[var]coneX_TightTTVA_ptY, the X works similarly as the minimum cone size, the optional [var] indicates whether the cone size is dependent on p_{T} and Y indicates the p_{T} requirement in MeV. Y can be chosen as 500 to include the consideration of softer tracks. The 'TightTTVA' requirement is defined as tracks used in vertex fit or has $|z_0 sin\theta| < 3$mm but is not associated to another vertex, to remove the effect from pile-up vertices. This TTVA requirement is optimized with the 2017 data pile-up regime and is tightened compared to the previous counterpart.

The lepton efficiencies of calorimeter-based variables with topo-cluster also decreases at large pile-up, because the increasing energy density causes a large fluctuation of $E_{\mathrm{T}}^{topocone}$ and mis-correction of pile-up effect. The new variable, neflowisol20, uses particle flow method described in the previous section to achieve improved track-cluster association. neflowisol20 uses the sum of neutral particle flow energy inside the cone, where neutral means clusters that were not associated to tracks [91], which helps to remove clusters from pile-up tracks. The 20 in the variable indicates that the ΔR equals

0.2.

Those new variables are combined to give new working points and their usage and optimization are described further in section 7.3.

5.6 Missing transverse energy

In initial state of of the pp collision particles are quarks and gluons, the partons inside protons. The energies of the head-on partons are unknown for each collision. We only know the parton distribution function inside a proton, which makes it impossible to know the precise longitudinal momentum of the system. However, the transverse momentum is conserved as zero and the recoil of all visible particles can be used to describe the particles like neutrinos escaping from detection. The magnitude of this transverse momentum is called missing transverse energy, E_{T}^{miss}. It is defined as

$$E_{\mathrm{T}}^{\mathrm{miss}} = |\sum_{i=\text{vis. hard object}} \boldsymbol{p}_{\mathrm{T}}^{i}| \tag{5.1}$$

where the sum is over of visible particles: electrons, muons, taus, photons, jets and soft terms from the tracking. The $E_{\mathrm{T}}^{\mathrm{miss}}$ is an indirect measurement of weakly-interacting particles like neutrinos and possible invisible exotic particles, but can also be faked by imperfect object reconstruction, detector flaws, pile-up and so on [92].

Chapter 6   Data and MC Simulation Samples

6.1   Data samples

Both analyses described in this thesis use Run 2 data at a center-of-energy $\sqrt{s}$ = 13 TeV with a 25 ns bunch spacing configuration. We only use events taken with stable beam condition and when detectors are fully functional. A peak luminosity of 21.4×10^{33} cm^{-2}s^{-1} and a pile-up of 80 is achieved in 2018. The pile-up distribution for each year can be found in Fig. 6.1.

The analysis on the Higgs coupling measurement is based on proton-proton collision data recorded between 2015 and 2018 and corresponding to an integrated luminosity of 138.4±2.4 fb^{-1}. The analysis on the inclusive ZZ^*lineshape measurement is based on data collected between 2015 and 2016 and corresponding to an integrated luminosity of 36.1±0.6 fb^{-1}.

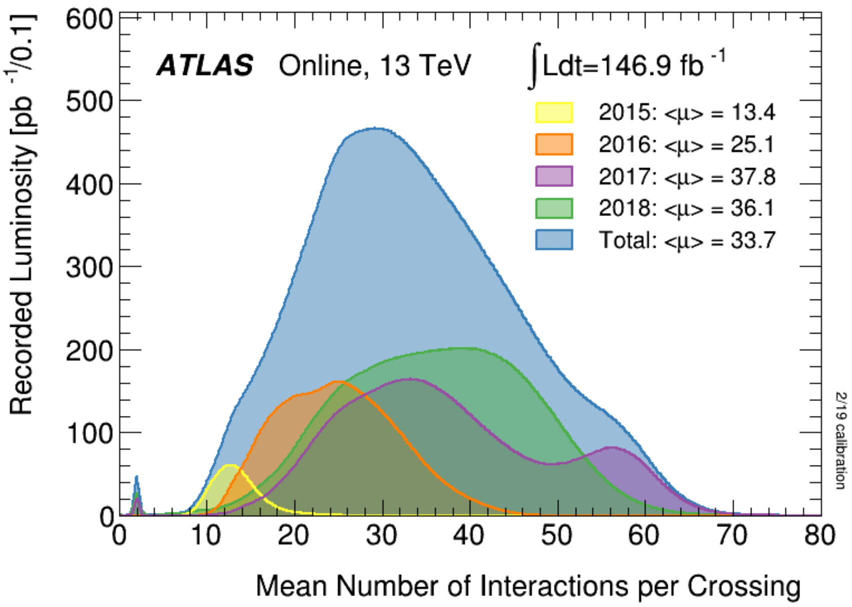

Fig. 6.1   The luminosity-weighted distribution of the mean number of interactions per crossing for 13 TeV data from 2015-2018.

6.2   Higgs signal MC samples

The Higgs MC samples used in both analyses are largely the same, except for minor changes with theoretical treatment, generator filters and statistics since the results of the two analyses are published at different times. In this chapter we will describe the latest Higgs samples used in the *coupling* measurement analysis. The Higgs process contributes only a small portion in the *inclusive lineshape* analysis, and the detailed information can be found in Reference [13].

The production of the SM Higgs boson via ggF, VBF, VH and ttH is modeled with Powheg-Box v2 MC generator [93-97] with PDF4LHC [98] PDF set. The ggF process uses NNLO precision PDF set, while the others uses NLO PDF set.

The ggF samples uses the Powheg method to merge the NLO Higgs plus jet cross section with the parton shower. The MiNLO method [99] is used to reach NLO accuracy for the inclusive Higgs boson production. The NNLOPS reweighting procedure [100-101] uses HNNLO [102-103] program is applied to reweight with exploiting the Higgs boson rapidity distribution, to achieve NNLO QCD precision. The Higgs p_{T} is compatible with the fixed-order calculation of HNNLO and the Hres2.3 calculation [104-105] performing resummation at next-to-next-to-leading-logarithm (NNLL) matched to a NNLO fixed-order calculation.

The VBF, VH and ttH processes are calculated up to NLO QCD. The MiNLO method is also used for VH to merge 0- and 1-jet events [99]. The gg initiated ZH contribution is modeled at LO QCD.

The production of bbH is simulated with MadGraph5_aMC@NLO v2.3.3 at NLO QCD [106]. The PDF set is CT10 NLO [107]. The tH samples are simulated with MadGraph5_aMC@NLO v2.6.0 using NNPDF3.0 PDF set [108].

The Higgs boson mass are set as m_H = 125 GeV for all simulation. All the production mechanisms except ttH uses Pythia 8 generator [109], with AZNLO [110] set of tuned parameter for $H \rightarrow ZZ^* \rightarrow 4\ell$ decay and the parton shower modeling. The branching ratio of the Higgs is modeled with Prophecy4F [111-112], with complete NLO EW corrections and interference effects. ttH uses Pythia 8 with A14 tuned parameter set [113] instead. The event generator is interfaced to EvtGen v1.2.0 [114] for simulation of the bottom and charm quark decays.

There are additional cross check samples for ggF generated with MadGraph5_aMC@NLO with NLO QCD accuracy for 0, 1 and 2 additional partons merged with the FxFx merging scheme [115-116].

The normalization of the samples from cross sections of different Higgs processes and Higgs branching ratio are mentioned in section 3.3, as well as the theoretical systematics are taken from [39, 108, 117-122]. Table 6.1 summarizes the Higgs sample used.

Table 6.1 Summary of Higgs samples. Cross sections do not include branching ratio of Higgs decay.

Process	Generator	Cross section (pb)	Precision	PDF
ggF	Powheg-Box v2 (NNLOPS)	48.6	NNLO+NNLL	PDF4LHC
VBF	Powheg-Box v2	3.78	NLO	PDF4LHC
WpH	Powheg-Box v2 MiNLO	0.840	NLO	PDF4LHC
WmH	Powheg-Box v2 MiNLO	0.530	NLO	PDF4LHC
ZH	Powheg-Box v2 MiNLO	0.760	NLO	PDF4LHC
(ggZH)	Powheg-Box v2	0.123	NLO	PDF4LHC
ttH	Powheg-Box v2	0.507	NLO	PDF4LHC
tWH	MadGraph5_aMC@NLO	0.0151	NLO	PDF4LHC
tHqb	MadGraph5_aMC@NLO	0.0771	NLO	PDF4LHC
bbH	MadGraph5_aMC@NLO	0.488	NLO	NNPDF23

6.3 The SM Four-lepton Background MC Samples

The ZZ^*continuum background from quark-quark annihilation process(qqZZ) is modeled using Sherpa 2.2.2 [123-126]. Sherpa provides a matrix element at NLO QCD for 0- and 1-jet final states and LO for 2- and 3-jet final states using Comix [123] and OpenLoops [125]. The merging with the Sherpa parton shower [127] is done with the ME+PS@NLO prescription [128]. For additional checks, a second qqZZ sample is generated at NLO precision using Powheg-Box v2 [93-97] with CT10 NLO [107] and uses Pythia 8 for parton shower modeling. A correction to higher-order precision (K-factor), defined as the ratio of the cross-section at NNLO QCD over the one at NLO QCD, was obtained using MATRIX [129-132] NNLO QCD prediction and applied as a function of the invariant mass of ZZ^*system, m_{ZZ^*}. For both samples, an NLO EW correction is also applied as a function of m_{ZZ^*} [133-134]. For the *coupling analysis*, a third qqZZ sample is modeled with MadGraph5_aMC@NLO at NLO QCD for 0- and 1-jet, merged with the FxFx merging scheme, simulated with fast simulation. The parton shower is modeled with Pythia 8.

The high-order electroweak contribution of vector-boson scattering of ZZ^*plus two jets (EWZZjj) is separately modeled with Sherpa 2.2.2. In the samples where the Higgs production process is included, a narrow Higgs mass window around 125 GeV is applied to avoid double-counting.

The gluon-gluon initiated ZZ^*(ggZZ) process is modeled by Sherpa 2.2.2 [123-

126] at LO QCD for 0- and 1-jet final states. This sample includes box diagram background, s-channel $gg \to H^* \to ZZ^*$ signal and the interference (SBI). For the *coupling analysis* a flat NLO QCD k-factor of 1.7 is applied with a 60% uncertainty for the conservativeness. For the *inclusive lineshape analysis*, a differential K-factor is applied as a function of m_{ZZ^*} to reweight the sample to NLO QCD precision. The K-factor is derived by dividing nominal Sherpa sample by MCFM NLO sample which is scaled from fixed-order LO to NLO QCD by applying weights on an event-by-event basis. This higher-order QCD effect is calculated for massless quark loops [135-136] above $2m_t$, and in the heavy top-quark approximation $1/m_t$ expansion below this threshold [137]. In the *coupling analysis*, the main interest lies in $m_{ZZ^*} < 2m_Z$ region where interference effect is negligible so only the box diagram processed is used in the background estimation. The ZZ^*samples above generated with Sherpa program uses NNPDF3.0NNLO PDF set.

In the *inclusive lineshape analysis*, the MCFM [138] program is also used to simulate additional ggZZ samples at LO QCD, using CT10 PDF set.

Table 6.2 summarizes the SM ZZ samples used.

Table 6.2 Summary of ZZ samples. The branching ratio of Z decay is included in the cross section.

Process	Generator	Cross section × filter efficiency (fb)	Precision	PDF
qqZZ	Sherpa 2.2.2	1252.3	NLO	NNPDF3.0NNLO
qqZZ	Powheg-Box v2	1269	NLO	CT10
qqZZjj	Sherpa 2.2.2	10.268	LO	NNPDF3.0NNLO
ggZZ	Sherpa 2.2.2	15.3015	NLO	NNPDF3.0NNLO
ggZZ	MCFM	15.3015	LO	CT10

6.4 Other Background MC Samples

Similar to the Higgs signal sample, only the latest samples are introduced in this section. The background consists of a small proportion in the *inclusive analysis*, readers can go to Reference [13] for the details of samples used.

The ttV(V = W, Z) events where V decays leptonically is modeled with MadGraph5_aMC@NLO interfaced to Pythia 8 and the total cross section is normalized to the calculation the includes two dominant terms at both LO and NLO in a mixed perturbative expansion in the QCD and EW couplings [139]. The modeling is also compared with SHERPA 2.2.1 at LO. The smaller processes in the tXX process, tWZ, $t\bar{t}W^+W^-$, $t\bar{t}W^\pm Z$, $t\bar{t}Z\gamma$, $t\bar{t}ZZ$, $t\bar{t}t$, $t\bar{t}t\bar{t}$ and $tZ$are modeled with MADGRAPH5_AMC@NLO interfaced to PYTHIA 8.

The WZ background is modeled with POWHEG-BOX v2 interface to PYTHIA 8 and EVTGEN v1.2.0 for simulation of bottom and charm hadron decays. The tri-boson processes ZZZ, WZZ and WWZ, together called VVV, with four or more prompt leptons, are modeled with SHERPA 2.2.2.

The $Z+$ jets process is modeled with SHERPA v2.2.1 generator up to two partons at NLO and four partons at LO with COMIX and OPENLOOPS, and merged with the SHERPA parton shower using the ME+PS@NLO prescription. The NNPDF3.0 PDF and a dedicated parton shower parameters tuning is used.

The $t\bar{t}$ background is modeled with POWHEG-BOX v2 interface to PYTHIA 8 and EVTGEN v1.2.0 for parton showering, hadronization, the underlying event and heavy hadron decays. The A14 tune [113, 140] is used for this sample.

Table 6.3 summarizes the samples of the background whose estimation are purely from simulation.

Table 6.3 Summary of other background samples.

Process	Generator	Cross section $\times$ filter efficiency (fb)	PDF
ttV	MADGRAPH5_AMC@NLO	691.66	NNPDF3.0NLO
VVV	Sherpa 2.2.2	0.385560	NNPDF3.0NNLO
WZ	Powheg-Box v2	5132.622	CT10

Chapter 7   Four-Lepton Event Selection and Background Estimation

This chapter describes a common four-lepton event selection for the HZZ *coupling* analysis and the *inclusive ZZ lineshape* measurement. There are minor differences in the selection of the two analyses because they are done with different dataset and also the analysis software and techniques are updating over time. The $H \to ZZ^* \to 4\ell$ event selection is described in detail. The 4ℓ selection for the *lineshape* analysis is similar and the difference will be mentioned inline and highlighted at the end of this section.

The SM Higgs boson decay to ZZ^* to four leptons channel, $H \to ZZ^* \to 4\ell$ ($l = e, \mu$), is suitable for measurement of Higgs properties due to its very good signal to background ratio. As all the final state particles can be fully reconstructed, we can identify the Higgs boson in a narrow mass window since ATLAS detector provides excellent energy and momentum measurements for electrons and muons. The requirement of four isolated leptons in the final state put strong constrains to other possible processes that can contaminant the selected Higgs event sample. Due to its clean signature but very small event rate of the $H \to ZZ^* \to 4\ell$ process the emphasis of the event selection is to maximize the Higgs event selection efficiency, rather than minimize the fake background contaminant. The major background with four leptons is the continuum SM $ZZ^* \to 4\ell$ production which takes up around 25% of the total 4ℓ events in the Higgs mass window. The ZZ^* continuum production is also the dominant process at higher mass. There are also minor background from non-prompt leptons, mostly from $Z+$jets and $t\bar{t}$ processes. They contribute about 5% in region of four-lepton invariant mass in mass window [100, 160] GeV. Detailed event selection at different steps are presented in sections below.

7.1 Trigger

Events are selected with a combination of single-lepton, dilepton, tri-lepton triggers with different momentum thresholds dependent on the lepton multiplicity . The lowes-p_T un-prescaled high-level triggers are used. Due to increased luminosity, the p_T requirement for single lepton triggers is set higher to satisfy the 100 kHz acceptance limit for L1 trigger. Tri-lepton triggers and electron-muon triggers are added to mitigate the efficiency loss. The triggers with high threshold but looser lepton selection criteria are also used to complement triggers with low threshold. The overall trigger efficiency for signal event passing the final selection is 98% with an uncertainty less than 1%.

7.2 Object selection

Electrons are reconstructed using the supercluster approach described in section 5.3 in the *coupling analysis* and with seed-cluster algorithm in the *inclusive lineshape measurement*. The identification likelihood criterion is set to “loose” combined with track hit requirements to achieve a high efficiency. Electrons are required to have $E_T > 7$ GeV and $|\eta| < 2.47$.

For muon, the “loose” criterion is used for identification. The kinematic requirements are $p_T > 5$ GeV and $|\eta| < 2.7$, except for calorimeter-tagged muons that must satisfy $p_T > 15$ GeV.

To make sure the four leptons are coming from the primary vertex, the electrons and muons are all required to have a longitudinal impact parameter ($|z_0 sin\theta|$) less than 0.5 mm. For muons, transverse impact parameter is required to be less than 1 mm to reject cosmic muons.

Jets are reconstructed with the anti-k_t algorithm with a radius parameter of R=0.4 using topo-clusters and particle-flow objects, for *inclusive lineshape measurement* and *coupling analysis* correspondingly, as mentioned in section 5.4. Jets need to pass $p_T >$ 30 GeV and $|\eta| < 4.5$ in the *coupling analysis*, while this requirement is removed in the *inclusive lineshape measurement*. Jets from pile-up with $|\eta| < 2.5$ are suppressed with a jet-vertex-tagger multivariate discriminant [141-142]. The MV2c10 b-tagger [89, 143] is used on jets with $|\eta| < 2.5$ to identify whether it contains b-hadrons. The 60%, 70%, 77% and 85% b-jet efficiency working points are used to provide pseudo-continuous b-tagging information.

Reconstruction objects using the same detector information are treated with overlap-removal algorithms. If two electrons use the same calorimeter clusters, the electron with the higher E_T is kept. If muon and electron are reconstructed from the same ID track, the muon is rejected if it is calorimeter-tagged, otherwise the electron is rejected. If jets overlap in a cone of radius $\Delta R = 0.1$ (0.2) with a muon (electron), the jet is rejected.

7.3 Quadruplet selection

The same-flavor opposite-sign leptons are grouped first into dilepton pairs. All the possible combinations of two non-overlapping dileptons form quadruplets. We only allow one calorimeter-tagged or extrapolated muon for each quadruplet. And we require the three highest-p_T leptons in the quadruplet to have p_T bigger than 20, 15, 10 GeV correspondingly.

For each quadruplet, the dilepton with an invariant mass closer to Z boson mass is defined as the leading lepton pair, and the other one as the subleading pair. The leading dilepton pair's mass is defined as m_{12} and the subleading one as m_{34}. It's worth noting that four same-flavor leptons can form two quadruplets under this algorithm.

All the quadruplets are ordered first by the flavor of the final state: 4μ, $2e2\mu$, $2\mu 2e$ and 4e, which denote the 4ℓ channels. In each channel, we sort the quadruplets by $|m_{12} - m_Z|$ and $|m_{34} - m_Z|$ in the ascending order and the first quadruplet is called nominal quadruplet. For each quadruplet, we require it to first pass a series of requirements described below.

First the leading dilepton pair must satisfy 50 GeV $< |m_{12}| <$ 106 GeV. For the subleading dilepton, we require it to pass $m_{min} < |m_{34}| <$ 115 GeV, where the m_{min} is a variable dependent on invariant mass of four-lepton (m_{4l}), optimized for higher signal acceptance. For the *coupling analysis*, it is defined as

$$m_{min} = \begin{cases} 12\,\text{GeV}, & \text{for}\, m_{4l} < 140\,\text{GeV} \\ 12\,\text{GeV} + 0.76 \times (m_{4l} - 140\,\text{GeV}), & \text{for}\, 140\,\text{GeV} \leqslant m_{4l} < 190\,\text{GeV} \\ 50\,\text{GeV}, & \text{for}\, m_{4l} \geqslant 190\,\text{GeV}. \end{cases} \quad (7.1)$$

For the *inclusive lineshape measurement* it is defined as

$$m_{min} = \begin{cases} 5\,\text{GeV}, & \text{for}\, m_{4l} < 100\,\text{GeV} \\ 5\,\text{GeV} + 0.7 \times (m_{4l} - 100\,\text{GeV}), & \text{for}\, 100\,\text{GeV} \leqslant m_{4l} < 110\,\text{GeV} \\ 12\,\text{GeV}, & \text{for}\, 110\,\text{GeV} \leqslant m_{4l} < 140\,\text{GeV} \\ 12\,\text{GeV} + 0.76 \times (m_{4l} - 140\,\text{GeV}), & \text{for}\, 140\,\text{GeV} \leqslant m_{4l} < 190\,\text{GeV} \\ 50\,\text{GeV}, & \text{for}\, m_{4l} \geqslant 190\,\text{GeV}. \end{cases} \quad (7.2)$$

This slightly loosened m_{34} cut enhances events statistics under the Z peak. In 4e and 4μ channel, any possible dilepton pair must have an invariant mass bigger than 5 GeV to suppress the J/ψ background. Any two leptons must have an angular separation of

$\Delta R > 0.1$. In the *inclusive analysis*, the $\Delta R > 0.2$ is required for different flavor leptons instead of 0.1.

To suppress contribution from reducible background, the impact parameter and isolation requirement are further applied. Each electron (muon) track must have a transverse impact parameter significance ($|d_0|/\sigma_{d_0}$) lower than 5 (3) with respect to the primary vertex to suppress the lepton background from heavy-flavor hadrons. The particle flow lepton isolation variables must satisfy the condition of max(ptcone20_TightTTVA_pt500, ptvarcone30_TightTTVA_pt500) + 0.4 neflowisol20 $< 0.16\, p_{\mathrm{T}}$. The optimization of particle flow lepton isolation variables will be described in section 7.3.1. While in the *inclusive analysis*, it uses $p_{\mathrm{T}}^{varcone30}/p_{\mathrm{T}} < 0.15$ and $E_{\mathrm{T}}^{topocone20}/E_{\mathrm{T}} < 0.30$ for muons and $p_{\mathrm{T}}^{varcone20}/p_{\mathrm{T}} < 0.15$ and $E_{\mathrm{T}}^{topocone20}/E_{\mathrm{T}} < 0.20$ for electrons. This is the so-called FixedCutLoose isolation working point.

Finally, to further suppress non-prompt low-pt leptons, the four leptons are required to be compatible with the common vertex. The χ^2 retrieved from the vertex fit using ID tracks is required to have $\chi^2/N_{dof} < 6(9)$ for 4μ (other) channels. This cut value corresponds to 99.5% efficiency for decay channels.

For all quadruplets that pass the aforementioned cuts, the following logic is used to make a choice if there is more than one quadruplet. The 4ℓ channels are first ordered by 4μ, $2e2\mu$, $2\mu 2e$ and 4e. An event can be accepted only if at least one nominal quadruplet passes all cuts. In *coupling analysis*, when a nominal quadruplet passes all cuts, we check if there is an additional extra lepton that has $p_{\mathrm{T}} > 12$ GeV and $\Delta R > 0.1$ with all of the leptons inside the nominal quadruplet. If such an extra lepton exists, all the quadruplet that passes the cuts are kept, and the pairing ambiguity is resolved by choosing the quadruplet with the highest matrix-element-based discriminant calculated at LO with MadGraph5_aMC @ NLO [144]. If no extra lepton exists for any nominal quadruplet or for the *inclusive analysis*, we select the first nominal quadruplet that passes all the cuts. If none of the nominal quadruplet passes the cuts, the whole event is rejected even if an alternative quadruplet pass the cut.

By selecting the quadruplet with m_{12} and m_{34} closest to the Z boson mass, it has a large chance of selecting the correct pair in four-lepton Higgs signal processes because one Z boson is on-shell and the other is off-shell. And for the processes like VH and ttH where an extra lepton can be produced in the decay of the associated particles, the matrix-element-based pairing helps to select the correct leptons. The impact on expected four lepton invariant mass for those events with extra leptons can be seen in Figure 7.1.

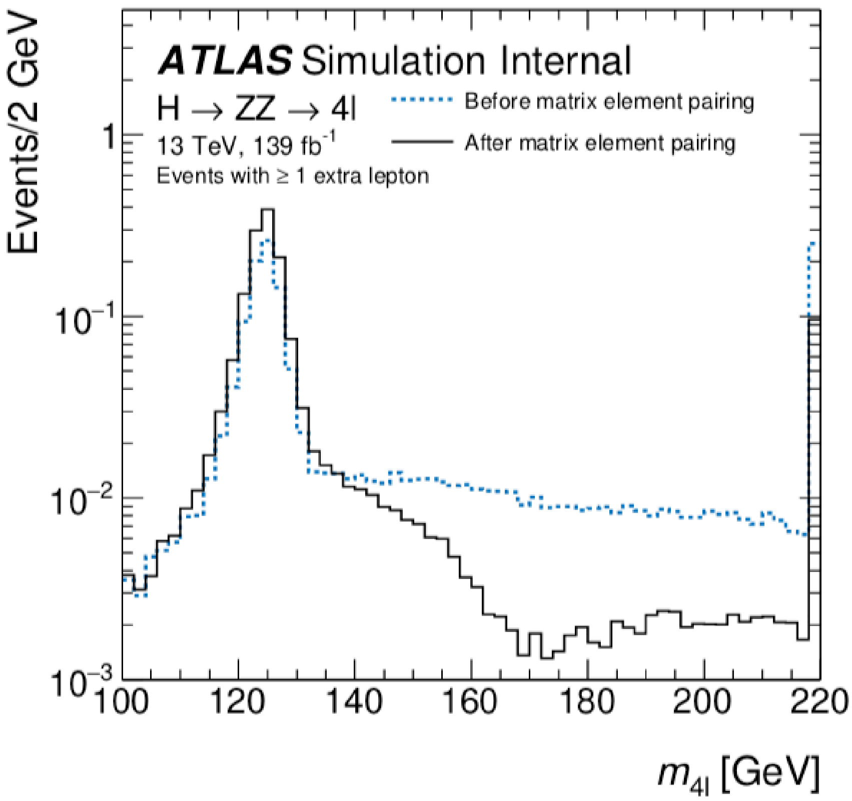

Fig. 7.1 Impact on the expected four lepton invariant mass due to ME, for candidates with at least one extra lepton [12].

The reconstructed final-state radiation(FSR) photons in the Z boson decays are recovered to improve the four-lepton invariant mass reconstruction. Collinear (non-collinear) FSR process is defined as photon having the ΔR < (>) 0.15 to the closest lepton in the quadruplet. For collinear FSR processes, muons from the leading dilepton pair are considered and in non-collinear FSR processes, electrons and muons from both pairs are considered. The FSR recovery affects approximately 3% of the Higgs candidates. More details can be found in [12-13].

In the *coupling analysis*, a $115 < m_{4l} < 130$ GeV mass window is used as the definition for signal category. Several sideband regions in $110 < m_{4l} < 350$ GeV regions are optimized for background estimation. More details can be found in section 9.3.1.

The selection efficiencies of the 4μ, $2e2\mu$, $2\mu 2e$ and 4e channels are 35%, 27%, 21% and 17%, respectively. In the *coupling analysis*, the number of expected Higgs signal events before and after the above selection and the efficiency is summarized in Table 7.1.

In summary, the difference in selecting 4ℓ events between the two analyses is summarized here:

Table 7.1 Expected events before and after the selection as well as the efficiency for Higgs signal processes, for the *coupling analysis* using 139 fb^{-1} dataset. The selection doesn't include mass window cut.

	ggF	VBF	WH	ZH	$t\bar{t}H + tH$
Before selection	838	65.2	23.6	15.22	10.33
Signal Region	186	17.0	5.0	3.97	2.13
Efficiency	0.22	0.26	0.22	0.26	0.21

- Electrons are reconstructed using slightly different algorithms.
- *Angular separation* of leptons. For *coupling analysis*, $\Delta R < 0.1$. For *inclusive analysis*, same-flavor lepton requires $\Delta R < 0.1$, different-flavor lepton requires $\Delta R < 0.2$.
- *Isolation* of leptons. For *coupling analysis*, the latest "FixedCutPflowLoose" isolation working point is used. For *inclusive analysis*, the "FixedCutLoose" working point is used.
- m_{34} lower cut. *Inclusive analysis* has a looser lower cut of m_{34} to recover enhance statistics under the Z peak.
- *Quadruplet selection*. For *coupling analysis*, the matrix-element based selection is used in the existence of an extra lepton. For *inclusive analysis*, only the channel priority is used for nominal quadruplets.

7.3.1 Optimization of isolation

The *coupling analysis* uses full run 2 data with unprecedented instantaneous luminosity, which also comes with high pile-up as a side effect. To mitigate the isolation efficiency loss for leptons, new isolation working points are optimized, balancing signal efficiency, background rejection, and pile-up robustness.

A small caveat of the study is that for standard isolation calculation includes a close-by correction to remove other leptons from consideration, so that if two otherwise isolated leptons are close together they do not cause each other to fail the selection. At the time of this study, the close-by correction is not available so a requirement of $\Delta R > 0.3$ between leptons is imposed to ensure that no lepton fell within the cone of any other lepton. This requirement is not imposed for final results. This requirement will reduce the efficiency but it is assumed that all samples are affected similarly so the optimization done on top of this will still be valid for final cuts.

In total, a number of possible WPs are considered, as shown in Table 7.2. There are three general types of selections. The simplest ones are the "TrackOnly" ones:

these are based on the fact that the track isolation is much more pile-up robust than the calorimeter isolation is. The second one being using are track-based and calorimeter-based separately, which includes FixedCutLoose, and FCLoose (previously named as FixedCutHighMuLoose). The remaining WPs fall into the third categories, which combines track-based and calorimeter-based isolation variables in a triangular-shaped cuts.

Table 7.2 Summary of the possible isolation cuts considered.

Name	Cut
FixedCutLoose	electron: topoetcone20 < 0.2 && ptvarcone20 < 0.15 muon: topoetcone20 < 0.3 && ptvarcone30 < 0.15
FCLoose	topoetcone20 < 0.30 && ptvarcone30_TightTTVA_pt1000 < 0.15
TrackOnly0p20	ptvarcone30_TightTTVA_pt1000 < 0.2
FixedCutPflowLoose	ptvarcone30_TightTTVA_pt500 + 0.4 * neflowisol20 < 0.16
Tri_HighMuLoose500	bump: topoetcone20 / 0.45 + ptvarcone30_TightTTVA_pt500 / 0.13 < 1 bar: topoetcone20 < 0.5
Tri_HighMuLoose	bump: topoetcone20 / 0.38 + ptvarcone30_TightTTVA_pt1000 / 0.15 < 1 bar: topoetcone20 < 0.5
Tri_PflowLoose	bump: newflowisol20 / 0.42 + ptvarcone30_TightTTVA_pt500 / 0.14 < 1 bar: newflowisol20 < 0.3
Tri_PflowLoose1000	bump: newflowisol20 / 0.45 + ptvarcone30_TightTTVA_pt1000 / 0.13 < 1 bar: newflowisol20 < 0.3

Among the official WPs, FixedCutLoose is the nominal working point used in previous analyses, and is used as a baseline to be tested against with other working points. FCLoose (aka FixedCutHighMuLoose) updates this working point to use the pile-up-robust version of ptvarcone; FixedCutPflowLoose uses a triangular-shaped cut to combine the new ptvarcone and the new particle-flow calorimeter isolation variable, neflowisol, into a single selection.

Additional customized working points are derived by first observing the distribution of isolation variables, followed by optimization of cut variables. Two different track isolation variables, the pile-up-robust version with a cutoff at 0.5 or 1 GeV and cone size of 0.3, and two different calorimeter isolation variables, the topoetcone20 and the neflowisol20 variables with cone size of 0.2, are used. Plots for some example combinations are shown in Figure 7.2 to 7.5.

As can be seen in the plots, for signal the distributions typically resolve into two pieces. The first is a "bump" for which the appropriate selection is a triangular cut (a, b) on variable (x, y), with the form of $x/a + y/b < 1$. The other is a "bar" for which track isolation variable is exactly 0 that requires a cut on the calorimeter isolation only. The procedure is to do a two-dimensional significance scan of cut parameter pair (a, b) to optimize the bump cut and a one-dimensional one to optimize the bar.

The optimization among the cut value is done by a scan for the highest significance [145]

$$Z_{\mathrm{A}} = \left[2 \left((s+b) ln \left[\frac{(s+b)(b+\sigma_b^2)}{b^2 + (s+b)\sigma_b^2} \right] - \frac{b^2}{\sigma_b^2} ln \left[1 + \frac{\sigma_b^2 s}{b(b+\sigma_b^2)} \right] \right) \right]^{1/2} \tag{7.3}$$

where the s and b are signal and background events corresponding and σ_b is absolute error of background. The signal includes all Higgs signals and background includes reducible background, with a conservatively large uncertainties of 100%. The irreducible ZZ^*background is not considered as isolation are not expected to help with removing them. Their values are estimated by MC samples.

The results of the scan for Tri_PflowLoose1000 where ptvarcone30_TightTTV_pt1000 and neflowisol20 are used can be seen in Figure 7.6, as an example. For 4e and 4μ separately, a 2D scan with coarse grid points are carried out, followed by a finer scan around the maximum point in the coarse scan. Finally, the 1D scan are carried independently with the 2D scan. The final cut points are selected to make a compromise between 4e and 4μ channels, and the value can be seen in Table 7.2.

The efficiency vs. $< \mu >$ of several promising cuts for different signal and background samples is shown in Figure 7.7. The performance of the old WP FixedCutLoose drops dramatically at high pile-up, while the new FCLoose (aka FixedCutHighMuLoose) with improved track variable has slight improvement, the FixedCutPflowLoose and two triangular-shaped cuts retain the efficiency the best at high pile-up.

The optimizations based on simulation provides a general direction to look at because scans using the full calculation would not be feasible. The final choice of isolation selection are made after carrying out the full data-driven reducible background calculation (see Section 7.5 for details).

Table 7.3 shows the yield of the reducible background and the associated significance, in the llee channels for the most promising isolation selections, and Table 7.4 the same for ll$\mu\mu$, both for $115 < m_{4l} < 130$ GeV. As a further check, Table 7.5 shows the significance obtained in each of the categories used in the previous couplings analysis in the llee final state over the full m_{4l} mass range: as the isolation will have a different impact in categories that are more or less busy, it's important to confirm that isolation selections which work well in the dominant 0-jet category are also successful in other categories.

As a result of all these studies, the FixedCutPflowLoose working point was chosen, as having the best or close to the best performance in all the tests.

Table 7.3 Yields and significances for various isolation selections using the llee reducible background calculation (signal taken from MC simulation).

Isolation selection	Signal	Fakes	Gammas	Heavy Flavor	Significance
FCLoose	20.43	1.10	0.26	0.27	8.31
FixedCutPflowLoose	21.13	0.76	0.17	0.17	9.33
TrackOnly0p20	23.66	1.58	0.26	0.32	8.61
Tri_HighMuLoose	22.58	1.17	0.23	0.22	8.95
Tri_PflowLoose1000	20.98	0.77	0.19	0.22	9.13

Table 7.4 Yields and significances for various isolation selections using the ll$\mu\mu$ reducible background calculation (signal taken from MC simulation).

Isolation selection	Signal	qqZZ	$t\bar{t}$	Z+jets	Significance
FCLoose	34.027	15.108	0.260	1.230	6.754
FixedCutPflowLoose	35.811	16.945	0.329	1.841	6.897
TrackOnly0p20	39.653	18.915	0.778	2.925	7.185
Tri_HighMuLoose	35.995	16.999	0.219	1.731	6.935
Tri_PflowLoose1000	35.488	16.628	0.258	1.588	6.898

The results above are derived without the isolation scale factor (SF) to correct for difference between MC and data, because it was not available during the time of the study. The use SF on MC reduces slightly the electron event rates, mainly due to less-than-1 SF for low-p_{T} electrons. The phenomenon is observed similarly in other isolation working points. It is hard to make a good measurement of low-p_{T} electron because of the large contamination of non-prompt background. Table 7.6 shows the changes in the

Table 7.5   Significances for various isolation selections using the llee reducible background calculation in each category. The best significance in each category is marked in bold (with the exception of the ttH-enriched leptonic category, where the reducible background is negligible).

Category	FCLoose	FixedCut PflowLoose	TrackOnly 0p20	Tri_High MuLoose	Tri_Pflow Loose1000
0-jet $p_{\mathrm{T}}^{4l} < 100$ GeV	3.05	3.87	3.04	3.45	3.84
0-jet $p_{\mathrm{T}}^{4l} > 100$ GeV	0.06	0.06	0.05	0.06	0.06
1-jet $p_{\mathrm{T}}^{4l} < 60$ GeV	1.91	2.38	1.91	2.12	2.35
1-jet $60 < p_{\mathrm{T}}^{4l} < 120$ GeV	1.52	1.87	1.57	1.7	1.83
1-jet $p_{\mathrm{T}}^{4l} > 120$ GeV	0.74	0.86	0.74	0.8	0.85
2-jet VH-enriched	1.21	1.47	1.18	1.29	1.41
2-jet VBF-enriched $p_{\mathrm{T}}^{j1} < 200$ GeV	1.56	2	1.58	1.73	1.96
2-jet VBF-enriched $p_{\mathrm{T}}^{j1} > 200$ GeV	0.09	0.09	0.08	0.08	0.08
VH-leptonic	1.07	1.05	**1.14**	1.1	1.04
ttH-enriched hadronic	0.59	0.7	0.52	0.62	0.69
ttH-enriched leptonic	0	0	0	0	0

total gluon-gluon fusion signal, and the changes in each of the four final states, both with and without the scale factors applied. As can be seen, the overall result of using the new WP is still an improvement. Also note that, as expected, the improvement increases with higher pile-up, since this working point should be more pile-up-robust.

Table 7.6 Change in the rate at which gluon-gluon fusion events are reconstructed using the new FixedCutPflowLoose isolation WP for each MC simulation campaign, with and without the data-MC isolation efficiency scale factors).

	Percent increase with scale factors			Percent increase without scale factors		
	mc16a	mc16d	mc16e	mc16a	mc16d	mc16e
all	3.0	4.8	5.6	2.4	4.6	5.2
4μ	6.8	9.9	10.2	3.8	6.9	7.1
$4e$	-1.8	-1.6	-0.1	1.0	2.5	3.7
$2\mu 2e$	0.4	0.8	2.4	2.4	3.7	4.7
$2e2\mu$	3.3	5.2	5.4	1.2	3.4	3.9

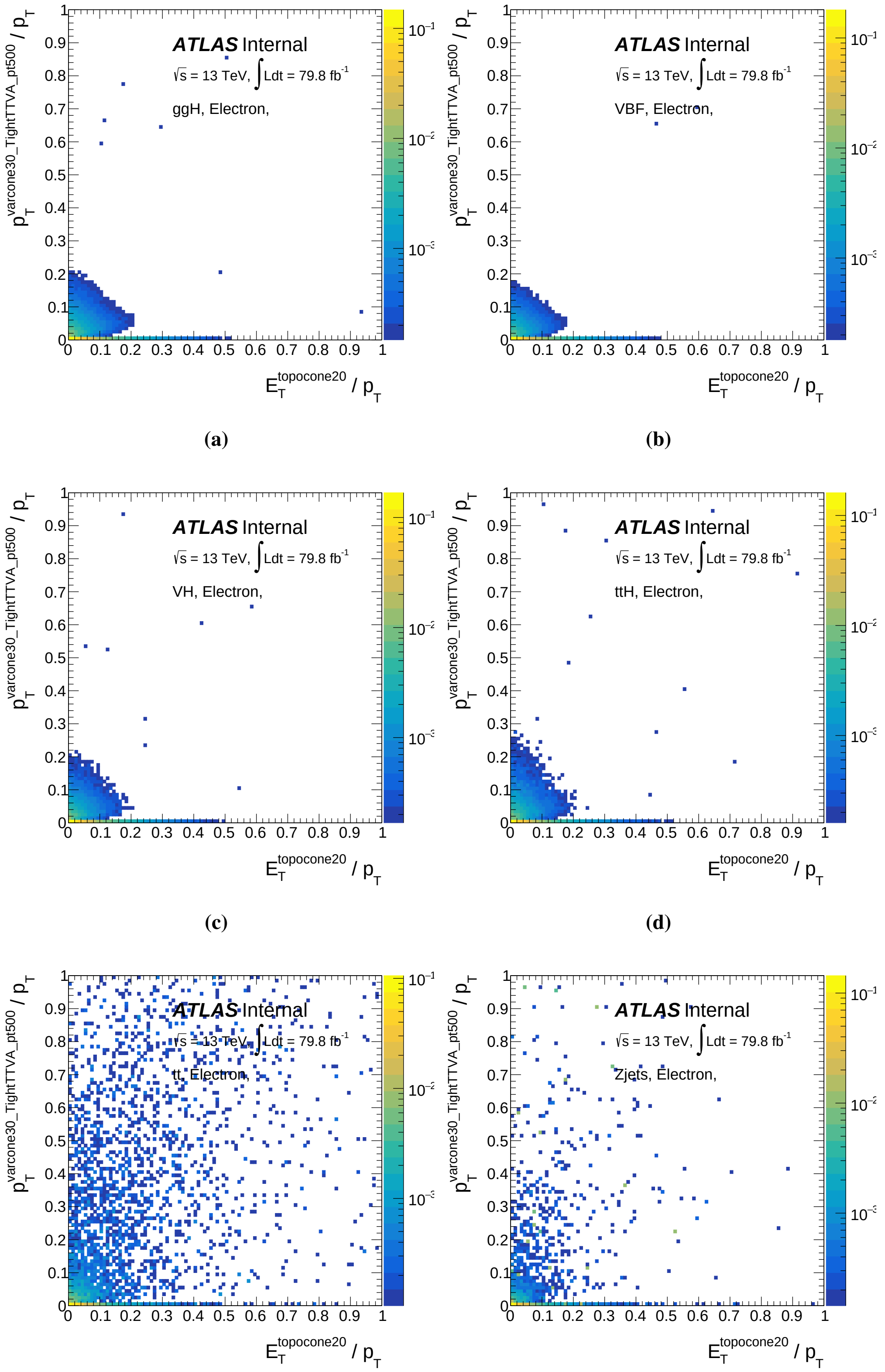

(a) (b) (c) (d) (e) (f)

Fig. 7.2 Distribution of track isolation variable vs. calorimeter isolation variable for 4e channel in (a) ggH, (b) VBF, (c) VH, (d) ttH, (e) $t\bar{t}$, and (f) Z+jets processes.

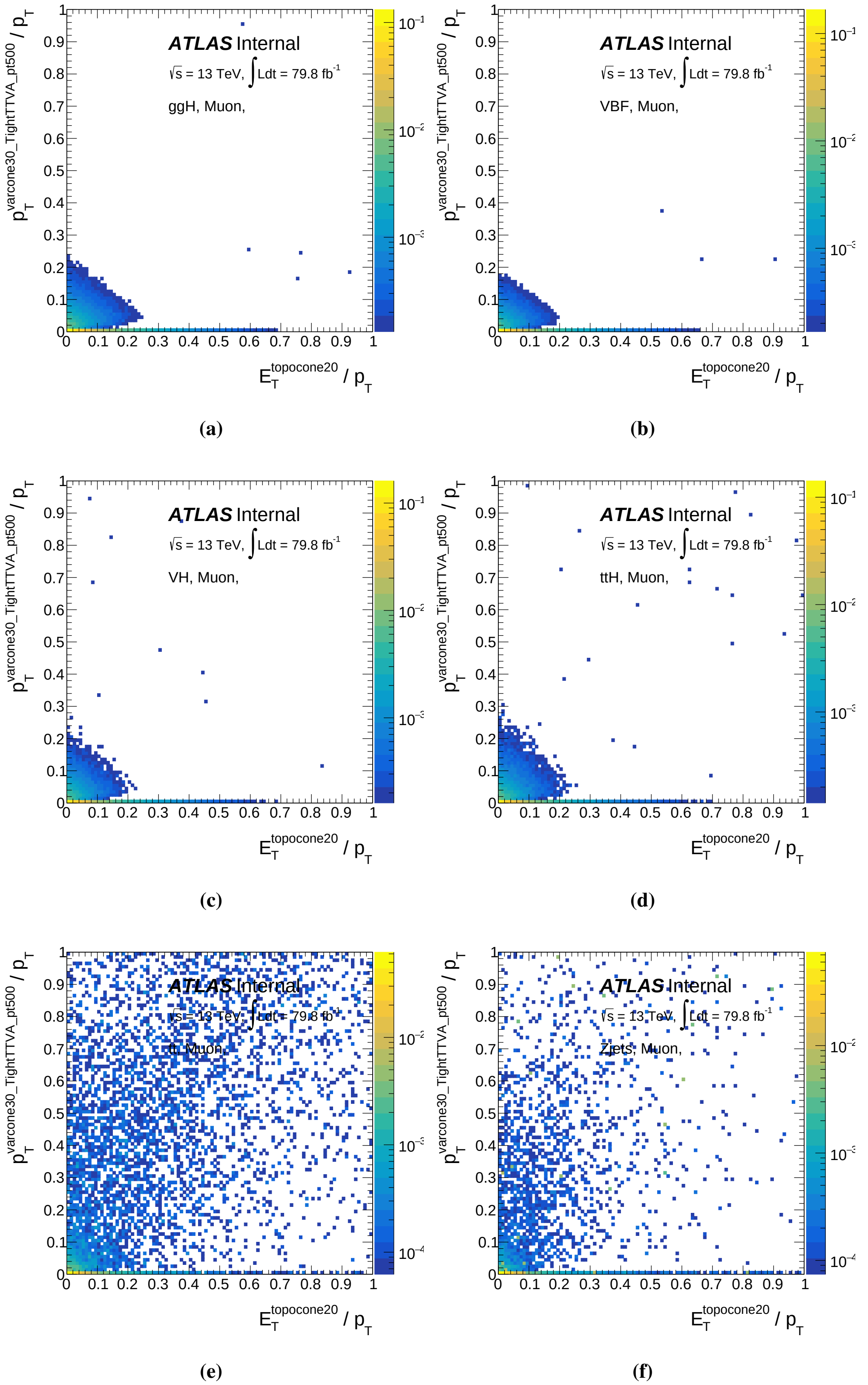

Fig. 7.3 Distribution of track isolation variable vs. calorimeter isolation variable for 4μ channel in (a) ggH, (b) VBF, (c) VH, (d) ttH, (e) $t\bar{t}$, and (f) Z+jets processes.

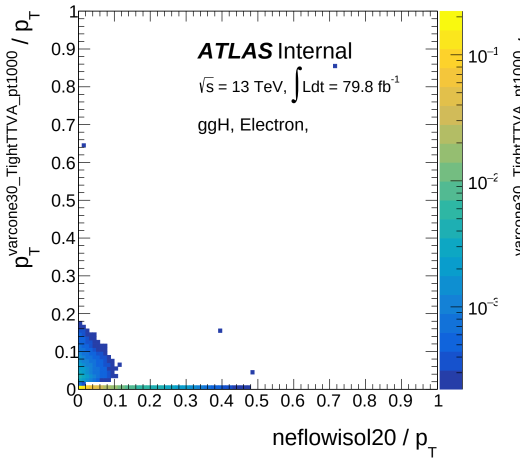

(a)

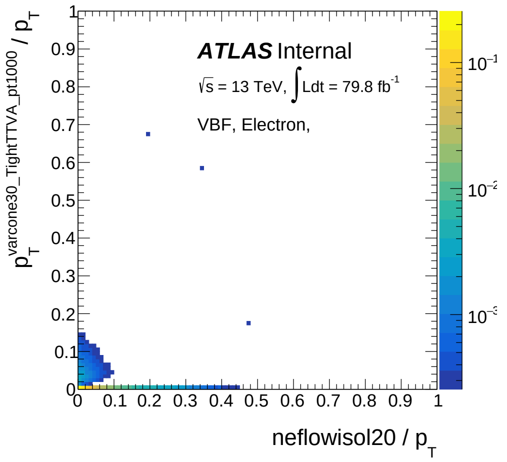

(b)

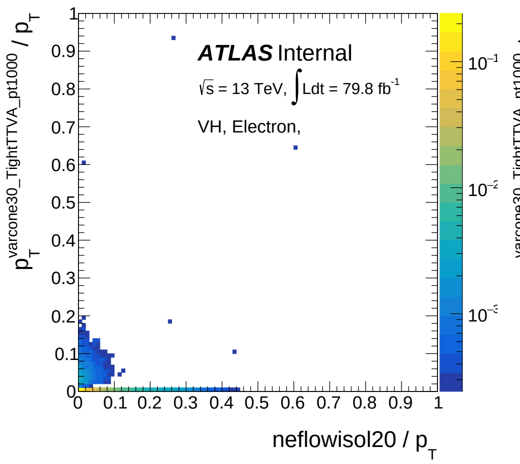

(c)

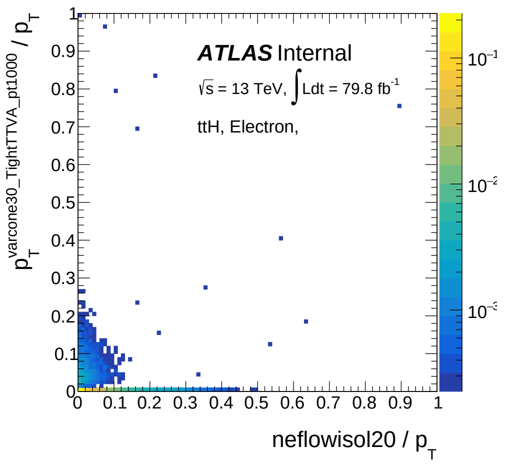

(d)

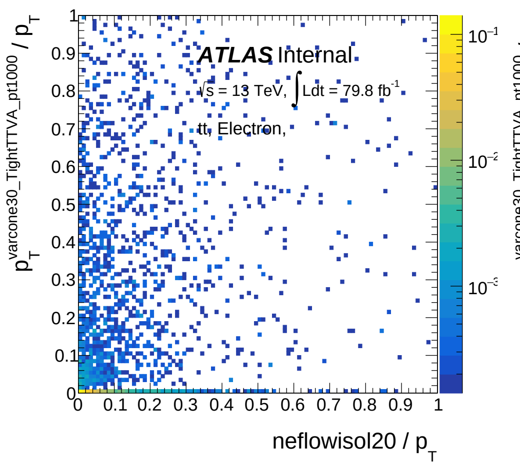

(e)

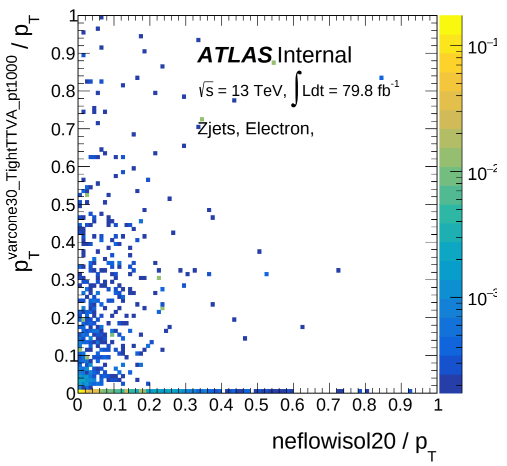

(f)

Fig. 7.4 Distribution of track isolation variable vs. particle-flow isolation variable for 4e channel in (a) ggH, (b) VBF, (c) VH, (d) ttH, (e) $t\bar{t}$, and (f) Z+jets processes.

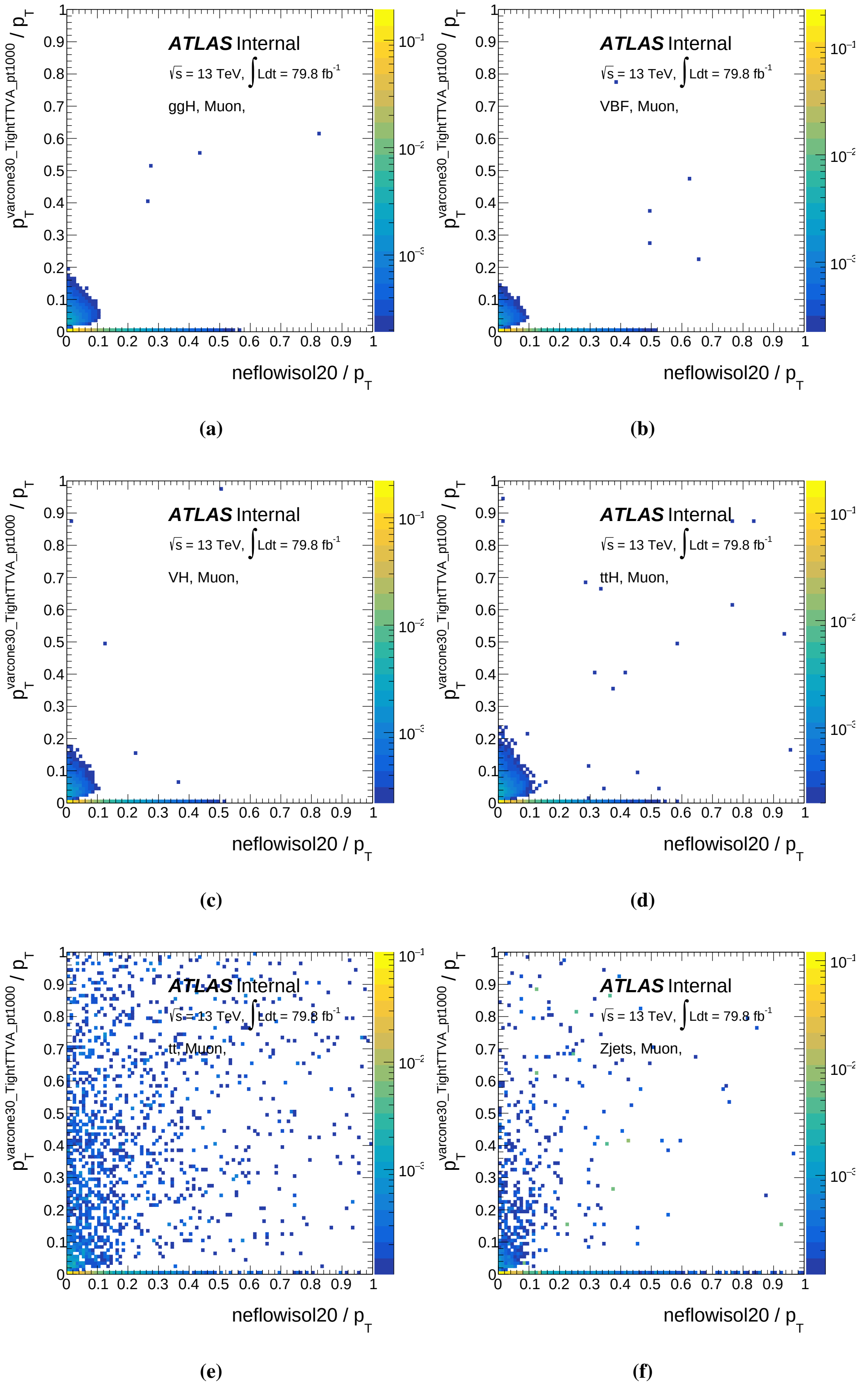

Fig. 7.5 Distribution of track isolation variable vs. particle-flow isolation variable for 4μ channel in (a) ggH, (b) VBF, (c) VH, (d) ttH, (e) $t\bar{t}$, and (f) Z+jets processes.

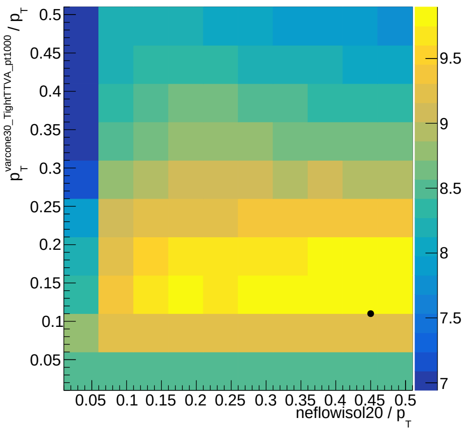

(a)

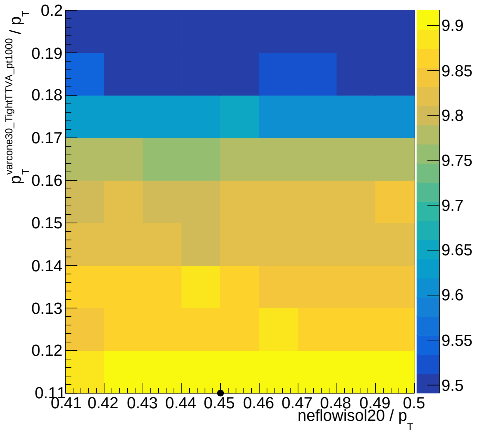

(b)

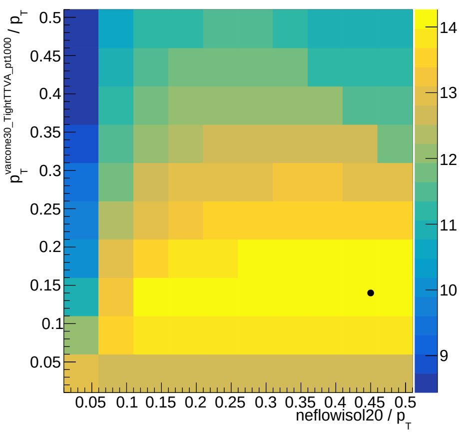

(c)

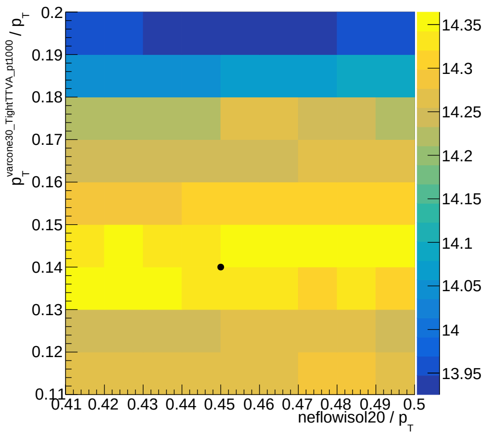

(d)

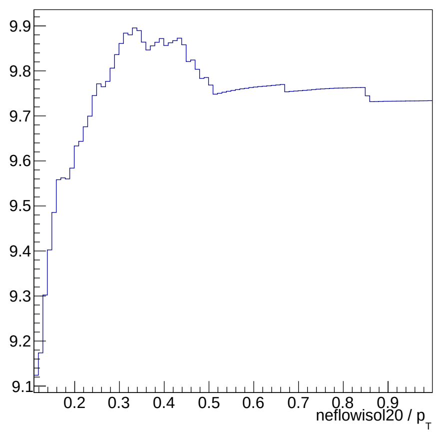

(e)

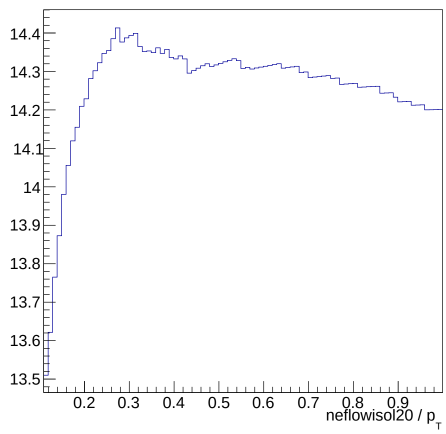

(f)

Fig. 7.6 Significance scan for isolation optimization for track isolation variable vs. particle-flow calorimeter isolation variable. The dot in the 2D plot is the where maximum significance is achieved. The 2D scan for the bump region is shown in (a) to (d). The 1D scan for the bar region where track isolation equals to zero is shown in (e) and (f) (a), (b) and (e) shows the scans in 4e channel and (c), (d) and (f) shows the scans in 4μ channel.

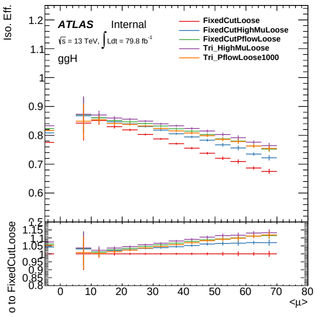

(a)

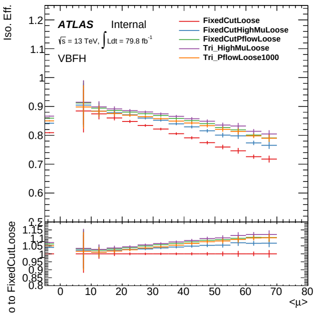

(b)

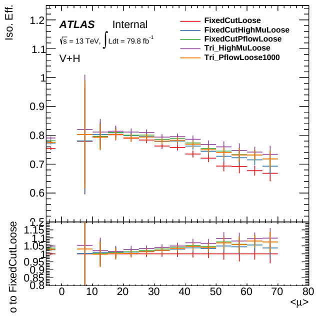

(c)

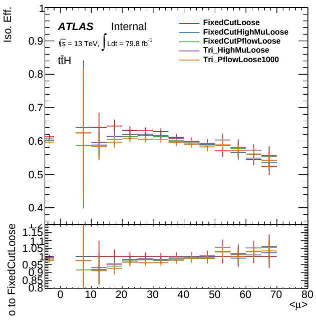

(d)

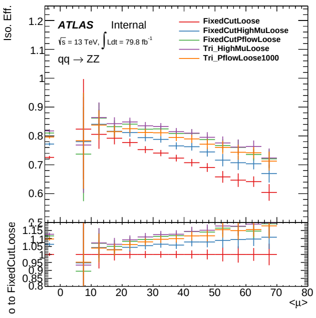

(e)

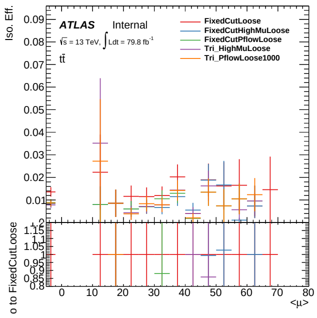

(f)

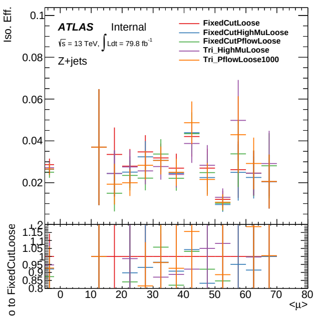

(g)

Fig. 7.7 Efficiency vs. $<\mu>$ for signal and background samples for several isolation working points. The samples include (a) ggH, (b) VBF, (c) VH, (d) ttH, (e) qqZZ, (f) $t\bar{t}$ and (g) Z+jets

7.4 Definition of the Fiducial Phase Space

In the *inclusive lineshape measurement*, the differential cross sections are measured at truth-particle level by unfolding technique. To reduce the dependence on detector geometry, the cross sections are measured in a fiducial phase space. The section of the fiducial volume is based on MC simulations and used in the *inclusive lineshape measurement*.

For the leptons at the truth particle level in MC simulations, three definitions of generator-level leptons are commonly used:

- *Born* lepton: leptons after the parton showering, before QED FSR.
- *Bare* lepton: leptons after the QED FSR.
- *Dressed* lepton: bare leptons whose four-momentum added with photons within $\Delta R < 0.005$ and not originating from hadrons. This matches better the reco-level with FSR recovery. The cone size is chosen to reduce dependence on the difference of QED FSR emission modeling in different Sherpa and Powheg generator.

Dressed leptons are used for fiducial observables in this analysis.

The fiducial phase space is defined by the kinematic thresholds applied in the reconstruction-level analysis, but without any isolation, impact parameter or vertex χ^2 requirements. Also the kinematic requirement on jets are removed to cover as much phase space as possible.

7.5 Background estimation

The main background component from the SM production of $ZZ^* \rightarrow 4\ell$ are estimated from MC simulations. In the *coupling analysis*. We use a simultaneous template fit within mass window and the Higgs mass side-band regions to constrain the total yield with data. This reduces the dependence of signal sensitivity on theory systematics. More details will be covered in the corresponding sections. In the *inclusive lineshape measurement*, the simulation is normalized to SM prediction for the estimation.

Other minor backgrounds, such as the VVV (V = W, and Z) processes, are also estimated from MC simulations.

The reducible background from the $Z+$jets, $t\bar{t}$ and WZ processes are estimated from data using dedicated control regions (CR) that have enriched events from the background processes. It is assumed that the non-prompt lepton contribution comes from the subleading dilepton pair because leptons from it have lower p_{T}. The estimation is done differently for $ll + \mu\mu$ and $ll + ee$ final states.

For $ll + \mu\mu$, the normalization of $Z+$jets and $t\bar{t}$ are determined by simultaneous fit inside four orthogonal control regions using mass of the leading lepton pair. The whole estimation procedure is done either inclusively, or in each single reconstructed categories in the *coupling analysis*. The control regions includes:

- enhance Z+heavy-flavor (HF) jets: inverted d_0 and relaxed isolation of subleading lepton pair, as well as relaxed χ^2 requirements,
- enhance $t\bar{t}$ by: opposite-flavor leading pair lepton and relaxed impact-parameter, isolation on subleading pair, as well as relaxed χ^2 requirements,
- enhance Z+light-flavor (LF) jets: invert isolation for at least one lepton in the subleading lepton pair,
- same-sign for subleading pair, with relaxed impact-parameter and isolation requirements.

The transfer factors are used to extrapolate to signal regions (SR) are calculated using simulation samples, separately for $Z+$jets and $t\bar{t}$. The events are first extrapolated in a relaxed control region with more statistics to allow for a reliable prediction of shapes of various distributions. The normalization of each background is extrapolated again from the relaxed region to signal regions, together with the shape to provide the final estimation.

For $ll + ee$, the control region are first formed by requiring both electrons in the subleading pair are required to have the same charge and the identification, impact parameter and isolation requirement are relaxed for the electron with lowest E_{T}. The fake electron can be contributed by a light-flavor jet, from an electron from photon conversion, or an electron from heavy hadron decay. The heavy-flavor background is estimated from MC simulation. The photon conversion and LF have different distribution in number of hits in innermost ID layer, which is used in a fit to determine the normalization, supplemented by next-to-innermost layer when the innermost layer is not available. Background components are then separated using sPlot method described in [146] for fake electron candidate binned by jet multiplicity and fake electron p_{T}. Simulated Z+X events with an on-shell Z boson plus an electron X which follows the same cut in $ll+ee$ control region are used to obtain the fitting templates and the transfer factors from CR to SR. Similar to $ll+\mu\mu$, the extrapolation is also performed inclusively or in the categories and the shape of distributions are also estimated in the CR with simulation events.

For the *coupling analysis*, the tXX process have an influence on ttH signal extraction that cannot be ignored. It is also constrained similarly like ZZ^* process with side-band, but only for the ttH categories. For *inclusive analysis*, this background is minor and we use estimation from MC.

Chapter 8 Statistical Methodology

After the events are selected, statistical analysis took place to extract information from data. Models are described by one or more parameters of interest (POI), such as cross section, signal strength, coupling strength and also nuisance parameters (NP) which describes systematic uncertainties.

Observational variables of selected data sample provide the distributions of event kinematics for the underlying physics processes. Similarly, Monte Carlo simulation can be used to construct the sampling under various hypothesis. Probability distribution functions of certain distributions would need to be constructed from both samplings and are tested against each other. The process of describing predicted distributions by POIs is called model parametrization.

In ATLAS, frequentist approach is more widely used in statistical interpretation than Bayesian approach. A frequentist confidence interval is derived at a certain confidence level of $1-\alpha$. The POI will be in the confidence interval $1-\alpha$ of the cases under a large number of repeated samples. This α is usually taken to be 0.32(0.05), which corresponds to a 1 σ(2 σ) interval for a Gaussian distribution. Given a data set, a point estimate of the POI set can be given, usually together with a confidence interval symmetric around the point estimate. For the case of single POI point estimate $\hat{\mu}$ and central interval $[a, b]$, the interval $[a, \hat{\mu}]$ and $[\hat{\mu}, b]$ both have half the confidence level.

This chapter briefly describes the statistical methodology used in this thesis.

8.1 Likelihood Construction

8.1.1 Unbinned Likelihood

Any two event are assumed to be measured independently. From a dataset of n observed events of $\{\vec{x}_1, \vec{x}_2 ... \vec{x}_n\}$, where $\vec{x}$ is an m-dimensional variable, the probability density function under POI set $\vec{\mu}$ can be expressed as

$$\mathcal{P}(\{\vec{x}_1, \vec{x}_2 ... \vec{x}_n\} | \vec{\mu}) = \prod_{e=1}^{n} f_{\text{unbinned}}(\vec{x}_e | \vec{\mu}), \tag{8.1}$$

where $f_{\text{unbinned}}(\vec{x}|\vec{\mu})$ is the probability density function of the event topology under the model $\vec{\mu}$. In reality, instead of a description of full event topology, a limited dimension of distribution with the highest sensitivity is selected as the *observable*. This is because the analytical function would be too complicated to write down otherwise and the sampling would be impractical due to the large MC samples needed.

For one measurement, the data is fixed, so the equation (8.1) can be re-expressed as the “likelihood function” that becomes a function of $\vec{\mu}$

$$L(\vec{\mu}) \equiv \mathcal{P}(\{\vec{x}_1, \vec{x}_2...\vec{x}_n\}|\vec{\mu}). \tag{8.2}$$

For use cases like measurement of total cross sections, the total number of events are allowed to change according to Poisson distribution, therefore we have [147]

$$L_{extended}(\vec{\mu}) = Pois(n|\vec{\mu}) \prod_{e=1}^{n} f_{\text{unbinned}}(\vec{x}_e|\vec{\mu}), \tag{8.3}$$

which is called “extended likelihood” [147]. In this thesis, all likelihood is extended so the subscript “extended” will be dropped from now on.

From the definition of likelihood, it can be understood as the compatibility of the model with the data. It is no longer a p.d.f. of data, but only a function of model parameters. To find the most compatible model is to locate the global maxima of the likelihood, and the results are also called the maximum likelihood estimators (MLE).

8.1.2 Binned Likelihood

Unbinned fit is usually time consuming because a large number of events leads to a large number of evaluations of p.d.f. By stacking the distribution into histogram, the likelihood becomes

$$L(\vec{\mu}) = Pois(n|\vec{\mu}) \prod_{i}^{\text{bins}} [f_{\text{binned}}(i|\vec{\mu})]^{n_i}, \tag{8.4}$$

where n_i is the number of events in bin i, and $f_{\text{binned pdf}}$ satisfies

$$f_{\text{binned}}(i) \equiv \overline{f(x_i)} = \frac{\int_{\text{bin } i} f_{\text{unbinned}}(\vec{x}) d\vec{x}}{\Delta_i}, \tag{8.5}$$

where Δ_i is the width of bin i. Binned likelihood reduces the number of p.d.f. evaluation from number of events, n, down to number of bins. With a proper selection of the binning, the precision can be kept at an acceptable level.

For a distribution where the expected yield in bin i is $\epsilon_i(\vec{\mu})$ and the total expected yield is $E(\vec{\mu}) = \sum_i^{bins} \epsilon_i(\vec{\mu})$, by definition we can rewrite the binned p.d.f. as

$$f_{\text{binned}}(i) = \frac{\epsilon_i(\vec{\mu})/E(\vec{\mu})}{\Delta_i}. \tag{8.6}$$

Plugging (8.6) back to (8.4), we can arrive at

$$
\begin{aligned}
L(\vec{\mu}) &= Pois(n|E)\prod_i^{\text{bins}}\left[\frac{\epsilon_i}{E\Delta_i}\right]^{n_i} \\
&= Pois(n|E)\times\prod_i^{\text{bins}}\frac{1}{\Delta_i^{n_i}}\prod_i^{\text{bins}}\left[\frac{\epsilon_i}{E}\right]^{n_i} \\
&= const\times Pois(n|E)\prod_i^{\text{bins}}\left[\frac{\epsilon_i}{E}\right]^{n_i}.
\end{aligned}
\tag{8.7}
$$

It is easy to prove that from (8.7) that we can derive [148]

$$
\begin{aligned}
L(\vec{\mu}) &= const\times Pois(n|E)\prod_i^{\text{bins}}\left[\frac{\epsilon_i}{E}\right]^{n_i} \\
&= const\times\mathcal{N}_{comb}\prod_i^{\text{bins}}Pois(n_i|\epsilon_i) \\
&= const\times\prod_i^{\text{bins}}Pois(n_i|\epsilon_i),
\end{aligned}
\tag{8.8}
$$

where $\mathcal{N}_{comb} = \frac{\prod_i n_i!}{n!}$ is a constant combinatorial factor. The equation can be interpreted as each bin follows a Poisson distribution independently.

8.1.3 Model Parametrization

The parametrization of the expected distributions from various processes can be done in two ways in general. The first one is where f_{unbinned} from each processes are described by analytical functions. The parameters of the analytical function can be derived from fitting with different Monte Carlo samples. The second method is taking f_{binned} directly from MC prediction, which is also called MC template. It should be noted that analytical function is not restricted to use unbinned likelihood, but the integral can be calculated and used in binned likelihood.

Once the p.d.f. description is derived separately for different process, they're put together to form the total expected, according to the physics assumptions. The most widely used formula is

$$E = \mu s + b, \tag{8.9}$$

where μ is the signal strength, E, s and b corresponds to total, signal and background prediction, correspondingly. This parametrization is designed for a model to test the existence of signal and is valid for both total yield and for the p.d.f. For binned likelihood it applies to yield in each bin.

8.1.4 Systematic Uncertainties

Systematic uncertainties on the prediction originate from various sources. They can be categorized into experimental, theory ones. Experimental ones includes object reconstruction efficiency correction, energy or momentum calibration, luminosity measurement, pileup reweighting and so on. All of those measurement of scale factors, energy scales have its uncertainty and is propagated to the predictions in the analysis.

Systematic uncertainties can be included in a likelihood construction in two parts. The first part is on the prediction dependent on a nuisance parameter (NP), θ, describing the size of the variation. The second part is to constrain the NP, since the variation is given at a certain confidence value, which is usually 1-sigma. The uncertainty is often further separated to normalization and shape.

For parametrization of the prediction, there are various ways for interpolating the systematics, and the linear interpolation formula for normalization and shape systematics for binned likelihood is

$$n = n_0 \times (1 + \sum_i^{var} \theta_i \cdot var_i). \tag{8.10}$$

The n_0 is the nominal value, and n is after the variation. This formula applies for both total yield and yield in each bin. The var_i is the relative uncertainty and the sign is dependent on the θ:

$$var_i = \begin{cases} var_i^+, & \theta_i > 0 \\ var_i^-, & \theta_i < 0 \end{cases}. \tag{8.11}$$

If a variation is asymmetric, i.e. $var_i^+ \neq -var_i^-$, a kink will appear at $\theta_i = 0$ for linear interpolation. Such a kink will cause instability for the fitting, but it suffices in scenario of a symmetric uncertainty. The shape systematics for analytical function would usually require some morphing techniques and is not discussed since it is not part of this thesis.

The constraint term for each $\vec{\theta}$ is simply a Gaussian multiplied on the likelihood

$$L(\vec{\mu}, \vec{\theta}) = L(\vec{\mu}) \prod_i^{var} G(\theta_i | \Theta_i, 1), \tag{8.12}$$

where $\vec{\Theta}$ is the *Global Observable*, which describe the centrality of the NP, and is 0 in the nominal experiment. In this case the variation corresponds to the value at 68% confidence level, or 1-sigma.

8.2 Test statistics

It is shown in the previous sections that the absolute value of likelihood is dependent on a constant term which only scales the likelihood and does not change the maxima. Therefore the profile likelihood ratio (PLR) is constructed as

$$\lambda(\vec{\mu}) = \frac{L(\vec{\mu}, \hat{\hat{\vec{\theta}}}(\vec{\mu}))}{L(\hat{\vec{\mu}}, \hat{\vec{\theta}})}, \tag{8.13}$$

where $\hat{\vec{\mu}}, \hat{\vec{\theta}}$ is the maxima, which is also called "best fit" values and $\hat{\hat{\vec{\theta}}}(\vec{\mu})$ is the maxima of $\vec{\theta}$ when $\vec{\mu}$ is fixed. By construction, the constant term is dropped conveniently. Furthermore the test statistics is defined from the PLR as

$$t_{\vec{\mu}} = -2\ln(\lambda(\vec{\mu})). \tag{8.14}$$

By definition, the test statistics is non-negative. For the binned likelihood (8.8) without systematics, the test statistics can be written down as

$$t_{\vec{\mu}} = 2\sum_{i}^{\text{bins}}(\epsilon_i - n_i \ln\epsilon_i), \tag{8.15}$$

and up to a constant. By requiring the first derivative to be zero, the minimum of $\vec{\mu}$ can be calculated. If each bin yield is a POI, the solution is simply $\epsilon_i = n_i$.

Each test statistics value corresponds to a data observation. In order to sample the p.d.f. distribution, a large number of observation is needed. We cannot do the same analysis twice under the exact same condition as the frequentist philosophy prescribed, because there is only one ATLAS detector. Instead, Monte Carlo pseudo-experiment is used to complete our observation ensemble under certain model.

During the generation of pseudo-experiments, the *Global Observable* and *Observable* are randomized to mimic an observation with a similar setup as ATLAS. The process is also called MC toy methods. The "Asimov" dataset should represent the median of distribution of the test statistics [149], i.e. the center of an interval. In order to derive an expected sensitivity, the SM process is used to throw the toy and the Asimov dataset $\boldsymbol{n}$ is equal to $\boldsymbol{\epsilon}$.

It is a time-consuming process to minimize all the toys and it is only needed for observation with a small number of events. Asymptotic formulae for test statistics are very close to the true distribution derived from MC toys when the expected data is around 10 events. The asymptotic formulae will be introduced in the next section.

8.2.1 Asymptotic Formulae for Test Statistics

According to the Wald theorem [150], in case of a single POI, t_μ is parabolic up to the sample size:

$$t_\mu = \frac{(\mu - \hat{\mu})^2}{\sigma^2} + \mathcal{O}(1/\sqrt{N}). \tag{8.16}$$

Here $\hat{\mu}$ is the best fit of one data in an data ensemble. $\hat{\mu}$ follows a Gaussian distribution with a mean μ' and standard deviation σ, where μ' stands for the model where the data ensemble is generated. Given a large number of data observed, from (8.16) we can derive the p.d.f. for for test statistics t_μ

$$f(t_\mu|\mu') = \frac{1}{\sqrt{2\pi}}\frac{1}{2\sqrt{t_\mu}}\left[exp\left(-\frac{1}{2}(\sqrt{t_\mu}+\frac{\mu-\mu'}{\sigma})^2\right)+exp\left(-\frac{1}{2}(\sqrt{t_\mu}-\frac{\mu-\mu'}{\sigma})^2\right)\right], \tag{8.17}$$

a *non-central chi-squared* distribution with one degree of freedom.

For a measurement, the μ' corresponds to the best fit value for a given ensemble, and μ corresponding to the model to be tested, should be equal to the the best fit value, μ'. The (8.17) becomes a *central chi-squared* distribution with one degree of freedom

$$f(t_\mu|\mu) = \frac{1}{\sqrt{2\pi}}\frac{1}{\sqrt{t_\mu}}e^{-t_\mu/2}, \tag{8.18}$$

And the cumulative distribution function (cdf) is

$$F(t_\mu|\mu) = 2(\Phi\left(\sqrt{t_\mu}\right) - 0.5), \tag{8.19}$$

where Φ is cumulative distribution of the standard (zero mean, unit variance) Gaussian. This c.d.f. is equal to the integral of standard Gaussian between $[-\sqrt{t}, \sqrt{t}]$. Therefore for a symmetric 1-sigma and 2-sigma confidence interval, the solution for t_μ is simply 1 and 4 correspondingly. The interval of μ can be derived as the region where t_μ is small than 1 or 4, for a confidence level of approximately 68% and 95%.

8.2.2 Alternative Test Statistics

Besides $t_{\overline{\mu}}$, there are other types of test statistics for different purposes. This section introduces the definition for the other test statistics while their asymptotic formulae can be found in Ref. [149]. The statistics are defined to follow certain physical constrains. For example, if there's a physical constrain for a non-negative POI μ, the test statistics $\tilde{t}_\mu$ can be used

$$\tilde{t}_\mu = \begin{cases} -2\ln\dfrac{L(\mu,\hat{\hat{\theta}}(\mu))}{L(\hat{\mu},\hat{\theta}(\mu))}, & \hat{\mu} > 0 \\ -2\ln\dfrac{L(\mu,\hat{\hat{\theta}}(\mu))}{L(0,\hat{\hat{\theta}}(0))}, & \hat{\mu} < 0 \end{cases}. \tag{8.20}$$

When one is interested in the upper limit on μ of a positive signal, rejecting the parameter space beyond the upper limit, the test statistics q_μ or $\tilde{q}_\mu$ can be used. They penalize the cases where $\mu < \hat{\mu}$ so that an excess in the data (larger $\hat{\mu}$) should not be used to rule out a signal model with lower yield (lower μ):

$$\tilde{q}_\mu = \begin{cases} t_\mu, & \mu > \hat{\mu} \\ 0, & \mu < \hat{\mu} \end{cases}, \tag{8.21}$$

$$q_\mu = \begin{cases} \tilde{t}_\mu, & \mu > \hat{\mu} \\ 0, & \mu < \hat{\mu} \end{cases}. \tag{8.22}$$

To derive the upper limit, the p-value of the hypothesized μ is defined as

$$p_\mu = 1 - F(\tilde{t}_\mu^{\text{data}}|\mu), \tag{8.23}$$

where the F is the cdf of $\tilde{t}_\mu$. By requiring p-value equal to 0.05 the 95%-CL upper limit can be derived. When data is Asimov data and observed data correspondingly, the limit stands for expected or observed limit. The discussion on the p-value follows:

1. if the data is similar to Asimov data under μ, the p-value is roughly 0.5;
2. if the data has excess compared to Asimov data under μ, the $\tilde{t}_\mu^{\text{data}}$ will be 0 and p-value is 1;
3. if the data has deficit compared to Asimov data under μ, $\tilde{t}_\mu^{\text{data}}$ will be large and the p-value will be small;

therefore we will have the power to reject μ in the third case.

However there is a flaw in this metric to rule out model. The pdf of μ-model $f(\tilde{t}_\mu|0)$ will be larger than bkg-model pdf $f(\tilde{t}_\mu|\mu)$ in average because the model and data are less compatible in the former case. If they are well separated, a bkg-like data will rule out μ-model without a problem. Now imagine a parameter space where the experiment has little sensitivity and an significant overlap exists between $f(\tilde{t}_\mu|\mu)$ and $f(\tilde{t}_\mu|0)$. In this case, the Asimov data under bkg-model should result in an p_μ approximately equal to 0.5 because bkg-model and μ-model are very similar. But a data from such ensemble can exclude the model by chance, which is not ideal. Therefore, the quantity CL_s [151] is introduced

$$\text{CL}_s(\mu) = \frac{p_\mu}{1 - p_b}, \tag{8.24}$$

where p_b is the p-value of background-only hypothesis

$$p_b = F(\tilde{t}_{\text{data}}|0). \tag{8.25}$$

In this case, we will require $\mathrm{CL}_s(\mu) = 0.05$ as the upper limit. When data is similar to or have excess than Asimov data, the conclusion rejection power remains. But when data becomes close to bkg-model, p_b will be similar to p_μ and the rejection power is lost. Therefore this metric will not reject phase space where the experiment has little sensitivity.

The calculation above concerns the median of the upper limit, which is the 50%-quantile of the upper limit. For calculation of limit bands of Nσ-quantile, reader can refer to Ref. [149, 152-153] for more details.

8.2.3 X^2 as test statistics

The Neyman's X^2 can be derived from formula (8.15):

$$\begin{aligned}
X^2_{Neyman} &= 2\sum_i^{\text{bins}}(\epsilon_i - n_i \ln\epsilon_i) \\
&= 2\sum_i^{\text{bins}}[\epsilon_i - n_i\ln(n_i) - n_i\ln(\frac{\epsilon_i}{n_i})] \\
&= 2\sum_i^{\text{bins}}\{\epsilon_i - n_i\ln[1 + (\frac{\epsilon_i}{n_i} - 1)] \quad \text{(dropping constant)}\} \\
&= 2\sum_i^{\text{bins}}\{\epsilon_i - n_i \cdot [(\epsilon_i/n_i - 1) - \frac{(\epsilon_i/n_i - 1)^2}{2} + \mathcal{O}((\epsilon_i/n_i - 1)^3)]\} \\
&\approx 2\sum_i^{\text{bins}}(\epsilon_i - \epsilon_i + n_i + \frac{(\epsilon_i - n_i)^2}{2n_i}) \quad (\epsilon_i \approx n_i) \\
&= \sum_i^{\text{bins}}(\frac{\epsilon_i - n_i}{\sqrt{n_i}})^2 \quad \text{(dropping constant)}
\end{aligned}, \tag{8.26}$$

where the error is taken from data $\sigma_i = \sqrt{n_i}$. Whereas the Pearson's X^2 uses the expected prediction as its error:

$$X^2_{Pearson} = \sum_i^{\text{bins}}(\frac{\epsilon_i - n_i}{\sqrt{\epsilon_i}})^2. \tag{8.27}$$

Those are special cases of the generalized X^2 without correlation between bins, where the covariance matrix are diagonal. The more generalized formula would be

$$X^2 = (\boldsymbol{\epsilon} - \boldsymbol{n})^T M^{-1}(\boldsymbol{\epsilon} - \boldsymbol{n}) \tag{8.28}$$

, where $\boldsymbol{\epsilon}$ and $\boldsymbol{n}$ are vector of expected and observed inside each bin, and M is the covariance matrix. Notice a X^2 can also be derived from a Gaussian likelihood:

$$L(\vec{\mu}) = \frac{1}{\sqrt{2\pi}\det M}e^{-\frac{1}{2}(\boldsymbol{\epsilon}-\boldsymbol{n})^T M^{-1}(\boldsymbol{\epsilon}-\boldsymbol{n})}, \tag{8.29}$$

as long as the determinant is constant and can be discarded.

Now we will explore the bias of X^2 compared to Poisson error. Consider a very simple single-bin observable, we can derive the derivatives of prediction separately for t_μ and two X^2:

$$t'_\mu = \frac{\partial t_\mu}{\partial \epsilon} = 2(1 - \frac{n}{\epsilon}), \tag{8.30}$$

$$X^{2'}_{Neyman} = \frac{\partial X^2_{Neyman}}{\partial \epsilon} = 2\frac{\epsilon}{n}(1 - \frac{n}{\epsilon}), \tag{8.31}$$

$$X^{2'}_{Pearson} = \frac{\partial X^2_{Pearson}}{\partial \epsilon} = (1 - \frac{n^2}{\epsilon^2}). \tag{8.32}$$

The minima for all three test statistics are all located at $\epsilon = n$, but it can be easily deduced that

$$\frac{X^{2'}_{Neyman}}{t'_\mu} = \frac{\epsilon}{n} = \begin{cases} > 1, & \epsilon > n \\ < 1, & \epsilon < n \end{cases}, \tag{8.33}$$

$$\frac{X^{2'}_{Pearson}}{t'_\mu} = \frac{1 + n/\epsilon}{2} = \begin{cases} < 1, & \epsilon > n \\ > 1, & \epsilon < n \end{cases}. \tag{8.34}$$

Therefore for $\epsilon > n$, X^2_{Neyman} will have a steeper curve than t_μ, which further have a steeper curve than $X^2_{Pearson}$. And for $\epsilon < n$, the trend is reversed. This indicates that the confidence interval derived for Pearson's X^2 is biased towards higher values of ϵ, i.e. bias up, compared to a Poisson likelihood. While Neyman's X^2 bias down on the other hand.

This bias effect can be generalized for multi-bin observable. It can be understood as applying invert of errors as weights in bins. The large the error, the smaller the weight, and less important the difference is to the total X^2. For Pearson's X^2, if the prediction is pulled up, the error in bins are increased and allow for the difference. For Neyman's X^2, if some bin have deficit, the error will penalize higher values, unlike Poisson distribution, where the error is $\sqrt{\epsilon}$ which scales with prediction.

8.2.4 Addressing Bias in Interpretation of Unfolded Spectrum

The usual way of utilizing unfolded spectrum in interpretation is to use Neyman's X^2. This will lead to an underestimation of the error and best fit due to the property described above. A concern is raised whether it is reasonable that an interpretation based on unfolded spectra have better sensitivity than an interpretation based on reco-level spectra.

In this thesis, a novel construction of X^2 is used to correct this effect and takes the systematic covariance into consideration. The matrix element of the covariance is defined as

$$C_{ij} = rel_i \times rel_j \times C_{ij}^{syst} + \sqrt{rel_i \times rel_j} \times C_{ij}^{stat} + C_{ij}^{bkg}, \tag{8.35}$$

where C^{syst}, C^{stat}, C^{bkg} are covariance derived from unfolding Asimov data, and $rel_i = pred_i(\boldsymbol{\mu}, \boldsymbol{\theta})/pred_i^{nom}$ is the ratio of the predicted yield for a given value of the parameter of interest compared to the predicted yield from the nominal standard model prediction, in bin i. This treatment lead to a statistical covariance similar to Pearson's X^2, which it is mostly diagonal. It assumes that the relative systematic covariance stays the same and fully-correlated, so the absolute covariance scales linearly. And the background systematic uncertainty is constant because background was subtracted from data before the unfolding.

Therefore this provides a result that is more conservative than the reco-level interpretation.

8.3 Technical Fitting Procedure

The process of maximization of likelihood is called "fitting", which is the most computationally intensive process in the whole statistical analysis.

The pdf functions that construct likelihood models are defined as the C++ classes of the RooFit [154] toolkit, which is a library based on ROOT [155]. RooFit acts an interface that uses the underlying utility Minuit2, from ROOT, to do minimization on functions. RooStat is a higher-level wrapper that book-keep all RooFit objects in a "workspace" and also provides fitting utility with an simpler interface.

The likelihood is usually converted to the "negative log likelihood"

$$\mathrm{NLL} = -\ln L, \tag{8.36}$$

for minimization, where the logarithm reduces the order of the quantity for a better numerical property. After the fitting is done, corresponding test statistics can be easily calculated from the NLL.

The default minimization algorithm from Minuit2 is Migrad, which calculates the minimum and a rough estimation of the 68% CL error during the minimization. The error calculation is supplemented by Hesse and Minos algorithm. Hesse calculates the full second-derivative matrix and inverts it at best fit value, which provides a symmetric error better than Migrad. Minos uses the same method describe in section 8.2.1 to calculate the error by solving the equation of test statistics equal to 1 [156].

Chapter 9 Higgs Production Cross Section and Coupling Measurements with 4ℓ Final State

As described previously, the $H \to ZZ^* \to 4\ell$ channel features a very high signal to background ratio, which is achieved by the requirement of four isolated leptons and the unique kinematic requirements for leptons originated from one on-shell Z and one off-shell Z boson. The contribution of production modes follows the order of the cross sections are ggF, VBF, VH and ttH (see Section 3.3). The ggF production has zero jets at the leading order, but large fraction of events has high p_{T} jets included due to large radiative process comes with the gluons initial state. The VBF production has two jets associated with Higgs production. The two jets have a large angular separation ($\Delta\eta$) and the di-jet invariant mass. The VH production can be further split as $V = W, Z$, and by the decay modes of the associated vector boson. The characteristics are that the H and the V boson are back-to-back and tend to have larger p_{T}, and is possible to have more lepton and jet multiplicity in the events. The ttH production mode has associative production of the Higgs boson and two top quarks, which further decay to bottom quarks and W bosons. The decay of W bosons also leads to a high lepton and jet multiplicity. The ggF and VBF have major contributions to the signal sensitivity of the four lepton channel. While only a few events are expected in the VH and ttH channels in the current dataset, but these events provide additional information in the coupling measurement.

The coupling measurement is first carried out in the simplified template cross section (STXS) framework [39], where Higgs signal is separated into production mode, and also further separated into categories targeting different event topology. Each production mode has a cross section as its POI, to be measured. The advantage of STXS is that it reduces the dependent on the theoretical uncertainties. The reconstructed events are also categorized in a way similar to the STXS categorization. The goal of similar categorization at the reconstruction and the truth-particle level is aimed to increase the purity of each reconstruction categories so as to increase the sensitivity and make the measurement as uncorrelated as possible. In order to reduce the dependence on theoretical prediction of Standard Model $ZZ^*$and tXX background, dedicated side-band regions are used to constrain the background separated in jet multiplicity from data.

In each signal categories with enough expected statistics, multivariate analysis using recurrent neural-network (RNN) is applied to further separate the signal from background. The RNN output is used as the discriminant the observable for statistical analysis to measure the different cross sections.

This chapter presents the analysis based on full Run 2 data at $\sqrt{s} = 13$ TeV with an integrated luminosity of 139 fb^{-1} collected during 2015 and 2018. The exceptions are that some studies were carried out early on when the latest samples were not available. The ttH category was introduced and optimized by the author of this thesis. Details on the ttH multivariate BDT discriminant was developed based on earlier Run 2 data of 80 fb^{-1}, and will be described in this chapter.

9.1 Event Categorization

9.1.1 Production Bins

The event categorization at the truth-particle level is separated into two "Stages". First of all, the acceptance requirement on Higgs rapidity, $|Y_H| > 2.5$, is applied on the born-leptons before event categorization.

The Stage-0 is simply done by specifying the production mode: ggF, VBF, VH and ttH. It is worth noting that VH includes the ggZH process. Minor production modes are merged with other production modes with a similar acceptance: the bbH is merged with the ggF and the tH is merged with the ttH.

The reduced Stage-1.1 (RS1.1) is a simplified form of full Stage-1.1 [157], where the truth bins that were tested to without enough sensitivity are merged with neighboring bins. Unlike in the Stage-0, the production of the ggZH where Z decays hadronically is merged with the ggF to form *gg2H* bin, so that $gg \to H$ process is included inclusively. Likewise, the VH where the vector boson decays hadronically is merged with VBF as *qq2Hqq* bin, which represents s- and t-channel contributions to the physical process of $qq \to V(\to q\bar{q})H$. Then the production modes are further split to 12 different production bins depending on the event topology.

The category of the *gg2H* production with $p_T^H > 200$ GeV (called gg2H-p_T^H-High) is separated out to probe physics beyond the Standard Model (BSM). The remaining events with $p_T^H < 200$ GeV are split into six bins as follows. For events with zero jets, they are split into $p_T^H < 10$ GeV (called gg2H-0j-p_T^H-Low) and $p_T^H > 10$ GeV (called gg2H-0j-p_T^H-High). For events with one jets, they are split into $p_T^H < 60$ GeV (called gg2H-1j-p_T^H-Low), $60 < p_T^H < 120$ GeV (called gg2H-1j-p_T^H-Medium) and $p_T^H < 120$ GeV (called gg2H-1j-p_T^H-High). Events with at least two jets themselves form the *gg2H-2j* category bin.

The *qq2H* categories are split into three bins: the *qqH2qq-BSM*, requiring $p_T^H >$

200 GeV and $m_{jj} > 350$ GeV which is sensitive to BSM physics; the *qqH2qq-VH-Like*, requiring $60 < m_{jj} < 120$ GeV where VH is enhanced; and *qqH2qq-Rest*, a third bin which contains the remaining events.

The VH where the vector boson decays leptonically is categorized in *qq/gg2HLep* bin, where the V decays to τ and neutrinos are also included. The ttH production has limited statistics and is a standalone bin in the Stage-0.

Figure 9.1 shows the detailed production bins in the left and middle-left panels, the middle-right and right panels show the reconstructed categories which will be described in the next section.

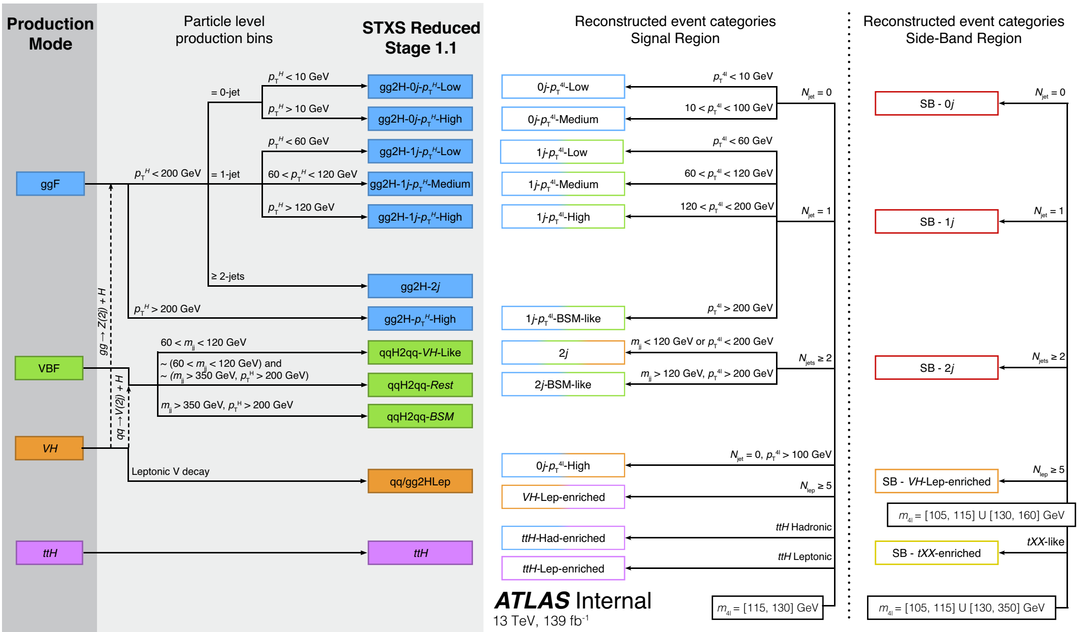

Fig. 9.1 **Event categorization scheme for STXS measurement with STXS: Reduced Stage 1.1 scheme. gg2H includes bbH and hadronically decaying ggZH. qq2Hqq include VBF and hadronically decaying qqZH. All leptonically decaying VH is categorized under VH-lep. The colored outline for the reconstructed categories indicate the targeted signal process within that category.**

9.1.2 Reconstructed Categories

In order to be sensitive to each Higgs boson production mechanism, and further to the bins at the truth-particle level defined above, each selected $H \to 4\ell$ candidate within the Higgs window $115 < m_{4l} < 130$ GeV is classified into one of 12 exclusive categories. Additionally, the events not in Higgs window but within a vicinity are categorized into 5 side-band categories to constrain $ZZ^*$and tXX background in the final simultaneous fit. The categorization algorithm starts categories with fewer events to the ones with more events, (from bottom to top in the middle-right panel of Figure 9.1) starting from the ttH to the VH, to the VBF and then to the ggF categories. This is to avoid mis-categorization that caused loss of efficiency.

First of all, for the ttH process, according to how the W bosons decays from top quarks, events are categorized into leptonic category which includes fully-leptonic and semileptonic decay modes and hadronic category which includes fully-hadronic decay mode. Both categories use pseudo-continuous b-tagging technique to extract the signal. For the leptonic category, the events are required to have at least one extra lepton with $p_{\mathrm{T}} > 12$ GeV and $\geqslant 2$ b-tagged jets with 85% b-tagging efficiency or $\geqslant 5$ jets with $\geqslant 1$ b-tagged jets with 85% b-tagging efficiency or $\geqslant 2$ jets with $\geqslant 1$ b-tagged jets with 60% b-tagging efficiency. For the hadronic category, events must have $\geqslant 5$ jets with $\geqslant 2$ b-tagged jets with 85% b-tagging efficiency or $\geqslant 4$ jets with $\geqslant 1$ b-tagged jets with 60% b-tagging efficiency. The details of optimization of the ttH categorization can be found in Section 9.1.2.1.

For events that fail the ttH categories, if they have additional leptons, they're categorized as the VH leptonic category.

The remaining events are further categorized according to the jet multiplicity, di-jet invariant mass m_{jj} and transverse momentum of the quadruplet $p_{\mathrm{T}}^{4\ell}$. Events with two jets are largely contributed by the VBF, the VH and the ggF production modes, while events with zero or one jets are mostly from the ggF, where the zero-jet category is filled up by approximately 56% of the ggF production. Events with at least two jets are put into the "2j-BSM-like" category if they satisfy $m_{jj} > 120$ GeV and $p_{\mathrm{T}}^{4\ell} > 200$ GeV. The remaining and majority of 2-jet events go into another 2-jet category.

The events with one jet are split into four categories with $p_{\mathrm{T}}^{4\ell} < 60$ GeV, $60 < p_{\mathrm{T}}^{4\ell} < 120$ GeV, $120 < p_{\mathrm{T}}^{4\ell} < 200$ GeV and $p_{\mathrm{T}}^{4\ell} > 200$ GeV, which matches with the bin requirements at the truth-particle level.

For events without jets, a $p_{\mathrm{T}}^{4\ell} > 100$ GeV category is separated out for enhancement of VH leptonic mode, and remaining events are put in $p_{\mathrm{T}}^{4\ell} < 10$ GeV and $10 < p_{\mathrm{T}}^{4\ell} < 100$ GeV categories.

The reconstructed signal categories are designed to match the truth categories as much as possible. However full exclusiveness could not be achieved completely and events from multiple production modes could contribute in the same reconstruction-category. The purity of signal under RS1.1 selection is shown in Figure 9.2. For example, the *ttH-Lep-enriched* category has signal purity of 98%, the other 2% contribution comes from the *VH-Lep* process.

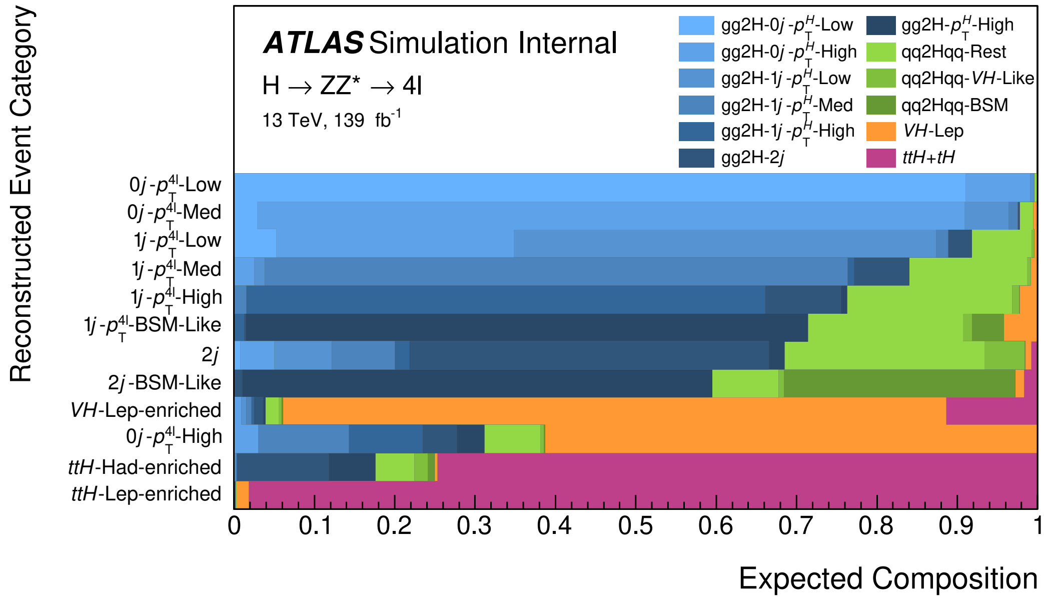

Fig. 9.2 Standard Model signal composition in terms of the Reduced Stage-1.1 production bins in each reconstructed event category. The gg2H production bins also include contribution from bbH and hadronically decaying ggZH. The qq2Hqq also include hadronically decaying VH.

The right panel of Figure 9.1 shows the logic of the side-band selection. For events with $105 < m_{4l} < 115$ GeV or $130 < m_{4l} < 350$ GeV, if they have at least two jets and one of which tagged as a b-jet with 60% efficiency, and a $E_{\mathrm{T}}^{\mathrm{miss}} > 100$ GeV, it is classified as the tXX-enriched category. The large mass range provides an enhancement for the tXX process, where the major contribution is from the ttV process.

In order to estimate the continuum SM ZZ^*production, the remaining events are required to pass $105 < m_{4l} < 115$ GeV or $130 < m_{4l} < 160$ GeV. Firstly, if at least one extra lepton exists in an event, the event is categorized as *SB-VH-Lep-enriched* category to preserve the sensitivity of the *VH-Lep* measurement. Jet multiplicity is used to categorize the rest of the events into zero jets, one jets and at least two jets. Section 9.3.1 will cover the details on optimization of side-band region selections.

9.1.2.1 Optimization of ttH Categories

The usage of pseudo-continuous b-tagging is explored to improve the ttH sensitivity. ttH categories are divided first into leptonic category and hadronic category, depending on how the two W's from the top quarks decays. Firstly we define n_bjets_η $(nQualX)$ as the number of b-tagged jets with b-jet selection efficiency of η% (quality of X) of the MV2C10 tagger: 85%(2), 77%(3), 70%(4), 60%(5). The symbol *nQual* is the jet multiplicity variable.

For leptonic category, first an extra lepton with $p_{\mathrm{T}} > 12$ GeV is required. The jet multiplicity and b-tagged jet multiplicity are shown in Figure 9.3. An observation can be made that a very pure region can be achieved by $n\_bjets\_85(nQual2) >= 2$. Then the same distributions were analyzed at for events failed the cut, and different combination of b-tagged jet number and jet number cut are applied. We found that it is possible to loosen the requirement of b-jets to $n\_bjets\_85\ (nQual2) >= 1$, and combined with a tightened $n\_jets\ (nQual1) >= 5$ requirement, to recover events that achieves higher significance. Finally an additional recovery requirement of $n\_jets\ (nQual1) >= 2$ and $n\_bjets\_60\ (nQual5) >= 1$ is required.

For those events that didn't pass leptonic category, we look at the shape of aforementioned distributions in Figure 9.4 and followed a similar procedure. With more hadronic decays of W and more jets in the final state, we end up with a tighter cut: (n_jets(nQual1) >= 5 and n_bjets_85(nQual2) >= 2) or (n_jets(nQual1) >= 4 and n_bjets_60(nQual5) >= 1). Note that any event that passes both hadronic cut and has an extra lepton will already pass leptonic category cut, therefore we are effectively asking for no extra leptons in the hadronic category.

The significance is calculated with the formula (9.1) [145], where $n = s + b$, and σ is the uncertainty (standard deviation) on the background. A conservative 100% ggH uncertainty and 60% ttV uncertainty are applied for this calculation. The performance based on cut and count analysis is summarized in Table 9.1. The improvement are within the range of 4% to 5% . The significance with fitting framework is carried out for a setup with similar normalization uncertainty for background, and the significance is improved from 1.638 σ to 1.691 σ with the choice of the cuts, more or less consistent with the cut-and-count calculation.

$$Z = +\sqrt{2\left(n\,ln\left[\frac{n(b+\sigma^2)}{b^2+n\sigma^2}\right] - \frac{b^2}{\sigma^2}ln\left[1+\frac{\sigma^2(n-b)}{b(b+\sigma^2)}\right]\right)} \tag{9.1}$$

Table 9.1 Process yield, S/B and significance comparison before and after the ttH optimization. The signal is ttH processes here.

Yield	Leptonic		Hadronic	
	Nominal	Optimized	Nominal	Optimized
ttH	0.394	0.396	0.716	0.693
ggH	0.001	0.002	0.168	0.131
VBF	0.000	0.000	0.035	0.025
VH	0.007	0.006	0.075	0.058
ZZ	0.003	0.002	0.082	0.058
VVV	0.000	0.000	0.000	0.000
ttV Full Sim	0.021	0.017	0.254	0.232
Bkg	0.032	0.028	0.614	0.503
Significance	1.179	1.225	0.749	0.790
S/B	12.179	14.316	1.165	1.378

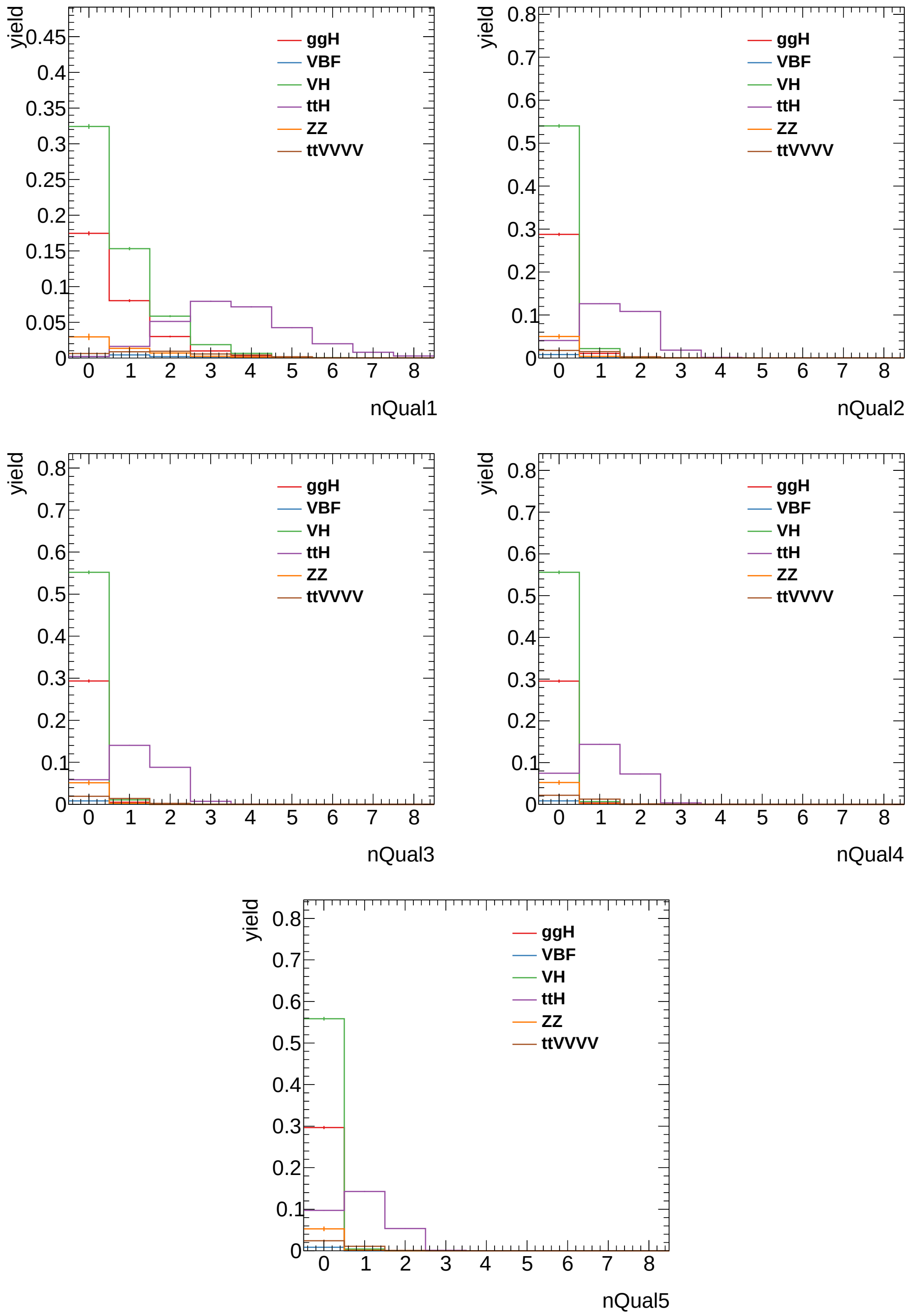

Fig. 9.3 **Yield distribution of number of jets passing certain MV2C10 b-tagging working points for events with at least one extra lepton. nQual1 is the number of jets without b-tagging requirement, equal to n_jets, nQual2 is the number of jets passing 85% WP, nQual3 is the number of jets passing 77% WP, nQual4 is the number of jets passing 70% WP, nQual5 is the number of jets passing 60% WP.**

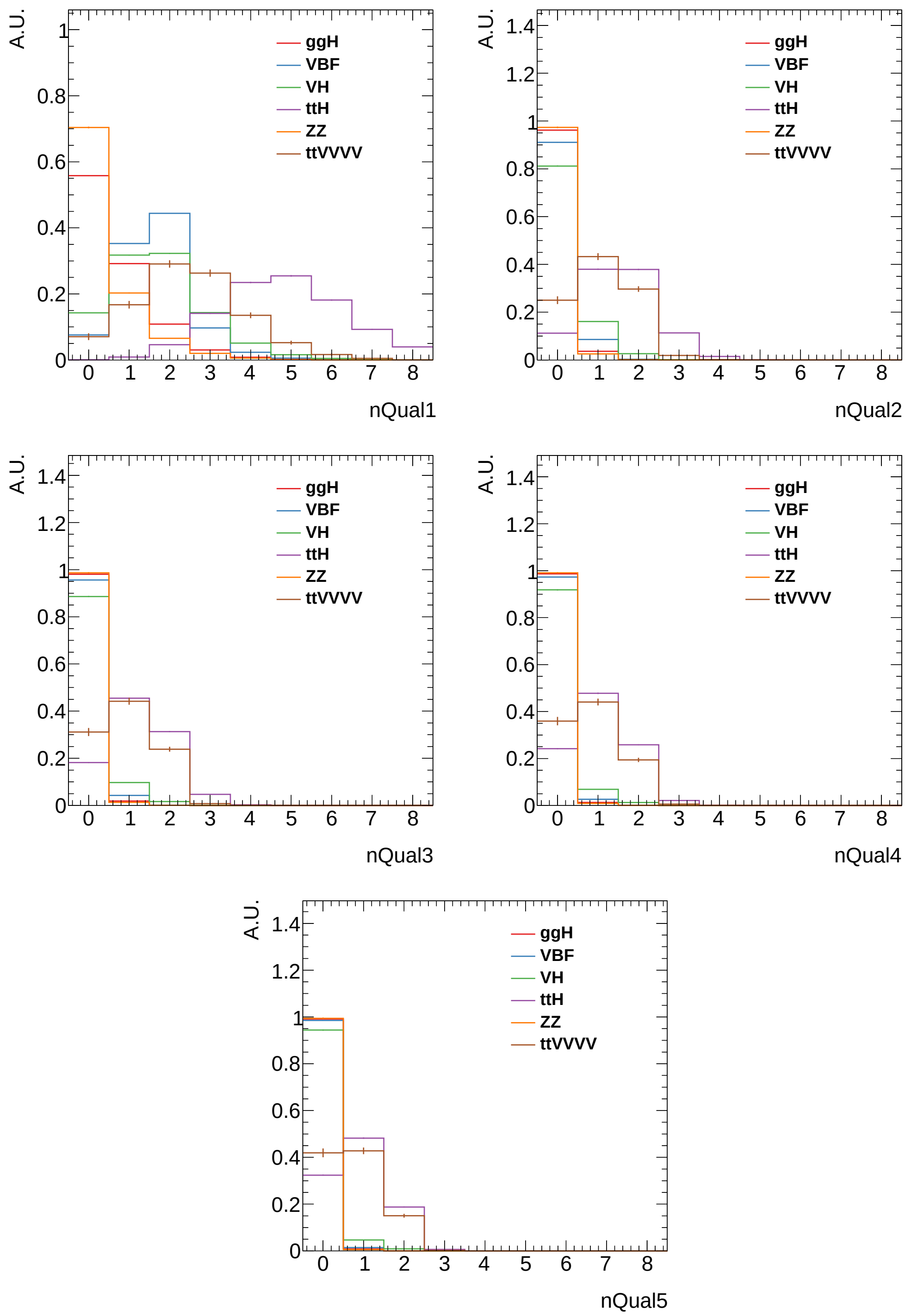

Fig. 9.4 Shape of distribution of number of jets passing certain MV2C10 b-tagging working points, for events that's not in the ttH leptonic category defined above. nQual1 is the number of jets without b-tagging requirement, equal to n_jets, nQual2 is the number of jets passing 85% WP, nQual3 is the number of jets passing 77% WP, nQual4 is the number of jets passing 70% WP, nQual5 is the number of jets passing 60% WP.

9.2 Multivariate Analysis

Once the events are categorized, the Higgs signal and background inside the categories can be further separated by some key variables. Multivariate analysis utilizes multiple variables and convert it to a single variable which is treated as observable in the final fitting in this analysis.

The nominal methodology for 139 fb^{-1} data analysis is Neural Network trained using Keras with TensorFlow [158-159], and it will be described in Section 9.2.1. In earlier analysis with 80 fb^{-1} data, Boosted Decision Tree (BDT) is used instead, trained with the Gradient Boost algorithm with TMVA [160] from ROOT [155]. Section 9.2.2 describes the BDT training in ttH hadronic category.

9.2.1 Neural Network

The Neural Network are trained in categories with enough statistics, that is, in all categories except $0j$-$p_{\mathrm{T}}^{4\ell}$-High, $1j$-$p_{\mathrm{T}}^{4\ell}$-BSM-like and ttH-Lep-enriched categories. Multilayer perceptron (MLP) [161] is trained over kinematic variables, and a maximum of two recurrent Neural Network (RNN) [161-162] takes lepton and jet p_{T} and η sequentially to account for variable number of the objects. A multi-class NN then takes the output of MLP and RNN to provide a approximation of probability of the event coming from a specific process. The probability sum up to one. For dual-class categories, one score is calculated and used as observable. For triple-class categories, two scores are calculated, and usually one score is used to define a smaller category, and then one of the score is selected as the observable in each of the sub-category. The details of discriminating observable trained in each category and the category observable used in the fitting are summarized in Table 9.2. Below is a summary of variables used in the multi-variate-analysis.

1. D_{ZZ^*} [163]: the logarithmic of ratio of Matrix Element (ME) of signal process over background process, where the ME is calculated with MG, the same one used in quadruplet pairing (see Section 7);
2. θ^*: the longitudinal angle of the leading Z boson θ^* in the four-lepton rest frame;
3. θ_1: the angle between the negatively charged lepton of the leading Z in the leading Z rest frame and the momentum of the leading Z in the four-lepton rest frame;
4. ϕ_{ZZ}: the angle between two Z decay planes in the four-lepton rest frame;
5. $\Delta R_{4\ell j}$: the angular separation between four-lepton and leading jet;
6. $p_{\mathrm{T}}^{4\ell jj}$: the transverse momentum of four-lepton plus two-jet system;
7. $\eta_{ZZ}^{\mathrm{Zepp}} = \left|\eta_{4\ell} - (\eta_{j1} + \eta_{j2})/2\right|$: the Zeppenfeld variable [164];

8. N_{jets}: jet multiplicity;
9. $N_{b-\text{jets}}$: number of b-jet passing 70% efficiency WP;
10. H_{T}: scalar sum of p_{T} of all jets.

Table 9.2 The input variables used to train the MLP, and the two RNNs for the four leptons and the jets (up to three). For each category, the processes which are classified by an NN, their corresponding input variables and the observable used are shown. Leptons and jets are denoted by "ℓ" and "j", respectively.

Category	Processes	MLP	Lepton RNN	Jet RNN	Discriminant
$0j$-$p_{\text{T}}^{4\ell}$-Low $0j$-$p_{\text{T}}^{4\ell}$-Med	ggF, ZZ^*	$p_{\text{T}}^{4\ell}$, D_{ZZ^*}, m_{12}, m_{34}, $\lvert\cos\theta^*\rvert$, $\cos\theta_1$, ϕ_{ZZ}	p_{T}^{ℓ}, η_ℓ	-	NN_{ggF}
$1j$-$p_{\text{T}}^{4\ell}$-Low	ggF, VBF, ZZ^*	$p_{\text{T}}^{4\ell}$, p_{T}^{j}, η_j, $\Delta R_{4\ell j}$, D_{ZZ^*}	p_{T}^{ℓ}, η_ℓ	-	NN_{VBF} for $\text{NN}_{ZZ} < 0.25$ NN_{ZZ} for $\text{NN}_{ZZ} > 0.25$
$1j$-$p_{\text{T}}^{4\ell}$-Med	ggF, VBF, ZZ^*	$p_{\text{T}}^{4\ell}$, p_{T}^{j}, η_j, $E_{\text{T}}^{\text{miss}}$, $\Delta R_{4\ell j}$, D_{ZZ^*}, $\eta_{4\ell}$	p_{T}^{ℓ}, η_ℓ	-	NN_{VBF} for $\text{NN}_{ZZ} < 0.25$ NN_{ZZ} for $\text{NN}_{ZZ} > 0.25$
$1j$-$p_{\text{T}}^{4\ell}$-High	ggF, VBF	$p_{\text{T}}^{4\ell}$, p_{T}^{j}, η_j, $E_{\text{T}}^{\text{miss}}$, $\Delta R_{4\ell j}$, $\eta_{4\ell}$	p_{T}^{ℓ}, η_ℓ	-	NN_{VBF}
$2j$	ggF, VBF, VH	m_{jj}, $p_{\text{T}}^{4\ell jj}$	p_{T}^{ℓ}, η_ℓ	p_{T}^{j}, η_j	NN_{VBF} for $\text{NN}_{VH} < 0.2$ NN_{VH} for $\text{NN}_{VH} > 0.2$
$2j$-BSM-like	ggF, VBF	η_{ZZ}^{Zepp}, $p_{\text{T}}^{4\ell jj}$	p_{T}^{ℓ}, η_ℓ	p_{T}^{j}, η_j	NN_{VBF}
VH-Lep-enriched	VH, $t\bar{t}H$	N_{jets}, $N_{b\text{-jets},70\%}$, $E_{\text{T}}^{\text{miss}}$, H_{T}	p_{T}^{ℓ}	-	NN_{ttH}
ttH-Had-enriched	ggF, $t\bar{t}H$, tXX	$p_{\text{T}}^{4\ell}$, m_{jj}, $\Delta R_{4\ell j}$, $N_{b\text{-jets},70\%}$,	p_{T}^{ℓ}, η_ℓ	p_{T}^{j}, η_j	NN_{ttH} for $\text{NN}_{tXX} < 0.4$ NN_{tXX} for $\text{NN}_{tXX} > 0.4$

9.2.2 BDT in ttH Hadronic Category

In the analysis with $80\,\text{fb}^{-1}$ data, multivariate analysis is first introduced in the ttH hadronic category to increase the separation between the ttH and the ggF, and the ttV. It also helps to separate the ttH from the VH and the VBF processes. The algorithm used is Gradient Boost Decision Tree (gBDT). The Decision-Trees is a technique where events are categorized iteratively by cutting on measured physics variables to achieve separation of the signal and background. The number of layers is the number of selection sequence applied to each event, which is usually called the depth. The end results of a tree is called leaves, which are subsets of original sample where categories tag are determined by usually majority of event types (signal or background) in them. A deep decision tree increases the separating power but is more prone to over-training by learning some statistical fluctuation in the limited training sample, instead of the underlying meaningful distribution. Boosting technique combines a number of shallow (weak) decision trees to form smoother boundaries for variables. In the end of the training process the discriminant is calculated from weighted sum of category tag in each of the weak decision tree.

To study the most sensitive variables, several jet related variables such as the m_{jj} combination between the four highest-p_T jets (one m_{jj} value for each possible pair), the b-tagging information of the jets for each of the m_{jj} combinations and the $\Delta R(ji, jk)$ between the reconstructed jets $i, k = 1, ..4$, have been investigated. Given the fact that for ggF only two jets are coming from the matrix element, it has been decided to use only a subset of 11 scrutinized variables to reduce bias from jets beyond the two leading ones. Moreover, the total number of variables to be used in the BDT has been trimmed by removing those showing a smaller distinguish power. The final configuration contains a subset of 11 variables which are robust and checked with respect to the modeling:

$\Delta\eta_{\mathrm{jj}}$, min($\Delta\mathrm{R}_{jZ}$), $\Delta R_{4\ell j}$, $\eta_{ZZ}^{\mathrm{Zepp}}$, $E_{\mathrm{T}}^{\mathrm{miss}}$, m_{jj} , $p_{T,jj}$, N_{jets}, $N_{b-\mathrm{jets}}$, H_{T}, log(HiggsME), where min($\Delta\mathrm{R}_{jZ}$) is the minimum ΔR between the one jet from two leading jets and one Z boson from the ZZ^*, and log(HiggsME) is the logarithm of MadGraph Matrix Element of Higgs process. Figure 9.5 shows the distributions of these input variables.

The signal sample size is 40765 events while the background sample size is only 4787 events due to the difficulty of an efficient generator filter that matches to ttH category with b-tagging requirement. Training and testing samples were randomly split in half. The configuration parameters used for the BDT training is optimized by maximizing the significance in an grid-scan manner. A total of 1300 decision-trees are trained with a maximum depth of 3. The BDT training parameter, 'shrinkage', is selected to be 0.03 to control the rate of the learning so that the loss function of Gradient Boosting can converge to a proper minimum. Half of the randomized events are used in each iteration of the training (each tree is an iteration). 9 variables randomly selected from all 11 variables for each iteration to help reduce the over-training.

Figure 9.6 shows a superimposition of the BDT response of the training and testing samples. The corresponding ROC curves are shown in Figure 9.7. Comparing the ROC curves the trend of over-training is in an acceptable extent.

Figure 9.8 shows BDT shape comparison for various process considered. On the left it can been seen that the ttH process (red) is well separated from other processes. On the right the shape difference for ggH process is presented when using two different generators: MadGraph5_aMC@NLO FxFx (blue) and Powheg NNLOPS (red).

Due to lack of MC statistics, only 2 bins in BDT discriminant have been used to evaluate the significance. A scan on the bin boundary to find the best significance have been

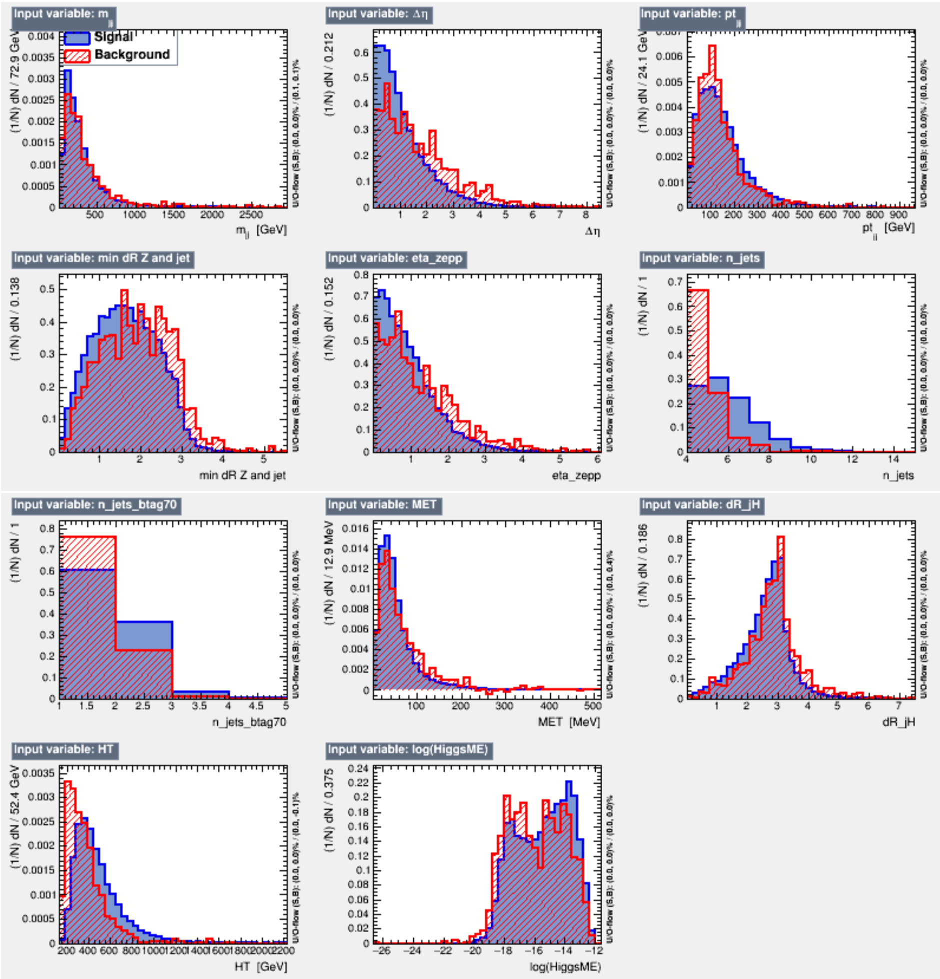

Fig. 9.5 Distributions of the discriminating variables used to train the BDT: $N_{b\text{-jets},70\%}$, $E_{\mathrm{T}}^{\mathrm{miss}}$, $\Delta R_{4\ell j}$, HT, log(HiggsME) for the signal (ttH) and the background (ggF, ttV, VBF and VH).

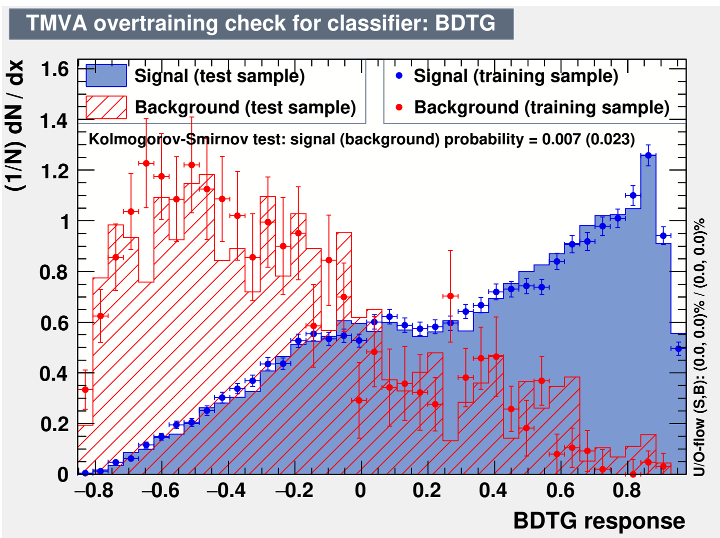

Fig. 9.6 Superimposed training and testing samples for the BDT in ttH-hadronic category to separpate ttH from ggF, ttV, VBF and VH.

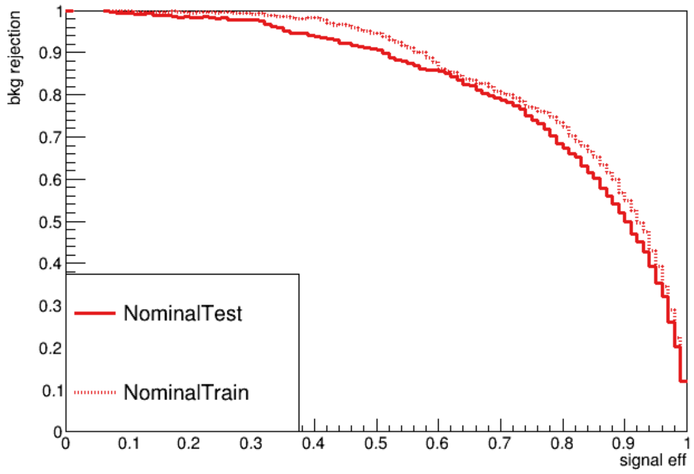

Fig. 9.7 ROC curve for training and testing samples. The dashed line is training ROC and solid line is testing ROC. They are pretty close meaning the shape is similar.

performed. The highest significance is found to be around a BDT score value between 0.45 to 0.65. Figure 9.9 shows the BDT discriminant distribution in the ttH-hadronic for signal and background processes and for two different binning configuration: (a) bin edge at BDT score value of 0.5 and (b) bin edge at BDT score value of 0.65. In both cases the expected significance of the ttH-hadronic category is about 0.8σ, which is improved by about 40% with respect to the simple counting method using in the previous publication. By using 2 bins, the shape difference observed for ggH process when comparing two generators (see Figure 9.8(b)), does not affect the sensitivity. The final BDT discriminant distribution used for the ttH-hadronic category is shown in Figure 9.9(a).

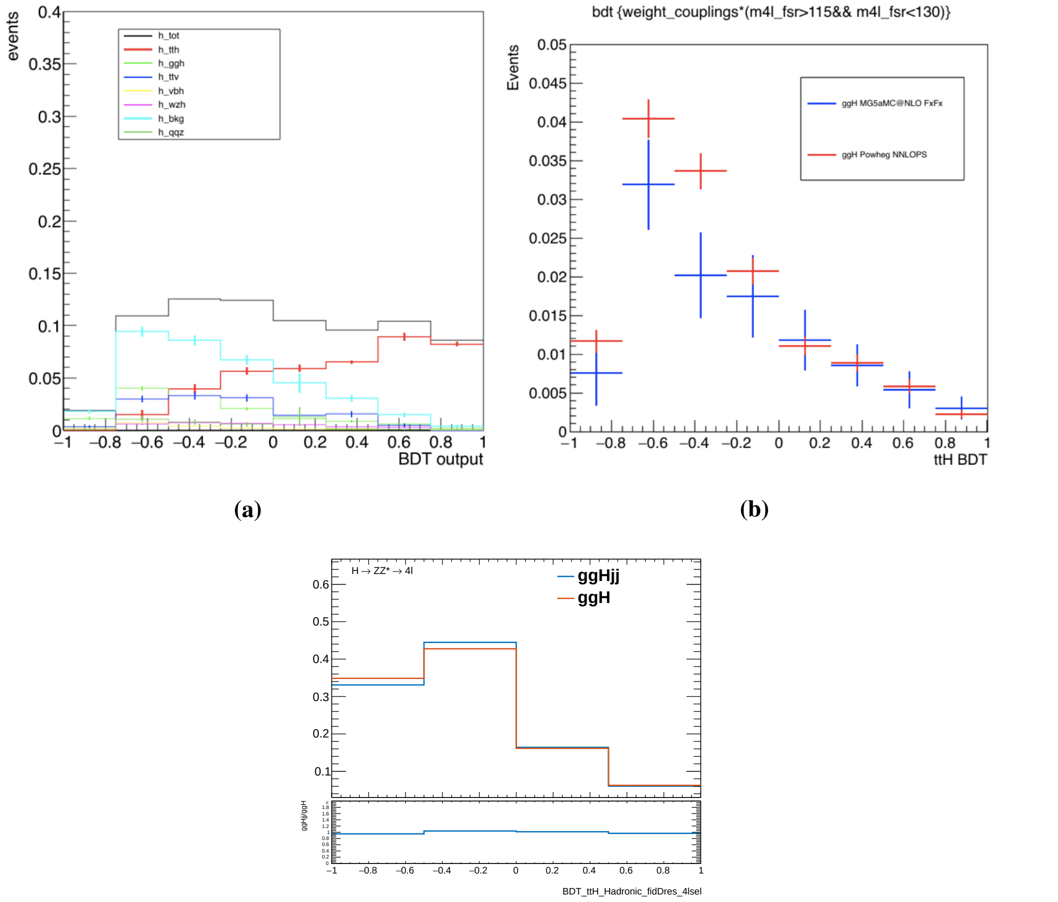

(a) (b)

(c)

Fig. 9.8 **(a) BDT shape comparison for various processes, (b) BDT shape comparison for ggH from FxFx and Powheg NNLOPS (c) BDT shape comparison for ggH from Powheg NNLOPS and MINLO H+jj.**

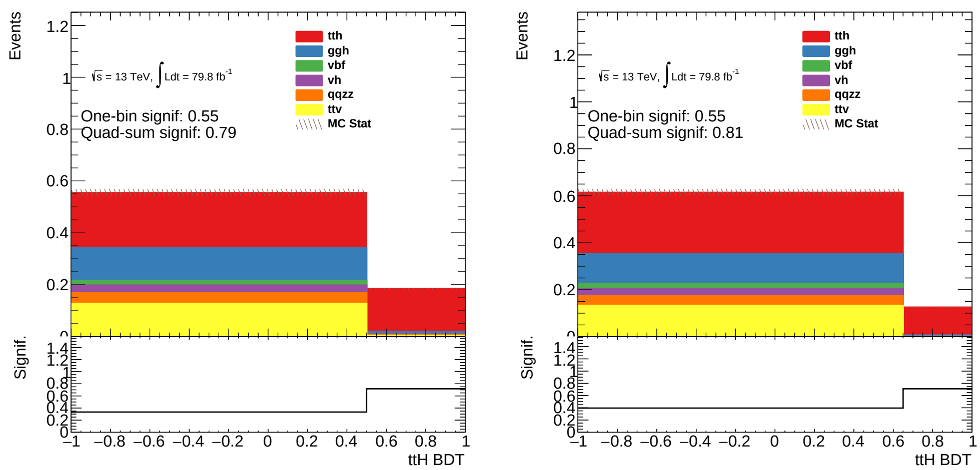

(a) (b)

Fig. 9.9 **Distribution of BDT shape with two different binning: (a) bin edge is at 0.5, (b) bin edge is at 0.65.**

9.3 Background Estimation

9.3.1 Using Data Side-Band Control Regions

As described in Section 6.3, the non-resonant SM ZZ^* including qqZZ, ggZZ and EWZZjj can produce four prompt leptons and pass signal region selection. The SM ZZ^* is the largest irreducible background in the overall 4ℓ analysis. The ttV in tXX process on the other hand, is the largest background in the ttH categories. Their contribution are estimated using data in the side-band which reduces the dependence on theoretical uncertainties and also luminosity uncertainties.

The normalization factors (NF) of ZZ^* background in the signal categories are largely determined in the side-band according to the jet multiplicity. The only exception is that the VH-leptonic side-band and other signal categories are grouped with the 0-jet category, sharing the same NF. The contribution of the ZZ in the ttH categories are estimated by MC simulations due to the lack of sensitivity. Conversely, the normalization factor of the tXX process is only correlated within the ttH categories and the ttV side-band, and the contribution in other categories are estimated by MC simulations. The normalization of background is derived by simultaneously fit together with the signal cross sections. Table Table 9.3 summarizes the correlation scheme of signal categories with the side-band categories.

Table 9.3 Summary of correlation scheme for jet multiplicity.

Category	Normalization Factor			
	0jet	1jet	2jet	tXX
0-jet $p_T^{4l} < 10$	X			
$10 <$ 0-jet $p_T^{4l} < 100$	X			
0-jet $p_T^{4l} > 100$ GeV	X			
1-jet $p_T^{4l} < 60$ GeV		X		
1-jet 60 GeV$< p_T^{4l} < 120$ GeV		X		
1-jet 120 GeV$< p_T^{4l} < 200$ GeV		X		
1-jet $p_T^{4l} > 200$ GeV		X		
2-jet			X	
2-jet VBF-enriched $p_T^{4l} > 200$ GeV			X	
VH-leptonic-enriched	X			
ttH-hadronic-enriched				X
ttH-leptonic-enriched				X

Figure 9.10 shows example plots of the distributions of data compared to the MC expectations in the side-band region after the fit. A good agreement is seen between observed and expected, demonstrating the ZZ^* background process is modeled reasonably well in the side-band and can be used to estimate the ZZ^* background in the signal region.

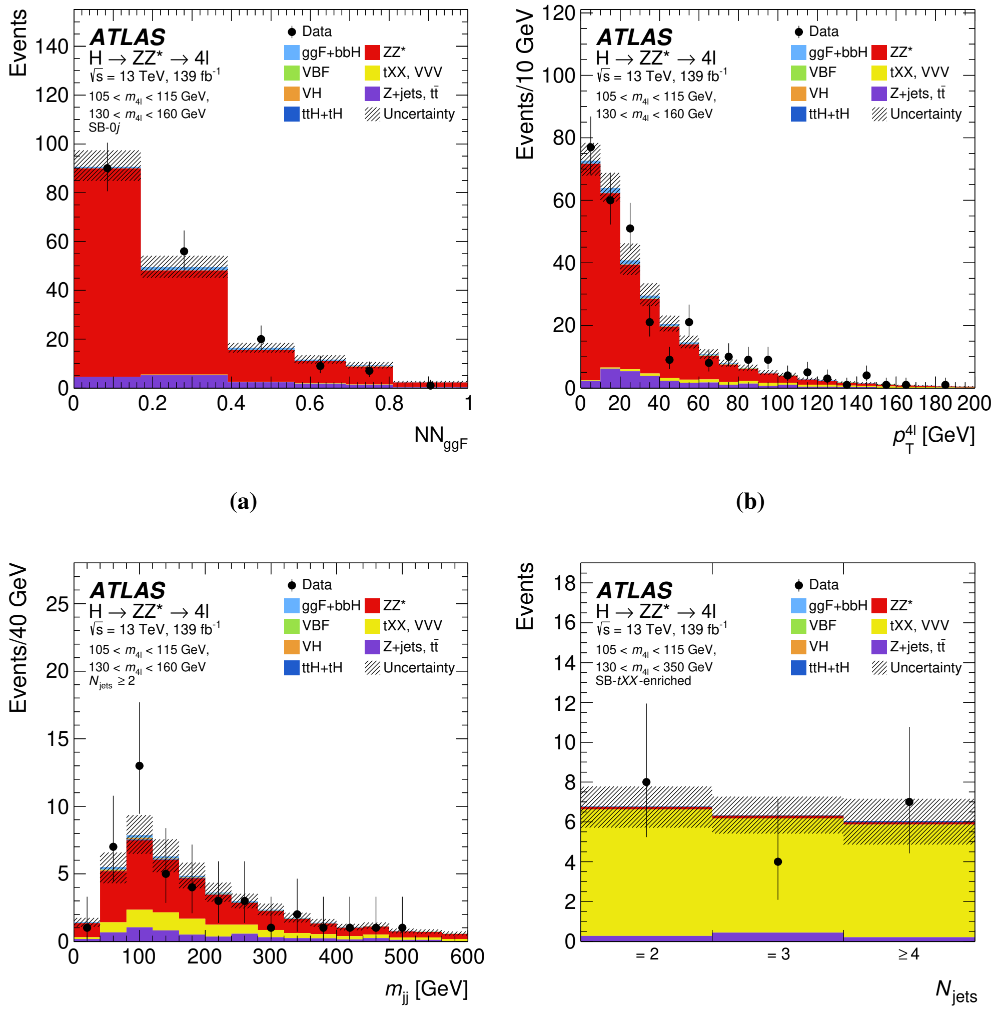

(a) (b) (c) (d)

Fig. 9.10 The observed and expected (post-fit) distributions in background enriched regions: (a) Neural network discriminant $\mathrm{NN}_{\mathrm{ggF}}$ in the SB-$0j$ sideband region, (b) $p_{\mathrm{T}}^{4\ell}$ in the sideband region combining the SB-$0j$, SB-$1j$ and SB-$2j$ categories, (c) m_{jj} in the SB-$2j$ category, and (d) N_{jets} in the SB-tXX-enriched region.

The following sections will discuss the optimization of side-band using Monte Carlo simulation sample targeted for 80 fb^{-1} data. The studies are discussed in chronological order and during the studies, samples were being updated. Therefore the results do not stand for the latest sensitivity but the conclusion should hold when scaled to the final methodologies. Also the systematic uncertainties are evaluated for the yields rather than the acceptances of the ZZ background. This leads to a small overestimation of the systematic uncertainties but it will not change the conclusion either.

9.3.1.1 Optimization of the ZZ Side-Band

This section reports the study on the sensitivity reduction of adding the normalization factors at the reconstruction-level. Three correlation schemes were studied for profiling of the ZZ contribution in the fit models listed below.

1. *Global Floating*: one normalization factor associated with ZZ in all categories;
2. *Category Floating*: each of the reconstruction-category has its own normalization factor. As such categories are not correlated.
3. *Jet Multiplicity*: each of the n-jets reconstruction-category has its own normalization factor, except for the ttH-like categories.

The assumption of the *Global Floating* scheme is that the ZZ contributing scales homogeneously in all the categories. By comparing the Sherpa vs Powheg MC samples, higher order effects can cause ZZ cross-section to scale differently in different jet multiplicity. Hence, if this case is to be used, the modelling uncertainty would need to be assigned to account for shape variation over different categories. For the *Category Floating* scheme, such correlation uncertainty is not needed. However with more free floating parameters, the model becomes less constrained and the error of signal POI increases. The *Jet Multiplicity* scheme is a middle-ground between *Category Floating* scheme and *Global Floating Scheme* to reduce theory systematics and prevent underconstrain.

In order to constrain the ZZ background, we studied two schemes of side-band regions for events satisfying $110 < m_{4\ell} < 115$ GeV and $130 < m_{4\ell} < 160$ GeV:

1. *The $m_{4\ell}$ side-band*: simply using invariant mass of four-lepton distribution the observable in the side-band;
2. *Category Side-band*: apply the categorization in signal region in the side-band as well, and use the yields as observable.

The use of the side-bands has an advantage that it will also constrain the ZZ background systematic uncertainty better, indirectly improving the sensitivity of the signal POIs.

The Monte Carlo simulation is used to estimate the expected errors and the performance of preliminary side-band optimization are summarized in Table 9.4. As a first test, the sensitivity can already be retained as similar to the nominal case without floating normalization factors.

By comparing the second and third columns of the errors, it can be clearly seen that the *Category Side-band* out-performs the m_{4l} *Side-band*, therefore it is chosen as the baseline of the side-band for later comparisons. In some cases, the sensitivity even get improved compared to the nominal. This is because some Higgs events are reconstructed outside the Higgs mass window of $115 < m_{4l} < 130$ GeV.

From the comparison between the third and the last columns, for some of the POIs the sensitivity is similar, which means the corresponding reconstruction-categories in the side-band have significant statistics to constrain the ZZ^*. For some other POI, the corresponding side-band categories does not have enough constraining power. The ttH sensitivity is largely unchanged since ZZ^* is not the major background, they are improved in *Category Side-band* because ttH events are more likely to migrate outside of the Higgs mass window. The *Global Floating* scheme performs the best but it underestimates the uncertainty, therefore we can not yet use this scheme.

Table 9.4 Summary of performance of m_{4l} *Side-band* and *Category Side-band* under the *Global Floating* and the *Category Floating* correlation schemes, compared to nominal model without normalization factor and side-bands. The 1-sigma errors of Stage 0 and Reduced Stage 1 signal strength are shown, except for ttH, the 95% CL interval upper boundary is shown.

POI	Nominal	*Global Floating* m_{4l} *Side-band*	*Global Floating* *Category Side-band*	*Category Floating* *Category Side-band*
μ_{ggF}	+0.135, -0.125	+0.131, -0.121	+0.132, -0.122	+0.133, -0.122
μ_{VBF}	+0.552, -0.451	+0.553, -0.451	+0.552, -0.451	+0.556, -0.454
μ_{VH}	+0.975, -0.713	+0.975, -0.714	+0.961, -0.707	+1.00, -0.755
μ_{ttH}	<4.28	<4.28	<4.18	<4.25
$\mu_{\text{ggF-0J}}$	+0.181, -0.166	+0.179, -0.163	+0.178, -0.161	+ 0.179, -0.163
$\mu_{\text{ggF-1J-}p_T^H\text{-Low}}$	+0.515, -0.464	+0.514, -0.463	+0.506, -0.449	+ 0.520, -0.461
$\mu_{\text{ggF-1J-}p_T^H\text{-Med}}$	+0.423, -0.344	+0.423, -0.343	+0.422, -0.343	+ 0.434, -0.357
$\mu_{\text{ggF-1J-}p_T^H\text{-High}}$	+0.872, -0.645	+0.872, -0.645	+0.870, -0.644	+ 0.891, -0.664
$\mu_{\text{ggF-2J}}$	+0.694, -0.572	+0.690, -0.570	+0.682, -0.558	+ 0.693, -0.572
$\mu_{\text{VBF-}p_T^H\text{-Low}}$	+0.634, -0.506	+0.634, -0.506	+0.634, -0.505	+ 0.635, -0.506
$\mu_{\text{VBF-}p_T^H\text{-High}}$	+3.34, -2.36	+3.34, -2.36	+3.33, -2.35	+3.48, -2.58
$\mu_{\text{VH-Lep}}$	+1.39, -0.81	+1.39, -0.81	+1.35, -0.80	+ 1.45, -0.91
$\mu_{\text{VH-Had}}$	+1.84, -1.64	+1.84, -1.64	+1.84, -1.64	+ 1.84, -1.65
μ_{ttH}	<4.31	<4.31	<4.21	<4.28

The comparison of three floating schemes(Global ZZ, Categorical ZZ, Jet Multiplicity ZZ) under category side-band can be seen in Table 9.5. Here the *Global Floating* has an additional floating ttV that's correlated the same way as *Jet Multiplicity* scheme.

And in *Category Floating*, ZZ is not floating in the two ttH categories but a ttV NF is floating only in the ttH categories. It can be seen that *Category Floating* is too aggressive and caused as much as 5% decrease in sensitivity. The *Global Floating* is an improper description of the ZZ^* processes and the systematics is expected to worsen the sensitivity. Therefore the *Jet Multiplicity* scheme is reasonable to be used.

Table 9.5 Summary of performance of *Category Side-band* under the three correlation schemes. The 1-sigma errors of Stage 0 and Reduced Stage 1 signal strength are shown.

POI	*Global Floating*	*Jet Multiplicity*	*Category Floating*
μ_{ggF}	+0.132, -0.122	+0.132, -0.122	+0.133, -0.122
μ_{VBF}	+0.552, -0.451	+0.553, -0.451	+0.556, -0.454
μ_{VH}	+0.964, -0.709	+0.963, -0.709	+1.00, -0.754
μ_{ttH}	+1.32, -0.73	+1.33, -0.74	+1.33, -0.74
$\mu_{\text{ggF-0J}}$	+0.178, -0.161	+0.179, -0.163	+0.179, -0.163
$\mu_{\text{ggF-1J-}p_T^H\text{-Low}}$	+0.508, -0.451	+0.522, -0.466	+0.525, -0.468
$\mu_{\text{ggF-1J-}p_T^H\text{-Med}}$	+0.422, -0.343	+0.428, -0.354	+0.435, -0.362
$\mu_{\text{ggF-1J-}p_T^H\text{-High}}$	+0.870, -0.644	+0.874, -0.648	+0.892, -0.670
$\mu_{\text{ggF-2J}}$	+0.682, -0.558	+0.694, -0.575	+0.696, -0.577
$\mu_{\text{VBF-}p_T^H\text{-Low}}$	+0.634, -0.505	+0.637, -0.518	+0.638, -0.519
$\mu_{\text{VBF-}p_T^H\text{-High}}$	+3.33, -2.35	+3.35, -2.44	+3.48, -2.64
$\mu_{\text{VH-Lep}}$	+1.35, -0.80	+1.36, -0.87	+1.46, -0.94
$\mu_{\text{VH-Had}}$	+1.84, -1.64	+1.85, -1.47	+1.86, -1.48
μ_{ttH}	+1.32, -0.73	+1.34, -0.74	+1.34, -0.74

9.3.1.2 Optimization of the tXX Side-Band

Since the tXX process is dominated by the ttV process, therefore in this study only ttV is considered.

We start by applying different b-jet quality and number of jets requirement, in the $m_{4\ell}$ window between 110 and 115 GeV or 130 and 550 GeV. The performance is summarized in the Table 9.6. The symbol of 'KinJet' listed in the table denotes jets passing $p_T > 20$ GeV and $\eta < 2.5$ cuts, which is the kinematic region where b-tagging is available. The significance is calculated with the formula:

$$Z = \sqrt{2(S+B)\ln(1+\frac{S}{B}) - 2S}. \tag{9.2}$$

Because the goal is to extract the ttV contribution in the control region, here the S

stands for the ttV yield and B stands for all other processes, which consists mostly of ZZ^* , $t\bar{t}$, and other Higgs processes.

Requiring one b-jet (with 60% efficiency) can remove a large amount of backgrounds already, while still retaining relatively high signal events. Requiring two b-tagged jets will cut away further half of the events and it is too tight for us to consider, although it achieves a higher significance. Requiring two jets in total will further reduce the background by 40%, while dropping 10% signal, so it is worth being evaluated. Requiring two KinJets has slightly higher significance, for its two-jet correspondence. But it's not very reasonable to require jets to come from only the region where b-tagging is available. For the simplicity, we will consider oneB60 and TwoJets cases.

Table 9.6 Performance of ttV CR under different jet-related cuts, estimated using MC simulation.

Cuts	ttV	background	ttV significance
Inclusive	53.5	3630.0	0.89
OneB85	44.6	157.7	3.40
OneB77	41.7	91.9	4.07
OneB70	39.1	70.1	4.31
OneB60	35.0	48.6	4.54
TwoB85	19.0	9.8	4.89
TwoB77	14.8	4.9	5.01
TwoJets	43.6	533.5	1.86
OneB85,TwoJets	38.8	92.2	3.79
OneB77,TwoJets	36.3	53.7	4.52
OneB70,TwoJets	34.2	41.0	4.78
OneB60,TwoJets	30.8	28.3	5.04
TwoKinJets	40.5	391.0	2.01
OneB85,TwoKinJets	36.7	80.6	3.83
OneB77,TwoKinJets	34.5	46.9	4.56
OneB70,TwoKinJets	32.6	35.8	4.83
OneB60,TwoKinJets	29.4	24.7	5.10

In the Figure 9.11, we can see that the most sensitive variable is $E_{\mathrm{T}}^{\mathrm{miss}}$. In Figure 9.12, we can also see that ZZ_1jet contribution is largely removed by requiring two jets. The combination of MET requirements and NJet requirement are then explored and summarized in Table 9.7.

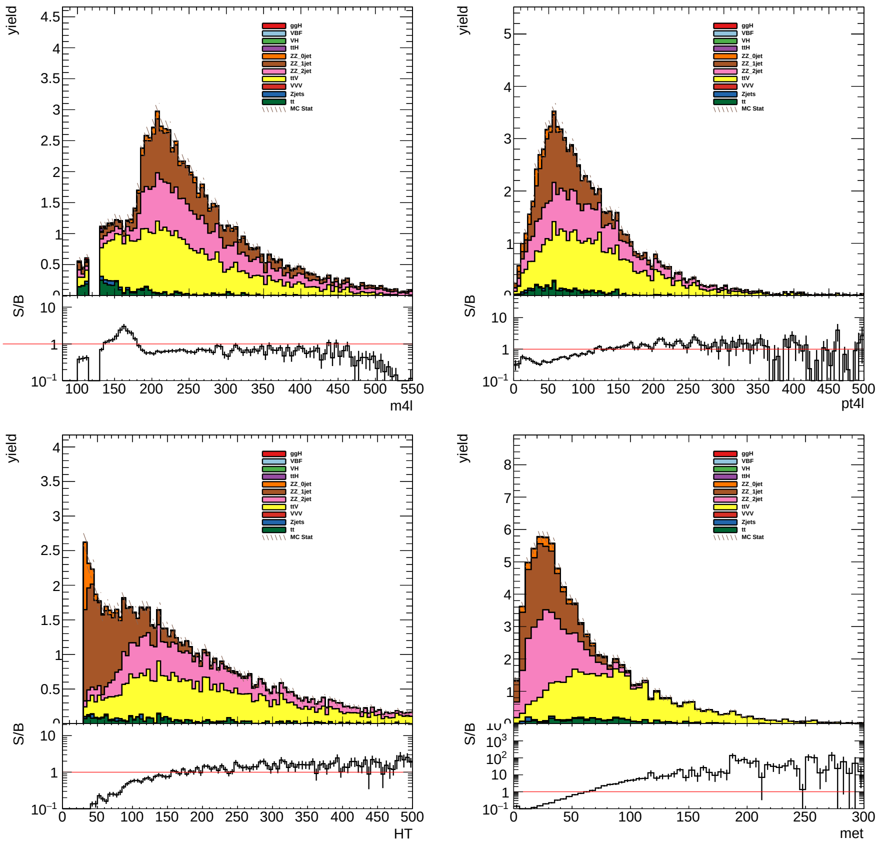

Fig. 9.11 Distribution of variable for studying sensitivity increase of ttV over other background, after requiring m4l in 100-115, 130-550 and OneB60 requirement. In the bottom panel the S/B ratio is plotted.

Table 9.7 Performance of ttV CR under the combination jet-related cuts and MET cuts, estimated using MC significance calculation

Cuts	ttV	background	ttV significance
OneB60	35.0	48.6	4.54
OneB60,MET50	27.2	11.0	6.39
OneB60,MET100	13.2	1.4	6.49
OneB60,TwoJets	30.8	28.3	5.04
OneB60,TwoJets,MET50	24.0	7.5	6.53
OneB60,TwoJets,MET100	11.8	1.1	6.39

Furthermore, the full estimation of several different ttV region and observable definitions are summarized in Table 9.8 for r_ttV and Table 9.9 for r_ZZ_2jet, using full fitting procedure, for reduced stage 1 model. The baseline is $m_{4\ell}$ between 110 and 115 GeV, and 130 to 550 GeV, with one b-jet (selected with 60% WP). The variable names MET50 and ME100 denote the cut values on $E_{\mathrm{T}}^{\mathrm{miss}} > 50$ GeV or 100 GeV, correspondingly. The symbol "METObs50" listed in the table is defined as "don't cut specifically

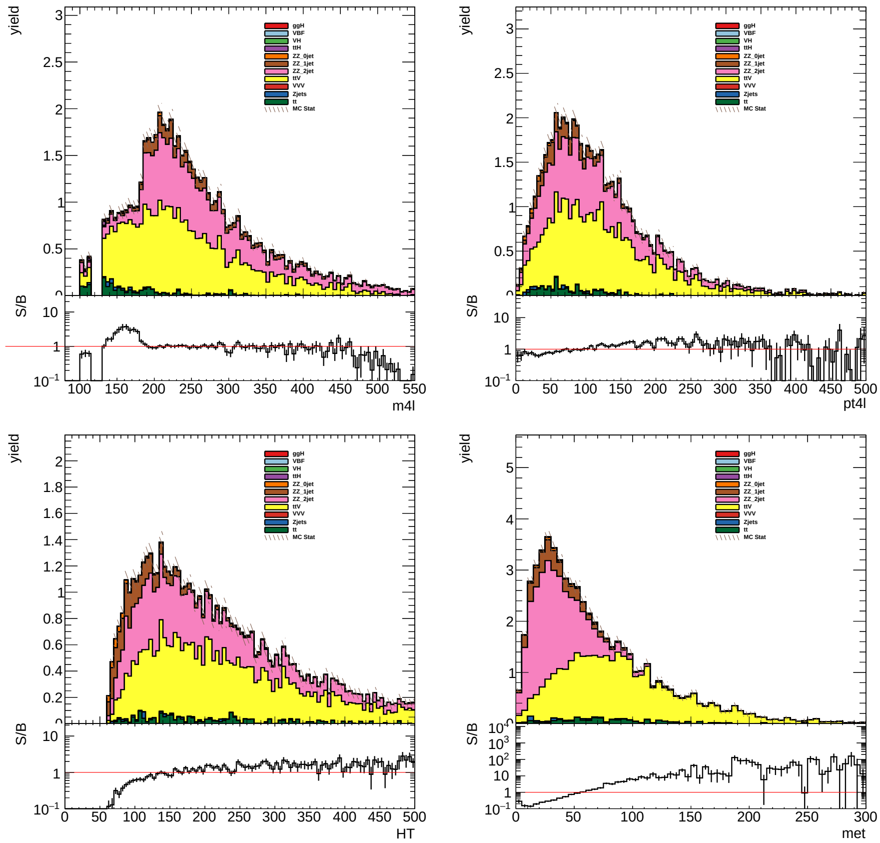

Fig. 9.12 Distribution of variable for studying sensitivity increase of ttV over other background, after requiring m4l in 100-115, 130-550 and OneB60,TwoJets requirement. In the bottom panel the S/B ratio is plotted.

on $E_{\mathrm{T}}^{\mathrm{miss}}$, but use the binning of [0, 50, 9999] as observable". The same rule applies for METObs100. To evaluate the impact of $E_{\mathrm{T}}^{\mathrm{miss}}$ systematics, the comparison are done both with statistic-only fitting and including the MET-related systematics.

The goal is to reduce the dependence of modeling of the $m_{4\ell}$ above two times the top mass and the correlation between r_ZZ_2jet and r_ttV and between r_ZZ_2jet and r_ZZ_1jet. First of all, it can be seen that $E_{\mathrm{T}}^{\mathrm{miss}}$ systematics has very little effect on the sensitivity of ttV normalization in any cases. The impact of the choices of ttV CR on other normalization factors and POIs are relatively similar, therefore we should focus on increasing the purity of the control region. Also, using $E_{\mathrm{T}}^{\mathrm{miss}}$ as observable leads to a large correlation between NFs, so it is not favored. The two jet requirement reduces ttV significance a bit but is applied nonetheless to reduce potential background which are note modeled well by Monte Carlo. In conclusion, $m_{4\ell}$ between 110 and 115 GeV, and 130 to 350 GeV, 60% b-jet, two total jets, and $E_{\mathrm{T}}^{\mathrm{miss}} > 100$ GeV is selected as the CR definition.

Table 9.8 Uncertainty of ttV normalization factor under different ttV region definition, for reduced stage 1 model, estimated using full fitting procedure. The Reco Scheme is the NJet scheme described in the previous section, and the Fiducial Scheme correlate ZZ according to its truth jet multiplicity and a global ttV normalization over all reco-categories.

Scheme	Stat-Only +1σ Err	Stat-Only -1σ Err	With MET syst +1σ Err	With MET syst -1σ Err
Reco Scheme	1.37	-0.80	X	X
Fid - Old SB	1.40	-0.84	X	X
Fid - MET50	0.23	-0.20	0.23	-0.20
Fid - MET100	0.31	-0.25	0.31	-0.25
Fid - METObs50	0.23	-0.20	0.23	-0.20
Fid - METObs100	0.25	-0.22	0.25	-0.22
Fid - 2Jets M4l<350 MET50	0.26	-0.23	0.26	-0.23
Fid - 2Jets M4l<350 MET100	0.35	-0.29	0.35	-0.29
Fid - 2Jets M4l<350 METObs50	0.26	-0.22	0.26	-0.22
Fid - 2Jets M4l<350 METObs100	0.29	-0.25	0.29	-0.25

Table 9.9 Uncertainty and correlation of ZZ_2jet normalization factor under different ttV region definition, for reduced stage 1 model, estimated using full fitting procedure. The Reco Scheme is the NJet scheme described in the previous section, and the Fiducial Scheme correlate ZZ according to its truth jet multiplicity and a global ttV normalization over all reco-categories.

Scheme	Stat-Only $+1\sigma$ Err	Stat-Only -1σ Err	With MET syst $+1\sigma$ Err	With MET syst -1σ Err	Correlation with ttV	Correlation with ZZ_1jet
Reco Scheme	0.27	-0.23	X	X	X	X
Fid - Old SB	0.50	-0.54	X	X	X	X
Fid - MET50	0.40	-0.35	0.40	-0.35	-0.26	-0.36
Fid - MET100	0.41	-0.36	0.41	-0.36	-0.18	-0.37
Fid - METObs50	0.35	-0.32	0.36	-0.32	-0.29	-0.52
Fid - METObs100	0.36	-0.33	0.37	-0.33	-0.34	-0.47
Fid - 2Jets M4l<350 MET50	0.40	-0.35	0.40	-0.35	-0.3	-0.36
Fid - 2Jets M4l<350 MET100	0.41	-0.36	0.41	-0.36	-0.2	-0.36
Fid - 2Jets M4l<350 METObs50	0.31	-0.28	0.31	-0.28	-0.39	-0.35
Fid - 2Jets M4l<350 METObs100	0.34	-0.31	0.34	-0.31	-0.50	-0.35

9.3.1.3 Optimization in Finalizing the Side-Bands

The category side-bands increase the complexity of the analysis and therefore they need to be merged in an optimization approach. Also the decision need to be made whether POI can be left floating as a truth variable considering the migration or only in the reconstruction bin as a yield. The following two cases are explored related to the overall detection sensitivity:

1. how sensitivity changes when merging the side-bands categories according to its jet multiplicity. Since jet multiplicity migration is dominating, merging the categories in terms of other variables should not have a large impact;
2. sensitivity changes under floating in the reconstructed jet multiplicity or floating in the truth jet multiplicity. In the truth floating, the ZZ floats under 0jet, 1jet, and >= 2jet bins, while the ttV floats over all categories.

The two scenarios were tested in the side-band simplification with reduced Stage-1 model: merging VH-Lep with zero jet category or splitting them. The result is summarized in Table 9.10 to 9.12. The rows with 'Simple merge' and 'Simple Split' represent the case how the side-bands are simplified. Merging VH-Lep with 0-jet has minimal impact on the ggH and the VBF POI, but it increases about 5% the error for the VH-Lep POI and 2% on the ttH POI. This is because some VH and ttH events fall into this side-band category due to Higgs mass resolution. Therefore splitting VH-Lep from 0-jet side-band will be beneficial and chosen. The impact of using reconstruction-level or fiducial-level floating can be compared as shown in the last two rows. Floating on the reconstruction-level has minimal impact on the POIs and it mainly affects the background normalization factors due to migration.

Table 9.10 Comparing ggH Reduced Stage 1 POI sensitivity due with simplification of side-band and reco/fid floating scheme

Schemes	$\mu_{\text{ggF-0J}}$	$\mu_{\text{ggF-1J Low}}$	$\mu_{\text{ggF-1J Med}}$	$\mu_{\text{ggF-1J High}}$	$\mu_{\text{ggF-2J}}$
Reco Scheme - Old SB	$1.00^{+0.15}_{-0.14}$	$1.00^{+0.45}_{-0.42}$	$1.00^{+0.38}_{-0.34}$	$1.00^{+0.80}_{-0.65}$	$1.00^{+0.57}_{-0.54}$
Fid - Old SB	$1.00^{+0.15}_{-0.14}$	$1.00^{+0.45}_{-0.41}$	$1.00^{+0.38}_{-0.34}$	$1.00^{+0.80}_{-0.65}$	$1.00^{+0.57}_{-0.54}$
Reco - Simple Merge VHLep	$1.00^{+0.15}_{-0.14}$	$1.00^{+0.46}_{-0.42}$	$1.00^{+0.38}_{-0.34}$	$1.00^{+0.81}_{-0.65}$	$1.00^{+0.57}_{-0.54}$
Fid - Simple Merge VHLep	$1.00^{+0.15}_{-0.14}$	$1.00^{+0.45}_{-0.42}$	$1.00^{+0.38}_{-0.34}$	$1.00^{+0.81}_{-0.65}$	$1.00^{+0.57}_{-0.54}$
Reco - Simple Split VHLep	$1.00^{+0.15}_{-0.14}$	$1.00^{+0.46}_{-0.42}$	$1.00^{+0.38}_{-0.34}$	$1.00^{+0.81}_{-0.66}$	$1.00^{+0.57}_{-0.54}$
Fid - Simple Split VHLep	$1.00^{+0.15}_{-0.14}$	$1.00^{+0.45}_{-0.42}$	$1.00^{+0.38}_{-0.34}$	$1.00^{+0.81}_{-0.66}$	$1.00^{+0.57}_{-0.54}$

Table 9.11 Comparing other Reduced Stage 1 POI sensitivity due with simplification of side-band and reco/fid floating scheme

Schemes	$\mu_{\text{VBF-2J Low}}$	$\mu_{\text{VBF-2J High}}$	$\mu_{\text{VH Had}}$	$\mu_{\text{VH Lep}}$	μ_{ttH}
Reco Scheme - Old SB	$1.00^{+0.64}_{-0.52}$	$1.00^{+3.27}_{-2.36}$	$1.00^{+1.87}_{-1.49}$	$1.00^{+1.40}_{-0.89}$	$1.00^{+1.35}_{-0.79}$
Fid - Old SB	$1.00^{+0.64}_{-0.52}$	$1.00^{+3.27}_{-2.36}$	$1.00^{+1.87}_{-1.50}$	$1.00^{+1.40}_{-0.89}$	$1.00^{+1.35}_{-0.79}$
Reco - Simple Merge VHLep	$1.00^{+0.64}_{-0.52}$	$1.00^{+3.27}_{-2.36}$	$1.00^{+1.87}_{-1.50}$	$1.00^{+1.44}_{-0.90}$	$1.00^{+1.35}_{-0.77}$
Fid - Simple Merge VHLep	$1.00^{+0.64}_{-0.52}$	$1.00^{+3.27}_{-2.36}$	$1.00^{+1.87}_{-1.50}$	$1.00^{+1.44}_{-0.90}$	$1.00^{+1.35}_{-0.77}$
Reco - Simple Split VHLep	$1.00^{+0.64}_{-0.52}$	$1.00^{+3.27}_{-2.35}$	$1.00^{+1.87}_{-1.49}$	$1.00^{+1.40}_{-0.89}$	$1.00^{+1.33}_{-0.76}$
Fid - Simple Split VHLep	$1.00^{+0.64}_{-0.52}$	$1.00^{+3.27}_{-2.35}$	$1.00^{+1.87}_{-1.49}$	$1.00^{+1.40}_{-0.89}$	$1.00^{+1.33}_{-0.76}$

Table 9.12 Comparing Reduced Stage 1 background normalization factor sensitivity due with simplification of side-band and reco/fid floating scheme

Schemes	r_{ttV}	$r_{\text{ZZ-0J}}$	$r_{\text{ZZ-1J}}$	$r_{\text{ZZ-2J}}$
Reco Scheme - Old SB	$1.00^{+1.37}_{-0.80}$	$1.00^{+0.08}_{-0.08}$	$1.00^{+0.17}_{-0.15}$	$1.00^{+0.27}_{-0.23}$
Fid - Old SB	$1.00^{+1.40}_{-0.84}$	$1.00^{+0.09}_{-0.09}$	$1.00^{+0.29}_{-0.26}$	$1.00^{+0.50}_{-0.54}$
Reco - Simple Merge VHLep	$1.00^{+0.35}_{-0.29}$	$1.00^{+0.08}_{-0.08}$	$1.00^{+0.16}_{-0.15}$	$1.00^{+0.26}_{-0.22}$
Fid - Simple Merge VHLep	$1.00^{+0.35}_{-0.29}$	$1.00^{+0.09}_{-0.09}$	$1.00^{+0.30}_{-0.27}$	$1.00^{+0.41}_{-0.36}$
Reco - Simple Split VHLep	$1.00^{+0.35}_{-0.29}$	$1.00^{+0.08}_{-0.08}$	$1.00^{+0.17}_{-0.15}$	$1.00^{+0.26}_{-0.22}$
Fid - Simple Split VHLep	$1.00^{+0.36}_{-0.29}$	$1.00^{+0.09}_{-0.09}$	$1.00^{+0.30}_{-0.27}$	$1.00^{+0.41}_{-0.37}$

9.4 Systematic Uncertainties

This section summarizes the sources of the systematics and their impact. The systematic uncertainties are categorized into experimental sources and theoretical sources. For each variation with different source, the normalization for categories and the shapes of the NN observables inside the categories are evaluated and tuned separately. The impact of major systematic uncertainties are summarized in Table 9.13.

9.4.1 Experimental uncertainties

The luminosity measurement uncertainty for full Run 2 data is 1.7%, and is assigned to signal model and background processes that are predicted by Monte Carlo. The pile-up reweighting accounts for the difference between pile-up distribution between MC and data. The uncertainties is evaluated by varying the ratio of reweighting, and is evaluated to be at 1-2% level. Due to the use of complex trigger scheme and overall high efficiency with combined triggers, the uncertainty from trigger is basically negligible.

Lepton efficiency uncertainties are considered through varying the scale factor of reconstruction, identification, isolation and trigger effects. The kinematic-changing sys-

Table 9.13 The impact of the dominant systematic uncertainties (in percent) on the cross sections in Stage 0 and the Reduced Stage 1.1. Systematic uncertainties with a similar source are grouped together.

Measurement	Experimental uncertainties [%]				Theory uncertainties [%]				
	Lumi.	e, μ, pile-up	Jets, flav. tag	Reducible bkg	Background ZZ^*	Background tXX	Signal PDF	Signal QCD	Signal Shower
Inclusive cross section									
	1.7	2.5	0.5	< 0.5	1	< 0.5	< 0.5	1	2
Production mode cross sections									
ggF	1.7	2.5	1	< 0.5	1.5	< 0.5	0.5	1	2
VBF	1.7	2	4	< 0.5	1.5	< 0.5	1	5	7
VH	1.9	2	4	1	6	< 0.5	2	13.5	7.5
ttH	1.7	2	6	< 0.5	1	0.5	0.5	12.5	4
Reduced Stage-1.1 production bin cross sections									
gg2H-0j-p_{T}^{H}-Low	1.7	3	1.5	0.5	6.5	< 0.5	< 0.5	1	1.5
gg2H-0j-p_{T}^{H}-High	1.7	3	5	< 0.5	3	< 0.5	< 0.5	0.5	5.5
gg2H-1j-p_{T}^{H}-Low	1.7	2.5	12	0.5	7	< 0.5	< 0.5	1	6
gg2H-1j-p_{T}^{H}-Med	1.7	3	7.5	< 0.5	1	< 0.5	< 0.5	1.5	5.5
gg2H-1j-p_{T}^{H}-High	1.7	3	11	0.5	2	< 0.5	< 0.5	2	7.5
gg2H-2j	1.7	2.5	16.5	1	12.5	0.5	< 0.5	2.5	10.5
gg2H-p_{T}^{H}-High	1.7	1.5	3	0.5	3.5	< 0.5	< 0.5	2	3.5
qq2Hqq-VH	1.8	4	17	1	4	1	0.5	5.5	8
qq2Hqq-VBF	1.7	2	3.5	< 0.5	5	< 0.5	< 0.5	6	10.5
qq2Hqq-BSM	1.7	2	4	< 0.5	2.5	< 0.5	< 0.5	3	8
VH-Lep	1.8	2.5	2	1	2	0.5	< 0.5	1.5	3
ttH	1.7	2.5	5	0.5	1	0.5	< 0.5	11	3

tematics including energy resolution and scale uncertainties are also evaluated. These uncertainties are typically around 1-2% for electrons and below 1% for muons.

The jet related uncertainties includes jet energy scale and jet resolution, which mostly affect VBF, VH and ttH with more jet activity, and also the Reduced Stage 1.1 cross sections which are categorized according to jet multiplicity. The impacts ranges from a few percent to about 17%.

The b-tagging affects ttH-related categories and side-bands. The contribution is less than 1% on ttH cross section. The $E_{\mathrm{T}}^{\mathrm{miss}}$ uncertainties only affect tXX control region therefore the impact is negligible.

The uncertainty coming from all data-driven background estimation are counted as experimental uncertainty as well. The source include the data statistics of the control region, the uncertainty of the extrapolation factors, inclusively and also independently in each categories.

9.4.2 Theoretical uncertainties

The theoretical uncertainties include PDF variation, QCD renormalization and factorization scale, parton showering modeling, generator comparison uncertainty and so on. The signal theoretical uncertainties are applied differently depending on the type of measurement. Because signal strength are multiplied on the yield dependent on the cross section, the normalization affects the cross section as well as the acceptance multiplied by reconstruction efficiency. For cross section measurements, the normalization effects only apply on the acceptance. Similarly for data-driven background processes estimated by data-driven method like ZZ^*, tXX, the theoretical uncertainty only affects the relative fraction between categories.

For ggF process, the truth categorization are done in different $N_{\mathrm{jets}}$and $p_{\mathrm{T}}^{4\ell}$regions, therefore the theoretical uncertainty evaluation takes those into consideration according to Refs. [39, 165]. To account for missing high-order contribution in the calculation, factorization, renormalization scale and NNLOPS scale uncertainty are considered as total yield changes in different jet multiplicity bins and migration between 0-jet and 1-jet bins and 1-jet and $\geqslant$ 2-jet bins. The QCD uncertainty over $p_{\mathrm{T}}^{4\ell}$are also obtained by reweighting events according to $p_{\mathrm{T}}^{4\ell}$in each N_{jets}. The variation dependence over $p_{\mathrm{T}}^{4\ell}$is derived by linear enveloping over various contributions, that is covering the maximum variation in each bin with a linear slope to be conservative. Figure 9.13 is an example . ggF process can contribute significantly in two jets categories, ggF events with VBF topology are assigned an additional QCD scale uncertainty. Additionally, uncertainty on higher-order correction on NN input $p_{\mathrm{T}}^{4\ell jj}$ is also evaluated using the difference with a MadGraph5_aMC@NLO sample with FxFx merging scheme. Similarly, VBF

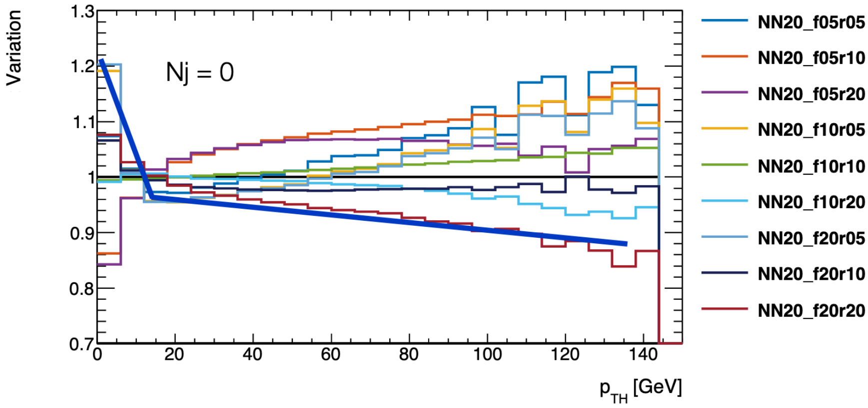

Fig. 9.13 The envelope of all QCD scale variation for the pT migration systematics in the 0-jet bin.

process, the QCD uncertainties are evaluated on N_{jets}, $p_{\mathrm{T}}^{4\ell}$, $p_{\mathrm{T}}^{4\ell jj}$ and m_{jj} [166] and cross-checked against fixed-order calculation. For VH leptonic decay, the QCD scale uncertainties are applied as migration effects on reco categories on $N_{\mathrm{jets}}$and p_{T} of the associated boson. For ttH and VH hadronic process, the QCD scales uncertainties are obtained by varying the nominal renormalization and factorization scales in a combination of 0.5 and 2, and applying a naive envelope in each categories and NN bins. This variation includes $(0.5, 1, 2) \times (0.5, 1, 2)$ nine combinations, and is called 9-point variation. In cases where extreme combination of 0.5×2 is excluded, the variation becomes 7-point variation.

For all the Higgs processes, PDF4LHC standard uncertainties are applied using 30 eigenvector variations of PDF set. Parton shower modeling uncertainties are evaluated with internal AZNLO tune variations, and also by comparing Pythia 8 with Herwig 7. The Higgs decay uncertainty are considered by comparing nominal Prophecy4F [111, 167] with Hto4L [168-169].

For the ZZ^* theoretical uncertainty, since the normalization in each jet multiplicity is constrained purely from the simultaneous fit, the variation on normalization are divided out, and uncorrelated between jet multiplicity bins. The variations include PDF from enveloping NNPDF3.0 PDF set, 7-point QCD scale variation, internal Sherpa parton shower internal tune. Also the comparison between Sherpa and Powheg are considered for qqZZ process. The composition variation is added to account for changed relative contribution between qqZZ, ggZZ and EWZZjj.

For tXX processes, the uncertainties are treated similarly as ZZ^*, but the normalization is divided out only in ttH signal regions and tXX side-band region. A generator comparison is done between MadGraph5_aMC@NLO and Sherpa as an additional systematics.

Finally for VVV processes purely coming from the Monte Carlo, fully uncertainty on cross section and shapes are derived from QCD scale, PDF and parton shower, which has negligible impact on results.

9.5 Statistical Analysis

The statistical model for this analysis is the extended binned likelihood introduced in Section 8.1.2. This section will briefly discuss about the parametrization.

9.5.1 STXS Parametrization

The parametrization of the expected yield inside the reconstructed categories are relatively straightforward. In the cross section type of parametrization, the yield in category i observable bin j can be expressed as

$$\begin{aligned}\text{Yield}_{\text{reco cat i, bin j}} = \sum_{s}^{\text{Production mode}} ((\sigma_s \cdot \mathcal{B})\mathcal{L}(\mathcal{A}\epsilon)_i^s f_{ij}^s) + \sum_{b}^{\text{Floating background}} (\beta_b N^b f_{ij}^b) \\ + \sum_{b}^{\text{Constant background}} (\sigma_b \mathcal{L}(\mathcal{A}e)^b f_{ij}^b),\end{aligned} \tag{9.3}$$

where σ_s is the cross section of one process p with branching ratio considered (signal in production bin or background), $\mathcal{B}$ is the Branching ratio of Higgs decaying to four-lepton, $\mathcal{L}$ is the integrated luminosity, $(\mathcal{A}e)_i^p$ is the acceptance times efficiency from one process (signal in production bin or background) p to a reconstructed categories i with migration effect considered, f_{ij}^p is the shape of observable of process p in reconstructed categories i and bin j, β_b is the normalization factor for a background component of a correlation scheme (one per each reconstructed category), and N^i is the yield of background component in the same correlation scheme, estimated by $\sigma_b\mathcal{L}$ but does not change with systematics. The systematic uncertainties are considered separately for $\mathcal{L}$, $(\mathcal{A}\epsilon)_i^p$, f_{ij}^p, and N_i^b. Uncertainties are correlated between different i and j, and correlated over all processes if it is experimental source, and usually uncorrelated for theoretical source. Most importantly, the $\sigma_p \cdot \mathcal{B}$ in all production bins form the group of parameter of interest (POI) for the type of model under study, either Stage-0 or Reduced Stage-1.1.

For signal-strength type of parametrization, the same parametrization as (9.3) is used but the signal cross section is replaced with

$$\sigma_p \cdot \mathcal{B} \to \mu_p \sigma_p^{SM} \cdot \mathcal{B}, \tag{9.4}$$

where the μ_p is the parameter of interest (such as the signal strength), and $\sigma_p^{SM} \cdot \mathcal{B}$ is fixed but the theoretical uncertainties need to be considered. For inclusive signal-strength measurement, the parametrization is done with one single strength μ as the parameter of interest:

$$\sigma_p \cdot \mathcal{B} \to \mu \sigma_p^{SM} \cdot \mathcal{B}. \tag{9.5}$$

This effectively combines the cross section from different production modes by correlating them together.

9.5.2 κ Framework

The cross section can also be expressed with coupling strength at leading-order, namely the κ-framework [117]. The coupling modifier are applied on cross section and branching ratio:

$$\kappa_i^2 = \frac{\sigma_i}{\sigma_i^{\mathrm{SM}}} \quad \text{and} \quad \kappa_f^2 = \frac{\Gamma_f}{\Gamma_f^{\mathrm{SM}}}, \tag{9.6}$$

where σ_i is the production cross section in mode i, Γ_f is the branching ratio final state, 4ℓ. So the cross section can be re-expressed as

$$\sigma_i \cdot \mathcal{B} = \sigma \cdot \mathcal{B}\,(i \to H \to f) = \kappa_i^2 \cdot \kappa_f^2 \cdot \sigma_i^{\mathrm{SM}} \cdot \frac{\Gamma_f^{\mathrm{SM}}}{\Gamma_H(\kappa_i^2, \kappa_f^2)}, \tag{9.7}$$

where the $\mathcal{B}$ is the branching ratio and Γ_H is the Higgs total width, which also dependents on κ.

The formula for parametrization of cross section and branching ratio modifier can be found in Table 9.14. For example, the ggF processes are contributed by top and bottom quark loop, their contribution shows up in the formula as square term. The destructive interference of the two Feynman diagrams contributes to the cross-multiplying term. Other formulae are derived in a similar manner In this analysis, we only consider such benchmark with two different Higgs boson coupling-strength modifiers to fermions and bosons, aiming to distinguish the strength of interaction between SM Higgs with gauge bosons and fermions. Therefore, all the boson coupling modifiers are assumed to be the same as κ_V, and all the fermion coupling modifiers the same as κ_f as expressed below,

$$\kappa_V = \kappa_Z = \kappa_W \tag{9.8}$$

$$\kappa_f = \kappa_t = \kappa_b = \kappa_c = \kappa_s = \kappa_\mu = \kappa_\tau. \tag{9.9}$$

Also, we assume that there are no Higgs boson directly decay particles undetected or invisible.

Table 9.14 Parametrizations of Higgs boson production cross sections σ_i, partial decay widths Γ^f, and the total width Γ_H, normalized to their SM values, as functions of the coupling-strength modifiers κ. For loop processes, the effective κ parameters is given. The modifier formula are obtained according to Ref. [117].

Production	Effective modifier	Resolved modifier
σ(ggF)	κ_g^2	$1.04\,\kappa_t^2 + 0.002\,\kappa_b^2 - 0.04\,\kappa_t\kappa_b$
σ(VBF)	-	$0.73\,\kappa_W^2 + 0.27\,\kappa_Z^2$
$\sigma(qq/qg \to ZH)$	-	κ_Z^2
$\sigma(gg \to ZH)$	$\kappa_{(ggZH)}$	$2.46\,\kappa_Z^2 + 0.46\,\kappa_t^2 - 1.90\,\kappa_Z\kappa_t$
$\sigma(WH)$	-	κ_W^2
$\sigma(t\bar{t}H)$	-	κ_t^2
$\sigma(tHWb)$	-	$2.91\,\kappa_t^2 + 2.31\,\kappa_W^2 - 4.22\,\kappa_t\kappa_W$
$\sigma(tHqb)$	-	$2.63\,\kappa_t^2 + 3.58\,\kappa_W^2 - 5.21\,\kappa_t\kappa_W$
$\sigma(bbH)$	-	κ_b^2
Decay width		
Γ^{ZZ}	-	κ_Z^2
$\Gamma^{\gamma\gamma}$	κ_γ^2	$1.59\,\kappa_W^2 + 0.07\,\kappa_t^2 - 0.67\,\kappa_W\kappa_t$
$\Gamma^{Z\gamma}$	$\kappa_{(Z\gamma)}^2$	$1.12\,\kappa_W^2 - 0.12\,\kappa_W\kappa_t$
Γ_H	κ_H^2	$0.58\,\kappa_b^2 + 0.22\,\kappa_W^2$ $+0.08\,\kappa_g^2 + 0.06\,\kappa_\tau^2$ $+0.03\,\kappa_Z^2 + 0.03\,\kappa_c^2$ $+0.0023\,\kappa_\gamma^2 + 0.0015\,\kappa_{(Z\gamma)}^2$ $+0.0004\,\kappa_s^2 + 0.00022\,\kappa_\mu^2$

9.6 Results

9.6.1 Data and Monte Carlo Comparison

The expected yield vs observed data in reconstruction categories are summarized in Table 9.15 and the breakdown of expected signal yield from different processes are summarized in Table 9.16 that follows. Generally speaking, the data are in a good agreement with the expectation.

The data and expected events comparison of the invariant mass of four-lepton system

Table 9.15 The expected yield and observed numbers of events in the signal region and side-band region in each reconstructed category assuming m_H = 125 GeV. Statistical and systematic uncertainties are summed up in quadrature and shown in the predictions. Yields are shown as "-" for those processes with contribution less than 0.2‰ in categories.

Reconstructed event category	Signal	ZZ^* background	tXX background	Other backgrounds	Total expected	Observed
Signal			$115 < m_{4\ell} < 130$ GeV			
$0j$-$p_T^{4\ell}$-Low	24.2 ± 3.5	30 ± 4	–	0.93 ± 0.13	55 ± 5	56
$0j$-$p_T^{4\ell}$-Med	76 ± 8	37 ± 4	–	6.5 ± 0.6	120 ± 9	117
$0j$-$p_T^{4\ell}$-High	0.355 ± 0.031	0.020 ± 0.012	0.0094 ± 0.0027	0.30 ± 0.05	0.69 ± 0.06	1
$1j$-$p_T^{4\ell}$-Low	34 ± 4	15.5 ± 2.7	–	1.91 ± 0.29	52 ± 5	41
$1j$-$p_T^{4\ell}$-Med	20.8 ± 2.8	4.0 ± 0.7	0.114 ± 0.013	1.02 ± 0.19	26.0 ± 2.9	31
$1j$-$p_T^{4\ell}$-High	4.7 ± 0.8	0.48 ± 0.10	0.043 ± 0.008	0.27 ± 0.04	5.5 ± 0.8	4
$1j$-$p_T^{4\ell}$-BSM-like	1.23 ± 0.23	0.069 ± 0.031	0.0067 ± 0.0031	0.062 ± 0.012	1.37 ± 0.23	2
$2j$	38 ± 5	9.1 ± 2.7	0.95 ± 0.08	2.13 ± 0.31	50 ± 6	48
$2j$-BSM-like	3.3 ± 0.6	0.18 ± 0.06	0.032 ± 0.005	0.091 ± 0.017	3.6 ± 0.6	6
VH-Lep-enriched	1.29 ± 0.07	0.156 ± 0.025	0.039 ± 0.009	0.0194 ± 0.0032	1.50 ± 0.08	1
ttH-Had-enriched	1.02 ± 0.18	0.058 ± 0.025	0.252 ± 0.032	0.119 ± 0.033	1.45 ± 0.18	2
ttH-Lep-enriched	0.42 ± 0.04	0.002 ± 0.005	0.0157 ± 0.0023	0.0028 ± 0.0029	0.44 ± 0.04	1
Sideband			$105 < m_{4\ell} < 115$ GeV or $130 < m_{4\ell} < 160$ GeV			
SB-$0j$	4.5 ± 0.5	150 ± 13	–	16.2 ± 2.2	171 ± 13	183
SB-$1j$	2.80 ± 0.30	51 ± 7	1.29 ± 0.16	8.4 ± 1.2	63 ± 7	64
SB-$2j$	2.02 ± 0.27	25 ± 7	4.4 ± 0.5	6.0 ± 0.9	38 ± 7	41
SB-VH-Lep-enriched	0.273 ± 0.015	0.48 ± 0.06	0.125 ± 0.018	0.126 ± 0.019	1.00 ± 0.07	3
			$105 < m_{4\ell} < 115$ GeV or $130 < m_{4\ell} < 350$ GeV			
SB-tXX-enriched	0.071 ± 0.012	0.32 ± 0.12	12.1 ± 1.3	0.84 ± 0.33	13.3 ± 1.4	19

after the fit is shown in Figure 9.14. Figure 9.15 to 9.16 shows additional kinematic distributions and neural network discriminants, which also demonstrate a good agreement between observed and expected.

9.6.2 Signal Strength and Cross Section Measurement

The inclusive Higgs production cross section times branching ratio for the Higgs rapidity range, $|y_H| < 2.5$, is measured to be

$$\begin{aligned}\sigma \cdot \mathcal{B} \equiv \sigma \cdot \mathcal{B}(H \to ZZ^*) &= 1.34 \pm 0.11(\text{stat.}) \pm 0.04(\text{exp.}) \pm 0.03(\text{th.})\ \text{pb} \\ &= 1.34 \pm 0.12\ \text{pb},\end{aligned} \tag{9.10}$$

which can be compared with the SM prediction of $(\sigma \cdot \mathcal{B})_{\text{SM}} \equiv (\sigma \cdot \mathcal{B}(H \to ZZ^*))_{\text{SM}} = 1.33 \pm 0.08$ pb. This results has a p-value of 98.6% compatible with the SM prediction.

Table 9.16 The expected number of SM Higgs signal event with m_H = 125 GeV in each reconstructed categories. Combined statistical and systematic uncertainties are summed in quadrature and shown in the predictions. Yields are shown as "-" for those processes with contribution less than 0.2% in categories.

Reconstructed	SM Higgs boson production mode					
event category	ggF	VBF	WH	ZH	$t\bar{t}H+tH$	$b\bar{b}H$
Signal	$115 < m_{4\ell} < 130$ GeV					
$0j$-$p_T^{4\ell}$-Low	23.9 ± 3.5	0.073 ± 0.006	0.0173 ± 0.0031	0.0131 ± 0.0023	–	0.17 ± 0.09
$0j$-$p_T^{4\ell}$-Med	74 ± 8	1.03 ± 0.15	0.37 ± 0.05	0.40 ± 0.05	–	0.8 ± 0.4
$0j$-$p_T^{4\ell}$-High	0.109 ± 0.026	0.0157 ± 0.0024	0.056 ± 0.005	0.173 ± 0.016	0.00065 ± 0.00023	–
$1j$-$p_T^{4\ell}$-Low	31 ± 4	1.99 ± 0.11	0.52 ± 0.05	0.35 ± 0.04	–	0.41 ± 0.21
$1j$-$p_T^{4\ell}$-Med	17.3 ± 2.8	2.50 ± 0.18	0.52 ± 0.06	0.40 ± 0.04	0.0078 ± 0.0013	0.09 ± 0.04
$1j$-$p_T^{4\ell}$-High	3.6 ± 0.8	0.84 ± 0.07	0.158 ± 0.015	0.166 ± 0.016	0.0044 ± 0.0006	0.011 ± 0.006
$1j$-$p_T^{4\ell}$-BSM-like	0.87 ± 0.23	0.246 ± 0.020	0.060 ± 0.007	0.054 ± 0.006	0.00156 ± 0.00032	0.0009 ± 0.0005
$2j$	25 ± 5	8.5 ± 0.6	1.94 ± 0.15	1.69 ± 0.13	0.46 ± 0.04	0.30 ± 0.15
$2j$-BSM-like	1.9 ± 0.6	1.08 ± 0.05	0.120 ± 0.016	0.122 ± 0.016	0.075 ± 0.007	0.0021 ± 0.0010
VH-Lep-enriched	0.050 ± 0.011	0.019 ± 0.004	0.80 ± 0.07	0.245 ± 0.021	0.166 ± 0.013	0.0027 ± 0.0014
ttH-Had-enriched	0.15 ± 0.16	0.021 ± 0.004	0.020 ± 0.005	0.055 ± 0.013	0.75 ± 0.07	0.020 ± 0.011
ttH-Lep-enriched	0.0019 ± 0.0022	0.00019 ± 0.00008	0.0046 ± 0.0026	0.0032 ± 0.0018	0.41 ± 0.04	–
Sideband	$105 < m_{4\ell} < 115$ GeV or $130 < m_{4\ell} < 160$ GeV					
SB-$0j$	4.2 ± 0.5	0.050 ± 0.010	0.096 ± 0.011	0.042 ± 0.005	–	0.044 ± 0.022
SB-$1j$	2.37 ± 0.29	0.241 ± 0.024	0.100 ± 0.013	0.063 ± 0.008	0.0049 ± 0.0009	0.023 ± 0.012
SB-$2j$	1.25 ± 0.26	0.43 ± 0.05	0.119 ± 0.014	0.103 ± 0.012	0.109 ± 0.010	0.016 ± 0.008
SB-VH-Lep-enriched	0.015 ± 0.005	0.0029 ± 0.0011	0.084 ± 0.008	0.104 ± 0.010	0.065 ± 0.006	0.0013 ± 0.0007
	$105 < m_{4\ell} < 115$ GeV or $130 < m_{4\ell} < 350$ GeV					
SB-tXX-enriched	0.001 ± 0.010	0.00012 ± 0.00009	0.0006 ± 0.0004	0.0008 ± 0.0004	0.068 ± 0.008	–
Total	186 ± 14	17.0 ± 0.8	5.0 ± 0.4	3.97 ± 0.29	2.13 ± 0.18	1.9 ± 1.0

The inclusive signal strength defined as measured cross section normalized by Standard Model cross section is measured to be

$$\mu = 1.01 \pm 0.08(\text{stat.}) \pm 0.04(\text{exp.}) \pm 0.05(\text{th.}) = 1.01 \pm 0.11. \tag{9.11}$$

The corresponding likelihood scan that used to extract the measurements can be seen in Figure 9.18.

The measurement precision is still statistically-dominated. For the cross section measurement, the dominant experimental systematic uncertainty are lepton efficiency, luminosity uncertainty and the dominant theoretical uncertainties are parton shower modeling on the acceptance. The signal-strength measurement have larger theoretical uncertainty due to the QCD uncertainty of the ggF cross section.

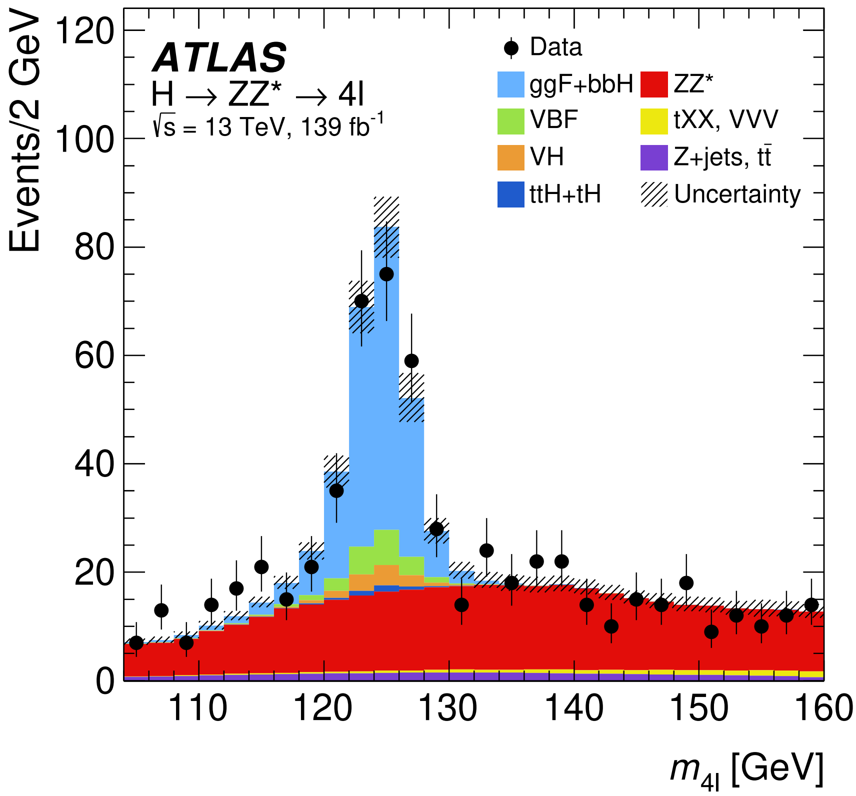

Fig. 9.14 **The observed and expected (post-fit) invariant mass of four-lepton system, after the signal region selection.**

The results for Stage-0 and Reduced Stage-1.1 cross sections $\sigma \cdot \mathcal{B}$ divided by SM expectation $(\sigma \cdot \mathcal{B})_{\text{SM}}$ are shown in Figure 9.19. The Stage-0 production mode results shows a good agreement between the measured and the expected. There are slight tension in Reduced Stage-1.1 but the SM values are not far away from the $\pm 1\sigma$ 68%-CL interval. Because ggF has the largest contribution to the overall Higgs signal, the dominant systematic uncertainties for ggF is similar to the inclusive measurement: lepton efficiency, luminosity uncertainty and parton shower modeling. Other non-ggF processes are also affected by the ggF modeling uncertainties. For other processes in Stage-0, and most of the cross sections in Reduced Stage-1.1, the jet energy scale and resolution become the dominant uncertainties, along with parton shower modeling.

All the results of the cross section measurements are summarized in Table 9.17.

Figure 9.20 shows the 2D likelihood contours in the (ggF, VBF), (ggF, VH), (VBF, VH) and (gg2H-0j-p_{T}^{H}-Low, gg2H-0j-p_{T}^{H}-High) planes. The compatibility with the SM expectation is in terms of p-values are 0.22, 0.25, 0.19 and 0.33 standard deviations, respectively.

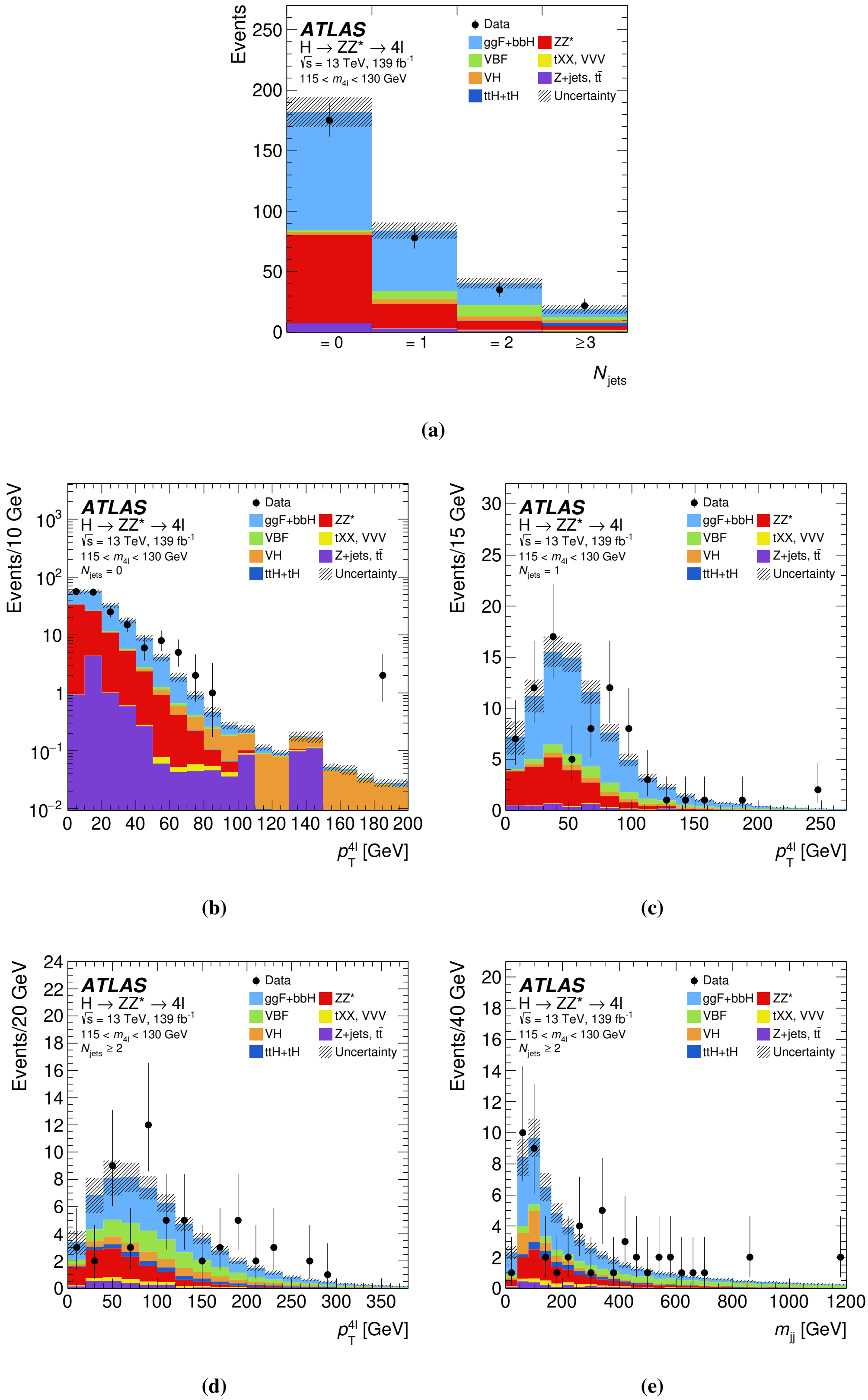

Fig. 9.15 **The observed and expected distributions (post-fit) of (a) the N_{jets}after the inclusive event selection, the four-lepton transverse momenta $p_{\text{T}}^{4\ell}$ for events with (b) exactly zero jets, (c) with exactly one jet and (d) with at least two jets and (e) the dijet invariant mass m_{jj} for events with at least two jets.**

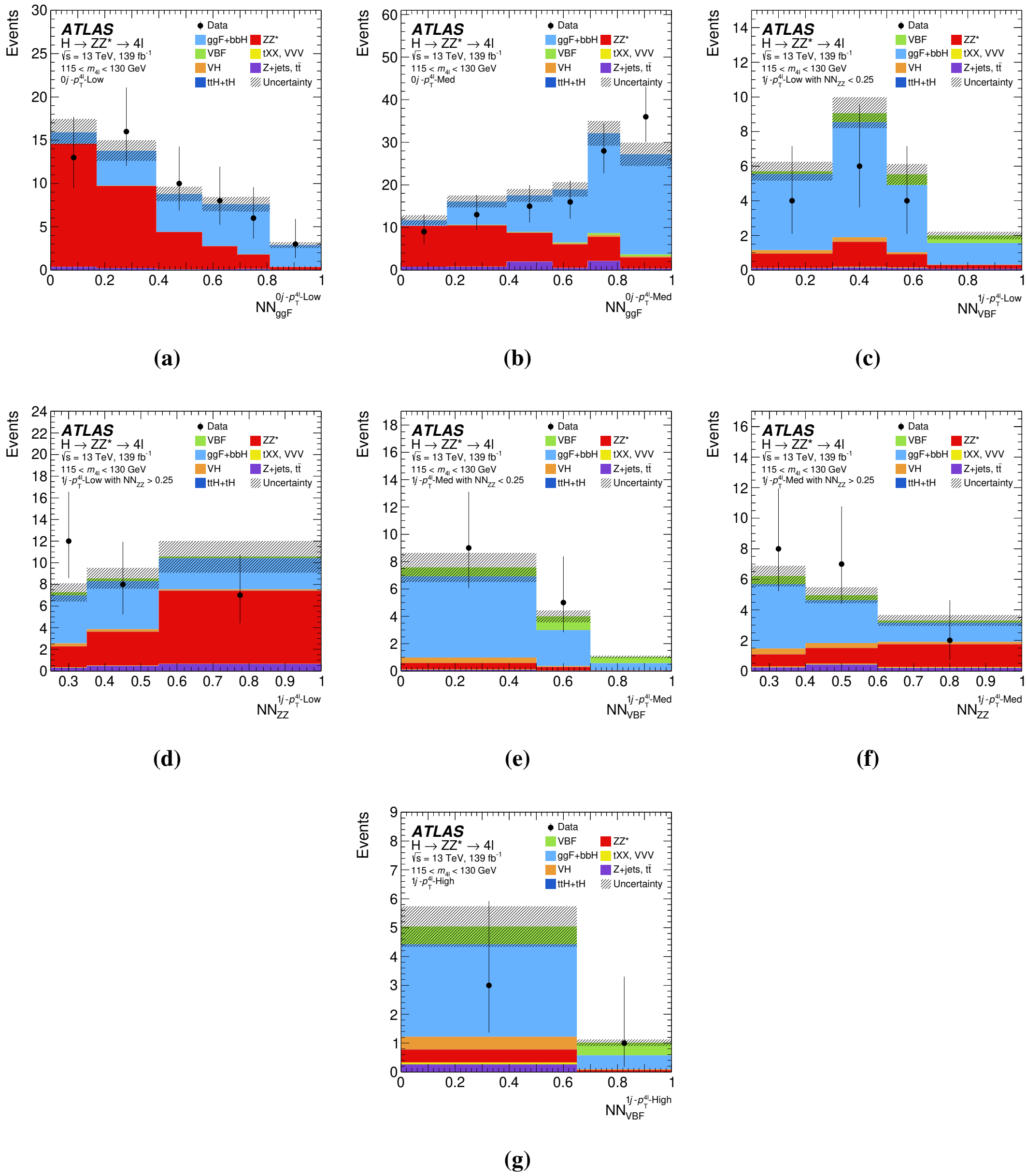

Fig. 9.16 The observed and post-fit expected NN output distributions in the different zero- and one-jet categories: (a) $\mathrm{NN_{ggF}}$ **in** $0j$-$p_{\mathrm{T}}^{4\ell}$-Low, **(b)** $\mathrm{NN_{ggF}}$ **in** $0j$-$p_{\mathrm{T}}^{4\ell}$-Med, **(c)** $\mathrm{NN_{VBF}}$ $1j$-$p_{\mathrm{T}}^{4\ell}$-Low **with** $\mathrm{NN}_{ZZ} < 0.25$, **(d)** NN_{ZZ} **in** $1j$-$p_{\mathrm{T}}^{4\ell}$-Low **with** $\mathrm{NN}_{ZZ} > 0.25$, **(e)** $\mathrm{NN_{VBF}}$ **in** $1j$-$p_{\mathrm{T}}^{4\ell}$-Med **with** $\mathrm{NN}_{ZZ} < 0.25$, **(f)** NN_{ZZ} **in** $1j$-$p_{\mathrm{T}}^{4\ell}$-Med **with** $\mathrm{NN}_{ZZ} > 0.25$ **and (g)** $\mathrm{NN_{VBF}}$ **in** $1j$-$p_{\mathrm{T}}^{4\ell}$-High.

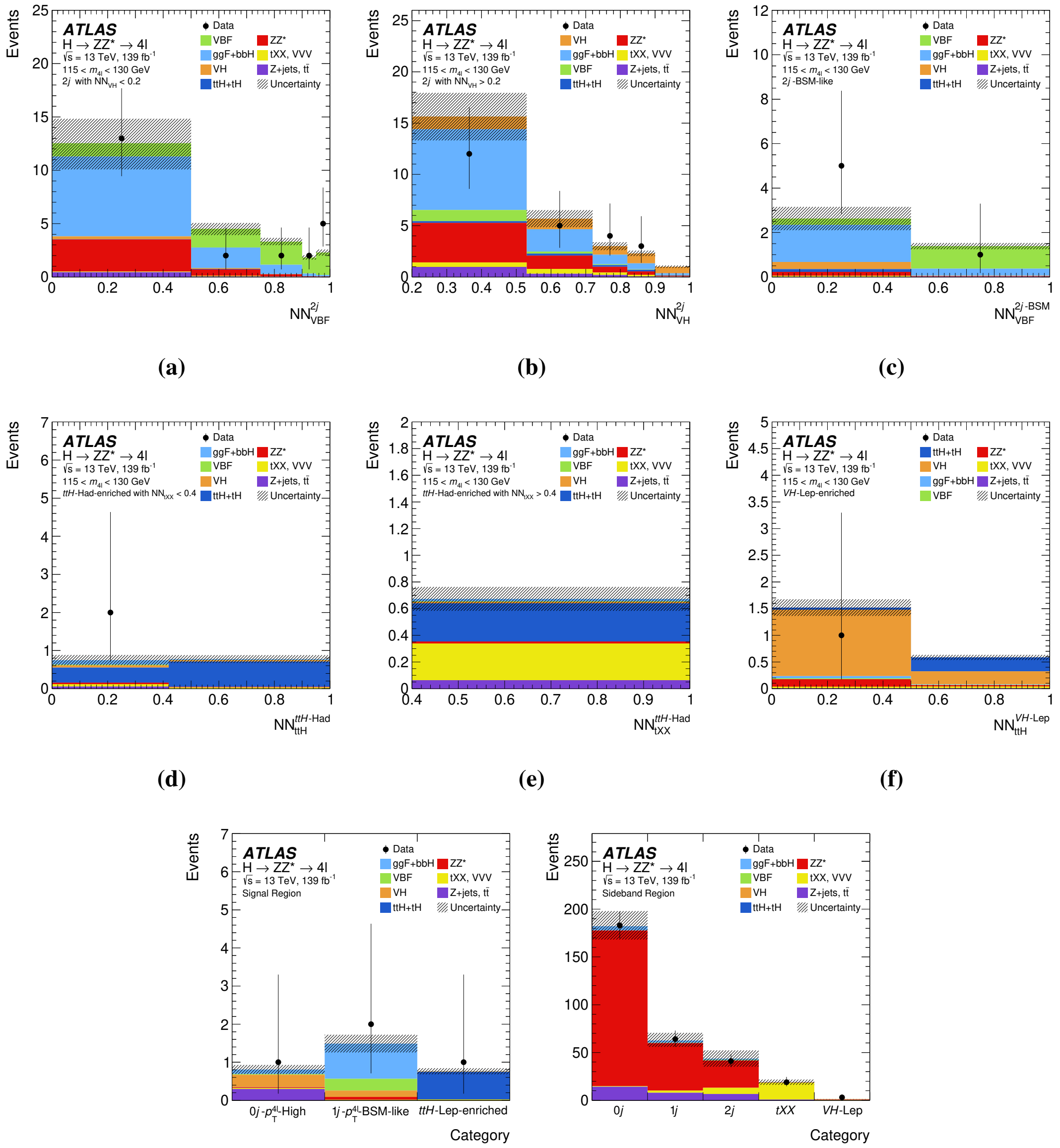

(a) (b) (c)

(d) (e) (f)

(g) (h)

Fig. 9.17 **The observed and expected NN output (post-fit) distributions in the different categories: (a)** $\mathrm{NN_{VBF}}$ **in** $2j$ **with** $\mathrm{NN}_{VH} < 0.2$**, (b)** NN_{VH} **in** $2j$ **with** $\mathrm{NN}_{VH} > 0.2$**, (c)** $\mathrm{NN_{VBF}}$ **in** $2j$**-BSM-like, (d)** NN_{ttH} **in** ***ttH*****-Had-enriched with** $\mathrm{NN}_{tXX} < 0.4$**, (e)** NN_{tXX} **in** ***ttH*****-Had-enriched with** $\mathrm{NN}_{tXX} > 0.4$ **and (f)** NN_{ttH} **in** ***VH*****-Lep-enriched. (g) shows the categories where no NN discriminant is used while (h) shows the sidebands used to constrain the** ZZ^* **and** tXX **backgrounds.**

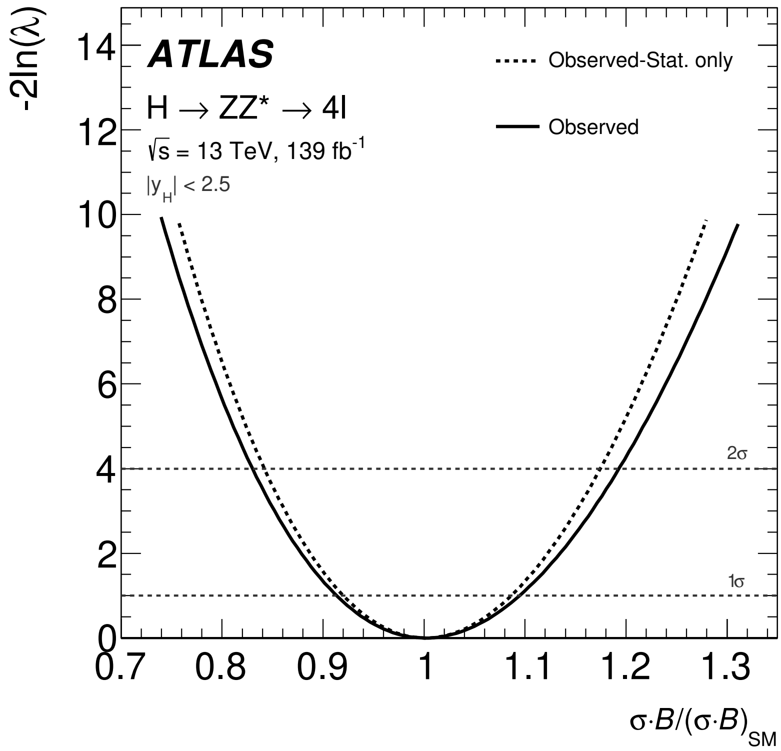

(a)

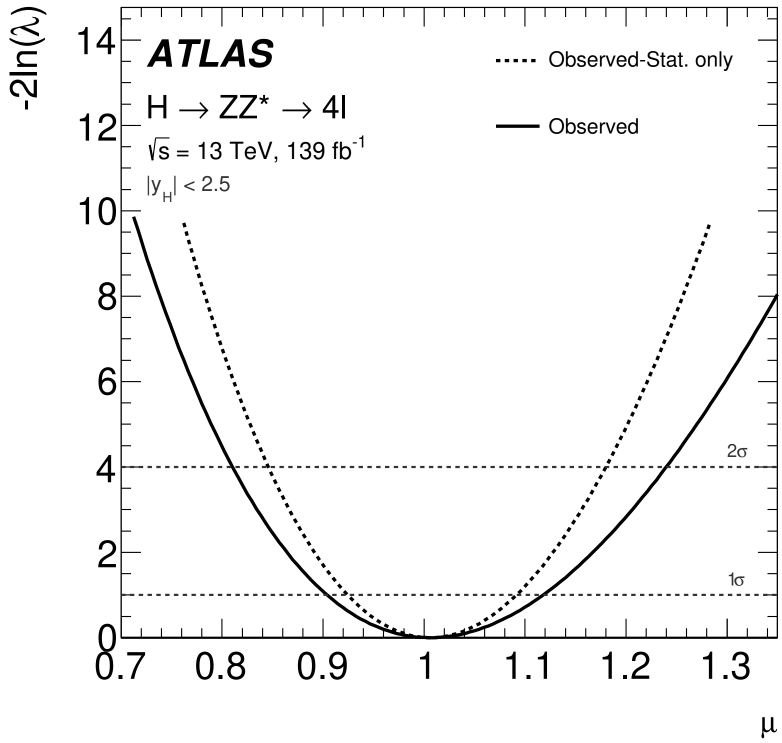

(b)

Fig. 9.18 Observed profile likelihood as a function of (a) $\sigma \cdot \mathcal{B}(H \to ZZ^{*})$ normalized by the SM expectation and (b) the inclusive signal strength μ; the solid lines are the ones with systematic uncertainties and the dashed lines are the ones without systematic uncertainties.

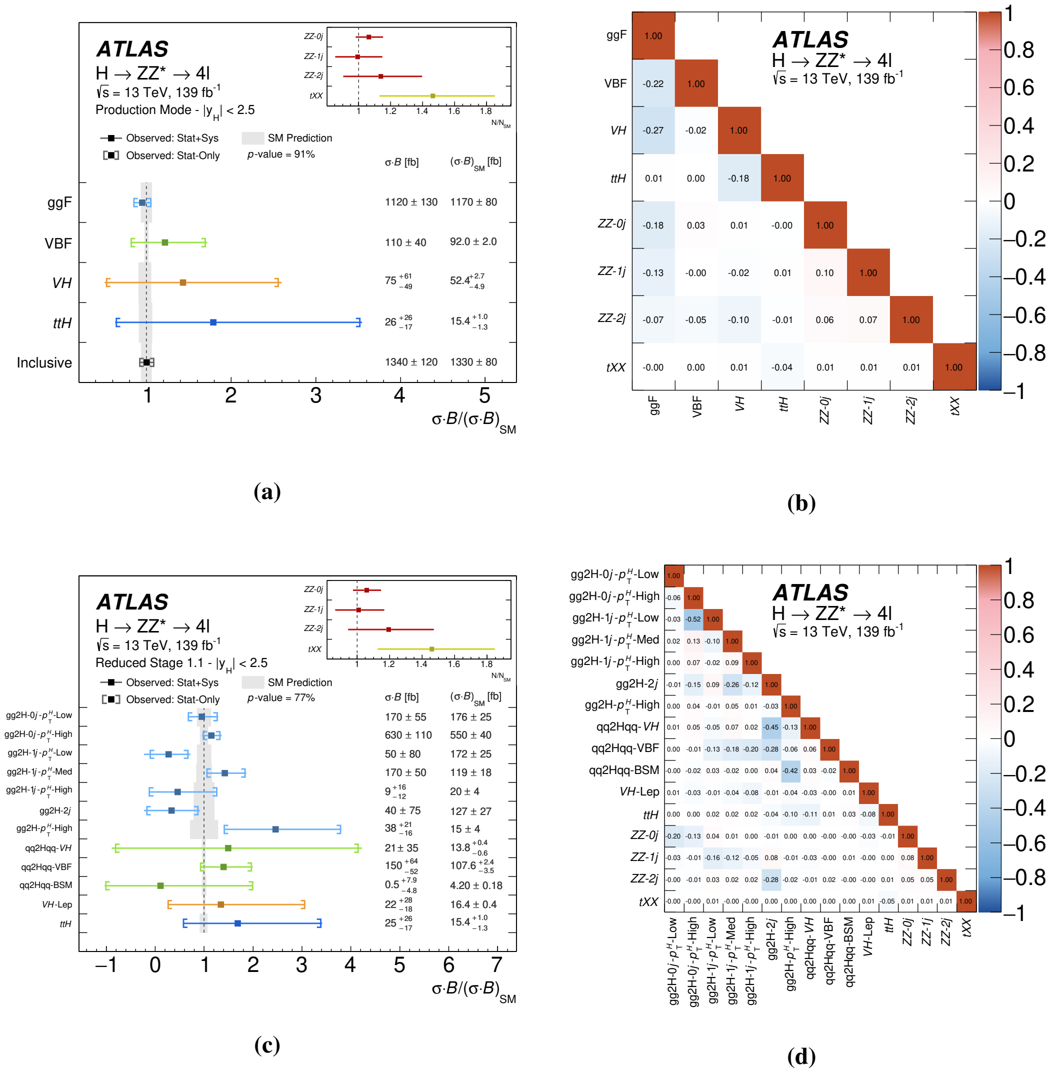

Fig. 9.19 The observed and expected values of the cross sections $\sigma \cdot \mathcal{B}$ normalized by the SM expectation $(\sigma \cdot \mathcal{B})_{\mathrm{SM}}$ of (a) the inclusive production and Production Mode Stage and (c) the Reduced Stage-1.1 production bins. The fitted normalization factors for the ZZ and tXX background are shown in the inserts. Different Higgs production modes and background use different colors. The theoretical uncertainty on the signal prediction is shown in the gray band. The correlation matrices between the parameter of interest and normalization factors are shown in (b) the Production Mode Stage and (d) the Reduced Stage 1.1.

Table 9.17 Summary of the cross section results for the expected SM cross section $(\sigma \cdot \mathcal{B})_{\mathrm{SM}}$, the observed value of $\sigma \cdot \mathcal{B}$, and their ratio $(\sigma \cdot \mathcal{B})/(\sigma \cdot \mathcal{B})_{\mathrm{SM}}$. The $b\bar{b}H$ (tH) contribution is included in the ggF (ttH) production bins. The uncertainties are given as (stat.)+(exp.)+(th.) for the inclusive cross section and the production bin cross sections. For the Reduced Stage 1.1, the uncertainties are given as (stat.)+(syst.).

Production bin	Cross section $(\sigma \cdot \mathcal{B})$ [pb]		$(\sigma \cdot \mathcal{B})/(\sigma \cdot \mathcal{B})_{\mathrm{SM}}$
	SM expected	Observed	Observed
Inclusive production, $\lvert y_H \rvert < 2.5$			
	1.33 ± 0.08	$1.34 \pm 0.11 \pm 0.04 \pm 0.03$	$1.01 \pm 0.08 \pm 0.03 \pm 0.02$
Production Mode Stage bins, $\lvert y_H \rvert < 2.5$			
ggF	1.17 ± 0.08	$1.12 \pm 0.12 \pm 0.04 \pm 0.03$	$0.96 \pm 0.10 \pm 0.03 \pm 0.03$
VBF	0.0920 ± 0.0020	$0.11 \pm 0.04 \pm 0.01 \pm 0.01$	$1.21 \pm 0.44\ ^{+0.13}_{-0.08}\ ^{+0.07}_{-0.05}$
VH	$0.0524^{+0.0027}_{-0.0049}$	$0.075^{+0.059}_{-0.047}\ ^{+0.011}_{-0.007}\ ^{+0.013}_{-0.009}$	$1.44^{+1.13}_{-0.90}\ ^{+0.21}_{-0.14}\ ^{+0.24}_{-0.17}$
ttH	$0.0154^{+0.0010}_{-0.0013}$	$0.026^{+0.026}_{-0.017} \pm 0.002 \pm 0.002$	$1.7^{+1.7}_{-1.2} \pm 0.2 \pm 0.2$
Reduced Stage-1.1 bins, $\lvert y_H \rvert < 2.5$			
gg2H-0j-p_{T}^{H}-Low	0.176 ± 0.025	$0.17 \pm 0.05 \pm 0.02$	$0.96 \pm 0.30 \pm 0.09$
gg2H-0j-p_{T}^{H}-High	0.55 ± 0.04	$0.63 \pm 0.09 \pm 0.06$	$1.15 \pm 0.17 \pm 0.11$
gg2H-1j-p_{T}^{H}-Low	0.172 ± 0.025	$0.05 \pm 0.07\ ^{+0.04}_{-0.06}$	$0.3 \pm 0.4\ ^{+0.2}_{-0.3}$
gg2H-1j-p_{T}^{H}-Med	0.119 ± 0.018	$0.17 \pm 0.05\ ^{+0.02}_{-0.01}$	$1.4 \pm 0.4 \pm 0.1$
gg2H-1j-p_{T}^{H}-High	0.020 ± 0.004	$0.009^{+0.016}_{-0.011} \pm 0.002$	$0.5^{+0.8}_{-0.6} \pm 0.1$
gg2H-2j	0.127 ± 0.027	$0.04 \pm 0.07 \pm 0.04$	$0.3 \pm 0.5 \pm 0.3$
gg2H-p_{T}^{H}-High	0.015 ± 0.004	$0.038^{+0.021}_{-0.016}\ ^{+0.003}_{-0.002}$	$2.5^{+1.3}_{-1.0}\ ^{+0.2}_{-0.1}$
qq2Hqq-VH	$0.0138^{+0.0004}_{-0.0006}$	$0.021^{+0.037}_{-0.029}\ ^{+0.009}_{-0.006}$	$1.5^{+2.7}_{-2.1}\ ^{+0.6}_{-0.4}$
qq2Hqq-VBF	$0.1076^{+0.0024}_{-0.0035}$	$0.15 \pm 0.05\ ^{+0.02}_{-0.01}$	$1.4 \pm 0.5\ ^{+0.2}_{-0.1}$
qq2Hqq-BSM	0.00420 ± 0.00018	$0.0005^{+0.0079}_{-0.0047} \pm 0.008$	$0.1^{+1.9}_{-1.1} \pm 0.2$
VH-Lep	0.0164 ± 0.0004	$0.022^{+0.028}_{-0.018}\ ^{+0.003}_{-0.001}$	$1.3^{+1.7}_{-1.1}\ ^{+0.2}_{-0.1}$
ttH	$0.0154^{+0.0010}_{-0.0013}$	$0.025^{+0.026}_{-0.017}\ ^{+0.005}_{-0.003}$	$1.6^{+1.7}_{-1.1}\ ^{+0.3}_{-0.2}$

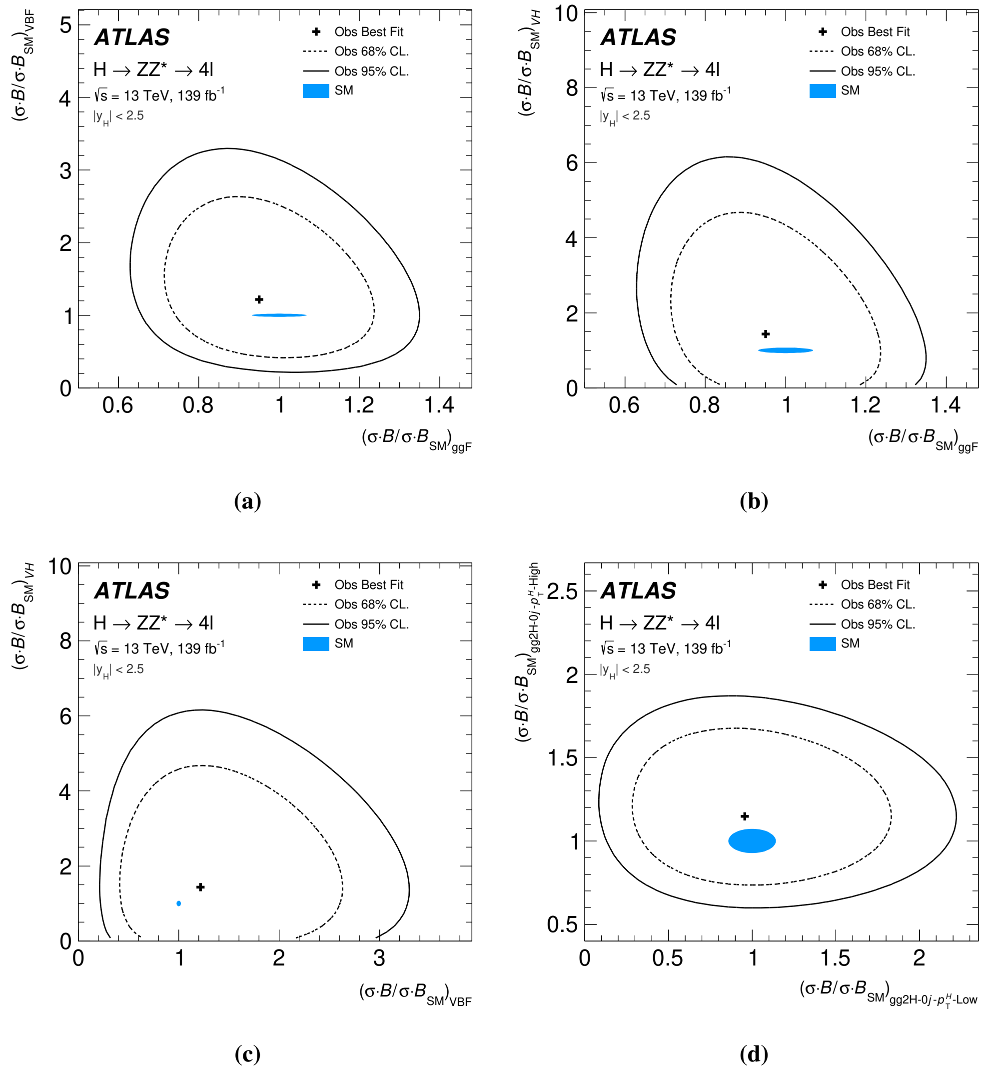

Fig. 9.20 **Likelihood contours at 68% and 95% CL in dashed and solid line respectively: (a)** (ggF, VBF)**, (b)** (ggF, VH)**, (c)** (VBF, VH) **and (d)** (gg2H-0j-p_T^H-Low, gg2H-0j-p_T^H-High) **plane. The best fit is shown as solid cross and the SM prediction and its theory uncertainty are shown in the filled ellipse. Notice the scale of the axis is very different in (a) and (b), but the predicted theoretical error is similar for different cross section times branching ratio but**

9.6.3 Coupling Measurement in the κ Framework

The cross sections model re-parametrized in the κ-framework described in Section 9.5.2. The observed likelihood contours in the κ_V–κ_F plane are shown in Figure 9.21 (only the quadrant $\kappa_F > 0$ and $\kappa_V > 0$ is shown since this channel is not sensitive to the relative sign of the two coupling modifiers). The best-fit value is $\hat{\kappa}_V = 1.02 \pm 0.06$ and $\hat{\kappa}_F = 0.88 \pm 0.16$. The correlation between the two modifiers is -0.17. The p-value for the compatibility with the Standard Model expectation is 75%, indicating a good agreement between the measured couplings and the SM predictions.

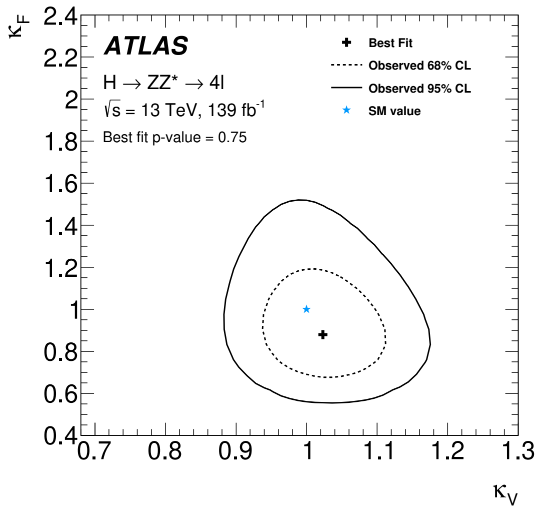

Fig. 9.21 Likelihood contours at 68% and 95% CL in dashed and solid line respectively of κ_V–κ_F. The best fit is shown as solid cross and the SM prediction is shown as star.

Chapter 10 Inclusive $m_{4\ell}$ Lineshape Measurement

This chapter presents the analysis of invariant four-lepton mass lineshape measurement using $\sqrt{s} = 13$ TeV data with an integrated luminosity of 36 fb^{-1}, collected by the ATLAS experiment in the first two years of the LHC Run 2 program. As described in Section 3.3.1, the major processes under study are the quark originated process qqZZ and gluon originated ggZZ process. In the high mass region where two Z bosons are both produced on-shell, the qqZZ is around ten times the size of ggZZ. Furthermore, the off-shell Higgs boson production in the high mass region will further reduce the event rate from the ggZZ process due to negative interference between ggH and ggZZ processes.

One-dimensional distribution of $m_{4\ell}$ and two-dimensional distributions $m_{4\ell}$ vs secondary variables are unfolded to remove the acceptance and detector effects, such as lepton detection efficiency loss and resolution. Then the spectra can be re-interpreted under various models for measurements. In this analysis, the following physics quantities are measured:

- the signal strength of ggZZ;
- the off-shell Higgs signal strength and the limit on the Higgs nature width;
- the branching ratio of the Z to four-lepton decays;
- the modified Higgs coupling.

10.1 Introduction to Unfolding

Unfolding is the technique broadly used in differential cross section measurements to correct detector efficiency, resolution, and acceptance. The measured differential cross section can be directly compared to theoretical predicted differential cross section distribution. The relation between a detector level observation and the underlying particle-level distribution within a given fiducial region can be parametrized by

- **reconstruction efficiency,** ϵ, a one-dimensional distribution which accounts for the acceptance and efficiency involved in reconstructing an event in the detector. This is measured in MC as the ratio of events passing both the reconstructed and fiducial selections to all those which pass the fiducial selection, as a function of the truth-level variable;
- **migration matrix, M**, a two-dimensional array which is used to correct for bin-to-

bin migrations between the reconstructed distribution and truth-level distribution. It is measured in MC using events which pass the event selection and fall into the fiducial volume at both truth and reconstructed levels. Each element M_{dp} gives the probability that a particle-level event in a given particle-level bin p which passes the reconstruction selection will be found in a given reconstructed bin d;

- **fiducial fraction, f**, a one-dimensional distribution which accounts for events which are outside of the fiducial region, but still pass the reconstructed selection and enter the measured distribution. This can be caused by the measurement resolution of the variables used to select events. In addition, events with electrons or muons from τ lepton decays fall into this category, since the fiducial regions requires $Z \to \mu\mu$ or $Z \to ee$ decays. This correction is measured in MC as the ratio of events which pass both the fiducial and reconstructed selections to all those which pass the reconstructed selection. Above the on-shell ZZ threshold, it is typically very close to 1;
- **fiducial purity**, defined as the fraction of reconstructed events in a given particle-level bin which populates the same bin at detector level. This is simply the diagonal element vector of the *migration matrix*;
- **reconstruction purity**, which defined as the fraction of reconstructed events in a given detector-level bin which originated from the same bin at fiducial level. While a related concept, this is different from the fiducial purity. This variable is not used in the unfolding procedures.

The reconstruction efficiency, migration matrix and fiducial fraction define the *response matrix*

$$R = f^{-1} \cdot M \cdot \epsilon, \tag{10.1}$$

where the *fiducial fraction* and *reconstruction efficiency* are matrix where diagonal terms are filled with those distributions. This describes the effect of the reconstruction in the detector on the original particle-level distribution. Each element R_{dp} in the R-matrix gives the probability that an event within the fiducial region in particle-level bin p results in a detector-level event in bin d, and it satisfy

$$\text{Reconstructed distribution} = R \cdot (\text{truth distribution}). \tag{10.2}$$

Monte Carlo simulation is used to study those quantities under each distribution, and then applied on data to give the unfolded observed spectrum at fiducial phase space. Distributions are transformed to differential cross sections and can be compared with various theories in re-interpretation with statistical analyses. The advantage is that physical model doesn't need to go through the detector simulations to compare with data. In this thesis, distributions are unfolded back to distributions in fiducial phase space, therefore the fiducial acceptance effect dose not need to be considered in the experimental reconstruction efficiency.

10.1.1 Unfolding Methods

There are various unfolding approaches. Two simple unfolding methods, the "*bin-by-bin*" and the "*matrix invert*", are first briefly introduced below. Following that the "*Iterative Bayesian unfolding*" method used in this thesis will be presented.

The *bin-by-bin* unfolding for a certain physics variable distribution is a naive procedure that assumes there is no migration between bins. Therefore the calculation is simplified to calculate a correction factor for each bin, defined as ratio of events that pass fiducial selections over ratio of events that pass reconstructed selections. To unfold the data we simply need to multiply the correction factor on the observed variable. The assumption of *bin-by-bin* method determines the quality of the unfolding. In cases of minor migration, the bias introduced by *bin-by-bin* unfolding is tolerated, such as the measurement with the Higgs to four-lepton differential analysis using 36 fb^{-1} data [170].

The *matrix invert* method, as its name indicates, just applies the inverse of (10.1) on the reconstructed spectrum. However this method would result in exaggerated statistical uncertainties compared to the intrinsic statistical error in each reconstructed variable-bin due to the off-diagonal terms in the inversion process.

The unfolding method used in this thesis is *Iterative Bayesian unfolding* based on Bayes' theorem [171]. First, all the efficiency corrections are applied on the truth distribution and the fiducial correction is applied on the reconstructed distribution. At this stage all events pass both the fiducial and reconstructed selection are normalized to unity so that probability theorems can be applied. In each iteration, a prior knowledge of the efficiency of the corrected fiducial normalized distribution and the migration matrix are used to calculate the contribution of a truth bin in a reconstructed bin. This contribution can be interpreted as the probability for an event in a given reconstruction-bin originating come from a truth-bin. Therefore the posterior distribution at the fiducial level can be calculated by simply multiplying this probability to the fiducial corrected reconstructed distribution. The predicted true distribution is used as the prior for the first iteration and the posterior of a iteration is used as the prior in the next iteration. This iteration converges eventually to *matrix invert* method so result from any intermediate number of iterations will provide a regularization of the statistical uncertainty. The optimization of the number of iterations is described in Section 10.1.3

10.1.2 Statistical and Systematic Uncertainty Calculations

MC toys are used to propagate statistical uncertainties of the data through the unfolding procedure. 2000 Poisson-distributed pseudo-data with the mean set to the observed value are used to model the data. The unfolding is repeated for each dataset and in each bin, the statistical uncertainty is evaluated as the root-mean-square (RMS) error of all unfolded toys. The covariance is calculated assuming full correlation between any two bins for a single MC toy, and the average is used as the final covariance.

The systematic uncertainties are propagated by repeating the unfolding with each systematic variation applied on the response matrix and taking the difference between the resulting distribution and the nominal unfolded distribution. The covariance of single variation is calculated treating any two bins as fully correlated. The sources of the systematic uncertainty are discussed in more detail in Section 10.3.

10.1.3 Optimization of Unfolding Method

Two effects need to be taken into account when optimizing the number of iterations when using the Bayesian unfolding. As described in Section 10.1.1, increasing the number of iterations will decrease the dependence on the initial input prior (the predicted truth distribution) decrease the regularization, therefore it will reduce the expected residual bias. However the unfolded distribution will have larger statistical uncertainty and be more probable to suffer from large bin-by-bin fluctuations. A standard approach for estimating the magnitude of residual biases is carried out in form of the data-driven closure test, as described in Section 10.3.1. In addition, a second method uses pseudo-dataset to make a choice of iterations independent of the observation on data, without suffering from observed statistical fluctuations, described below.

For each distribution, 1000 toy distributions are generated based on the predicted yields from Monte Carlo at detector level with the Poisson assumption. Each of these is unfolded using the nominal response matrix. For each toy experiment, the residual bias is defined as difference between unfolded toy to the invert unfolded toy :

$$bias = (\text{Unfolded toy}) - R^{-1} \cdot (\text{toy}) \tag{10.3}$$

By sampling all of the toys, we obtain the *root-mean-square "bias significance"*, defined as the RMS of bias over average of statistical uncertainty. It is a measure of how significant the bias is expected to be when compared to the quoted statistical uncertainty.

Its behavior is sensitive to the fiducial purity, where a high fiducial purity typically leads to a small bias compared to the statistical error.

The number of iterations used in the unfolding is then chosen to be the smallest possible number for which the root-mean-square bias significance is below 0.2 for every bin. This represents an expected factor 5 suppression of the bias compared to the statistical error. The choice made in this way is finally tested using the standard data-driven closure test in order to confirm its validity. In summary, two iterations are chosen as the optimal number for all the distributions.

10.2 Unfolding Observables

Differential or double-differential distributions are measured in this analysis for five observables of interest:

1. the invariant mass of the four-lepton system, $m_{4\ell}$,
2. the $m_{4\ell}$ and the transverse momentum of the four-lepton system, $p_{\mathrm{T}}^{4\ell}$,
3. the $m_{4\ell}$ and the rapidity of the four-lepton system, $y_{4\ell}$,
4. the $m_{4\ell}$ and a matrix element discriminant (MELA) designed to discriminate between the s-channel, Higgs boson mediated process and all other contributions.
5. the $m_{4\ell}$ individually for each of the three lepton flavor combinations (4μ,$4e$,$2e2\mu$) that can occur in the final state.

The double-differential distributions provide a greater sensitivity to the $gg \to ZZ$ production rate and the potential presence of anomalous triple gauge couplings ($p_{\mathrm{T}}^{4\ell}$) or the contribution by the off-shell s-channel Higgs boson mediated production channel (MELA, $y_{4\ell}$). The double differential with respect to lepton flavor channel allows for lepton universality cross-checks.

The binning to use for the measurement is chosen by aiming to attain the highest possible granularity (number of bins) while ensuring that

- each bin is expected to contain at least 10 signal events at detector-level according to MC simulation and
- a large fraction (around 80%) of the events in a given bin at particle level should also belong to this same bin at detector-level, if successfully reconstructed - this is the fiducial purity defined earlier.

Usually, the first constraint is the dominant one in the tails of the spectra, where wide bins have to be chosen in order to collect sufficient events. Close to the maxima of the lineshape, the binning decision is driven by avoiding a large bin migrations.

10.2.1 $m_{4\ell}$ Differential Distribution

The differential distribution of $m_{4\ell}$ is measured in 15 bins with bin edges at

- $m_{4\ell} = [75, 100, 120, 130, 150, 180, 200, 225, 255, 290, 325, 370, 440, 540, 680, 1200]$ GeV.

Figure 10.1 depicts the key unfolding metrics as well as the total expected particle- and detector-level yields for the signal processes. A fiducial purity in excess of 80% is reached for the entire distribution, with the lowest values being in the range $200 < m_{4\ell} < 400$ GeV, where statistics are high and the purity is the dominant constraint to the achievable granularity of the measurement. The final bin is chosen to start as high in $m_{4\ell}$as possible while still retaining a predicted population of 10 detector-level events. Separate bins intended for the observation of single-resonant $Z \rightarrow 4\ell$ production and resonant $H \rightarrow 4\ell$ production are included at low $m_{4\ell}$. It can be seen that the majority of events in each fiducial bin will be measured in the same reconstructed bin, with migrations of up to 17% to adjacent bins, and some smaller migrations to other bins. The efficiency increases as a function of the invariant four lepton mass up to 180 GeV as the transverse momentum of the component leptons increases. The fiducial fraction has some structure in the low mass region, due to two different contributions. Below 120 GeV softer leptons lead to more out-of-acceptance events passing the reconstruction selection due to resolution effects at detector-level. Between 120 GeV and 180 GeV an additional effect is seen due to qq → ZZ events with decays to τ leptons, which in turn decay to electrons or muons. This decay is not included in the fiducial region and leads to a further drop in the fiducial fraction. This contribution is enriched at low reconstructed $m_{4\ell}$ values, since here the Z mass windows allow a lower mass for the subleading lepton pair, increasing the acceptance to pairs of leptons from τ decays which do not inherit their parent's full momentum due to the presence of escaping neutrinos.

Figure 10.2 presents the composition of the predicted detector-level yield for the differential $m_{4\ell}$ measurement.

Figure 10.3 shows the mean statistical uncertainty and the RMS bias significance defined in Section 10.1.3 for the differential $m_{4\ell}$ measurement. With two Bayesian iterations, the required factor 5 suppression of the bias compared to the statistical error is achieved. The statistical error for this choice is observed to be slightly above the one that would be obtained by bin-by-bin unfolding. Hence, two iterations are used to unfold this distribution.

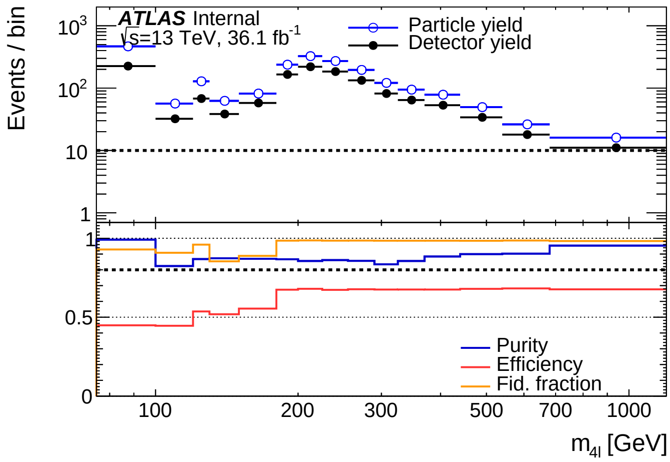

(a)

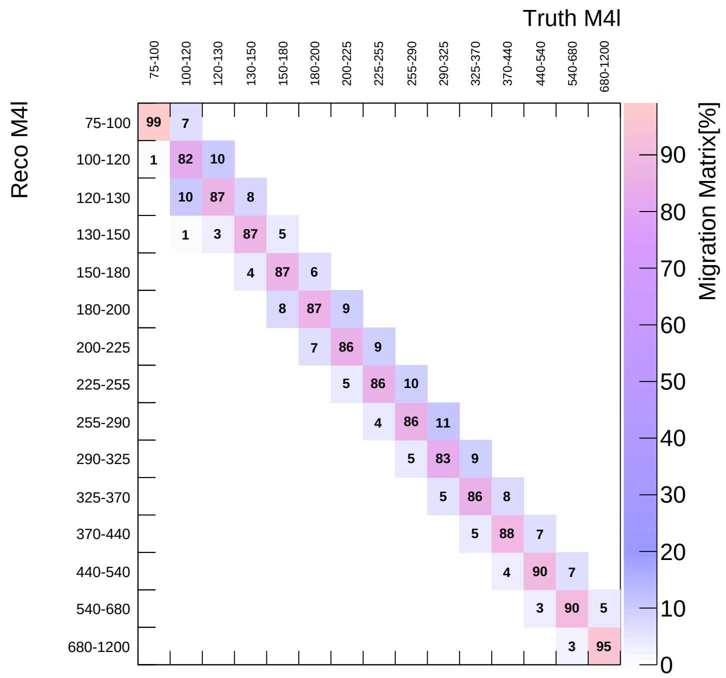

(b)

Fig. 10.1 Key unfolding metrics for the $m_{4\ell}$lineshape measurement. (a) Predicted detector and particle level yields, efficiency, fiducial fraction and fiducial purity as well as (b) the migration matrix.

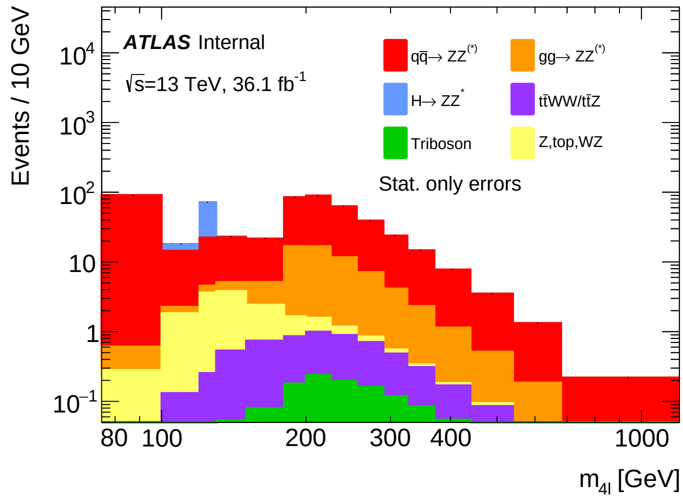

Fig. 10.2 **Predicted detector-level yields for the differential $m_{4\ell}$ distribution, after the full event selection.**

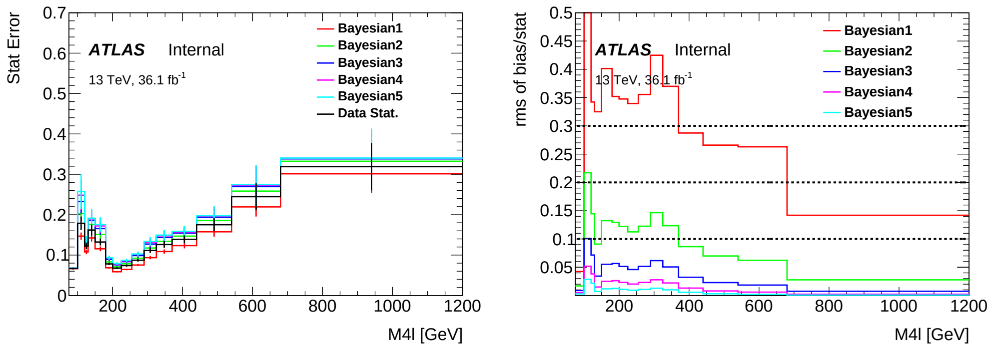

(a) (b)

Fig. 10.3 **(a) Relative statistical uncertainty and (b) bias significance for a number of unfolding methods in the 1D $m_{4\ell}$ differential distribution. The error bars displayed in (a) give the RMS variation of the statistical error across the toys. (a) additionally shows the mean bin-by-bin pseudo-data statistical uncertainty obtained as square root of the detector-level yield.**

10.2.2 Double Differential $m_{4\ell}$ - $p_{\mathrm{T}}^{4\ell}$ Distribution

When extracting the double differential $m_{4\ell}$ - $p_{\mathrm{T}}^{4\ell}$ distribution, four slices in $p_{\mathrm{T}}^{4\ell}$ are used. In each slice, the $m_{4\ell}$ bins are optimised to yield the maximum attainable granularity while still satisfying the requirements defined before. Table 10.1 lists the resulting bin locations.

Figures 10.4 depict the key unfolding metrics as well as the total expected particle- and detector-level yields for the signal processes. At low transverse momenta of the four-lepton system, the fiducial purity is the main limitation of the achievable granularity. This can be due to migration between neighbouring $m_{4\ell}$ bins (at medium masses of

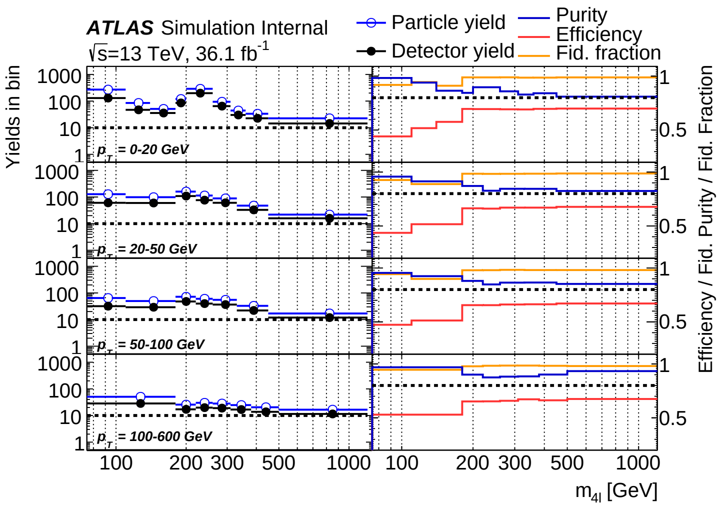

(a)

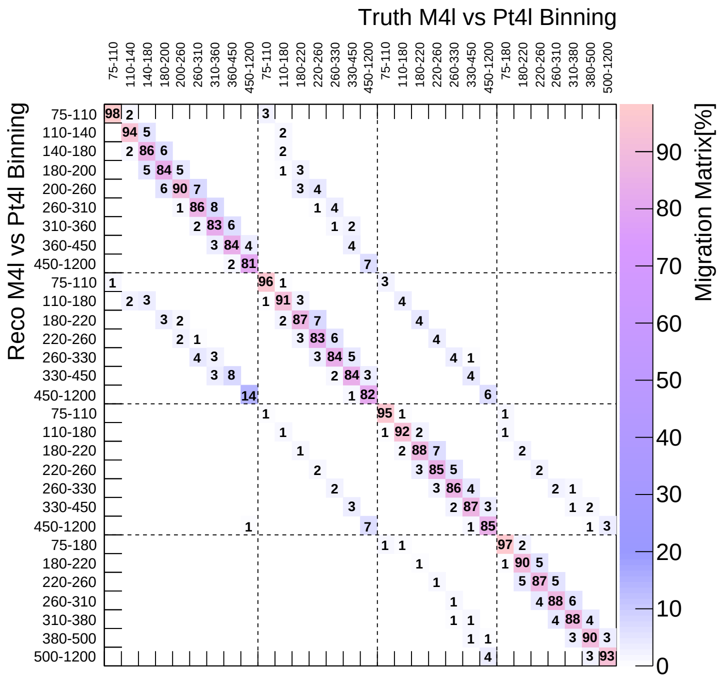

(b)

Fig. 10.4 Key unfolding metrics for the double differential $m_{4\ell}$ - $p_{\mathrm{T}}^{4\ell}$ distribution. (a) Predicted detector and particle level yields, efficiency, fiducial fraction and fiducial purity and (b) the double differential migration matrix. Dashed gray lines indicate the boundaries of slices in $p_{\mathrm{T}}^{4\ell}$.

Table 10.1 $p_{\mathrm{T}}^{4\ell}$ **bins and corresponding binning of** $m_{4\ell}$**used when extracting the two-dimensional** $p_{\mathrm{T}}^{4\ell}$**-**$m_{4\ell}$**distribution.**

$p_{\mathrm{T}}^{4\ell}$ bin [GeV]	$m_{4\ell}$ bins
0-20 GeV	[75, 110, 140, 180, 200, 260, 310, 360, 450, 1200] GeV
20-50 GeV	[75, 110, 180, 220, 260, 330, 450, 1200] GeV
50-100 GeV	[75, 110, 180, 220, 260, 330, 450, 1200] GeV
100-600 GeV	[75, 180, 220, 260, 310, 380, 500, 1200] GeV

$m_{4\ell}$ < 450GeV) or, in the final mass bin, migration between the $p_{\mathrm{T}}^{4\ell}$ slices. Starting with $p_{\mathrm{T}}^{4\ell} > 50$ GeV, the lowest and highest mass bins become limited by the achievable detector-level yields. Migrations mainly occur between $m_{4\ell}$ bins. The fiducial fraction is observed to decrease for low $m_{4\ell}$ due to the same reasons described earlier. The reconstruction efficiency within a $p_{\mathrm{T}}^{4\ell}$ slice shows the same behavior as discussed for the differential $m_{4\ell}$ measurement. The variation in $p_{\mathrm{T}}^{4\ell}$ is very limited.

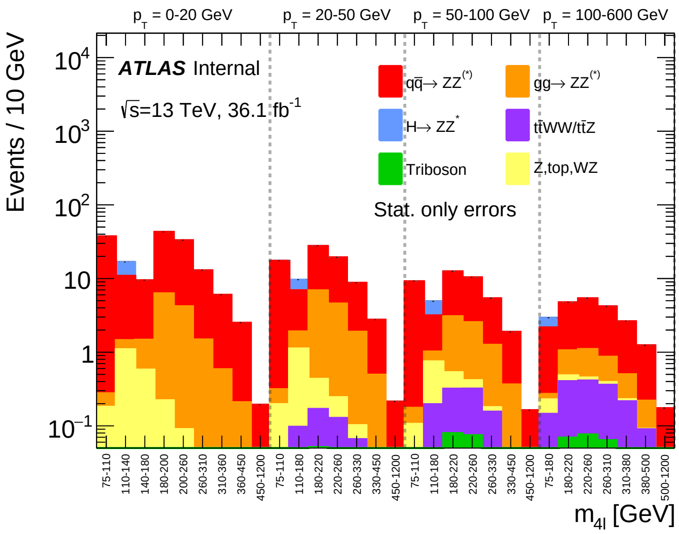

Fig. 10.5 **Predicted detector-level yields for the double differential** $m_{4\ell}$ **-** $p_{\mathrm{T}}^{4\ell}$ **lineshape measurement, after the full event selection. Dashed gray lines indicate the boundaries of slices in** $p_{\mathrm{T}}^{4\ell}$**.**

Figure 10.5 presents the composition of the predicted detector-level yield for the double differential $m_{4\ell}$ - $p_{\mathrm{T}}^{4\ell}$ measurement. The role of irreducible background processes is observed to increase with $p_{\mathrm{T}}^{4\ell}$. The relative contributions of the quark- and gluon-initiated ZZ production processes also varies with the four-lepton momentum. For the two medium $p_{\mathrm{T}}^{4\ell}$ slices, ggZZ contribution of up to 24% of the total yield are observed, with an admixture of above 15% into the far tails of the $m_{4\ell}$ spectrum for the third slice. Meanwhile, the first and the last slice feature a smaller ggZZ contribution of less than 15%, while especially the lowest $p_{\mathrm{T}}^{4\ell}$ slice is highly enriched in qqZZ. Since theory predictions ggZZ + 0,1 jets are only available at leading order precision, and any additional emission is provided by the parton shower, this measurement provides an interesting experimental constraint to the recoil behavior in ggZZ events.

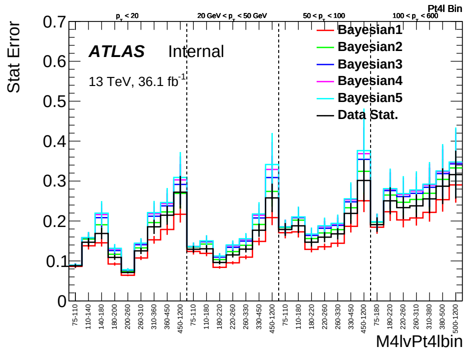

(a)

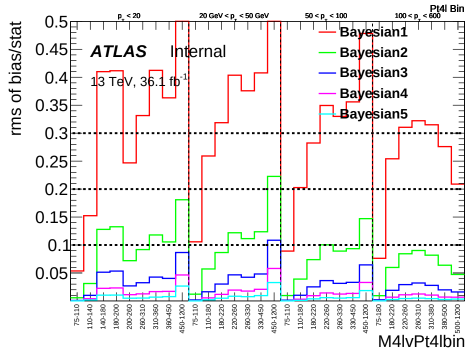

(b)

Fig. 10.6 (a) Relative statistical uncertainty and (b) bias significance for a number of unfolding methods in the double differential $m_{4\ell}$ - $p_{\mathrm{T}}^{4\ell}$ distribution. The error bars displayed in (a) give the RMS variation of the statistical error across the toys. (a) additionally shows the mean bin-by-bin pseudo-data statistical uncertainty obtained as square root of the detector-level yield.

Figure 10.6 depicts the mean statistical uncertainty and the RMS bias significance defined in Section 10.1.3 for the double differential $m_{4\ell}$ - $p_{\mathrm{T}}^{4\ell}$ measurement. With two Bayesian iterations, the required factor 5 suppression of the bias compared to the statistical error is achieved for all but one bin, and in that bin the suppression is very close to the target value. This is acceptable and two iterations are used to unfold this distribution.

10.2.3 Double Differential $m_{4\ell}$ - $y_{4\ell}$ Distribution

When extracting the double differential $m_{4\ell}$ - $y_{4\ell}$ distribution, four slices in the absolute value of $y_{4\ell}$ are used. Again, the $m_{4\ell}$ bins in each slice are optimized to yield the

Table 10.2 $p_{\mathrm{T}}^{4\ell}$ bins and corresponding binning of $m_{4\ell}$used when extracting the two-dimensional $p_{\mathrm{T}}^{4\ell}$-$y_{4\ell}$distribution.

Rapidity interval in $\lvert y_{4l}\rvert$	$m_{4\ell}$bin edge locations [GeV]
0 - 0.4	[75, 110, 140, 180, 220, 260, 310, 380, 500, 1200]
0.4 - 0.8	[75, 110, 140, 180, 220, 260, 310, 380, 480, 1200]
0.8 - 1.2	[75, 110, 140, 180, 220, 260, 330, 440, 1200]
1.2 - 3	[75, 110, 140, 180, 220, 260, 310, 400, 1200]

maximum attainable granularity while still satisfying the requirements defined before. Table 10.2 lists the resulting bin locations.

Figures 10.7 depict the unfolding metrics as well as the total expected particle-and detector-level yields for the signal processes. Bin migrations are well under control, yielding high fiducial purities. In the optimization, an effort was made to ensure a smooth variation of the predicted detector-level bin contents (and hence the expected statistical uncertainties) between adjacent bins. The highest-mass bin boundaries are determined by the available detector-level events. Migrations primarily take place between adjacent $m_{4\ell}$ bins within a given rapidity slice. The fiducial fraction shows the same mass-dependent behavior discussed previously. The reconstruction efficiency is observed to decrease with $|y_{4\ell}|$. This is due to lepton reconstruction in the forward region.

Figure 10.8 presents the composition of the predicted detector-level yield for the double differential $m_{4\ell}$ - $y_{4\ell}$ measurement. The relative fraction of ggZZ in the sample decreases with increasing $|y_{4\ell}|$. Comparison to Figure 10.5 shows that this measurement is less sensitive to the ggZZ admixture than the $m_{4\ell} - p_{\mathrm{T}}^{4\ell}$ measurement. However, a more reliable MC modelling of this behavior is expected with the available simulations compared to $m_{4\ell} - p_{\mathrm{T}}^{4\ell}$, making this distribution a candidate for extracting a ggZZ signal strength parameter. The irreducible background also shows a preference for low $|y_{4\ell}|$ values.

Finally, Figure 10.9 depicts the mean statistical uncertainty and the RMS bias significance defined in Section 10.1.3 for this measurement. Due to the observed high fiducial purity, rapid prior convergence is observed, and the required factor 5 suppression of residual biases compared to the statistical error is significantly surpassed already using two unfolding iterations, making this the obvious choice for this measurement. Even with the high purity, a single iteration is not feasible and two iteration is used.

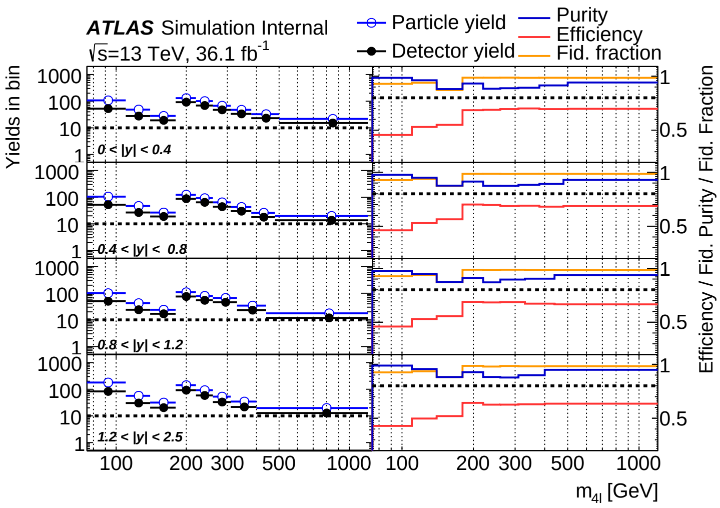

(a)

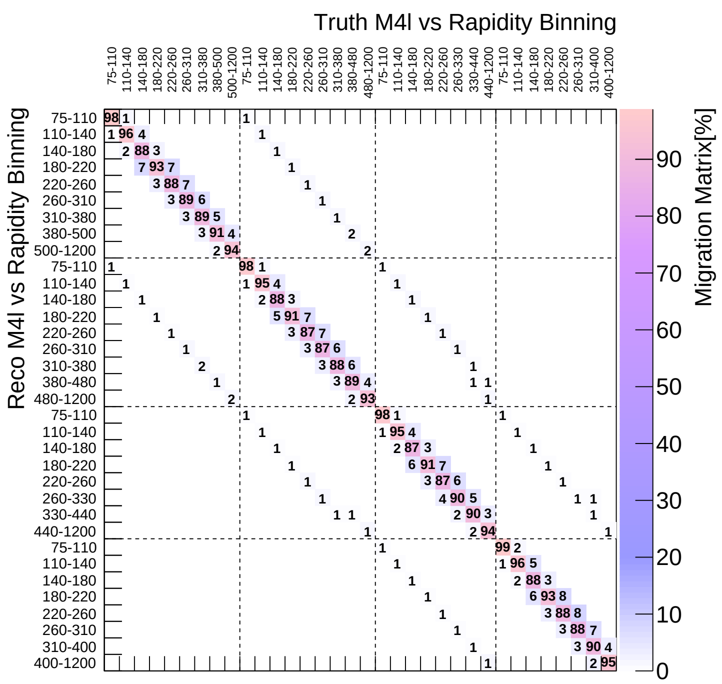

(b)

Fig. 10.7 **Key unfolding metrics for the double differential $m_{4\ell}$ - $y_{4\ell}$ lineshape measurement. (a) Predicted detector and particle level yields, efficiency, fiducial fraction and fiducial purity and (b) the double differential migration matrix. Dashed gray lines indicate the boundaries of slices in $y_{4\ell}$.**

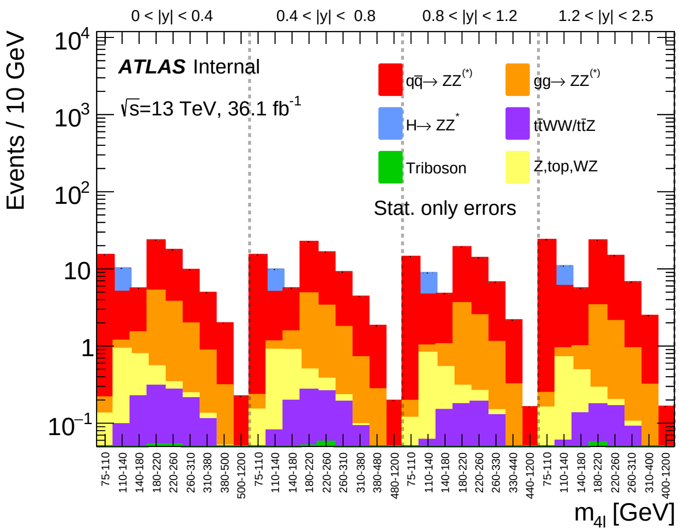

Fig. 10.8 **Predicted detector-level yields for the double differential $m_{4\ell}$ - $y_{4\ell}$ lineshape measurement, after the full event selection. Dashed gray lines indicate the boundaries of slices in $|y_{4\ell}|$.**

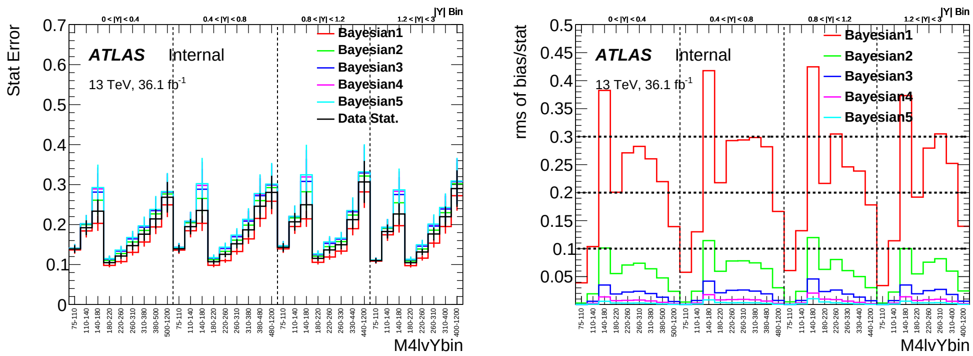

(a) **(b)**

Fig. 10.9 **(a) Relative statistical uncertainty and (b) bias significance for a number of unfolding methods in the double differential $m_{4\ell}$ - $y_{4\ell}$ distribution. The error bars displayed in (a) give the RMS variation of the statistical error across the toys. (a) additionally shows the mean bin-by-bin pseudo-data statistical uncertainty obtained as square root of the detector-level yield.**

10.2.4 Double Differential $m_{4\ell}$ - MELA Distribution

10.2.4.1 Matrix Element Discriminant

The matrix element discriminant used for this analysis is defined as

$$\mathrm{MELA} = \log_{10} \frac{\tilde{M}^2_{gg\to H^{(*)}\to ZZ^{(*)}\to 4\ell}\left(p^{\mu}_{1,2,3,4}\right)}{\tilde{M}^2_{gg(\to H^{(*)})\to ZZ^{(*)}\to 4\ell}\left(p^{\mu}_{1,2,3,4}\right) + 0.1 \cdot \tilde{M}^2_{q\bar{q}\to ZZ^{(*)}\to 4\ell}\left(p^{\mu}_{1,2,3,4}\right)} \tag{10.4}$$

, with

$$\tilde{M}_X^2\left(p^{\mu}_{1,2,3,4}\right) = \frac{\mathrm{ME}_X^2\left(p^{\mu}_{1,2,3,4}\right)}{\left\langle \mathrm{ME}_X^2 \right\rangle \left(m_{4\ell}\right)}, \tag{10.5}$$

where $\mathrm{ME}_X^2\left(p^{\mu}_{1,2,3,4}\right)$ indicates the squared differential matrix element for process X evaluated for the specific four-momenta and flavors of the leptons in the given event, and $\left\langle \mathrm{ME}_X^2 \right\rangle \left(m_{4\ell}\right)$ represents the *averaged* squared matrix element for process X, averaged over all events of process X in the fiducial region with the observed four-lepton invariant mass. This is a modified version of the MELA observable defined in a previous measurement of the off-shell Higgs boson signal strength [172]. By dividing out the explicit mass-dependence of the squared matrix element in this way, the correlation between the MELA observable and the four-lepton invariant mass is greatly reduced without losing separation power. The first matrix element in the denominator includes the non-Higgs box diagram, Higgs-mediated production as well as the interference of the two. A constant factor 0.1 in front of the t-channel matrix element in the denominator is chosen as roughly the contribution ratio of gg over qq in order to scale the two ME to a similar. However the variation of this parameter does not have a significant impact on the separation power of this observable. The numerator represents the s-channel matrix element involving the Higgs boson produced via gluon fusion.

The squared matrix elements are computed using MCFM 8.0. For the gluon fusion diagrams, analytical quark loop integrals account for the top and bottom quark masses. The strong coupling constant is evaluated at the scale of the four-lepton invariant mass. The Higgs boson mass is set to $m_H = 125.0$ GeV, and its width to the standard model prediction for this mass. Since only the squared matrix element values are used, no PDF information is required. The incoming parton momenta are approximated by assuming the four-lepton centre-of-mass system is produced at rest. This is done since only leading-order precision is a available for the $gg \to ZZ$ matrix element in MCFM.

Figure 10.10 shows the distribution of the MELA discriminant at particle level for events within the fiducial region of the analysis, for four slices of the invariant mass spectrum. The contribution of the s-channel Higgs boson mediated process is seen to increase towards higher values of the discriminant, indicating the sensitivity of this observable to the amount of off-shell Higgs boson production in the data.

In Equation 10.5, the mass dependence is evaluated by interpolating between the tabulated values obtained by averaging the ME^2 in bins of the mass for simulated events of the physics process under consideration, using the Sherp samples also utilized in the main analysis for qqZZ and ggZZ (SBI). For the Higgs process, the Sherpa Higgs-only

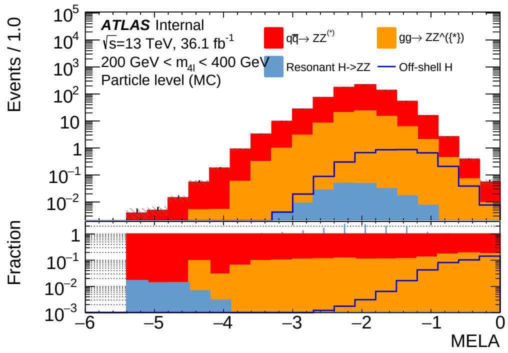

(a) 200-400 GeV

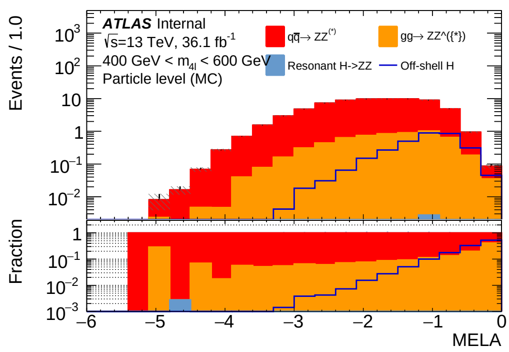

(b) 400-600 GeV

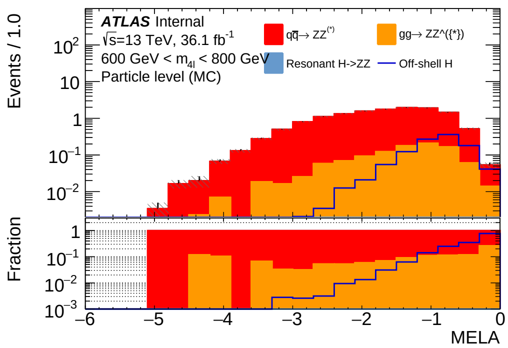

(c) 600-800 GeV

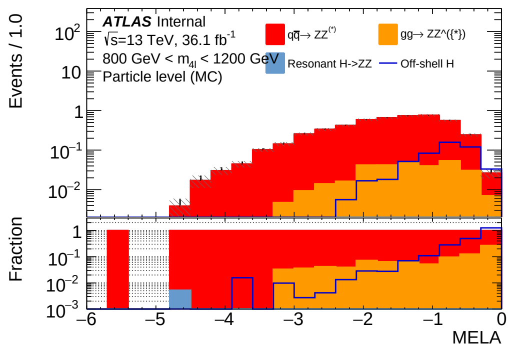

(d) 800-1200 GeV

Fig. 10.10 Distribution of the MELA discriminant at particle level after the full fiducial selection, for four slices of the invariant mass spectrum. The bottom pad indicates the fractional contributions of the various processes to the total yield. The s-channel Higgs contribution is not stacked but superimposed, since it is included in the $gg \to ZZ$ prediction. It can exceed the total predicted yield of the $gg \to ZZ$ process as the latter is affected by destructive interference between the s-channel and box diagrams.

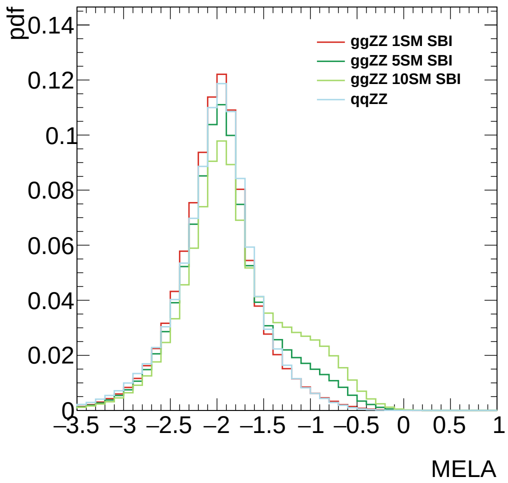

Fig. 10.11 Predicted particle density as a function of the MELA variable of events with $m_{4\ell} >$ 180 GeV after the full event selection. It is plotted for the SM qqZZ and ggZZ SBI processes assuming Higgs boson signal strength is 1, 5, and 10 times the SM prediction. The SBI process includes the off-shell Higgs signal, the SM gg continuum background and their interference.

sample is used instead of Powheg, in order to have population also above $m_{4\ell} = m_H$. The shapes are different from the $m_{4\ell}$-dependent differential cross-section as only the squared matrix elements of the hard scatter process are considered, without including the contribution of parton density functions.

10.2.4.2 Double Differential Distribution

Using the MELA discriminant defined above, a double double differential $m_{4\ell}$ - MELA distribution is measured using two slices in the MELA observable. Figure 10.11 shows the particle-level probability density function for the MELA discriminant for the ggZZ and qqZZ processes in the SM as well as for the assumptions of a factor 5 or 10 enhancement of the off-shell Higgs boson signal strength in events with $m_{4\ell}$ >180 GeV. The crossing between the distributions for nominal off-shell Higgs boson production and the scenario of an enhanced off-shell Higgs boson signal strength is observed around MELA=-1.4, motivating the use of this value to define the two MELA categories. For $m_{4\ell}$ < 180 GeV, bin migrations become large, and the processes the MELA is intended to isolate are not important in this mass range. Hence, a single bin is added to the measurement collecting all events of $m_{4\ell}$ < 180 GeV regardless of the MELA observable. The resulting set of bins is presented in Table 10.3.

Figures 10.12 depict the unfolding metrics as well as the total expected particle-and detector-level yields for the signal processes resulting from this optimization.

The population in the low MELA slice is significantly higher than for high MELA,

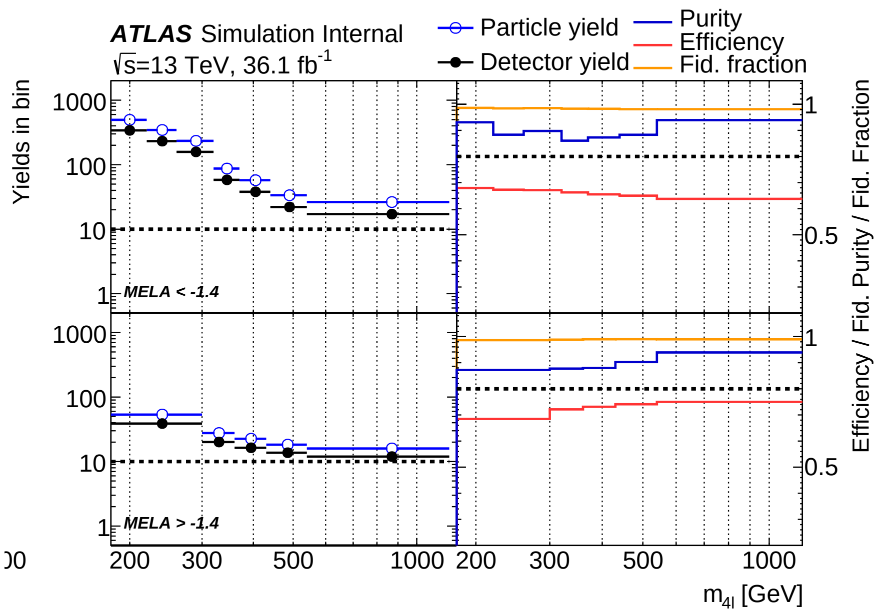

(a)

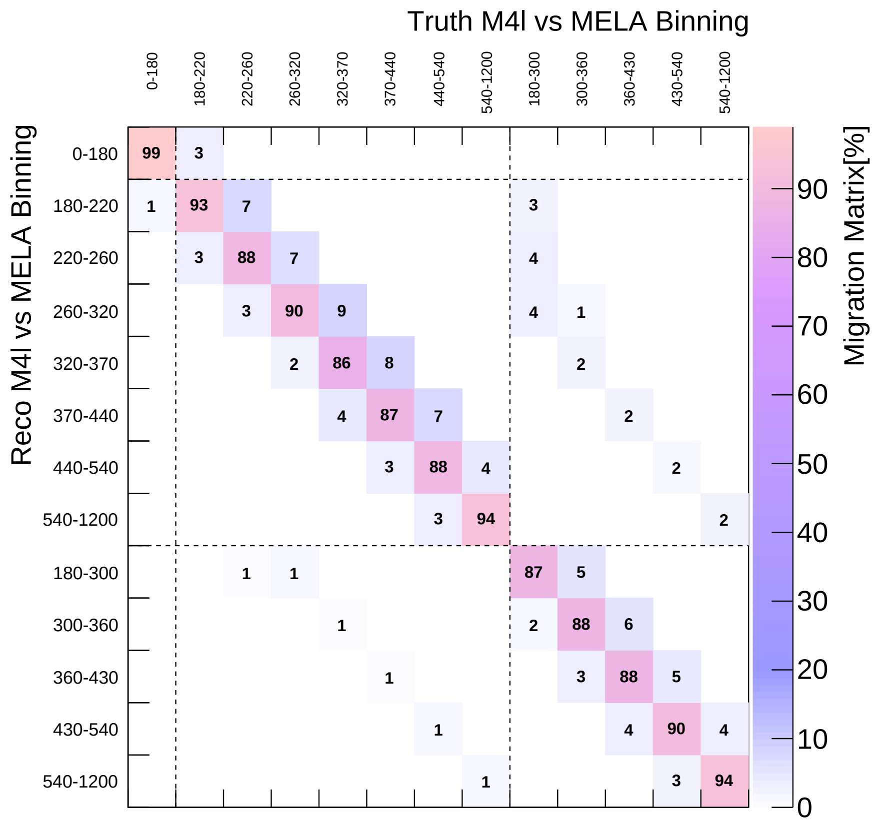

(b)

Fig. 10.12 Key unfolding metrics for the double differential $m_{4\ell}$ - MELA lineshape measurement. (a) Predicted detector and particle level yields, efficiency, fiducial fraction and fiducial purity and (b) the double differential migration matrix . Dashed gray lines indicate the boundaries of slices in the MELA observable.

Table 10.3 MELA slices and corresponding binning of $m_{4\ell}$used when extracting the two-dimensional $m_{4\ell}$-MELA distribution.

MELA interval	mass bin edge locations [GeV]
N/A	[0, 180]
< -1.4	[180, 220, 260, 320, 370, 440, 540, 1200]
> -1.4	[180, 300, 360, 430, 540, 1200]

allowing a larger number of $m_{4\ell}$ bins to be used here. Migration between the MELA slices is very limited and primarily occurs at low to medium $m_{4\ell}$. The larger migrations occur between neighboring $m_{4\ell}$ bins within one slice. The inclusive low-$m_{4\ell}$ bin shows a very high purity, isolating the remaining measurement from this phase-space region. The fiducial purity is generally high. A smooth variation of the detector-level yield and hence the statistical uncertainty as well as sufficient per-bin statistics are the main limitations for the bin placement in particular for the low-population high-MELA category. Since the MELA preferentially selects scalar-like production signatures with central leptons, a slight enhancement of the reconstruction efficiency in the high-MELA category is observed, in particular for high $m_{4\ell}$.

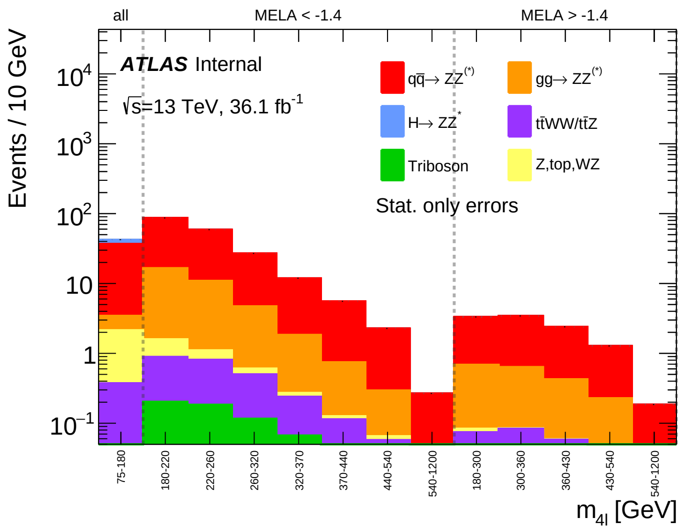

Fig. 10.13 Predicted detector-level yields for the double differential $m_{4\ell}$ - MELA lineshape measurement, after the full event selection. Dashed gray lines indicate the boundaries of slices in the MELA.

Figure 10.13 presents the composition of the predicted detector-level yield for this measurement. In Figure 10.14 the mean statistical uncertainty and the RMS bias significance are shown for a range of unfolding iterations. As for the other measurements presented in this note, two iterations present the optimum choice, with a bias suppressed

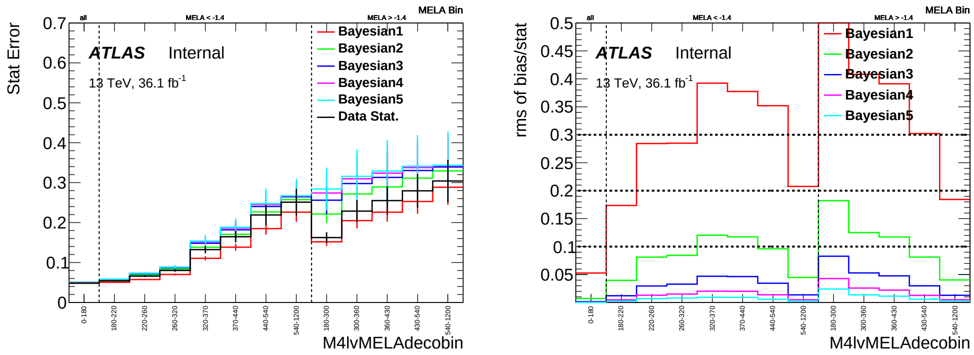

(a) (b)

Fig. 10.14 (a) Relative statistical uncertainty and (b) bias significance for a number of unfolding methods in the double differential $m_{4\ell}$ - MELA distribution. The error bars displayed in (a) give the RMS variation of the statistical error across the toys. (a) additionally shows the mean bin-by-bin pseudo-data statistical uncertainty obtained as square root of the detector-level yield.

by a factor 10 compared to the statistical uncertainty for nearly every bin. Again, the use of a single iteration is not feasible in spite of the high purity.

10.2.5 Differential $m_{4\ell}$ - Final State Lepton Flavor

Finally, a measurement of the differential $m_{4\ell}$ distribution is performed separately for each final state lepton flavor configuration.

To allow a direct comparison, the same bins are used for all channels, as indicated in Table 10.4. As shown in Figure 10.15, the number of bins is mainly limited by the available detector-level statistics for the $4e$ final state. The electron reconstruction and identification efficiency is significantly below the one of muon, with differences of up to 15% at low p_{T} decreasing to around $3-5\%$ at high p_{T} [173-174]. This results in a decrease of the efficiency with an increasing number of final-state electrons. Since electrons and muons are well separable during reconstruction, migration between the channels is negligible. Tiny nonzero channel migrations can originate from ZH production with leptonic Z boson decays. The fiducial fraction at very low masses is slightly

Table 10.4 Binning of $m_{4\ell}$used when extracting the differential $m_{4\ell}$distribution in each final state lepton flavor configuration.

Channel	$m_{4\ell}$bin edge locations [GeV]
4μ	[75,110,140, 180, 220, 260, 300, 360, 450, 1200]
$4e$	[75,110,140, 180, 220, 260, 300, 360, 450, 1200]
$2e2\mu$	[75,110,140, 180, 220, 260, 300, 360, 450, 1200]

higher for final states with muons, due to the better p_{T} resolution at very low momenta, which reduces migrations into the fiducial acceptance. In addition, the muon reconstruction efficiency degrades sharply below the kinematic threshold of 5 GeV, so that migrations from outside the fiducial region are further suppressed by efficiency effects.

Figure 10.16 presents the composition of the predicted detector-level yield. Since only the Z boson decay branching ratio determines the population of the three channels, the composition is very similar. One difference is the low-mass region, where the muon channel shows a much larger population from single-resonant Z boson production than the channels with electrons. This is due to the larger kinematic acceptance to muons ($p_{\mathrm{T}} > 5$GeV instead of 7GeV).

Figure 10.17 depicts the mean statistical uncertainty and the RMS bias significance for this measurement. As for all measurements documented in this note, two iterations represent the optimal choice, with a sufficient suppression of residual biases.

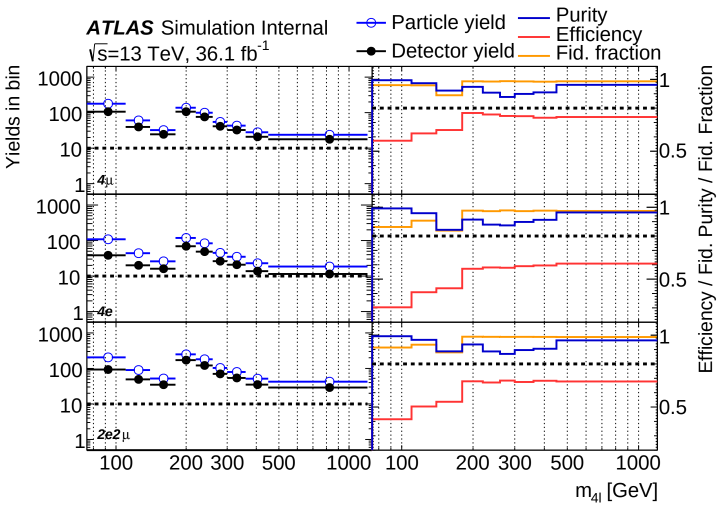

(a)

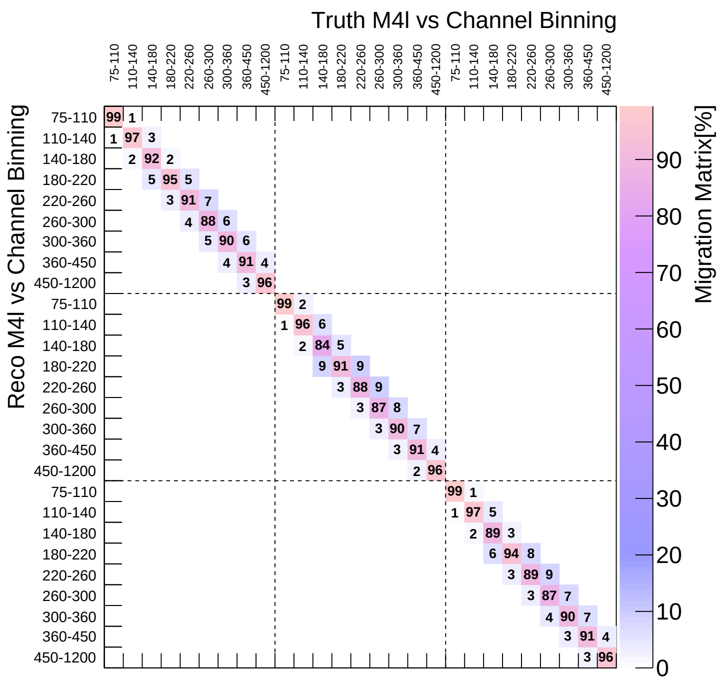

(b)

Fig. 10.15 Key unfolding metrics for the differential $m_{4\ell}$ measurement in each final state lepton flavor configuration. (a) Predicted detector and particle level yields, efficiency, fiducial fraction and fiducial purity as well as (b) the migration matrix. Dashed gray lines indicate the boundaries of slices in lepton flavor channels.

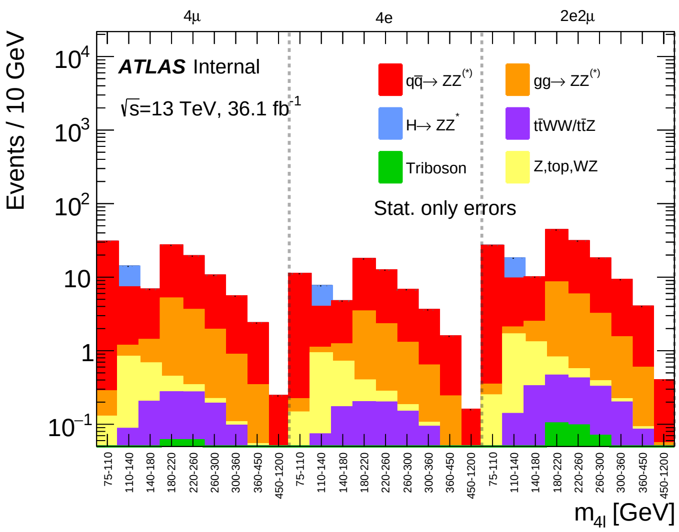

Fig. 10.16 **Predicted detector-level yields for the differential $m_{4\ell}$ measurement for each final state lepton flavor configuration, after the full event selection. Dashed gray lines indicate the boundaries of lepton flavor channels.**

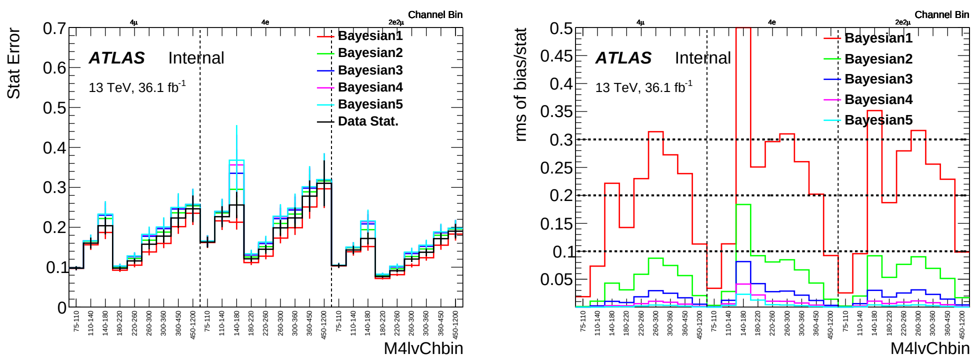

(a) (b)

Fig. 10.17 **(a) Relative statistical uncertainty and (b) bias significance for a number of unfolding methods in the differential $m_{4\ell}$ measurement in each final state lepton flavor configuration. The error bars displayed in (a) give the RMS variation of the statistical error across the toys. (a) additionally shows the mean bin-by-bin pseudo-data statistical uncertainty obtained as square root of the detector-level yield.**

10.3 Systematic Uncertainties

This section will talk about the systematic uncertainty considered in this analysis. They can generally be separated into two components:

1. the variations that enter the covariance matrix. Those are the ones that either changes *response matrix* (see Section 10.1.2) and therefore changes the unfolding results or the ones that is evaluated and added in the covariance matrix. This one includes uncertainties from experimental, theoretical sources.
2. The theoretical uncertainties that are parametrized on the fiducial prediction in

interpretations.

The experimental uncertainties include the lepton reconstruction, identification, isolation and trigger efficiencies, muon Track-to-Vertex-Association (TTVA) as well as the energy and momentum scales and resolutions, and the uncertainty on the pile-up reweighting.

The reducible non-prompt background have minimal contribution in the whole spectrum, mainly concentrating at low $m_{4\ell}$regions due to the relatively low p_{T} of leptons from the region. The related systematic uncertainties are thus small and is around 1 2%. The Monte-Carlo statistical uncertainty is also included but have minor effect.

The luminosity uncertainty for 2015+2016 data is 2.1%, which is applied to the covariance after the unfolding is derived. This is because luminosity variation is homogeneous and will modify the response matrix.

The unfolding systematics related to the unfolding method itself is estimated via the residual non-closure observed in the data-driven closure test described in Section 10.3.1.

The theoretical uncertainties plays a large role compared to other uncertainties. The largest source comes from QCD scale uncertainties for qqZZ and ggZZ processes. The qqZZ uses the envelope of 7-point variation similar to the one described in the *coupling analysis*. The ggZZ QCD scale uncertainty is evaluated using the variation of the $m_{4\ell}$-differential NLO k-factor. Those evaluation enters in both the covariance and the prediction parametrization. Additionally, for ggZZ process, a 7-point QCD scale variation is evaluated but only the acceptance variation is considered to avoid over-estimation. This additional uncertainty has smaller impact and is applied on covariance matrix.

The PDF uncertainties for Sherpa qq and gg to ZZ processes are evaluated with the standard receipt of NNPDF3.0 set with an ensemble of 100 varied PDFs where the RMS is taken as variation. Then it is combined with MMHT 2014 and CT14 NNLO PDF sets. Similar to QCD scale, only the acceptance is considered for ggZZ.

For both ggZZ and qqZZ, parton shower modeling uncertainties are derived using the internal Sherpa tune: CKKW matching scale, resummation scale as well as a different parton shower recoil scheme. Similarly, only the acceptance is considered for ggZZ.

A generator uncertainty is calculated by comparing the results of the unfolding when using Powheg + Pythia8 samples for the qqZZ processes rather than the nominal Sherpa samples. This is sensitive to differences in the modeling, for example the FSR modeling which motivate the dressing cone of truth FSR size as $\Delta R = 0.005$.

In the interpretation step presented in Section 10.4.2, the effect of the theoretical uncertainties is split into two components for each source: a normalization component and a shape component. The shape component varies the differential shapes but keeps the total normalization intact, while the normalization component absorbs the normalization changes. They are conservatively implemented as independent nuisance parameters.

Table 10.5 is a breakdown of the the uncertainties in different mass region, at the detector level. Figures 10.18 to 10.20 shows the contributions of uncertainty from the leading sources in each of the distributions for the unfolded measurement. Only the leading uncertainty sources are shown in the figures, and the statistical and total uncertainty are both included. The figures show the addition of the total uncertainty as various sources are added iteratively in the stacked histogram.

From the figures it can be seen that this analysis is still statistically limited.

Table 10.5 Relative systematic uncertainties on the total predicted detector-level yield, inclusive and for three consecutive intervals in $m_{4\ell}$.

	Uncertainty [%]				
Source	Inclusive	$m_{4\ell}$ interval [GeV]			
		75 – 100	100 – 180	180 – 290	290 – 1200
Electron ID	0.9	1.7	1.2	0.7	0.8
Electron Iso	0.4	0.7	0.5	0.1	0.5
Electron Reco	0.9	1.8	1.3	0.6	0.7
Electron Resolution & Scale	0.3	1.1	0.1	0.1	0.5
Muon Iso	0.7	2.1	1.9	2.1	2.1
Muon Reco	0.7	1.6	0.9	0.5	0.5
Muon Resolution & Scale	0.1	0.9	0.7	0.7	0.6
Muon TTVA	0.5	0.3	0.2	0.1	0.2
Pile-up	0.9	0.6	0.4	0.4	0.5
Reducible	0.2	1.5	1.5	0.6	0.6
Luminosity	2.1	0.1	1.2	0.1	0.1
Theory	5.9	6.6	4.1	5.7	7.8

10.3.1 Data-driven Closure Test

The recommended procedure to estimate the uncertainty due to prediction and method bias in the unfolding involves a data-driven closure test. This also validates the unfolding method chosen. In this section the closure test result of $m_{4\ell}$ and $m_{4\ell}$ - MELA distributions are described as an example.

The MC is reweighted at truth-level using a smooth function which is derived by fitting on the ratio of data over reco-prediction to produce effective ‘pseudo-data’. In our analysis, the double differential distributions require a separate function to fit the ratio of data over prediction in each slice of the second variable. The functions used can be found in Figures 10.21 and 10.22. At the ends of the spectra it is sometimes necessary to 'fix' the fit values to avoid fluctuations which is visible as an additional red line in the plots. In Figures 10.23 the resulting reweighted reconstruction-level MC is compared to data and the original unweighted reconstruction-level MC. The reweighted MC should show better agreement with the data overall, apart from statistical fluctuations, and this appears to be true, so the functions used are adequate. The next step is to unfold the reweighted reconstruction-level MC using the response matrix from the unweighted MC, and compare the unfolded result to the reweighted truth MC. The difference between the two gives the systematic uncertainty for this source, and is shown per-bin for each distribution in Figures 10.24. In the majority of bins this difference is very small, validating the two iterations of Bayesian unfolding which were selected as a result of optimization.

The relative difference is applied finally as a source of systematic uncertainty.

10.4 Results

10.4.1 Unfolded Spectra

Comparison of the SM expectation and the observed data for each of the variables measured are shown in Figures 10.25 to 10.27. The data generally agrees well with the prediction. These results are then unfolded as described in Section 10.1.1 to give the distributions of observed data compared to SM prediction at particle level in Figures 10.28 to 10.31. The nominal prediction from Sherpa 2.2.2 agrees well in general with the alternative prediction from Powheg + Pythia. A fixed-order MATRIX inclusive prediction for $ZZ^* \rightarrow 4\ell$ containing LO $gg \rightarrow ZZ^*$ is also shown on the plot. The MATRIX prediction falls short in regions below 180 GeV, mainly because the missing photon emission effect [175]. Besides, the other two prediction contains higher order correction that enhances the yield which MATRIX doesn't have. But generally MATRIX provides an reasonable prediction for the comparison.

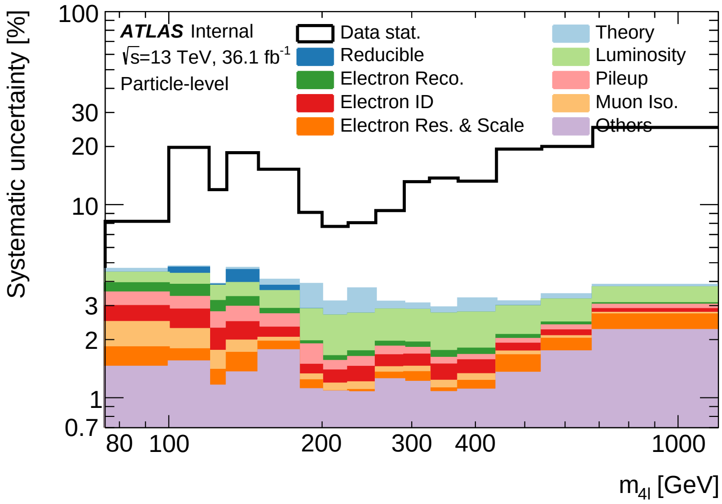

(a) $m_{4\ell}$

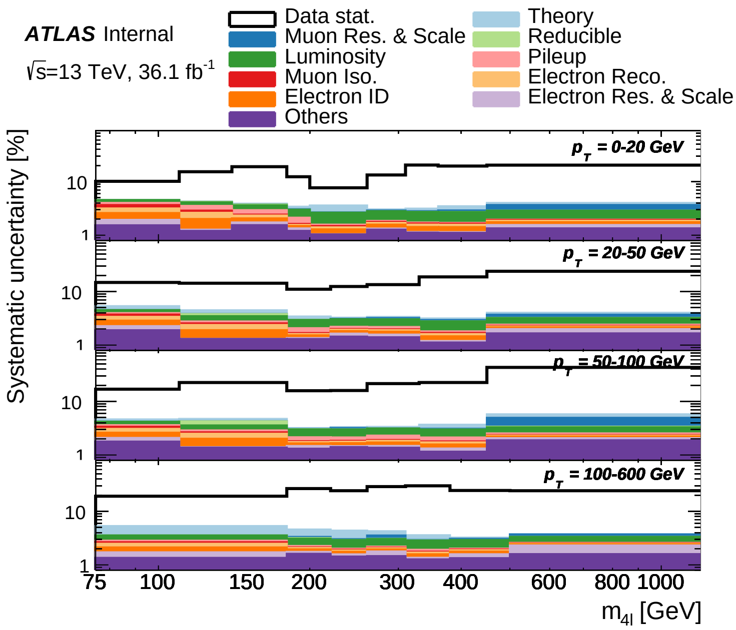

(b) $m_{4\ell}$- $p_{\mathrm{T}}^{4\ell}$

Fig. 10.18 **Evolution of the percentage error in the unfolded cross section for two of the differential distributions used when adding in quadrature each of the leading systematic uncertainty sources. The filled areas for each uncertainty source include the contribution from all sources stacked below via quadratic addition. Contributions that do not affect any bin to more than** 1.5% **are shown as "other" sources.**

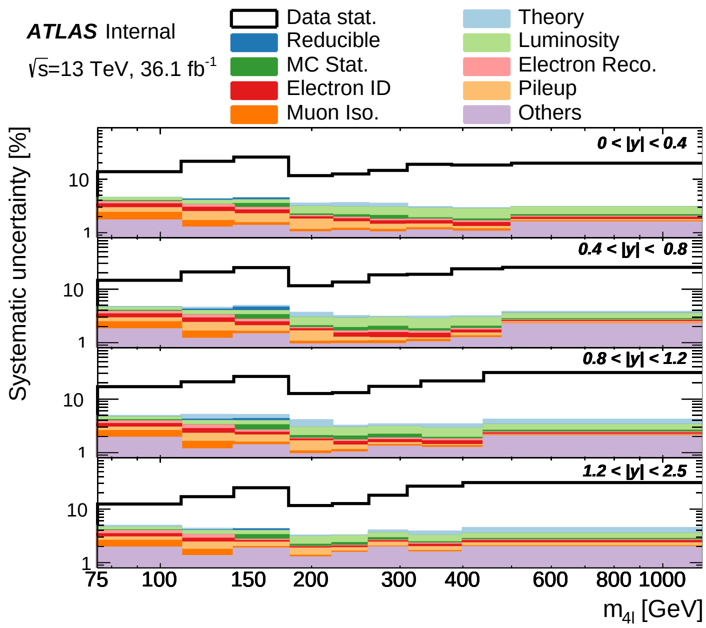

(a) $m_{4\ell}$- $y_{4\ell}$

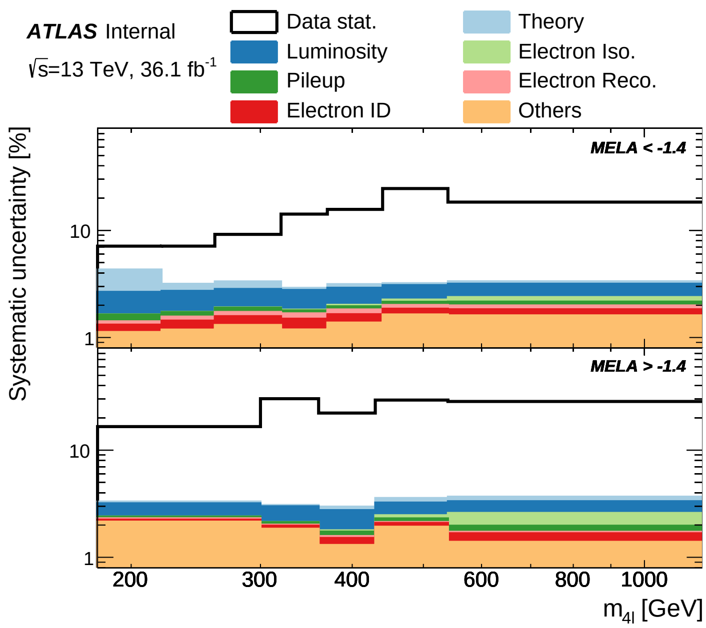

(b) $m_{4\ell}$- MELA

Fig. 10.19 **Evolution of the percentage error in the unfolded cross section for two of the differential distributions used when adding in quadrature each of the leading systematic uncertainty sources. The filled areas for each uncertainty source include the contribution from all sources stacked below via quadratic addition. Contributions that do not affect any bin to more than 1.5% are shown as "other" sources.**

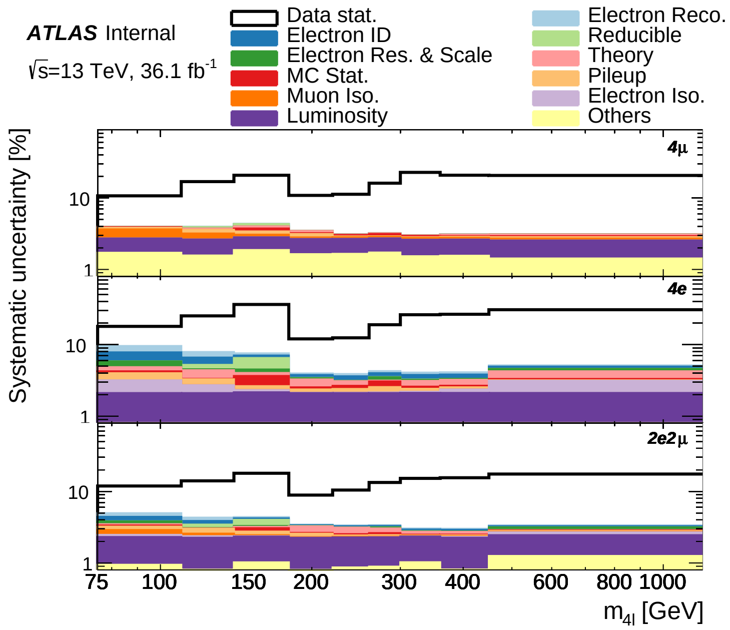

Fig. 10.20 **Evolution of the percentage error in the unfolded cross section for two of the differential distributions used when adding in quadrature each of the leading systematic uncertainty sources for 2D $m_{4\ell}$- lepton flavor distribution. The filled areas for each uncertainty source include the contribution from all sources stacked below via quadratic addition. Contributions that do not affect any bin to more than 1.5% are shown as "other" sources.**

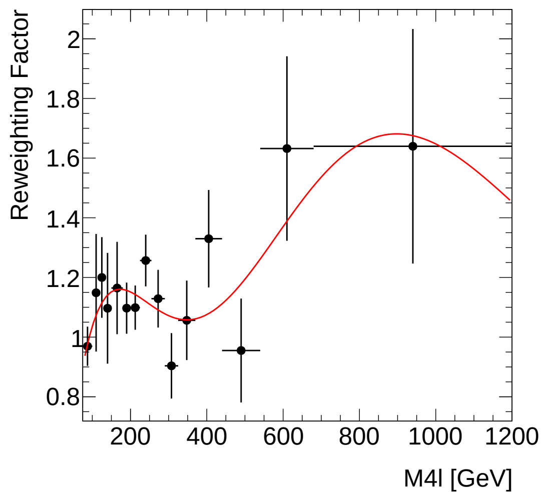

Fig. 10.21 **Smoothed function calculated using the ratio of background subtracted data to reconstructed MC for the $m_{4\ell}$distribution used in this analysis.**

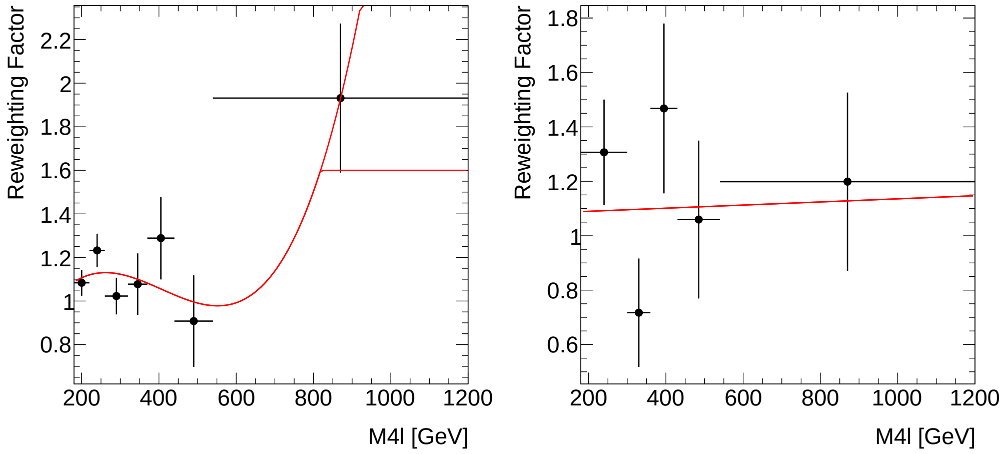

(a) MELA bin < -1.4 **(b) MELA bin > -1.4**

Fig. 10.22 Smoothed functions calculated using the ratio of background subtracted data to reconstructed MC in each of the MELA bins in the $m_{4\ell}$- MELA distribution used in this analysis.

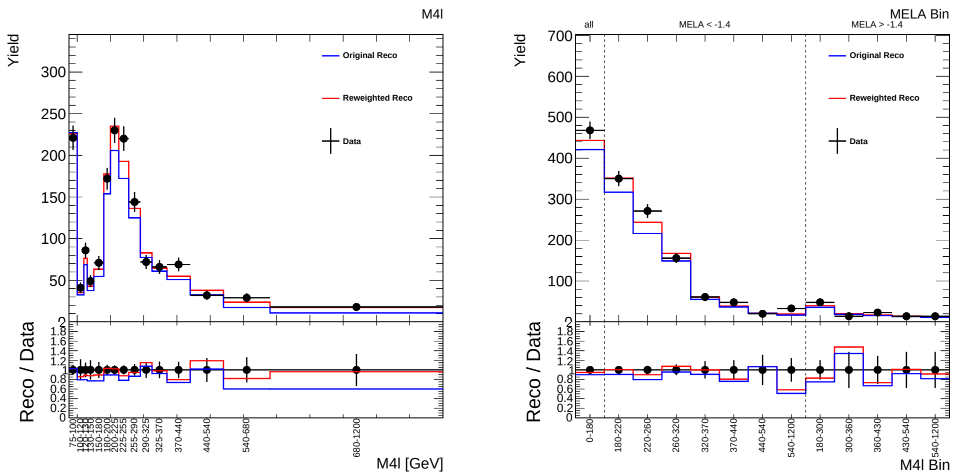

(a) $m_{4\ell}$ **(b) $m_{4\ell}$- MELA**

Fig. 10.23 Comparison of unfolded reweighted truth MC and unfolded reconstructed MC with data for two of the distributions used in this analysis. The error bars on the data give the statistical uncertainty.

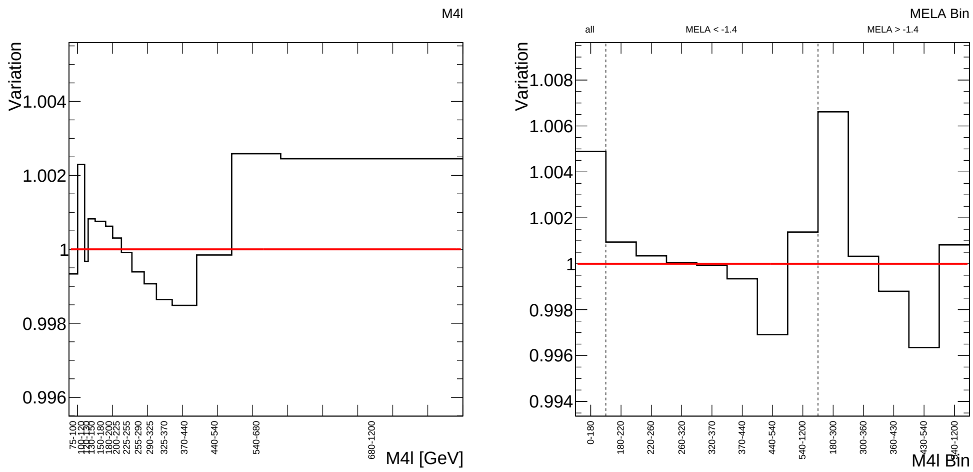

(a) $m_{4\ell}$

(b) $m_{4\ell}$**- MELA**

Fig. 10.24 Systematic uncertainty obtained by comparing unfolded reweighted detector-level MC to reweighted truth MC for two of the distributions used in this analysis.

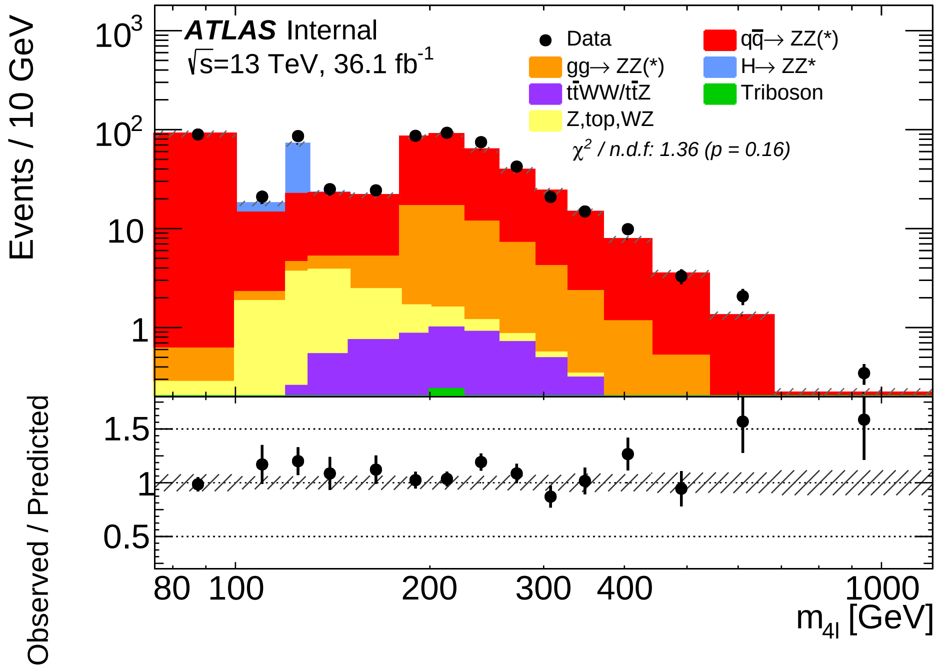

(a) inclusive $m_{4\ell}$

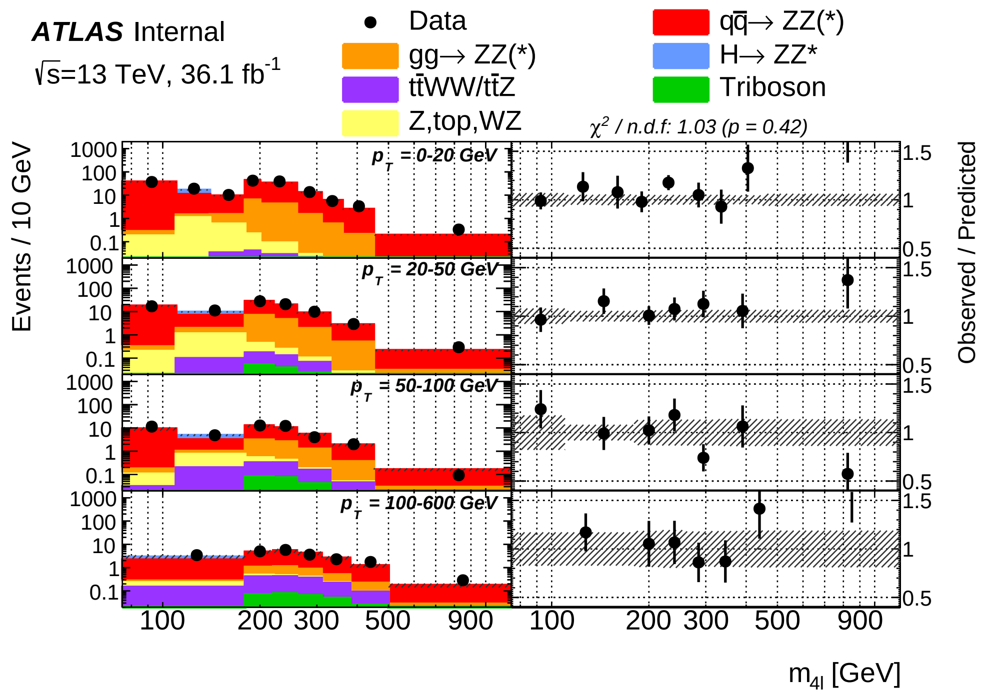

(b) double-differential $p_{\mathrm{T}}^{4\ell} - m_{4\ell}$

Fig. 10.25 Observed data compared to SM prediction for each of the considered distributions. Statistical uncertainty on the data is displayed as error bars, and the total statistical and systematic uncertainty on the SM prediction is displayed as a hashed band. The ratio of the data to MC prediction is shown in the lower panel.

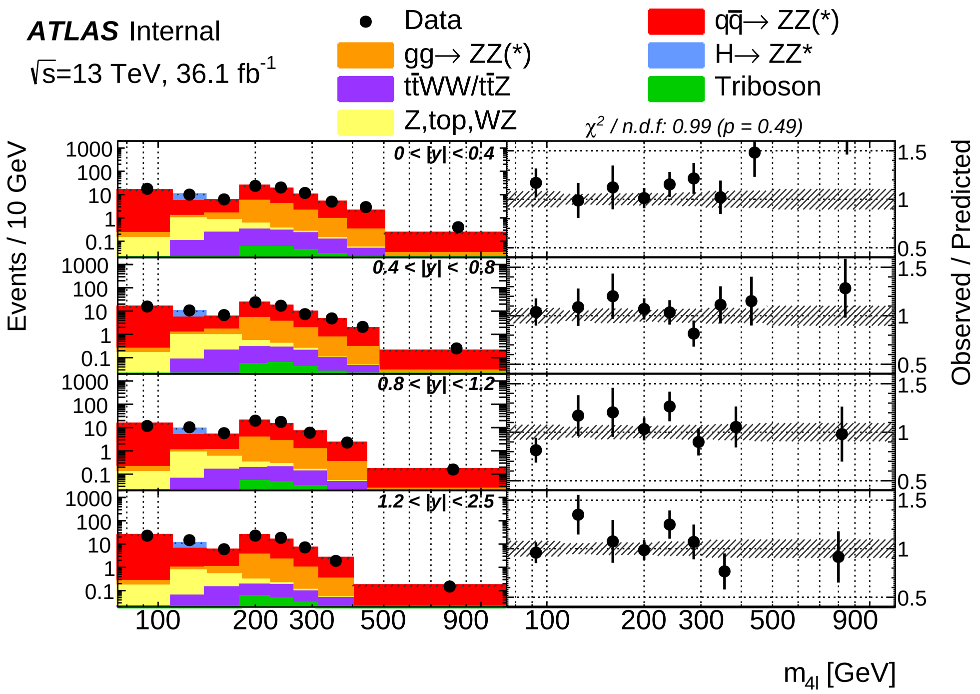

(a) double-differential $|y_{4\ell}| - m_{4\ell}$

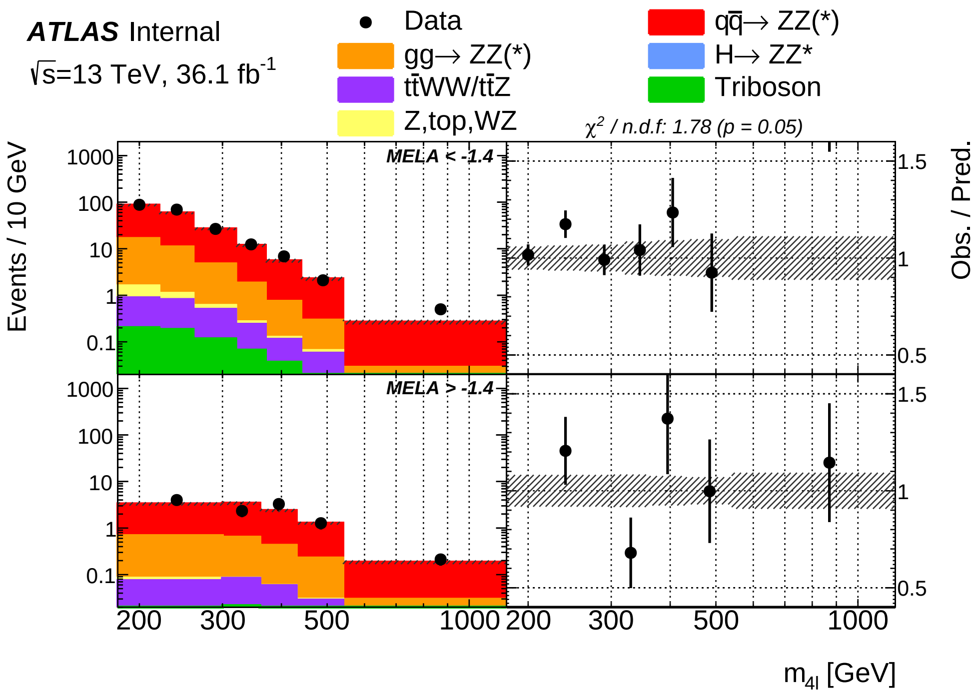

(b) double-differential MELA - $m_{4\ell}$

Fig. 10.26 **Observed data compared to SM prediction for each of the considered distributions. Statistical uncertainty on the data is displayed as error bars, and the total statistical and systematic uncertainty on the SM prediction is displayed as a hashed band. The ratio of the data to MC prediction is shown in the lower panel.**

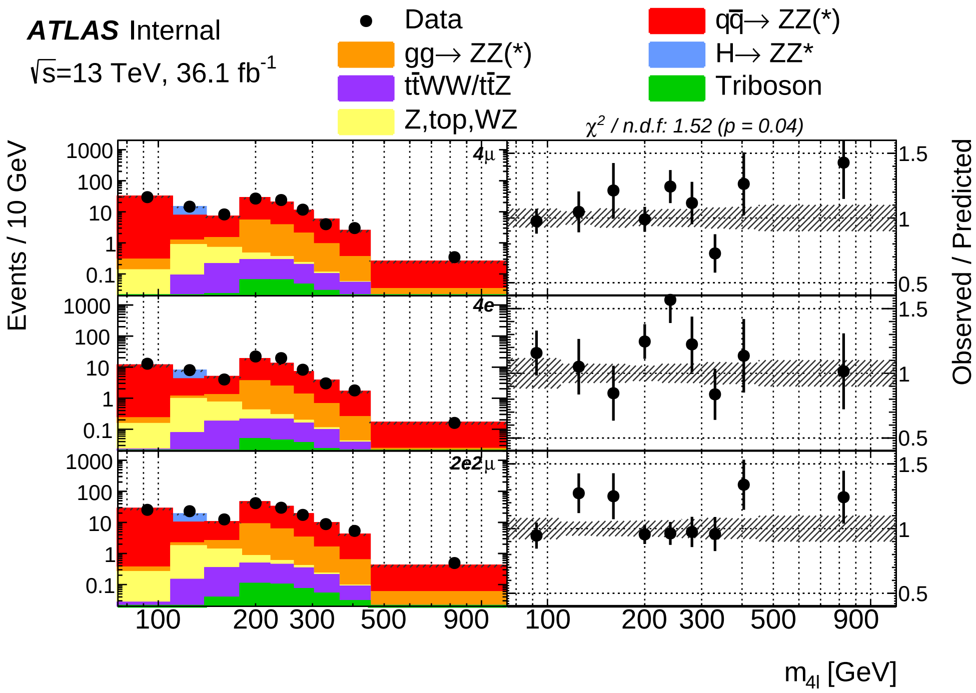

(a) $m_{4\ell}$ **per lepton flavor channel**

Fig. 10.27 Observed data compared to SM prediction for each of the considered distributions. Statistical uncertainty on the data is displayed as error bars, and the total statistical and systematic uncertainty on the SM prediction is displayed as a hashed band. The ratio of the data to MC prediction is shown in the lower panel.

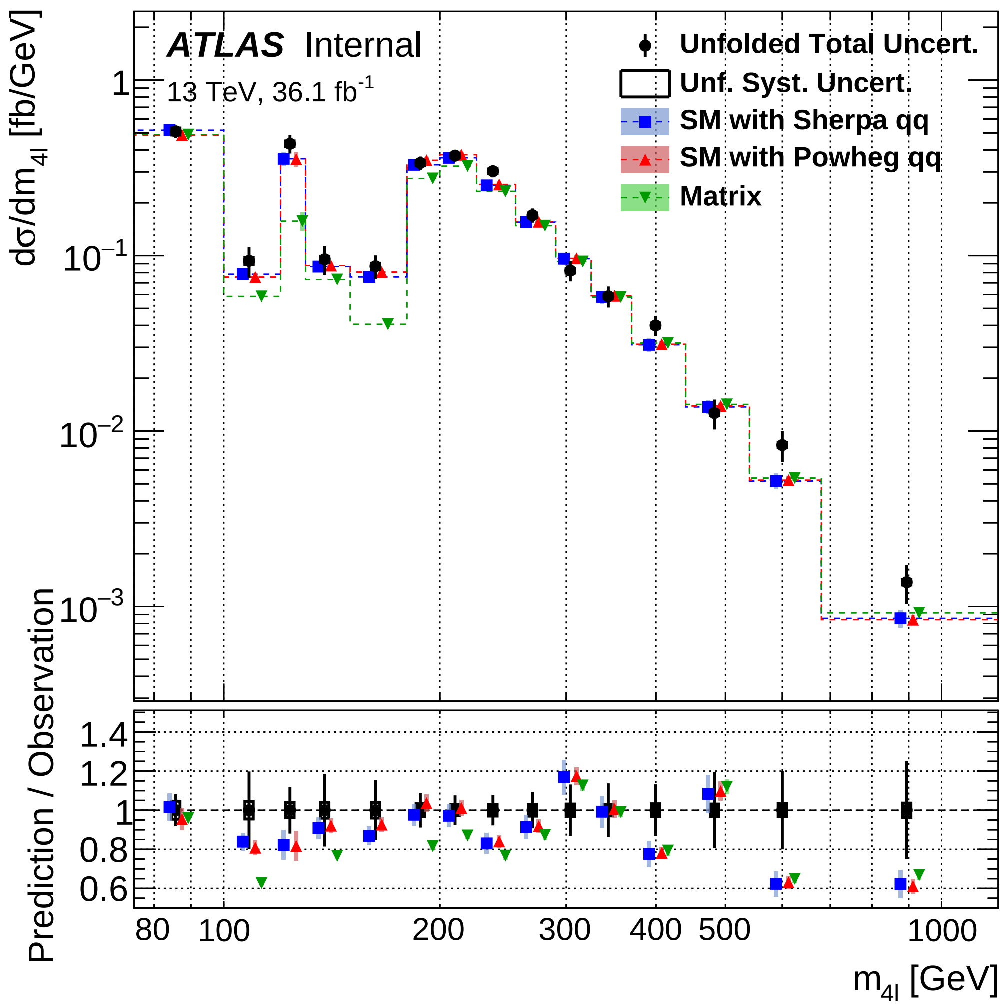

Fig. 10.28 Unfolded data compared to particle level SM prediction for $m_{4\ell}$distribution. Statistical uncertainty on the data is displayed as error bars, the systematic uncertainty from the unfolding method is displayed as a red band and the total statistical and systematic uncertainty on the particle level SM prediction is displayed as a hashed band. The ratio of the unfolded data to particle level MC prediction is shown in the lower panel in the plot.

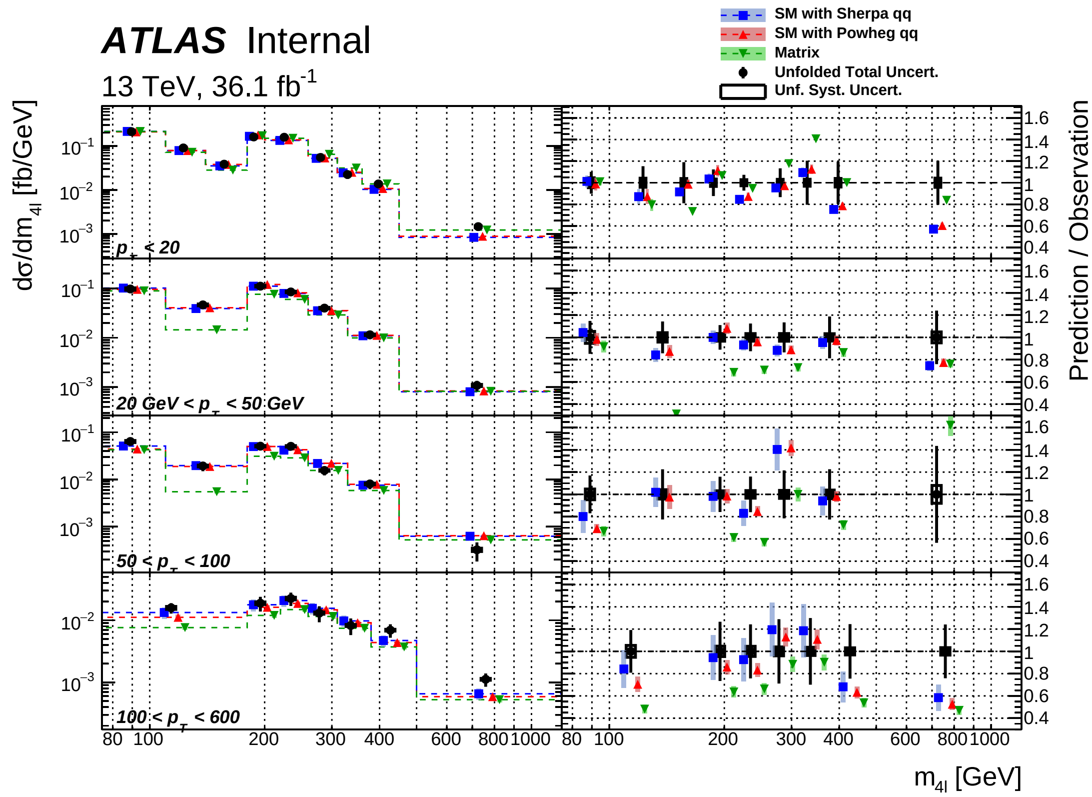

Fig. 10.29 Unfolded data compared to particle level SM prediction for $m_{4\ell}$- $p_{\mathrm{T}}^{4\ell}$ distribution. Statistical uncertainty on the data is displayed as error bars, the systematic uncertainty from the unfolding method is displayed as a red band and the total statistical and systematic uncertainty on the particle level SM prediction is displayed as a hashed band. The ratio of the unfolded data to particle level MC prediction is shown in the panels to the right for each of the double differential slices.

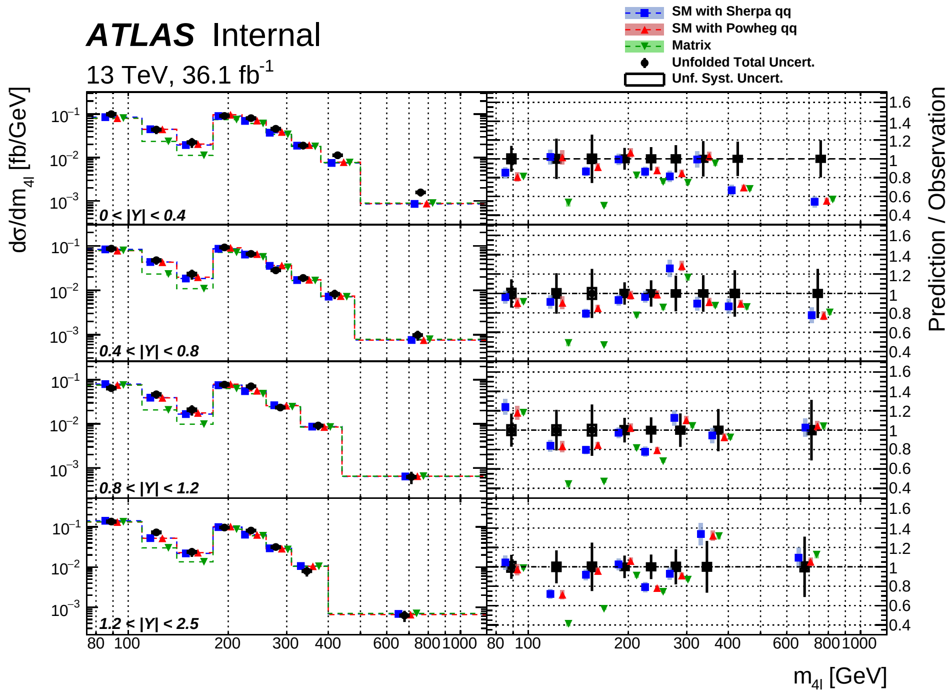

(a) 2D $m_{4\ell}$- $y_{4\ell}$

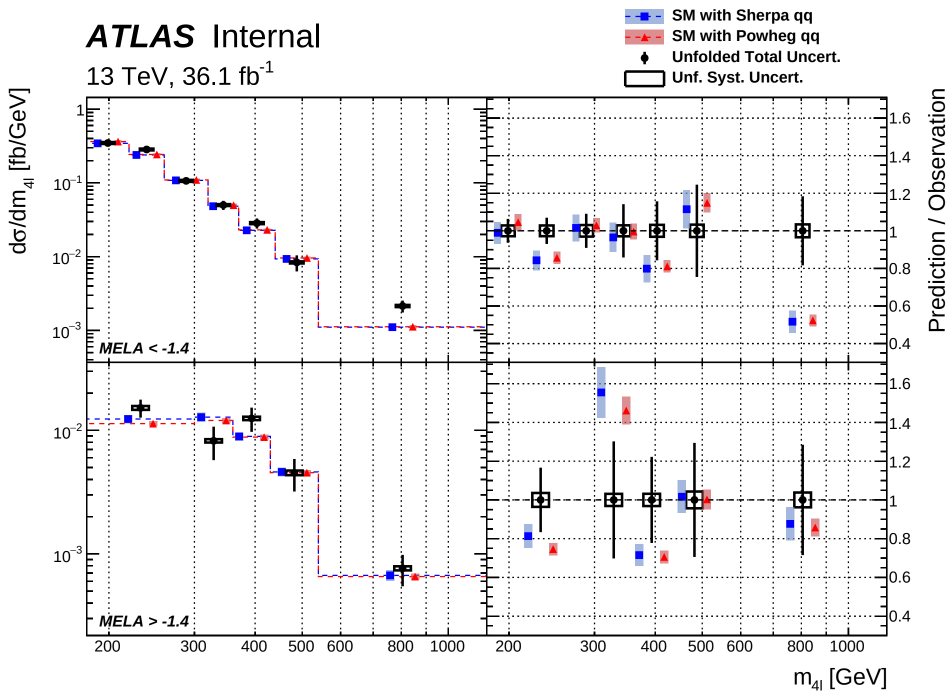

(b) 2D $m_{4\ell}$- MELA

Fig. 10.30 Unfolded data compared to particle level SM prediction for two of the considered distributions. Statistical uncertainty on the data is displayed as error bars, the systematic uncertainty from the unfolding method is displayed as a red band and the total statistical and systematic uncertainty on the particle level SM prediction is displayed as a hashed band. The ratio of the unfolded data to particle level MC prediction is shown in the panels to the right for each of the double differential slices.

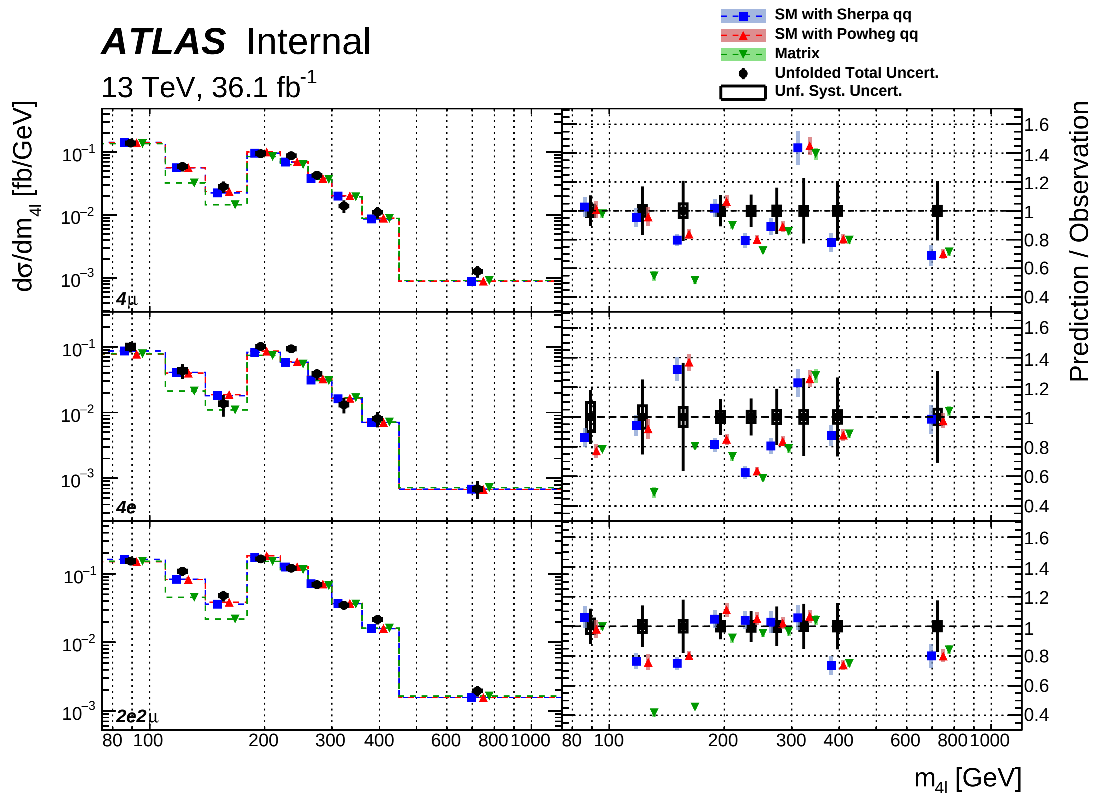

Fig. 10.31 Unfolded data compared to particle level SM prediction for $m_{4\ell}$- Lepton flavor distribution. Statistical uncertainty on the data is displayed as error bars, the systematic uncertainty from the unfolding method is displayed as a red band and the total statistical and systematic uncertainty on the particle level SM prediction is displayed as a hashed band. The ratio of the unfolded data to particle level MC prediction is shown in the panels to the right for each of the double differential slices.

10.4.2 Interpretations

The unfolded differential spectra are used to measure SM parameters and test BSM models. The test statistics used for interpreting unfolded spectrum is described in Section 8.2.4. The detailed parametrization is briefly described in each interpretation below.

10.4.2.1 $gg \to ZZ^{(*)}$ Signal Extraction

The region above 2 m_Z is the region where ggZZ process begins to show significant contribution. Signal strengths μ_{ggZZ} or μ_{ggZZ}^{LO} are extracted with best available MC from Sherpa and LO MC from MCFM, respectively. All distributions except $m_{4\ell}$ - MELA are studied using bins with $m_{4\ell} > 180$ GeV. All contribution to the $gg \to ZZ^*$ process (SBI) are considered as signal which scales linearly with μ_{ggZZ} and all other process as background.

Table 10.6 provides the expected and observed signal strength obtained from all four distributions. The sensitivity of different distributions are pretty similar, and the result from $m_{4\ell}$ is chosen as the final result for the reliability of the modeling. The measured signal strength is $\mu_{ggZZ} = 1.32 \pm 0.45$, and the LO signal strength result is $\mu_{ggZZ} = 2.68 \pm 0.94$. It should be noted that the $m_{4\ell}$ - $p_{\mathrm{T}}^{4\ell}$ distribution is known to have limitations with the modeling of the jet recoil in the $gg \to ZZ^*$ process, since only one jet is modeled at leading order matrix element level. The result can also be compared with ATLAS Run 1 LO signal strength measurement of $\mu_{ggZZ} = 2.4 \pm 1.4$ [176] with 20 fb^{-1} data. The central value is consistent and the relative uncertainty difference is around 20%, which is consistent with the luminosity difference since the analysis is statistically dominated.

The limiting factor of the measurement is that the shapes of $gg \to ZZ^*$ and $q\bar{q} \to ZZ^*$ are very similar and the limited statistics doesn't allow for further study in double differential distributions. Also the scale uncertainty of $q\bar{q} \to ZZ^*$ process also allows for a large confidence interval for the signal strength of $gg \to ZZ^*$.

Table 10.6 Expected and observed μ_{gg} and μ_{gg}^{LO} (using LO MC) values and total associated uncertainties for all distributions.

Type	μ_{ggZZ}		μ_{ggZZ}^{LO}	
Distribution	Expected	Observed	Expected	Observed
$m_{4\ell}$	$1.00^{+0.43}_{-0.43}$	$1.32^{+0.45}_{-0.45}$	$2.16^{+0.90}_{-0.91}$	$2.68^{+0.94}_{-0.93}$
$m_{4\ell}$ - $p_{\mathrm{T}}^{4\ell}$	$1.00^{+0.39}_{-0.38}$	$0.97^{+0.42}_{-0.41}$	$1.87^{+0.71}_{-0.69}$	$1.61^{+0.74}_{-0.71}$
$m_{4\ell}$-$y_{4\ell}$	$1.00^{+0.41}_{-0.41}$	$1.40^{+0.45}_{-0.44}$	$2.14^{+0.87}_{-0.85}$	$2.91^{+0.93}_{-0.90}$
$m_{4\ell}$-channel	$1.00^{+0.44}_{-0.43}$	$1.51^{+0.47}_{-0.47}$	$2.16^{+0.92}_{-0.92}$	$3.18^{+0.98}_{-0.96}$

A profiled likelihood ratio scan is used to obtain the measured μ_{gg}'s and their uncertainties for each distribution and the results are shown in Figure 10.32 and Figure 10.33.

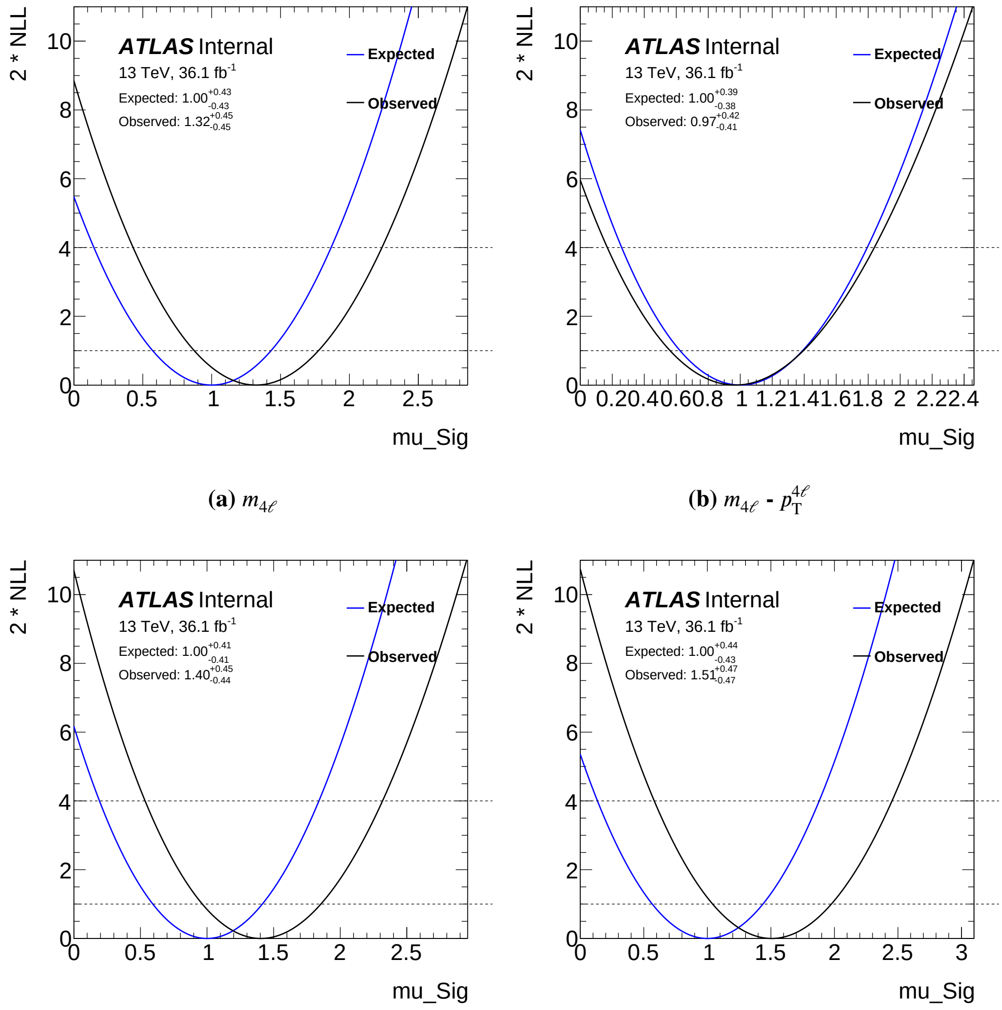

(a) $m_{4\ell}$

(b) $m_{4\ell}$ - $p_T^{4\ell}$

(c) $m_{4\ell}$ - $y_{4\ell}$

(d) $m_{4\ell}$ **- channel**

Fig. 10.32 Scans of the ggZZ signal strength for the expected and observed fits of all distributions.

10.4.2.2 Off-Shell Higgs Boson Signal Strength

The $m_{4\ell}$ >180 GeV region of the double differential $m_{4\ell}$ - MELA distribution is used to give constraint of the signal strength of off-shell Higgs production. The parametrization of different process follows the assumption of matrix element (ME) calculation: the signal process is proportional to the signal ME square, and the cross-multiplication interference term is proportional to the ME. Therefore if the signal process is proportional to off-shell Higgs boson signal strength r, the interference process is proportional to $\sqrt{r}$. The yield of inclusive $gg \to ZZ^*$ process for an assumed r can be extrapolated

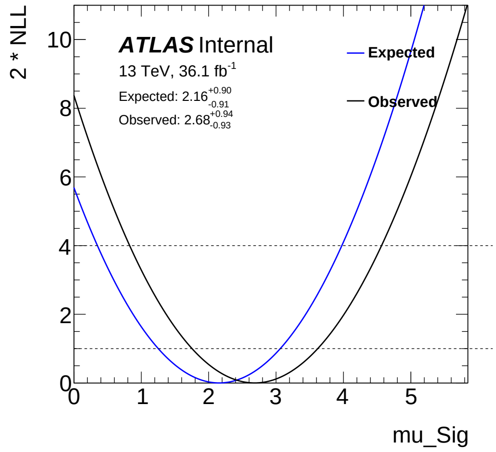

(a) $m_{4\ell}$

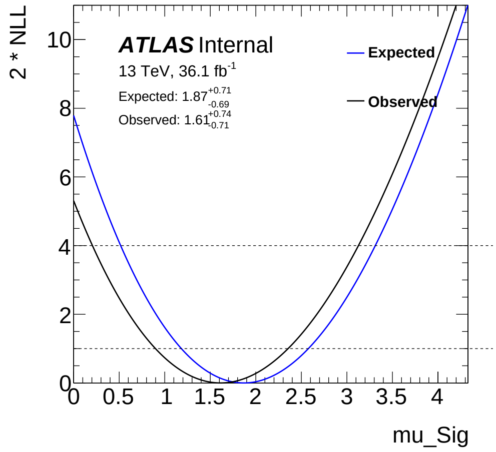

(b) $m_{4\ell}$ - $p_{\mathrm{T}}^{4\ell}$

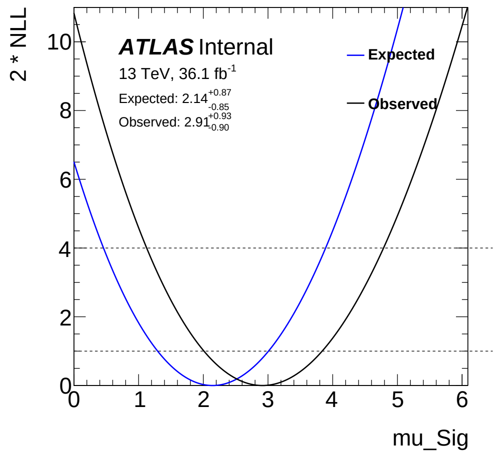

(c) $m_{4\ell}$ - $y_{4\ell}$

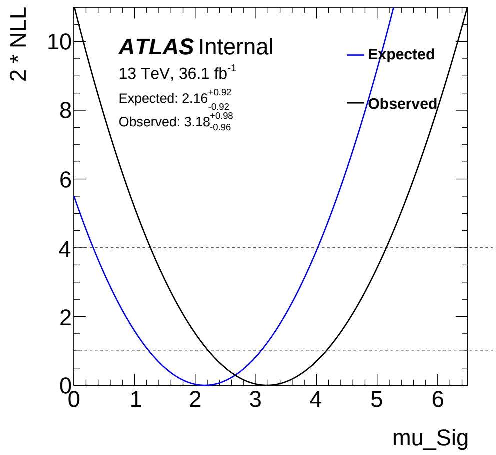

(d) $m_{4\ell}$ **- channel**

Fig. 10.33 Scans of the ggZZ signal strength (using LO MC) for the expected and observed fits of all distributions.

from the prediction for a simulated signal strength, r_0, as

$$
\begin{aligned}
gg^{SBI}(\mu) &= \mu \cdot gg^S + \sqrt{\mu} \cdot gg^I + gg^B \\
&= \mu \cdot gg^S + \sqrt{\mu} \cdot gg^I_{\mu_0}/\sqrt{\mu_0} + gg^B \\
&= \mu \cdot gg^S + \sqrt{\mu/\mu_0} \cdot (gg^{SBI}_{\mu_0} - \mu_0 \cdot gg^S - gg^B) + gg^B \\
&= gg^S(\mu - \sqrt{\mu_0 \mu}) + gg^B(1 - \sqrt{\frac{\mu}{\mu_0}}) + gg^{SBI}_{\mu_0}(\sqrt{\frac{\mu}{\mu_0}}),
\end{aligned}
\tag{10.6}
$$

where gg^{SBI} is the total number of events in the high mass region, and gg^S, gg^B, gg^I, $gg^{SBI}_{r_0}$ are the events expected from the off-shell Higgs production process (S), the quark loop ZZ production process (B) the destructive interference between the two (I) evaluated at $r = 1$ and the total including interference between the two[172], evaluated at $r = r_0$. The SBI sample used in this measurement has $r_0 = 1$. The mass-dependent k-factor is applied individually for the signal, SBI and background components.

The 95% CL expected upper limit on the off-shell Higgs signal strength is 5.43 with a range of [4.19, 7.17] for $\pm 1\sigma$ uncertainty. The observed upper 95% CL limit is measured as 6.51, which agrees within the 1σ band.

This result is more conservative compared to the upper limit result of 4.5 from Ref. [40] which is based on detector-level measurement as the unfolding procedure increases the statistical uncertainty. The use of a covariance scaling with prediction also help reduce the down-bias from Neyman's X^2. Besides, the de-correlated MELA loses some separating power compared to the original MELA, and the binning of MELA is limited to two with smaller sensitivity due to the data statistics constrain for a two-dimensional distribution.

Figure 10.34 shows the expected and observed scan of the parameter of interest, r. The scan shape shows a feature caused by a singularity in the derivative of the NLL at zero, with a positive sign. The parametrization((10.6)) determines that there are two solutions, one is positive and the other one is either a smaller positive value, or does not exist. These combined to result in this peaked shape close to zero. The expected scan shows a less prominent version of the shape visible in the observed scan, and the reconstructed analysis sees similar behavior.

10.4.2.3 $Z \to 4\ell$ Branching Ratio Extraction

The first bin of $m_{4\ell}$ distribution ranging from 75 to 100 GeV is dominated by on-shell Z production (Figure 3.5(b)). It can be used to extract the Z decay branching ratio in the targeted phase space $80 < m_{4\ell} < 100$ GeV and $m_{\ell\ell} > 4$ GeV, defined as

$$
\mathcal{B}_{Z\to 4\ell} = \frac{N_{fid} \times (1 - f_{non-res})}{\sigma_Z \times A_{fid} \times \mathcal{L}},
\tag{10.7}
$$

where N_{fid} is the number of fiducial events in the bin, the $f_{non-res}$ is the fraction of events that is t-channel (Figure 3.5(a)) and $gg \to ZZ^*$ contribution, σ_Z is single Z production cross section, A_{fid} is the acceptance, defined as ratio of events passing fiducial selection in the analysis bin over the targeted phase space defined above and $\mathcal{L}$ is the integrated luminosity. The acceptance and the non-resonant fraction is calculated from Monte Carlo simulation as $A_{fid} = (4.75 \pm 0.02)\%$ and $f_{non-res} = (4.8 \pm 0.5)\%$ respectively.

A predicted value of $\sigma_{Z\to\ell\ell} = (1.886 \pm 0.05(\text{PDF}) \pm 0.03(\text{scale}) \pm 0.03(\text{other}))$ nb [177] is extrapolated to the total cross-section using the $Z \to \ell\ell$ branching fraction of 3.3658% and a transfer factor 0.935 relating the cross-section in the $80-100$GeV window used for the branching ratio extraction to the one in the $66-116$GeV window used for the quoted value [178-179]. Alternatively, the measured value of $\sigma^{\text{meas}}_{Z\to\ell\ell} = (1.981 \pm 0.007(\text{stat}) \pm 0.038((\text{syst}) \pm 0.042(\text{lumi}))$ nb [177] can be used with the same extrapolation factors.

The branching fraction for a Z boson decaying to four leptons is measured as

$$\mathcal{B}_{Z\to 4l} = (4.93 \pm 0.33(\text{stat.}) \pm 0.20(\text{sys.}) \pm 0.15(\text{theo.}) \pm 0.10(\text{lumi})) \times 10^{-6} \quad (10.8)$$

if the expected value of the total Z production cross-section is used, and

$$\mathcal{B}_{Z\to 4l} = (4.70 \pm 0.32(\text{stat.}) \pm 0.21(\text{sys.}) \pm 0.03(\text{theo.}) \pm 0.14(\text{lumi})) \times 10^{-6} \quad (10.9)$$

if the measured cross-section is used and uncertainties are presumed to be uncorrelated, which is overly conservative.

The result is compatible with the results of $(4.31 \pm 0.34(\text{stat.}) \pm 0.17(\text{syst.})) \times 10^{-6}$ [180] and $(4.83 \pm 0.23(\text{stat.}) \pm 0.32(\text{syst.}) \pm 0.08(\text{theo.}) \pm 0.12(\text{lumi}))\times 10^{-6}$ [178] by the ATLAS and CMS collaborations, respectively.

10.4.2.4 Modified Higgs Coupling

An effective field theory is used to describe a benchmark model [181] where BSM physics modifies the Higgs couplings to the top quark (c_t) and the gluon (c_g), but leaves all other couplings unchanged with respect to the Standard Model. While the on-shell Higgs production rates are only sensitive to $|c_g^2 + c_t^2|$, the parameter's contributions to off-shell production exhibit different scaling behavior with $\sqrt{s}$, enabling this measurement to further constrain the 2D parameter space. In the Standard Model, the Higgs boson couples with a strength of 1 to the top quark, with a contribution of zero for the coupling directly to gluons. The differential cross-section for the total gluon-induced

ZZ production can be parametrized in terms of these couplings:

$$\frac{d\sigma(c_t, c_g)}{dm_{4\ell}} = F_0 + F_1\left(c_t + c_g\frac{F_\Delta(\text{inf})}{\text{Re}F_\Delta(m_t)}\right)^2 + F_3\left(c_t + c_g\frac{F_\Delta(\text{inf})}{\text{Re}F_\Delta(m_t)}\right) + F_2c_t^2 + F_4c_t \tag{10.10}$$

where F_i are $m_{4\ell}$-dependent coefficients, F_Δ is the fermion LO loop function for single Higgs production and m_t is the top mass. These coefficients can be calculated using MC samples which include the signal, background and interference with the m_T =173 GeVand the additional BSM setting of m_t =1 TeV. The parameters are related between the samples with the following equations:

$$\text{Only signal}: \ |M_h|^2 \ F_1 + F_2,$$

$$\text{Only interference}: \ |M_h + M_{bkg}|^2 - |M_h|^2 - |M_{bkg}|^2 \ F_3 + F_4,$$

$$\text{Only interfering background}: \ |M_{bkg}|^2 \ F_0,$$

$$\text{Only signal with } m_t = M \ : |M_h|^2_{m_t=M} \ F_1c_R(M)^2 + F_2c_I(M)^2,$$

$$\text{Only interference with } m_t = M \ :$$
$$|M_{h(m_t=M)} + M_{bkg}|^2 - |M_{h(m_t=M)}|^2 - |M_{bkg}|^2 \ F_3c_I(M) + F_4c_R(M).$$

The results then allow the couplings c_t and c_g to be probed. Exclusion limits are set in 2D planes of the varied parameters. Bins with $m_{4\ell}$ >200 GeVin the $m_{4\ell}$ distribution are used in this interpretation. Figure 10.35 shows the expected and observed 95% CL exclusion contours set on values of c_t and c_g using CL$_s$ method.

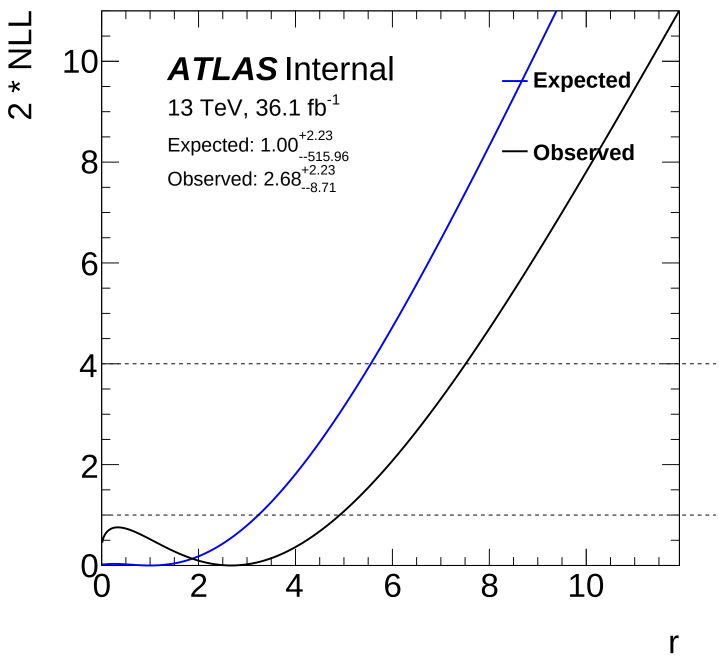

Fig. 10.34 The scan of the off-shell Higgs strength, r. The blue line is the expected curve and the black line is the observed curve.

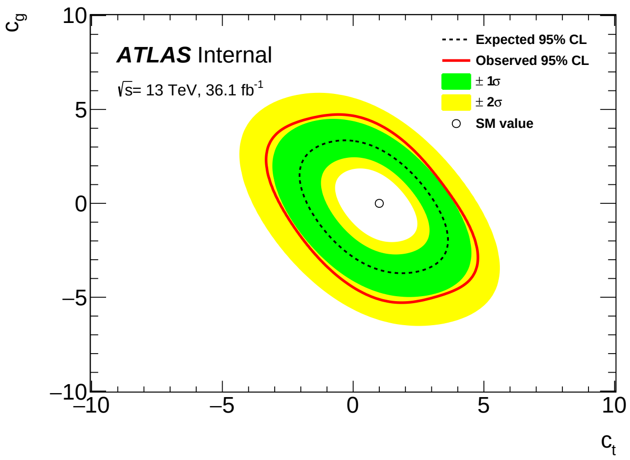

Fig. 10.35 Expected and observed exclusion limits using asymptotic contours with ± 1 and 2σ uncertainty bands on the expected, in the c_g versus c_t plane for an effective field theory with modified $t\bar{t}H$ and ggH couplings. The Standard Model coupling values are denoted with a hollow black circle.

Chapter 11 Conclusion and Prospects

This dissertation presents the measurements of the SM Higgs boson production cross section with the $H \to ZZ^* \to 4\ell$ channel under the Simplified Template Cross Section (STXS) framework and the inclusive $ZZ^{(*)} \to 4\ell$ lineshape with unfolding technique. Datasets of the proton-proton collisions at a center-of-mass energy of $\sqrt{s} = 13$ TeV collected by the ATLAS experiment at the LHC are used in these measurements. The Higgs production cross section measurement uses the full Run 2 dataset of an integrated luminosity of $139\,\text{fb}^{-1}$, and the inclusive 4ℓ lineshape analysis uses $36\,\text{fb}^{-1}$ data collected in 2015 and 2016. These measurements are made with great collaborative efforts in ATLAS, and the author of this thesis played essential roles in both analyses by developing and implementing important analysis techniques and tools to extract physics results from data. Details of the analyses are described in this thesis.

The Higgs production cross section on the reaction of $pp \to H \to ZZ^*$ is measured in the Higgs production rapidity range, $|y_H| < 2.5$, as

$$\sigma(pp \to H \to ZZ^*) = 1.34 \pm 0.12 \text{ pb},$$

which is consistent with the SM prediction of 1.33 ± 0.08 pb, calculated with N^3LO higher-order QDC corrections. The overall uncertainty of the measurement is less than 9%, dominant by the statistical uncertainty. The reduction of the uncertainty of the measurement is a result of many improvements in the analysis, including increasing the signal detection efficiency, better separation between signal and background, and removing the theoretical dependence on background modeling. Specifically, the analysis uses novel techniques including the lepton *particle-flow isolation* that boosts performance at high pile-up, the RNN discriminant to enhance the separation between different Higgs production mode and background, data-driven ZZ^* background estimation with dedicated side-band categories, and improved reducible background estimates. To improve the detection sensitivity the production-bin and the event selection categorization were getting finer and finer as luminosity increases.

With an expected $300\,\text{fb}^{-1}$ of pp-collision data and increased center-of-mass energy to 14 TeV from the LHC Run 3 which will start in 2021, the precision of the cross section measurement of the $H \to ZZ^* \to 4\ell$ will be further improved to 5%. In an even longer plan, the property measurement of SM Higgs will remain a key interest of the High Luminosity LHC (HL-LHC). A projection measurement of the $H \to ZZ^* \to 4\ell$ production cross section, assuming an improved muon p_{T} resolution with upgraded

ATLAS detector, is shown in Figure 11.1.

It is exciting to learn that the high energy physics community has put high priority for Higgs coupling measurement for the future super-collider experiments. The proposals include to build dedicated Higgs factories with e^+e^- collisions, such as ILC [182-183], CLIC [184] and CEPC [185-186]. The collisions of electron and positron provide the simplest initial state and a much cleaner experimental environment compared to the hadron colliders. Studies show that the HZZ coupling constant can be measured with an accuracy roughly ten times better than that measured at the HL-LHC experiments [187].

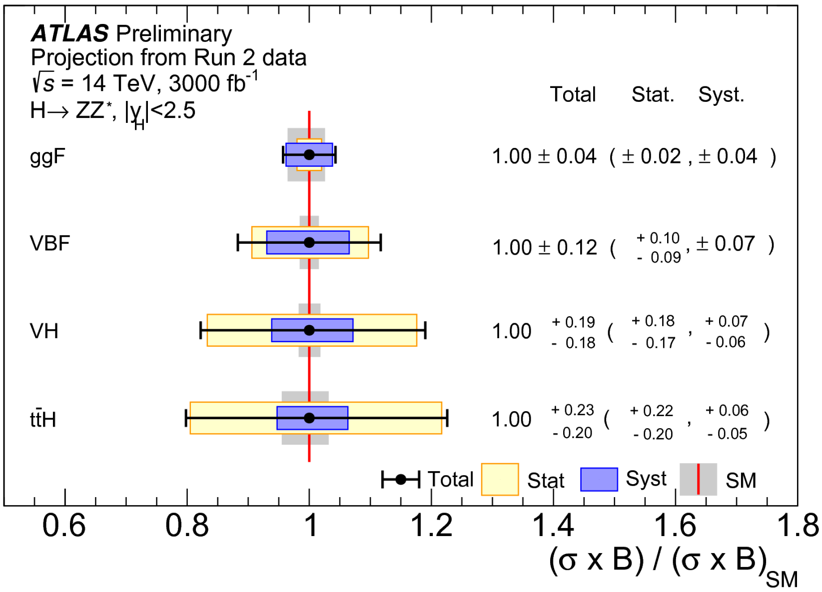

Fig. 11.1 The expected sensitivity for the measurement of cross section times branching ratio normalized to their SM prediction, in $H \to ZZ^* \to 4\ell$ channel, for Higgs boson with $|y_H| < 2.5$, on HL-LHC with $3\,000\,\mathrm{fb}^{-1}$ data, assuming p_T resolution of 45 GeV muon is improved by 30%. The yellow band stands for statistical error and the blue band stands for systematic error on the measurement. The gray band stands for error on the SM prediction [188].

The ZZ^* lineshape measurement is made in a wide kinematic range. It covers resonant production of Z and H bosons, on-shell ZZ threshold, and interference between different production mechanisms, allowing to probe important electroweak parameters, such as the H boson nature width, while controlling QCD effects, such as $gg \to ZZ$ production. This measurement has attracted a lot of attention in high energy physics community and will remain interesting in longer term at the LHC. Measurements included in this thesis are the 1-dimensional $m_{4\ell}$ spectrum and several double differential

$m_{4\ell}$ spectra. These spectra are unfolded to the truth particle-level distributions in the experimental fiducial phase space. The measured differential cross sections are further interpreted in several different theoretical models and the measured results are consistent with the SM predictions. The current binning in the measurement is rather coarse due to the limitation of data statistics. The analysis with full Run 2 dataset is ongoing in ATLAS, aiming to measure distributions of the 1-d and 2-d differential cross sections with improved precision and interpreted with SM Effective Field Theory (SMEFT). With more data to be collected in Run 3 and beyond, this measurement can provide stringent test of the SM with very rich physics contents, such as interplay with the Higgs and the SM continuum ZZ production and interference, as well as the interplay between the Electroweak and the QCD sectors of the SM.

To match the great physics opportunities provided by the upgraded LHC with increasing luminosity and energy the ATLAS Collaboration is organizing the detector upgrades in different phases. The most challenging projects are the New Small Wheel for MS end-cap inner station [189] as the Phase-1 upgrade project, and the Phase-II Inner Tracker Upgrade [190], High Granularity Trigger Detector [191] for the trigger system. These detector upgrades will allow making new discoveries and precision measurements at the HL-LHC in the next twenty years.

Appendix A Study of high luminosity performance in Monitored Drift Tube chambers

On ATLAS, the monitored drift tubes (MDT) are used as the precision chamber in the Muon Spectrometer both in barrel and end-cap regions. When μ tracks traverse the MDT, the gas are ionized to produce primary electrons and ions. Primary electrons drift under the influence of electric field towards the anode wire and avalanche under the strong field near the wire, inducing large current signal that is collected by electrodes. The drift time of primary electrons is used to estimate the coordinates of the hits and is used to reconstructed μ tracks. The byproduct of the process is the large number of positive ions of working gas that is 1000 times slower than electron drifting to cathode tube that creates a reversed electric signal. It is assumed that under a constant instantaneous luminosity, the ions are being constantly produced and absorbed at the cathode, creating an equilibrium inside the tube, which is called the space charge effect. The space charge will distort the local electric field inside the tube and possibly causes loss of gain, efficiency drop for hit detection and worse resolution for tracks.

This chapter describes the study of those effect at increasing instantaneous luminosity using muon calibration data. The chambers in the innermost stations of the end-cap have the largest hit rate therefore they are the focus of the study.

First of all the hit rates are estimated as a function of the luminosity, the run 339849 collected during 2018 is used. It is worth mentioning that the hit rate from muon calibration stream is somewhat biased due to the muon trigger requirement, but they are still an indication of the operating condition. Figure A.1 shows the the hit rate per unit area per second as a function of the instantaneous luminosity. As can be seen, the EIL1 and EIS1 chambers are the busiest chambers, followed by EIS2, then the middle station, and chambers in the barrel. The BEE chambers are located near the gap between barrel and end-cap regions, therefore they are in a noisier environment than neighboring chambers. The hit rate all follows an almost linear increase with respect to luminosity. The slight non-linearity (e.g. BEE) indicates a hidden dependence on some underlying quantities like pile-up. The chambers are entering a rate region where some loss of efficiency and resolution is expected.

The gain of the detector is proportional to the charge collected at the electrodes. The ADC (analog-to-digital) count collected at front-end electronics can be used to study the effect of gain. To study the effect of ADC vs luminosity, data are first grouped by

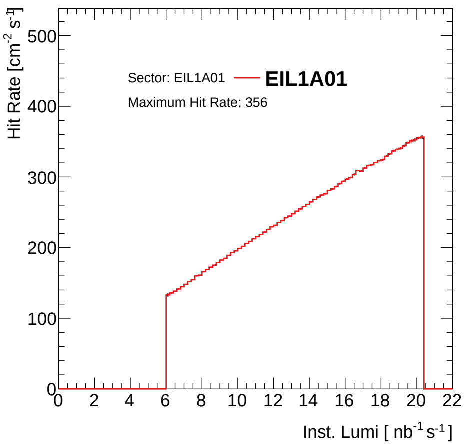

(a) EIL1A01

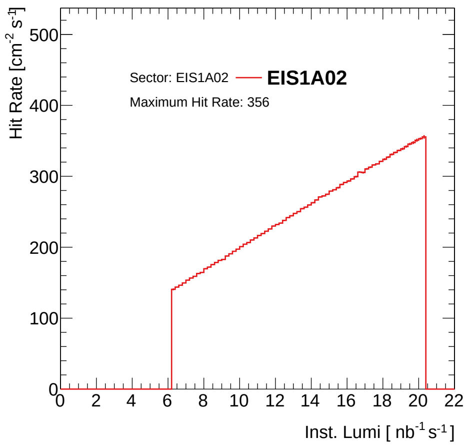

(b) EIS1A02

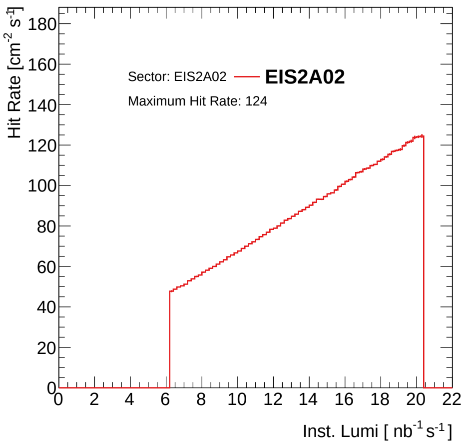

(c) EIS2A02

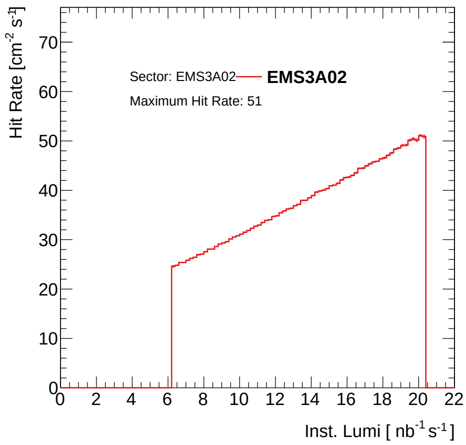

(d) EMS3A02

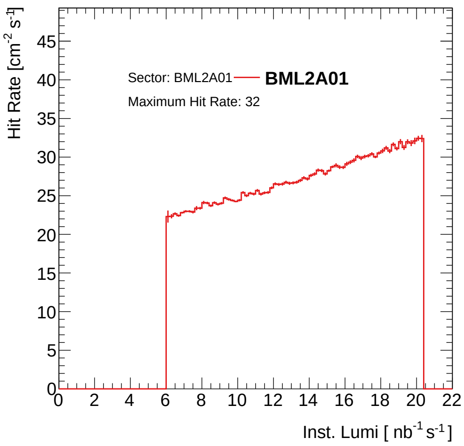

(e) BML2A01

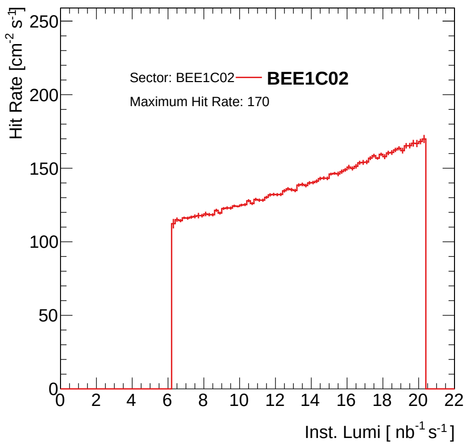

(f) BEE1C02

Fig. A.1 Hit rate [Hz/cm^2] as a function of the instantaneous luminosity in different chambers.

their luminosity, from 6×10^{33} $cm^{-2}s^{-1}$ (or 6 $nb^{-1}s^{-1}$) to around $2.1 \times 10^{34} cm^{-2}s^{-1}$ (or 21 $nb^{-1}s^{-1}$), at a step of 0.4 $nb^{-1}s^{-1}$. The ADC distribution in each luminosity slice is fitted with a skew Gaussian function. Figure A.2 shows the ADC distribution of EIS1A02 chamber as an example. The fitting parameters for EIS1A02 as a function of the luminosity of each slice is shown in Figure A.3. A linear fit is carried and the slope of the line indicates the dependency on luminosity. It can be seen that the skew of the Gaussian does not change with luminosity, however the mean number and the width is at a consistent reduction with increasing luminosity, indicating the existence of the space charge effect. The average gain changes of different chambers is shown in Figure A.4. The size of luminosity dependency correlates with the hit rates of chambers shown above, which further proves that the reduction effect is correlated to the increasing space charge density at higher hit rate.

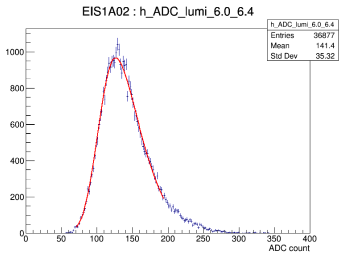

(a) 6-6.4 $nb^{-1}s^{-1}$

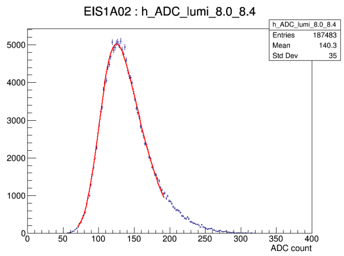

(b) 8-8.4 $nb^{-1}s^{-1}$

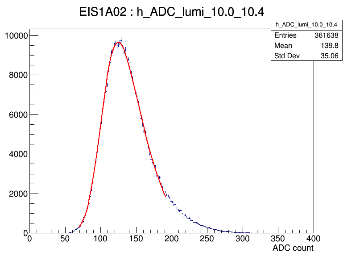

(c) 10-10.4 $nb^{-1}s^{-1}$

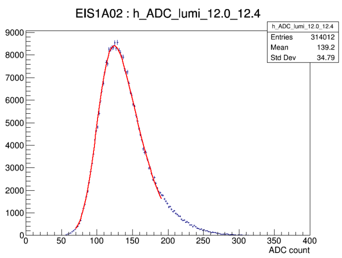

(d) 12-12.4 $nb^{-1}s^{-1}$

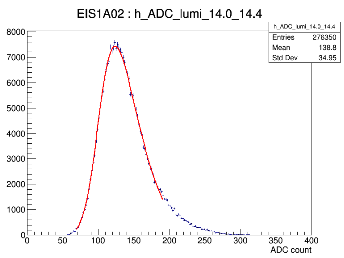

(e) 14-14.4 $nb^{-1}s^{-1}$

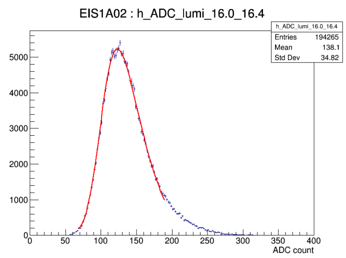

(f) 16-16.4 $nb^{-1}s^{-1}$

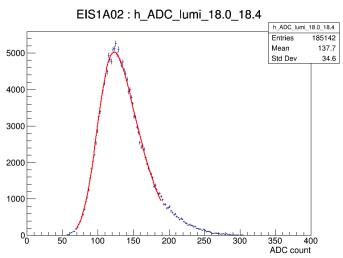

(g) 18-18.4 $nb^{-1}s^{-1}$

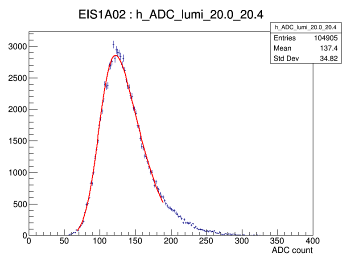

(h) 20-20.4 $nb^{-1}s^{-1}$

Fig. A.2 The distribution of ADC in different instantaneous luminosity bins for chamber EIS1A02. A selected slices of luminosity is plotted, each with a width of 0.4 $nb^{-1}s^{-1}$**, from** 6 $nb^{-1}s^{-1}$ **to** 20 $nb^{-1}s^{-1}$**.**

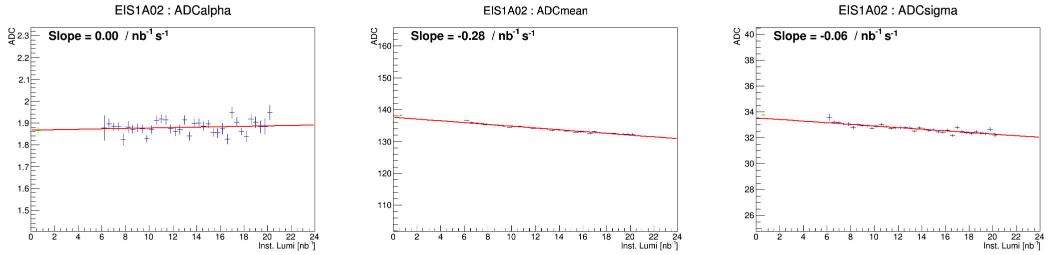

(a) skew α **(b) mean** **(c) width σ**

Fig. A.3 The fitting parameters of skew Gaussian fit of the ADC count as a function of instantaneous luminosity bins for chamber EIS1A02.

The efficiency of the hits can only be calculated when hits are expected in the corresponding location. This can easily be simulated in Monte Carlo simulation or in a carefully designed testing station. In the calibration stream, segment fit is carried out on real hits and the intersection of segments at each layer of tubes is counted as a hole under the absence of a hit. The efficiency is then defined as number of hits over number of hits and holes. The Figure A.5 shows the efficiency as a function of luminosity. There is a $2 - 4$ % loss of efficiency for the innermost chambers and The reduction is almost negligible for chambers with smaller hit rate.

Finally, the most important performance property that is studied is the resolution of MDT chambers. The hit residual is defined as the difference between measured drift radius and the radius extrapolated by the segment fit. The distribution is shown in Figure A.6. The dispersion reflects the resolution in the measurement. Empirically, a double Gaussian function is used for the fitting, and the standard deviation of the two Gaussian can be used to study the impact of luminosity (see Figure A.7). The slope of σ - luminosity is higher in EIL1 and EIS1 chambers than EIL2 chambers, likely due to the larger hit rate. But hit rate alone cannot explain why EIS1 chambers have smaller slope than EIL1 chambers considering both chambers have similar hit rates. More studies would need to be done to understand this behavior.

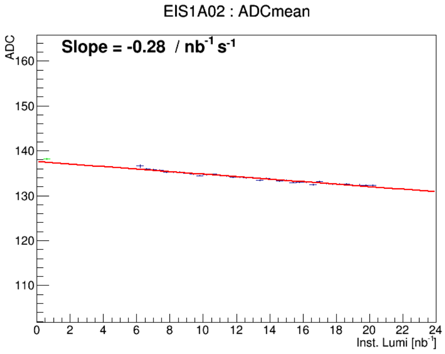

(a) EIS1A02

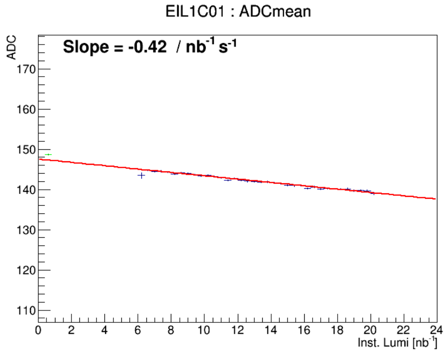

(b) EIL1C01

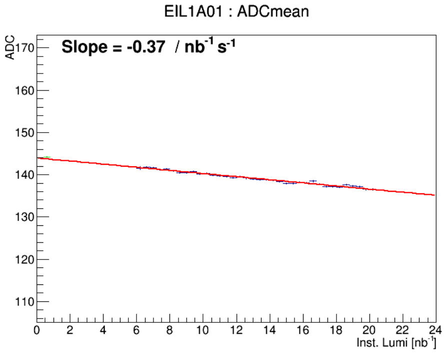

(c) EIL1A01

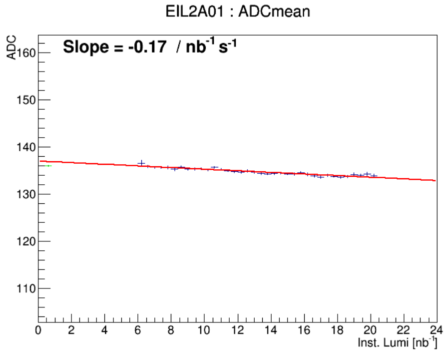

(d) EIL2A01

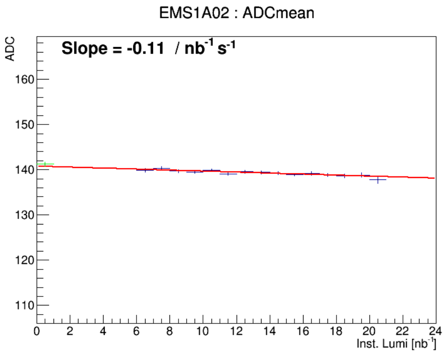

(e) EMS1A02

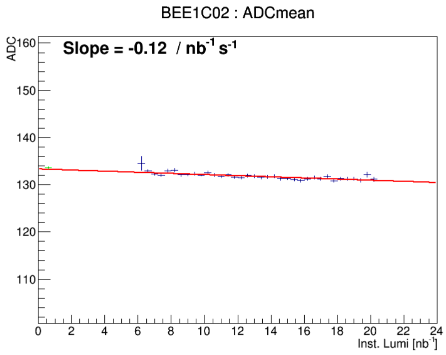

(f) BEE1C02

Fig. A.4 The mean of skew Gaussian fit of the ADC count as a function of instantaneous luminosity for various chambers listed above.

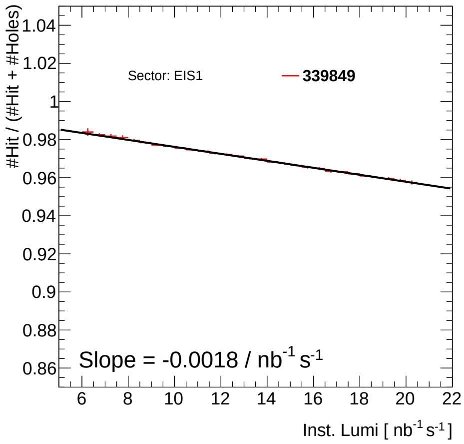

(a) EIS1

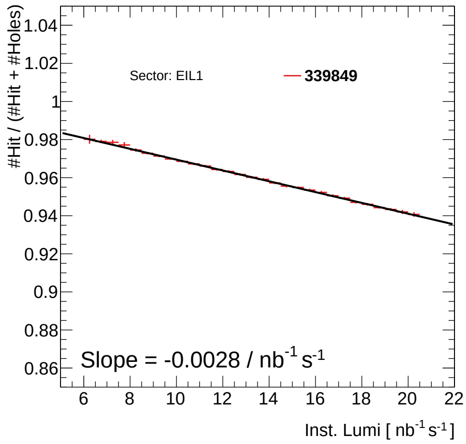

(b) EIL1

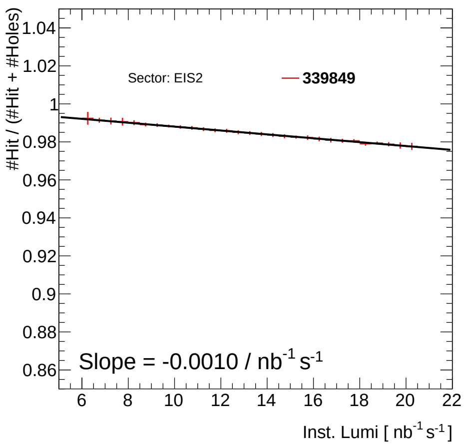

(c) EIS2

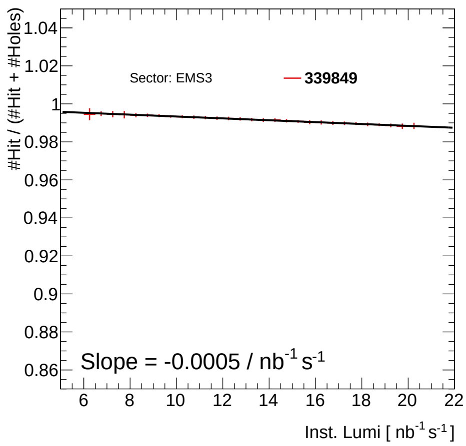

(d) EMS3

Fig. A.5 The efficiency as a function of instantaneous luminosity for different chambers.

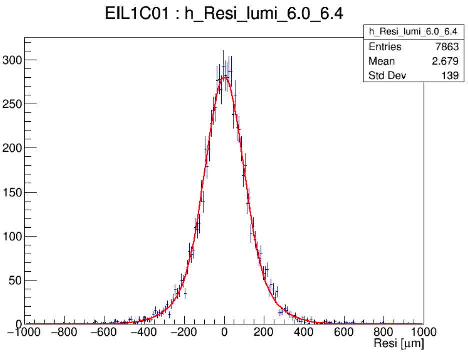

(a) 6-6.4 $nb^{-1}s^{-1}$

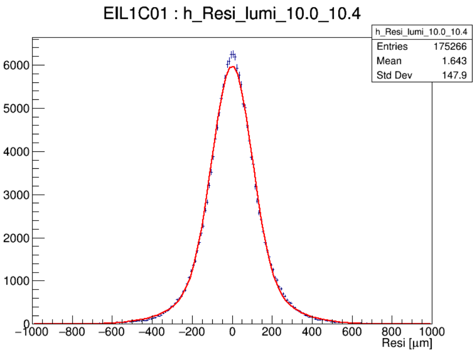

(b) 10-10.4 $nb^{-1}s^{-1}$

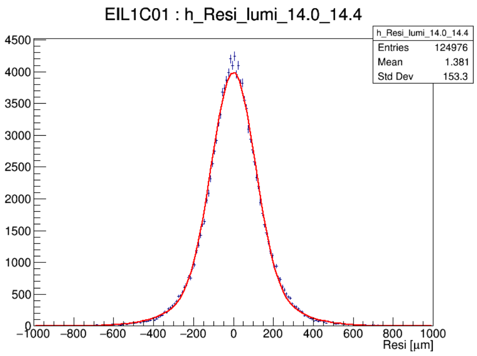

(c) 14-14.4 $nb^{-1}s^{-1}$

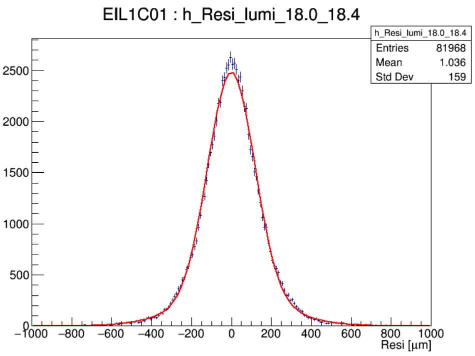

(d) 18-18.4 $nb^{-1}s^{-1}$

Fig. A.6 The distribution of hit residual in different instantaneous luminosity for chamber EIL1C01.

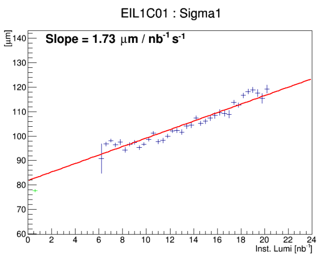

(a) EIL1C01 - σ_1

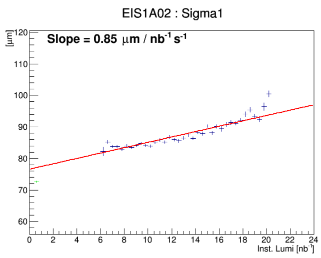

(b) EIS1A02 - σ_1

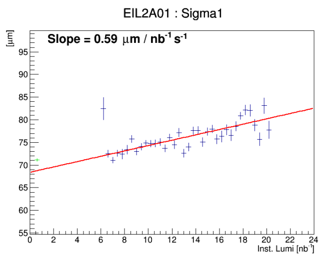

(c) EIL2A01 - σ_1

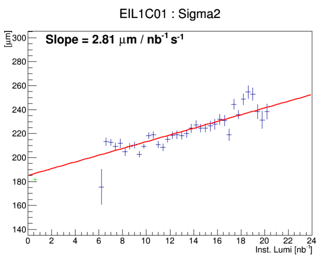

(d) EIL1C01 - σ_2

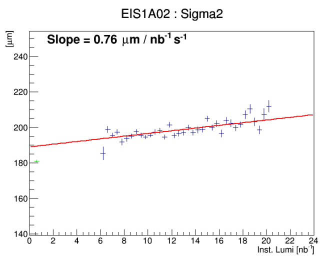

(e) EIS1A02 - σ_2

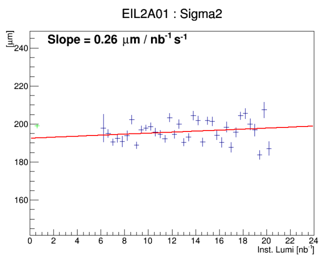

(f) EIL2A01 - σ_2

Fig. A.7 The σ in the double Gaussian fitting of hit residual as a function of instantaneous luminosity for different chambers.

Appendix B Electronics integration and commissioning of the sTGC on NSW

The New Small Wheel (NSW) [189] is the Phase 1 muon upgrade project that will replace the current Small-Wheel, or the end-cap inner station of the ATLAS Muon Spectrometer. The major reason for this upgrade is to add Level-1 trigger information from the inner station of the Muon Spectrometer to reduce large fake-trigger rate of the muon system. The fake trigger rates contributed by particles not originated from the IP will be too high for the HL-LHC operations. The NSW is expected also improving the tracking performance for offline muon reconstruction. The NSW is planned to be installed during the LHC Long Shutdown 2 (LS2, 2019 - 2021) and commissioned in Run 3 in order to be better prepared for the HL-LHC operations.

The NSW consists of two detector technologies, Micromegas (MM) and small-strip Thing Gap Chambers (sTGC). Two new small-wheels (Side-A and Side-C) consist of 128 MM Chambers with 2,000,000 readout channels, and 192 sTGC chambers with 354,000 readout channels. These chambers will be assembled to 32 Sectors, consist of 128 wedges. Each new small-wheel is assembled with a MM double-wedge (total eight active detection layers) sandwiched by two four-layer sTGC wedges. Both detector technologies use the same home-made integrated "VMM" ASIC chips which play the roles of amplifier-shaper-discriminator in a compact way. Commissioning of the NSW electronics requires deep knowledge on the VMM operation parameter setting for many different operational modes for different applications. During the past 20 months the author of this thesis spent large portion of his efforts on the integration and commissioning of the sTGC at CERN, which will be described in this chapter.

Figure B.1 shows the schematics of a sTGC gaseous gap. In the middle of the gap, the wires with high electrical potential (2.9 kV) acts as the anode for primary ionization electron amplification. The cathodes are provided by large pads at one side of the gap, and finer strips at the other side, coated with resistive graphite-epoxy mixture to ensure the chamber high-rate capability. The the coincidence of the sTGC pads in four layers (3 out of 4) will provide fast muon trigger at stage-0, which will trigger the sTGC sending out the Level-1 trigger signal from the strips. The strips have a pitch size of 3.2 mm that provides a good spatial resolution which gives itself the name "small TGC". The resistive material ensures a good timing resolution and small recovery time to meet the fast timing requirement.

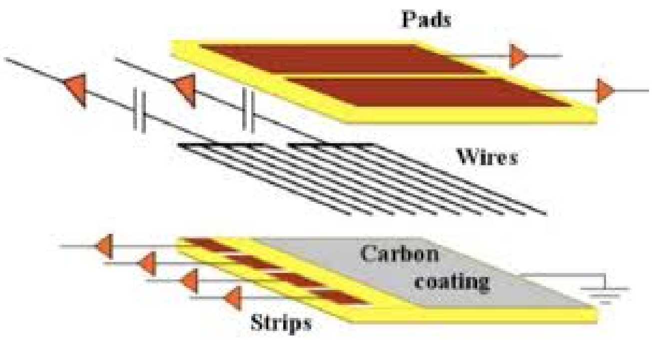

Fig. B.1 Schematics of the sTGC chamber technology. [192]

Figure B.2 is a diagram which shows the Input/Output of the NSW electronics system. There are two types of front-end (FE) boards for sTGC chambers: sFEB and pFEB, which connects to strips and pad+wires, respectively. The VMM chips collect and process the electronic signals from the detectors. In the readout chain, data is passed to "ReadOut Controller" (ROC) for assembling over the channels. The L1DDC is an on-chamber electronics that hosts the GBTx chip (made at CERN), which convert electric signal from ROC to light signal for long distance transmission from the ATLAS cavern to back-end TDAQ systems. The trigger chain instead, starts with hits on pFEBs, the hits information are passed in parallel to "Trigger Data Serializer" (pTDS) chip to be serialized. The pTDS then pass the data to the pad trigger board which is based a customized FPGA. The algorithm on pad trigger board determines with the information from eight layers of sTGC whether to send trigger signal to the sTDS on sFEBs. If the sTDS on sFEB receives trigger from pad trigger, it will read corresponding strip information from VMM and send to the trigger processor for ATLAS L1 trigger decision together with the Big-Wheel trigger processor. This layered on-chamber trigger system reduces the trigger rate of strips to allow for bandwidth limit downstream systems. The Level-1 muon trigger signal will enter the ATLAS TDAQ center trigger system for high level trigger process and finally decide if an event should be recorded.

As can be seen in Figure 4.10, the center piece of the data flow is the FELIX (FrontEnd LInk eXchange) system [193]. The FELIX system is basically a data router with industrial-standard FPGA (Field Programmable Gate Arrays) hosted on PC. During the ATLAS operation, the FELIX acts as a back-end system that will sit in USA15 and receive the front-end data from the detector through fibers connecting to L1DDC boards. FELIX passes readout data to software-based Readout Driver (swROD) for assembling data from different sub-detectors. As can be seen in Figure 4.10, FELIX+swROD combination replaces the traditional hardware Readout Driver+Readout System. Users

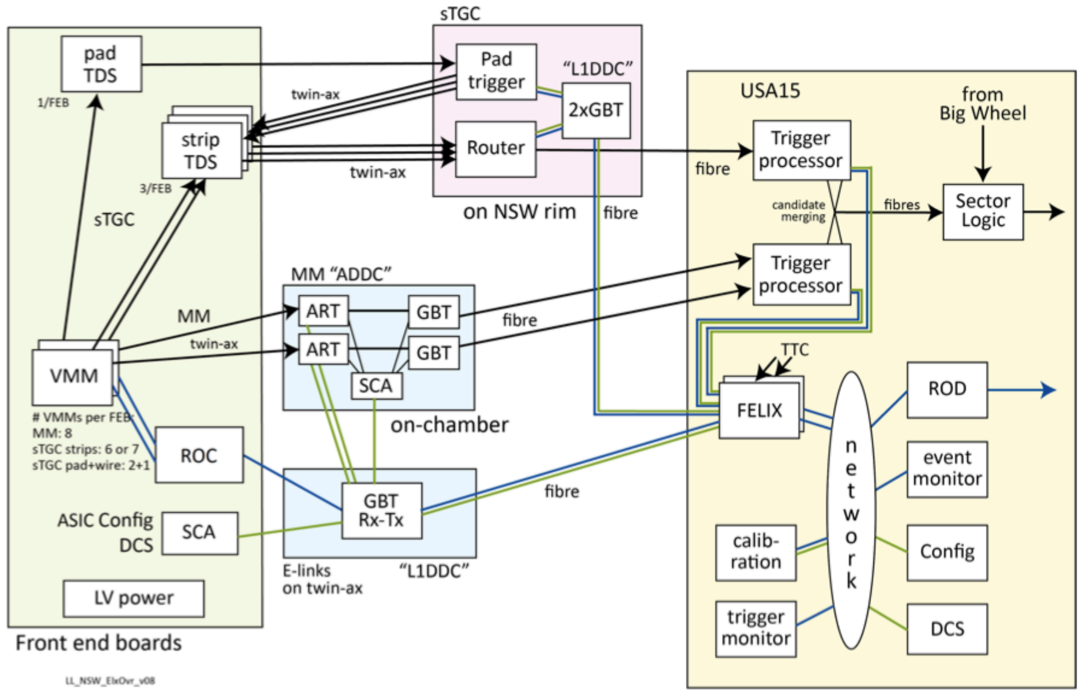

Fig. B.2 Data I/O flow of the New Small Wheel.

would only need to design customized software plugins under the swROD framework rather than investing in more expensive customized hardware Readout Driver. The FELIX system is also responsible for sending Timing Trigger and Control (TTC), FE configuration, detector monitoring and other services.

In order to integrate the NSW with the FELIX system, a set of softwares that fulfills FE configuration and TTC is provided by theNSW community. The FE configuration is saved in a *json* file format which has a layered map structure, with string as keyword and values being numbers, string or another map. An example would be a FE board name as keyword pointing to a map that contains again maps of VMM, TDS and ROC chips, which further contains register names and values. Those register values are closely related to the actual register bit value for the ease of programming, however reduce the readability from a human's point of view. A Qt-based sTGC-FELIX GUI is designed to interpret those register values in a more human readable way of the real FE parameters. The interface is shown in Figure B.3, whose template is taken from MiniDaq GUI (developed at Michigan), to allow people with experience of MiniDaq system to easily migrate to FELIX. The MiniDaq GUI implements the interaction between clicking buttons on configuration panel and changing *xml* files on disks through intermediate in-memory payload objects to store configuration for chips, one for each type of chip. The sTGC-FELIX GUI instead uses multiple objects corresponding to the actual number of chips on the board. Those objects' payload can be copied over to original object which is used to trigger updates to the GUI elements upon users' actions. The schematics of this implementation is shown in Figure B.4.

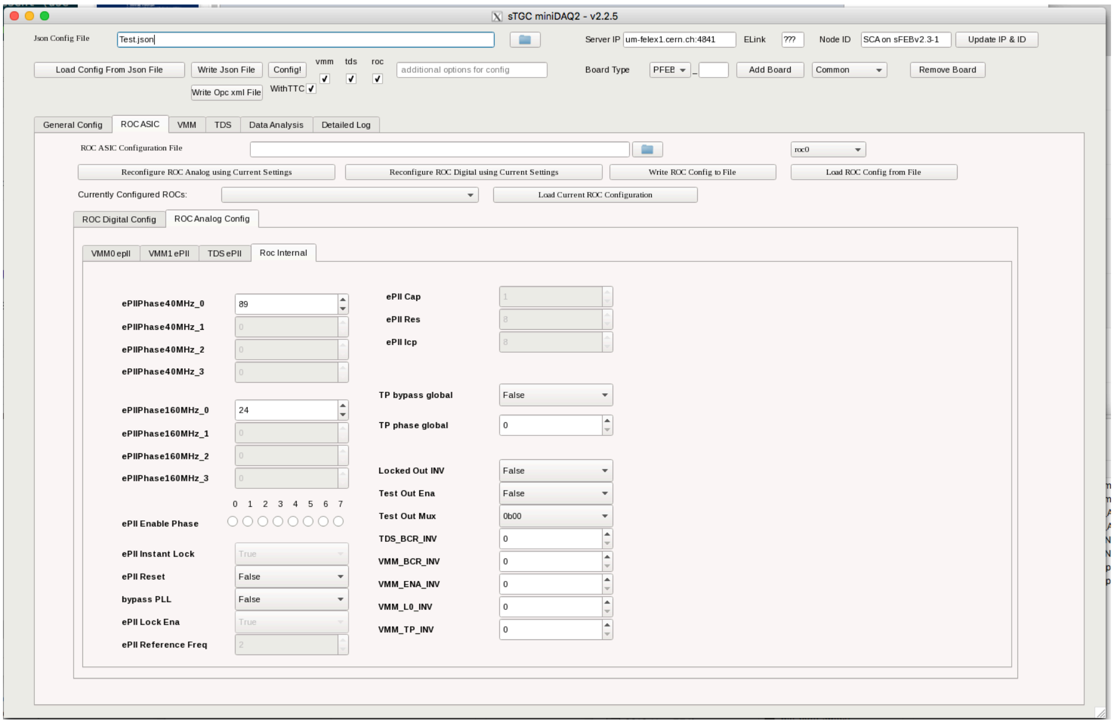

Fig. B.3 Showcase of sTGC-FELIX GUI.

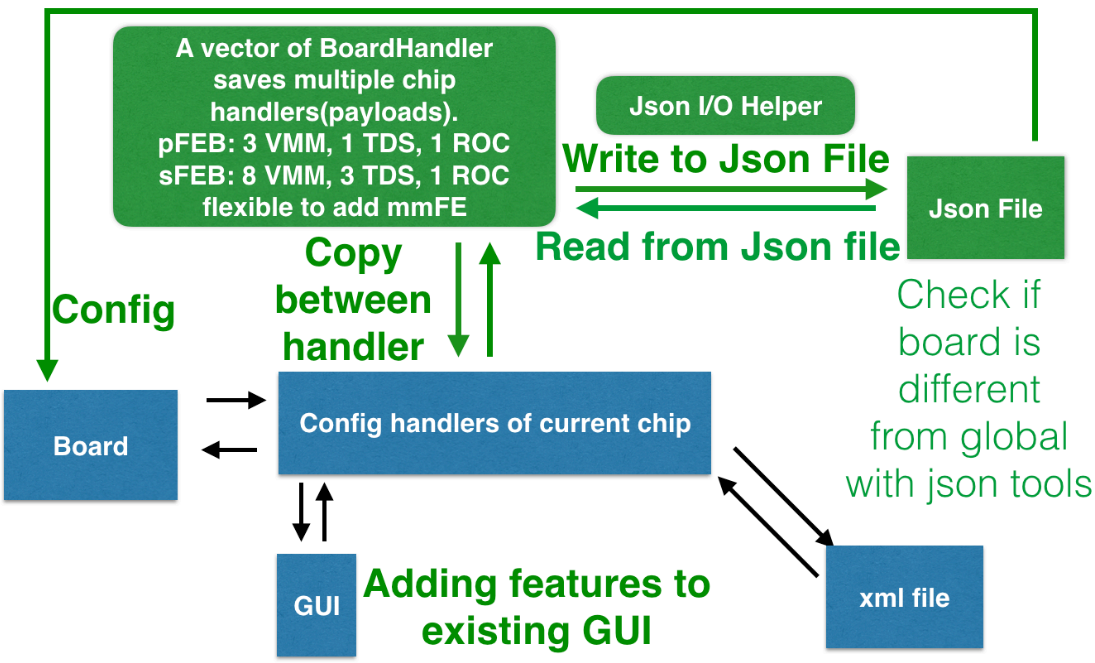

Fig. B.4 Core concept of configuration module in sTGC-FELIX GUI.

On top of easing the modification of FE configuration, the sTGC-FELIX GUI also implements the function to send TTC signal by querying lower-level commands so that the correct TTC sequence together with configuration can be done in one click. A data decoder based on ROOT TTree is integrated into the GUI to analyze data from FELIX including channel occupancy, pdf, TDO, BCID, L1ID distributions. The same software module is also regularly used to convert bit files from to TTree for more analysis.

One additional task raised during the integration process is to achieve automatic calibration of ADC and TDC response with test pulses. The test pulses is generated by VMM itself while the control bit is sent through TTC stream. The test pulse height can be configure through a register of VMM. Similarly the test pulse can be set with a configurable delay. Generally a set of parameters needs to be scanned over and check the response of the chips. The difficulty lies on the fact that the system have unexpected breakdown from time to time. A calibration control sequence is demonstrated in Figure B.5, based on ATLAS partition, achieved by using the tool of the command-line to control partition to configure, start run and change name, etc. A empirical timeout period is set at each step to catch system crash and resume the calibration procedure. The scanned ADC and TDC spectra and their linearity can be found in Figure B.6. The TDC is actually equivalent to an ADC measuring the charge which starts charging at the time of pulse arrival, to the end of the time window. Therefore later arrival would mean a late start time of charging procedure, thus smaller TDC value. The time window is 8 bunch crossing, namely 200 ns, therefore a well delayed test pulse will enter the next time window and be assigned a different BCID. And the charging time is actually much advanced in the new time window, which explain the jump in the Figure B.6(d).

The novel tool of jsROOT [194] is recently explored in the implementation of an offline data monitoring website [195] for better portability and user interactivity. The demonstration is shown in Figure B.7. The website is programmed largely in JavaScript and uses query string in url to achieve portability of exactly plots the website will show upon opening.

The trigger chain, specifically the I/O of pFEB and sFEB TDS, are tested with customized firmware due to unavailability of official hardware at the time of integration. Related analysis tool is also developed based on python panda dataframe [196], in order to visualize the output data in text format.

For pFEB trigger chain tests, the pseudo-random binary sequence is sent from TDS to test connectivity between TDS and downstream hardwares. On top of this, the most tell-tale demonstration is the noise identification plot, as shown in Figure B.8. A uniform distribution is a good sign of perfectly behaving VMM-TDS which means all 32 VMM channels that is pulsed at the same time are showing up in the TDS correctly. A noisy plot like the bottom one indicates some TDS channel “sees” pulse while some other

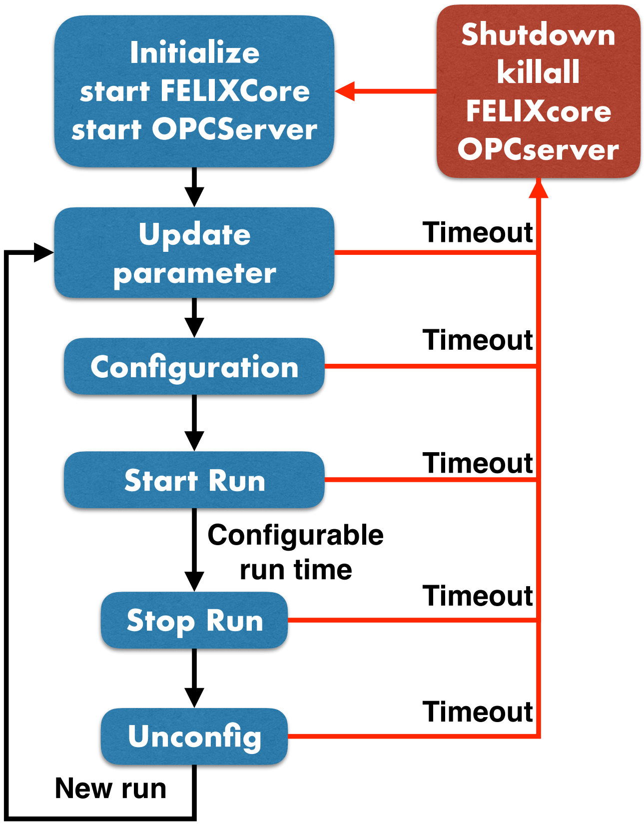

Fig. B.5 Calibration sequence.

channels doesn't, indicating a problematic configuration or a noisy channel.

For sFEB trigger chain test, the phase between TDS and VMM is scanned (Figure B.9) to find the the working phase with enough margin. The response linearity of the 6-bit ADC in VMM is also tested as shown in Figure B.10, similar to the one in readout-chain. Those are defined as the standard criteria in the FE receival test and wedge integration test.

In Building 191 at CERN, the sTGC sector A12 was successfully integrated during the time this thesis was written, marking the largest integration unit at the time for sTGC, on a semi-final operational system of FELIX-swROD. All the eight layers in the sector are correctly read-out with test pulses, and the integration results in Building 180 (where the sTGC wedges are integrated and tested) are reproduced. The threshold and trimmers based on baseline measurements are tuned and some cosmic muon data is taken with the external coincidence trigger provided by two 10×10 cm^2 scintillator pads. Despite the low trigger rate due to small scintillator size and low efficiency caused by non-operational drift gas, track segments were able to be identified in those sparse data.

Finally, the author of this thesis is also involved in some scripting, software up-

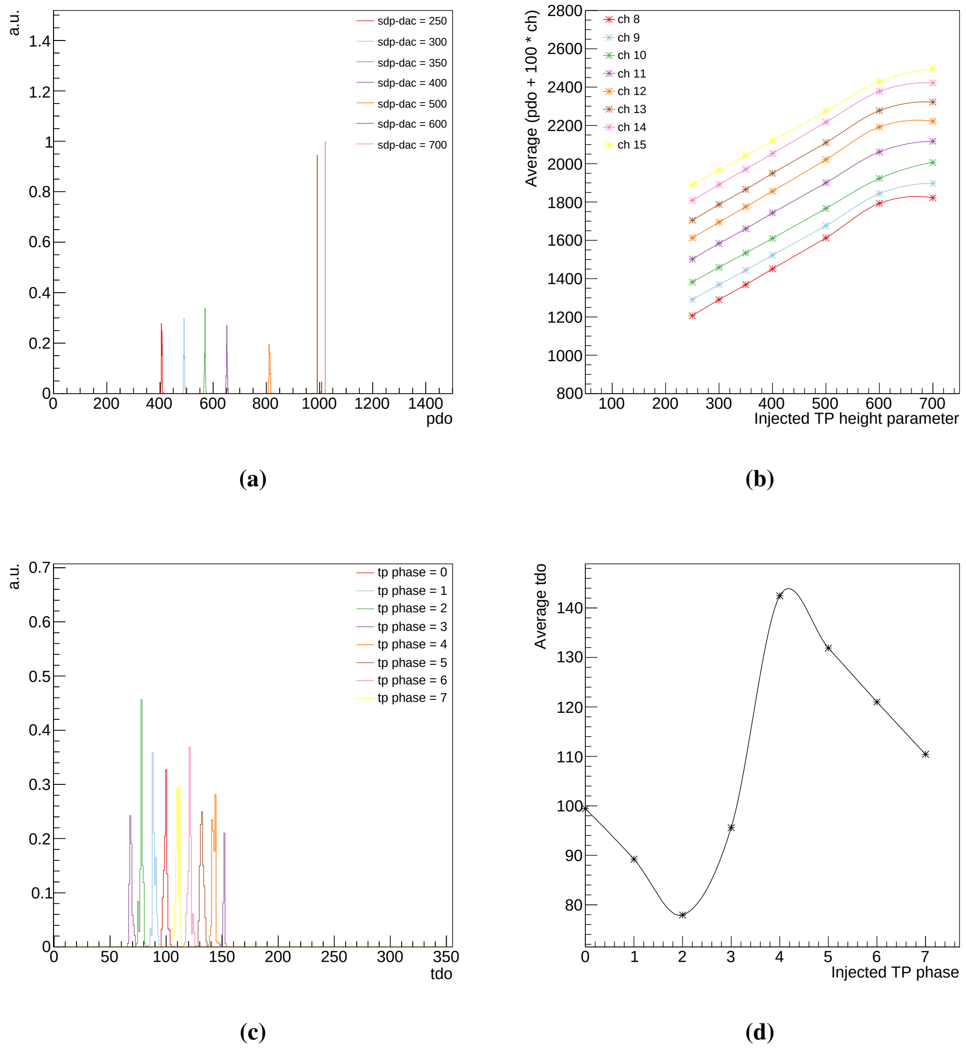

Fig. B.6 (a) ADC distribution of vmm1 channel 8 at different pulse height parameter ; (b) average of ADC vs pulse height parameters for 8 channels; (c) TDC distribution of vmm0 channel 1 at different test pulse delay; (d) average of TDC vs pulse height parameters for 8 channels

grading as-per-needed. This is mainly to deal with the unavailability of certain tools in integration platform or short of manpower in most scenarios.

The big effort for the NSW integration and commissioning is ongoing at CERN, aiming to install both new small wheels to the ATLAS Muon Spectrometer during LS2. The author of this thesis will continue to play a major role in the NSW I&C project and look forward to seeing muon data from the new detector in Run 3.

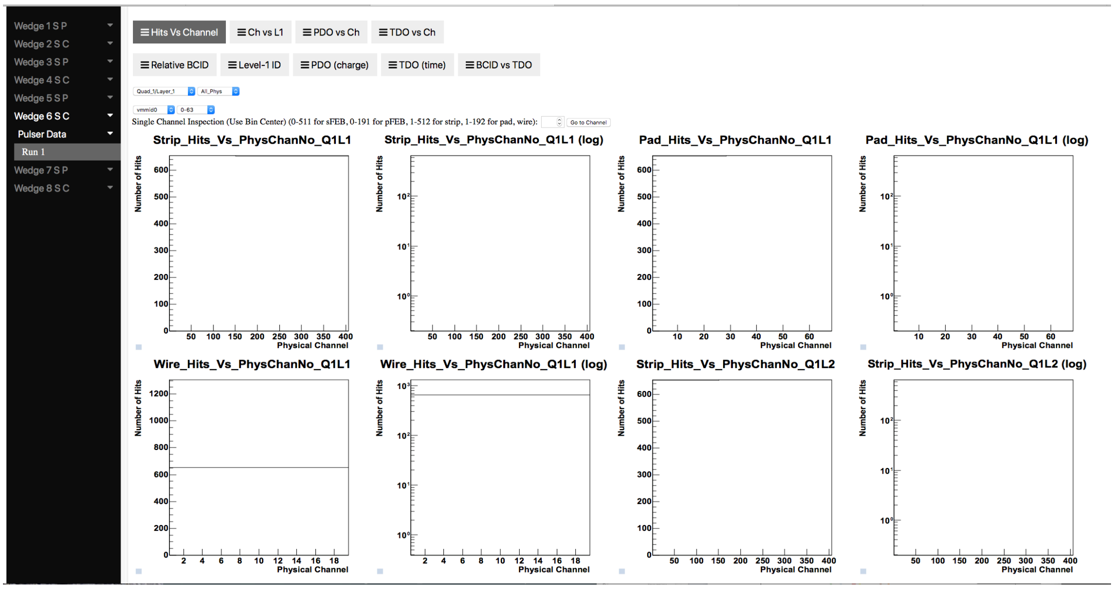

Fig. B.7 Demonstration of the monitoring website. The plots currently shown is channel occupancy. More options can be chosen by clicking the buttons.

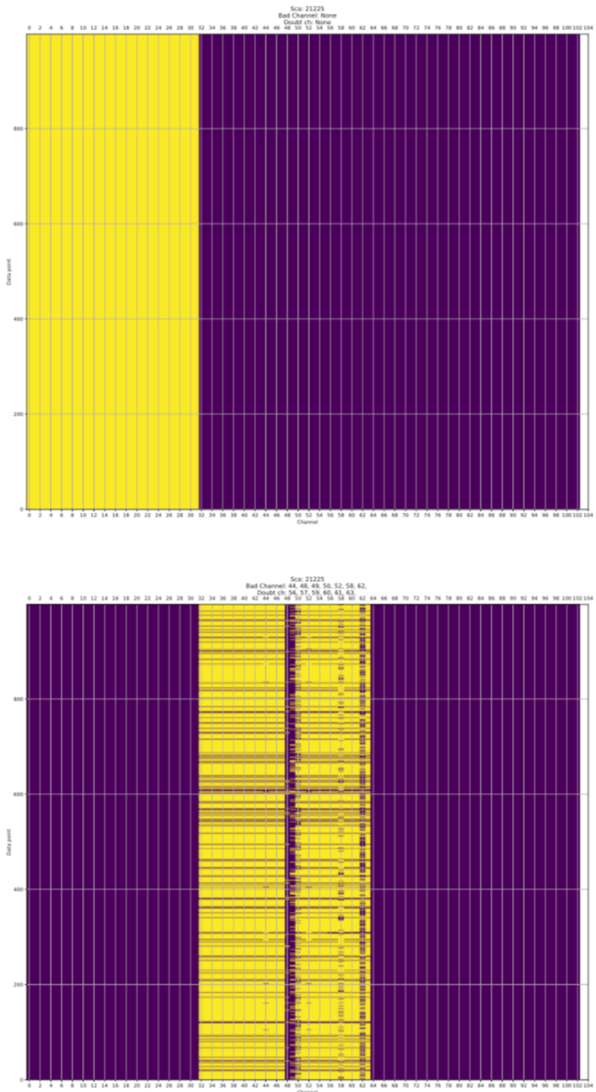

Fig. B.8 The noise identification plot for pFEB trigger chain test. The x axis is channel and the y axis is the index of hit. The yellow color indicate there's a hit while purple is without hit.

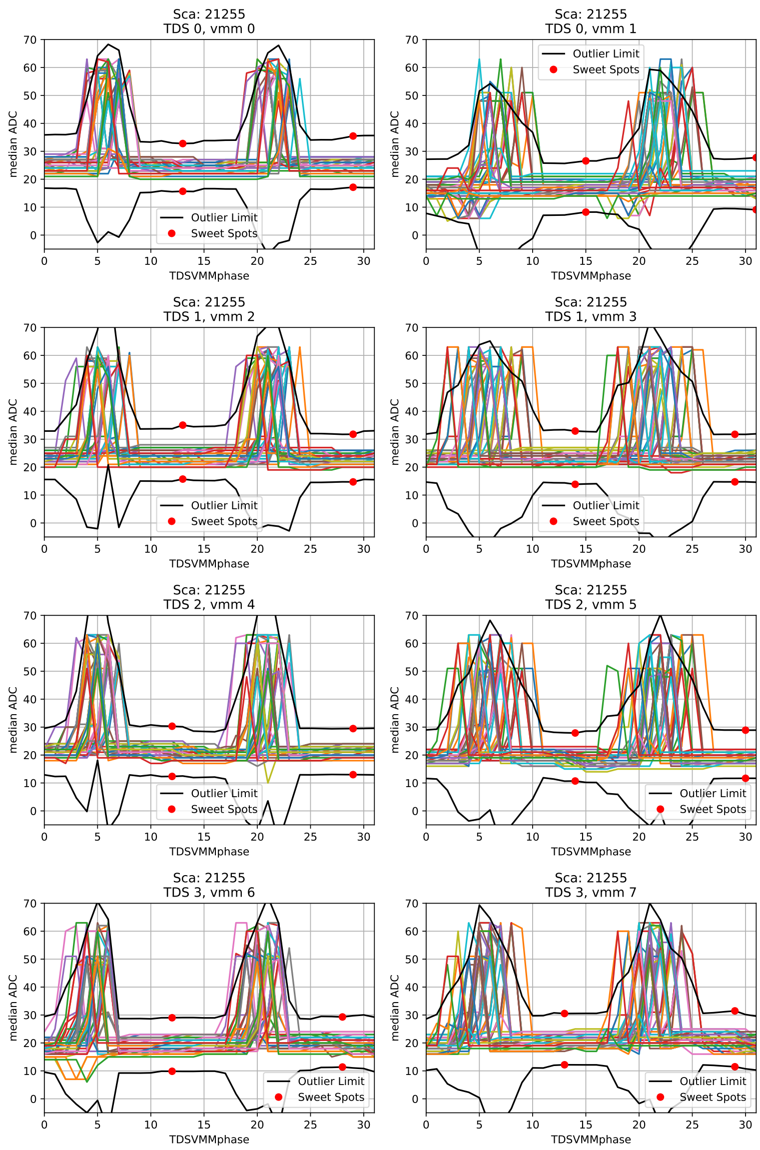

Fig. B.9 The ADC readback as a function of the TDS-VMM phase

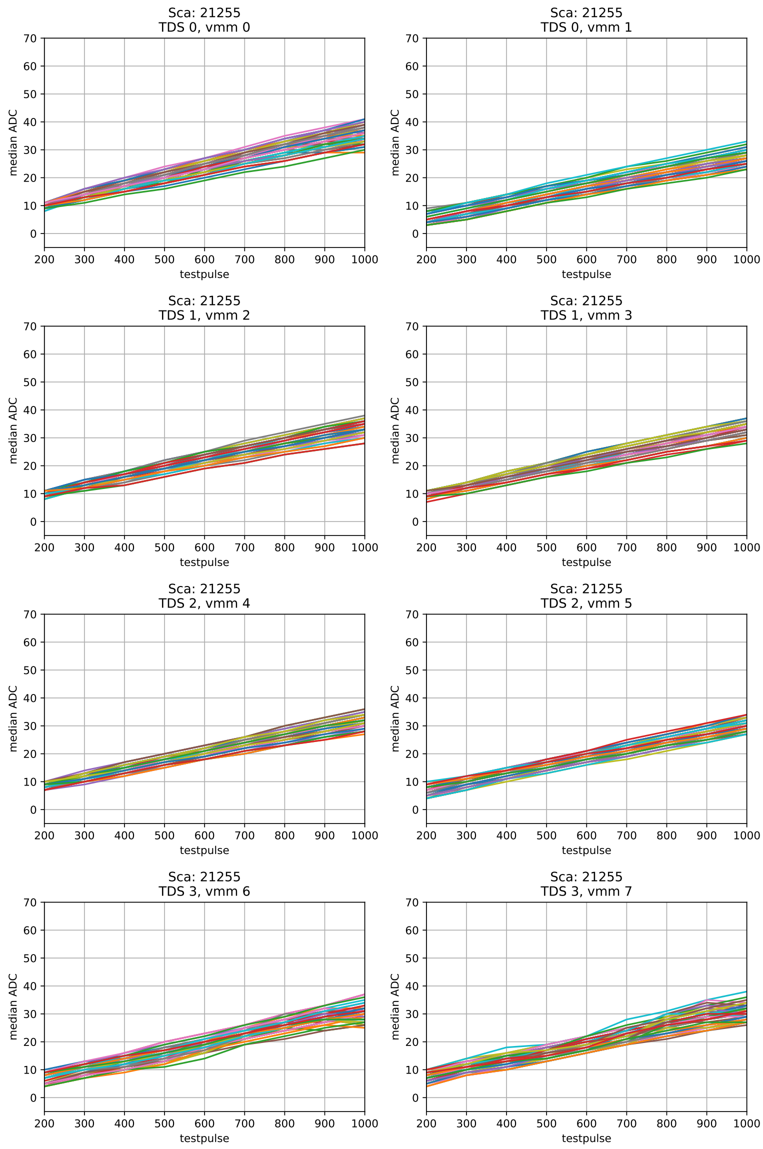

Fig. B.10 The ADC readback as a function of the test pulse height

Bibliography

[1] Y. Nambu, *Quasiparticles and Gauge Invariance in the Theory of Superconductivity*, Phys. Rev. **117** (1960) 648–663, [,132(1960); ,132(1960)].

[2] J. Goldstone, *Field Theories with Superconductor Solutions*, Nuovo Cim. **19** (1961) 154–164.

[3] J. Goldstone, A. Salam, and S. Weinberg, *Broken Symmetries*, Phys. Rev. **127** (1962) 965–970.

[4] P. W. Higgs, *Broken symmetries, massless particles and gauge fields*, Phys. Lett. **12** (1964) 132–133.

[5] P. W. Higgs, *Broken Symmetries and the Masses of Gauge Bosons*, Phys. Rev. Lett. **13** (1964) 508–509, [,160(1964)].

[6] F. Englert and R. Brout, *Broken Symmetry and the Mass of Gauge Vector Mesons*, Phys. Rev. Lett. **13** (1964) 321–323, [,157(1964)].

[7] G. S. Guralnik, C. R. Hagen, and T. W. B. Kibble, *Global Conservation Laws and Massless Particles*, Phys. Rev. Lett. **13** (1964) 585–587, [,162(1964)].

[8] P. W. Higgs, *Spontaneous Symmetry Breakdown without Massless Bosons*, Phys. Rev. **145** (1966) 1156–1163.

[9] T. W. B. Kibble, *Symmetry breaking in nonAbelian gauge theories*, Phys. Rev. **155** (1967) 1554–1561, [,165(1967)].

[10] ATLAS Collaboration, *Observation of a new particle in the search for the Standard Model Higgs boson with the ATLAS detector at the LHC*, Phys. Lett. **B716** (2012) 1–29, `arXiv:1207.7214 [hep-ex]`.

[11] CMS Collaboration, *Observation of a New Boson at a Mass of 125 GeV with the CMS Experiment at the LHC*, Phys. Lett. **B716** (2012) 30–61, `arXiv:1207.7235 [hep-ex]`.

[12] ATLAS Collaboration, G. Aad et al., *Higgs boson production cross-section measurements and their EFT interpretation in the 4ℓ decay channel at $\sqrt{s}$ = 13 TeV with the ATLAS detector*, `arXiv:2004.03447 [hep-ex]`.

[13] ATLAS Collaboration, *Measurement of the four-lepton invariant mass spectrum in 13 TeV proton-proton collisions with the ATLAS detector*, JHEP **04** (2019) 048, `arXiv:1902.05892 [hep-ex]`.

[14] M. E. Peskin and D. V. Schroeder, *An Introduction to quantum field theory*. Addison-Wesley, Reading, USA, 1995.

[15] C. Quigg, *Gauge Theories of the Strong, Weak, and Electromagnetic Interactions: Second Edition*. Princeton University Press, USA, 9, 2013. URL: http://www.jstor.org/stable/j.ctt3fgx94.

[16] P. A. Dirac, *Quantum theory of emission and absorption of radiation*, Proc. Roy. Soc. Lond. A **A114** (1927) 243.

[17] E. Fermi, *Quantum Theory of Radiation*, Rev. Mod. Phys. **4** (1932) 87–132, URL: https://link.aps.org/doi/10.1103/RevModPhys.4.87.

[18] F. Bloch and A. Nordsieck, *Note on the Radiation Field of the Electron*, Phys. Rev. **52** (1937) 54–59, URL: https://link.aps.org/doi/10.1103/PhysRev.52.54.

[19] J. R. Oppenheimer, *Note on the Theory of the Interaction of Field and Matter*, Phys. Rev. **35** (1930) 461–477, URL: https://link.aps.org/doi/10.1103/PhysRev.35.461.

[20] B. P. K. R. C. S. F. Z. W. Rodejohann, *Particles and Nuclei, An Introduction to the Physical Concepts*. Springer-Verlag Berlin Heidelberg, 2015.

[21] H. Fritzsch, M. Gell-Mann, and H. Leutwyler, *Advantages of the color octet gluon picture*, Physics Letters B **47** (1973) 365 – 368, URL: http://www.sciencedirect.com/science/article/pii/0370269373906254.

[22] D. J. Gross and F. Wilczek, *Ultraviolet Behavior of Non-Abelian Gauge Theories*, Phys. Rev. Lett. **30** (1973) 1343–1346, URL: https://link.aps.org/doi/10.1103/PhysRevLett.30.1343.

[23] H. D. Politzer, *Reliable Perturbative Results for Strong Interactions?*, Phys. Rev. Lett. **30** (1973) 1346–1349, URL: https://link.aps.org/doi/10.1103/PhysRevLett.30.1346.

[24] S. Glashow, *Partial Symmetries of Weak Interactions*, Nucl. Phys. **22** (1961) 579–588.

[25] S. Weinberg, *A Model of Leptons*, Phys. Rev. Lett. **19** (1967) 1264–1266.

[26] Particle Data Group Collaboration, Particle Data Group, *Review of Particle Physics*, Phys. Rev. D **98** (2018) 030001, URL: https://link.aps.org/doi/10.1103/PhysRevD.98.030001.

[27] C. N. Yang and R. L. Mills, *Conservation of Isotopic Spin and Isotopic Gauge Invariance*, Phys. Rev. **96** (1954) 191–195, URL: https://link.aps.org/doi/10.1103/PhysRev.96.191.

[28] C. S. Wu, E. Ambler, R. W. Hayward, D. D. Hoppes, and R. P. Hudson, *Experimental Test of Parity Conservation in Beta Decay*, Phys. Rev. **105** (1957) 1413–1415, URL: https://link.aps.org/doi/10.1103/PhysRev.105.1413.

[29] M. Goldhaber, L. Grodzins, and A. W. Sunyar, *Helicity of Neutrinos*, Phys. Rev. **109** (1958) 1015–1017, URL: https://link.aps.org/doi/10.1103/PhysRev.109.1015.

[30] T. Nakano and K. Nishijima, *Charge Independence for V-particles**, Progress of Theoretical Physics **10** (1953) 581–582, `https://academic.oup.com/ptp/article-pdf/10/5/581/5364926/10-5-581.pdf`, URL: https://doi.org/10.1143/PTP.10.581.

[31] M. Gell-Mann, *The interpretation of the new particles as displaced charge multiplets*, Il Nuovo Cimento (1955-1965) **4** (1956) 848–866, URL: https://doi.org/10.1007/BF02748000.

[32] M. Kobayashi and T. Maskawa, *CP Violation in the Renormalizable Theory of Weak Interaction*, Prog. Theor. Phys. **49** (1973) 652–657.

[33] A. Djouadi, *The anatomy of electroweak symmetry breaking*, Physics Reports **457** (2008) 1–216, URL: http://dx.doi.org/10.1016/j.physrep.2007.10.004.

[34] ATLAS Collaboration, CMS Collaboration, *Combined Measurement of the Higgs Boson Mass in pp Collisions at $\sqrt{s} = 7$ and 8 TeV with the ATLAS and CMS Experiments*, Phys. Rev. Lett. **114** (2015) 191803, arXiv:1503.07589 [hep-ex].

[35] J. C. Collins, D. E. Soper, and G. Sterman, *Factorization of Hard Processes in QCD*, 2004.

[36] H.-W. Lin, E. R. Nocera, F. Olness, K. Orginos, J. Rojo, A. Accardi, C. Alexandrou, A. Bacchetta, G. Bozzi, J.-W. Chen, and et al., *Parton distributions and lattice QCD calculations: A community white paper*, Progress in Particle and Nuclear Physics **100** (2018) 107–160, URL: http://dx.doi.org/10.1016/j.ppnp.2018.01.007.

[37] C. Grojean, *Higgs Physics*, URL: https://cds.cern.ch/record/2243593, 12 pages, contribution to the CERN in the Proceedings of the 2015 CERN-Latin-American School of High-Energy Physics, Ibarra, Ecuador, 4 - 17 March 2015.

[38] R. Harlander, J. Klappert, C. Pandini, and A. Papaefstathiou, *Exploiting the WH/ZH symmetry in the search for New Physics*, Eur. Phys. J. C **78** (2018) 760. 22 p, URL: https://cds.cern.ch/record/2315170, 22 pages, 10 figures. v2: Minor changes; matches published version.

[39] LHC Higgs Cross Section Working Group, *Handbook of LHC Higgs Cross Sections: 4. Deciphering the Nature of the Higgs Sector*, arXiv:1610.07922 [hep-ph].

[40] ATLAS Collaboration, *Constraints on off-shell Higgs boson production and the Higgs boson total width in $ZZ \to 4\ell$ and $ZZ \to 2\ell 2\nu$ final states with the ATLAS detector*, Phys. Lett. B **786** (2018) 223, arXiv:1808.01191 [hep-ex].

[41] L. Evans and P. Bryant, *LHC Machine*, Journal of Instrumentation **3** (2008) S08001–S08001, URL: https://doi.org/10.1088%2F1748-0221%2F3%2F08%2Fs08001.

[42] O. S. Brüning, P. Collier, P. Lebrun, S. Myers, R. Ostojic, J. Poole, and P. Proudlock, *LHC Design Report*. CERN Yellow Reports: Monographs. CERN, Geneva, 2004. URL: http://cds.cern.ch/record/782076.

[43] O. S. Brüning, P. Collier, P. Lebrun, S. Myers, R. Ostojic, J. Poole, and P. Proudlock, *LHC Design Report*. CERN Yellow Reports: Monographs. CERN, Geneva, 2004. URL: https://cds.cern.ch/record/815187.

[44] M. Benedikt, P. Collier, V. Mertens, J. Poole, and K. Schindl, *LHC Design Report*. CERN

Yellow Reports: Monographs. CERN, Geneva, 2004. URL: https://cds.cern.ch/record/823808.

[45] S. P. Martin, *A Supersymmetry Primer*, Advanced Series on Directions in High Energy Physics (1998) 1–98, URL: http://dx.doi.org/10.1142/9789812839657_0001.

[46] B. Diaz, M. Schmaltz, and Y.-M. Zhong, *The leptoquark Hunter's guide: Pair production*, JHEP **10** (2017) 097, arXiv:1706.05033 [hep-ph].

[47] M. Gazdzicki, M. Gorenstein, and P. Seyboth, *Brief history of the search for critical structures in heavy-ion collisions*, arXiv:2004.02255 [hep-ph].

[48] ATLAS Collaboration, ATLAS Collaboration, *Luminosity determination in pp collisions at $\sqrt{s} = 8$ TeV using the ATLAS detector at the LHC*, Eur. Phys. J. **C76** (2016) 653, arXiv:1608.03953 [hep-ex].

[49] E. Halkiadakis, *Introduction to the LHC Experiments*, URL: https://cds.cern.ch/record/1263062, TASI 2009 Proceedings/ 32 pages/ 14 figures/ To be published in World Scientific.

[50] B. Salvachua, *Overview of proton runs during run 2*, URL: https://indico.cern.ch/event/751857/contributions/3259373/attachments/1783143/2910577/belen-Evian2019.pdf.

[51] ATLAS Collaboration, *Luminosity Public Results Run2*, URL: https://twiki.cern.ch/twiki/bin/view/AtlasPublic/LuminosityPublicResultsRun2.

[52] ATLAS Collaboration, *ATLAS detector and physics performance: Technical Design Report, 1*. Technical Design Report ATLAS. CERN, Geneva, 1999. URL: https://cds.cern.ch/record/391176.

[53] ATLAS Collaboration, *ATLAS detector and physics performance: Technical Design Report, 2*. Technical Design Report ATLAS. CERN, Geneva, 1999. URL: https://cds.cern.ch/record/391177.

[54] ATLAS Collaboration, *Computer generated image of the whole ATLAS detector*, URL: https://cds.cern.ch/images/CERN-GE-0803012-01.

[55] ALTAS Collaboration, *The ATLAS Experiment at the CERN Large Hadron Collider*, Journal of Instrumentation **3** (2008) S08003–S08003, URL: https://doi.org/10.1088%2F1748-0221%2F3%2F08%2Fs08003.

[56] ATLAS Collaboration, *ATLAS Insertable B-Layer Technical Design Report*, Tech. Rep. CERN-LHCC-2010-013. ATLAS-TDR-19, CERN, Sep, 2010. URL: https://cds.cern.ch/record/1291633.

[57] ATLAS Collaboration, *ATLAS Insertable B-Layer Technical Design Report Addendum*, Tech. Rep. CERN-LHCC-2012-009. ATLAS-TDR-19-ADD-1, CERN, May, 2012. URL: https://cds.cern.ch/record/1451888. Addendum to CERN-LHCC-2010-013,

ATLAS-TDR-019.

[58] ATLAS Collaboration, *The Expected Performance of the ATLAS Inner Detector*, Tech. Rep. ATL-PHYS-PUB-2009-002. ATL-COM-PHYS-2008-105, CERN, Geneva, Aug, 2008. URL: http://cds.cern.ch/record/1118445.

[59] ATLAS Collaboration, *Performance of the ATLAS track reconstruction algorithms in dense environments in LHC Run 2*, The European Physical Journal C **77** (2017) 673, URL: http://dx.doi.org/10.1140/epjc/s10052-017-5225-7.

[60] ATLAS Collaboration, *Public Liquid-Argon Calorimeter Plots on Detector Status*, URL: https://twiki.cern.ch/twiki/bin/view/AtlasPublic/LArCaloPublicResultsDetStatus.

[61] ATLAS Collaboration, A. Henriques, *The ATLAS tile calorimeter*, tech. rep., 2015.

[62] ATLAS Muon Collaboration, E. Diehl, *ATLAS Muon Detector Commissioning*, in *Meeting of the Division of Particles and Fields of the American Physical Society (DPF 2009)*. 10, 2009. arXiv:0910.2767 [physics.ins-det].

[63] ATLAS Collaboration, *Resolution of the ATLAS muon spectrometer monitored drift tubes in LHC Run 2*, arXiv:1906.12226 [hep-ex].

[64] G. Avoni et al., *The new LUCID-2 detector for luminosity measurement and monitoring in ATLAS*, JINST **13** (2018) P07017.

[65] ATLAS Collaboration, *Luminosity determination in pp collisions at $\sqrt{s}$ = 13 TeV using the ATLAS detector at the LHC*, Tech. Rep. ATLAS-CONF-2019-021, CERN, Geneva, Jun, 2019. URL: http://cds.cern.ch/record/2677054.

[66] S. van der Meer, *Calibration of the effective beam height in the ISR*, Tech. Rep. CERN-ISR-PO-68-31. ISR-PO-68-31, CERN, Geneva, 1968. URL: https://cds.cern.ch/record/296752.

[67] P. Grafström and W. Kozanecki, *Luminosity determination at proton colliders*, Progress in Particle and Nuclear Physics **81** (2015) 97 – 148, URL: http://www.sciencedirect.com/science/article/pii/S0146641014000878.

[68] ATLAS TDAQ Collaboration, *The ATLAS Data Acquisition and High Level Trigger system*, Journal of Instrumentation **11** (2016) P06008–P06008, URL: https://doi.org/10.1088%2F1748-0221%2F11%2F06%2Fp06008.

[69] GEANT4 Collaboration, *Geant4—a simulation toolkit*, Nucl. Instrum. Meth. A **506** (2003) 250 – 303, URL: http://www.sciencedirect.com/science/article/pii/S0168900203013688.

[70] W. Lukas, *Fast Simulation for ATLAS: Atlfast-II and ISF*, Journal of Physics: Conference Series **396** (2012) 022031, URL: https://doi.org/10.1088%2F1742-6596%2F396%2F2%2F022031.

[71] ATLAS Collaboration, *The new Fast Calorimeter Simulation in ATLAS*, Tech. Rep.

ATL-SOFT-PUB-2018-002, CERN, Geneva, Jul, 2018. URL: http://cds.cern.ch/record/2630434.

[72] C. Kourkoumelis and S. Vourakis, *HYPATIA—an online tool for ATLAS event visualization*, Physics Education **49** (2013) 21–32, URL: https://doi.org/10.1088%2F0031-9120%2F49%2F1%2F21.

[73] ATLAS Collaboration, *Concepts, Design and Implementation of the ATLAS New Tracking (NEWT)*, Tech. Rep. ATL-SOFT-PUB-2007-007. ATL-COM-SOFT-2007-002, CERN, Geneva, Mar, 2007. URL: https://cds.cern.ch/record/1020106.

[74] R. Fruhwirth, *Application of Kalman filtering to track and vertex fitting*, Nucl. Instrum. Meth. A **262** (1987) 444–450.

[75] ATLAS Collaboration, *Vertex Reconstruction Performance of the ATLAS Detector at $\sqrt{s}$ = 13 TeV*, Tech. Rep. ATL-PHYS-PUB-2015-026, CERN, Geneva, Jul, 2015. URL: http://cds.cern.ch/record/2037717.

[76] ATLAS Collaboration, *Muon reconstruction performance of the ATLAS detector in proton–proton collision data at $\sqrt{s}$ =13 TeV*, Eur. Phys. J. **C76** (2016) 292, arXiv:1603.05598 [hep-ex].

[77] J. Illingworth and J. Kittler, *A survey of the hough transform*, Computer Vision, Graphics, and Image Processing **44** (1988) 87 – 116, URL: http://www.sciencedirect.com/science/article/pii/S0734189X88800331.

[78] ATLAS Collaboration, ATLAS Collaboration, *Electron reconstruction and identification in the ATLAS experiment using the 2015 and 2016 LHC proton-proton collision data at $\sqrt{s}$ = 13 TeV*, Eur. Phys. J. **C79** (2019) 639, arXiv:1902.04655 [physics.ins-det].

[79] W. Lampl, S. Laplace, D. Lelas, P. Loch, H. Ma, S. Menke, S. Rajagopalan, D. Rousseau, S. Snyder, and G. Unal, *Calorimeter clustering algorithms: Description and performance*,.

[80] ATLAS Collaboration, *Electron and photon performance measurements with the ATLAS detector using the 2015-2017 LHC proton–proton collision data*, JINST **14** (2019) P12006, arXiv:1908.00005 [hep-ex].

[81] T. G. Cornelissen, M. Elsing, I. Gavrilenko, J. Laporte, W. Liebig, M. Limper, K. Nikolopoulos, A. Poppleton, and A. Salzburger, *The global X^2 track fitter in ATLAS*, J. Phys. Conf. Ser. **119** (2008) 032013.

[82] D. W. Scott, *Multivariate Density Estimation: Theory, Practice, and Visualization, Second Edition*. Wiley, second edition ed., 2015.

[83] M. Cacciari, G. P. Salam, and G. Soyez, *The anti-k_t jet clustering algorithm*, JHEP **04** (2008) 063, arXiv:0802.1189 [hep-ph].

[84] M. Cacciari, G. P. Salam, and G. Soyez, *FastJet User Manual*, Eur. Phys. J. **C72** (2012) 1896, arXiv:1111.6097 [hep-ph].

[85] ATLAS Collaboration, *Jet reconstruction and performance using particle flow with the ATLAS Detector*, Eur. Phys. J. **C77** (2017) 466, arXiv:1703.10485 [hep-ex].

[86] ATLAS Collaboration, *Performance of b-jet identification in the ATLAS experiment*, Journal of Instrumentation **11** (2016) P04008–P04008, URL: https://doi.org/10.1088%2F1748-0221%2F11%2F04%2Fp04008.

[87] ATLAS Collaboration, *Expected Performance of the ATLAS Experiment - Detector, Trigger and Physics*, arXiv:0901.0512 [hep-ex].

[88] ATLAS Collaboration, *Optimisation of the ATLAS b-tagging performance for the 2016 LHC Run*, Tech. Rep. ATL-PHYS-PUB-2016-012, CERN, Geneva, Jun, 2016. URL: https://cds.cern.ch/record/2160731.

[89] ATLAS Collaboration, *Measurements of b-jet tagging efficiency with the ATLAS detector using $t\bar{t}$ events at $\sqrt{s} = 13$ TeV*, JHEP **08** (2018) 089, arXiv:1805.01845 [hep-ex].

[90] Matthew Klein, *Muon Isolation Optimization*, URL: https://indico.cern.ch/event/683359/contributions/2802465/attachments/1563892/2463432/muon20171120.pdf.

[91] ATLAS Collaboration, *Run 2 Isolation Harmonisation*, URL: https://twiki.cern.ch/twiki/bin/view/AtlasProtected/Run2IsolationHarmonisation.

[92] ATLAS Collaboration, M. Aaboud et al., *Performance of missing transverse momentum reconstruction with the ATLAS detector using proton-proton collisions at $\sqrt{s} = 13$ TeV*, Eur. Phys. J. **C78** (2018) 903, arXiv:1802.08168 [hep-ex].

[93] S. Alioli, P. Nason, C. Oleari, and E. Re, *A general framework for implementing NLO calculations in shower Monte Carlo programs: the POWHEG BOX*, JHEP **06** (2010) 043, arXiv:1002.2581 [hep-ph].

[94] S. Frixione, P. Nason, and C. Oleari, *Matching NLO QCD computations with Parton Shower simulations: the POWHEG method*, JHEP **11** (2007) 070, arXiv:0709.2092 [hep-ph].

[95] P. Nason, *A New method for combining NLO QCD with shower Monte Carlo algorithms*, JHEP **11** (2004) 040, arXiv:hep-ph/0409146 [hep-ph].

[96] P. Nason and C. Oleari, *NLO Higgs boson production via vector-boson fusion matched with shower in POWHEG*, JHEP **02** (2010) 037, arXiv:0911.5299 [hep-ph].

[97] G. Luisoni, P. Nason, C. Oleari, and F. Tramontano, *$HW^{\pm}$/HZ + 0 and 1 jet at NLO with the POWHEG BOX interfaced to GoSam and their merging within MiNLO*, JHEP **10** (2013) 083, arXiv:1306.2542 [hep-ph].

[98] J. Butterworth et al., *PDF4LHC recommendations for LHC Run II*, J. Phys. **G43** (2016) 023001, arXiv:1510.03865 [hep-ph].

[99] K. Hamilton, P. Nason, C. Oleari, and G. Zanderighi, *Merging H/W/Z + 0 and 1 jet at NLO with no merging scale: a path to parton shower + NNLO matching*, JHEP **05** (2013) 082, arXiv:1212.4504 [hep-ph].

[100] K. Hamilton, P. Nason, E. Re, and G. Zanderighi, *NNLOPS simulation of Higgs boson production*, JHEP **10** (2013) 222, arXiv:1309.0017 [hep-ph].

[101] K. Hamilton, P. Nason, and G. Zanderighi, *Finite quark-mass effects in the NNLOPS POWHEG+MiNLO Higgs generator*, JHEP **05** (2015) 140, arXiv:1501.04637 [hep-ph].

[102] S. Catani and M. Grazzini, *An NNLO subtraction formalism in hadron collisions and its application to Higgs boson production at the LHC*, Phys. Rev. Lett. **98** (2007) 222002, arXiv:hep-ph/0703012 [hep-ph].

[103] M. Grazzini, *NNLO predictions for the Higgs boson signal in the H —> WW —> lnu lnu and H —> ZZ —> 4l decay channels*, JHEP **02** (2008) 043, arXiv:0801.3232 [hep-ph].

[104] G. Bozzi, S. Catani, D. de Florian, and M. Grazzini, *Transverse-momentum resummation and the spectrum of the Higgs boson at the LHC*, Nucl. Phys. **B737** (2006) 73–120, arXiv:hep-ph/0508068 [hep-ph].

[105] D. de Florian, G. Ferrera, M. Grazzini, and D. Tommasini, *Transverse-momentum resummation: Higgs boson production at the Tevatron and the LHC*, JHEP **11** (2011) 064, arXiv:1109.2109 [hep-ph].

[106] M. Wiesemann, R. Frederix, S. Frixione, V. Hirschi, F. Maltoni, and P. Torrielli, *Higgs production in association with bottom quarks*, JHEP **02** (2015) 132, arXiv:1409.5301 [hep-ph].

[107] H.-L. Lai, M. Guzzi, J. Huston, Z. Li, P. M. Nadolsky, J. Pumplin, and C. P. Yuan, *New parton distributions for collider physics*, Phys. Rev. **D82** (2010) 074024, arXiv:1007.2241 [hep-ph].

[108] NNPDF Collaboration, R. D. Ball et al., *Parton distributions for the LHC Run II*, JHEP **04** (2015) 040, arXiv:1410.8849 [hep-ph].

[109] T. Sjostrand, S. Mrenna, and P. Z. Skands, *A Brief Introduction to PYTHIA 8.1*, Comput. Phys. Commun. **178** (2008) 852–867, arXiv:0710.3820 [hep-ph].

[110] ATLAS Collaboration, *Measurement of the Z/γ^* boson transverse momentum distribution in pp collisions at $\sqrt{s} = 7$ TeV with the ATLAS detector*, JHEP **09** (2014) 145, arXiv:1406.3660 [hep-ex].

[111] A. Bredenstein, A. Denner, S. Dittmaier, and M. Weber, *Precise predictions for the Higgs-boson decay H —> WW/ZZ —> 4 leptons*, Phys. Rev. D **74** (2006) 013004, arXiv:hep-ph/0604011.

[112] A. Bredenstein, A. Denner, S. Dittmaier, and M. Weber, *Precision calculations for the Higgs decays H —> ZZ/WW —> 4 leptons*, Nucl. Phys. B Proc. Suppl. **160** (2006) 131–135, arXiv:hep-ph/0607060.

[113] ATLAS Collaboration, *ATLAS Pythia 8 tunes to 7 TeV data*, Tech. Rep. ATL-PHYS-PROC-2014-273, CERN, Geneva, 2014. URL: https://cds.cern.ch/record/1966419.

[114] D. Lange, *The EvtGen particle decay simulation package*, Nucl. Instrum. Meth. A **462** (2001) 152–155.

[115] J. Alwall, R. Frederix, S. Frixione, V. Hirschi, F. Maltoni, O. Mattelaer, H. S. Shao, T. Stelzer, P. Torrielli, and M. Zaro, *The automated computation of tree-level and next-to-leading order differential cross sections, and their matching to parton shower simulations*, JHEP **07** (2014) 079, arXiv:1405.0301 [hep-ph].

[116] R. Frederix and S. Frixione, *Merging meets matching in MC@NLO*, JHEP **12** (2012) 061, arXiv:1209.6215 [hep-ph].

[117] LHC Higgs Cross Section Working Group, *Handbook of LHC Higgs Cross Sections: 3. Higgs Properties*, arXiv:1307.1347 [hep-ph].

[118] LHC Higgs Cross Section Working Group, *Handbook of LHC Higgs Cross Sections: 1. Inclusive Observables*, arXiv:1101.0593 [hep-ph].

[119] LHC Higgs Cross Section Working Group, *Handbook of LHC Higgs Cross Sections: 2. Differential Distributions*, arXiv:1201.3084 [hep-ph].

[120] A. Djouadi, J. Kalinowski, and M. Spira, *HDECAY: A Program for Higgs boson decays in the standard model and its supersymmetric extension*, Comput. Phys. Commun. **108** (1998) 56–74, arXiv:hep-ph/9704448 [hep-ph].

[121] S. Dulat, T.-J. Hou, J. Gao, M. Guzzi, J. Huston, P. Nadolsky, J. Pumplin, C. Schmidt, D. Stump, and C. Yuan, *New parton distribution functions from a global analysis of quantum chromodynamics*, Phys. Rev. D **93** (2016) 033006, arXiv:1506.07443 [hep-ph].

[122] L. A. Harland-Lang, A. D. Martin, P. Motylinski, and R. S. Thorne, *Parton distributions in the LHC era: MMHT 2014 PDFs*, Eur. Phys. J. **C75** (2015) 204, arXiv:1412.3989 [hep-ph].

[123] T. Gleisberg and S. Hoeche, *Comix, a new matrix element generator*, JHEP **12** (2008) 039, arXiv:0808.3674 [hep-ph].

[124] T. Gleisberg, S. Hoeche, F. Krauss, M. Schonherr, S. Schumann, F. Siegert, and J. Winter,

Event generation with SHERPA 1.1, JHEP **02** (2009) 007, arXiv:0811.4622 [hep-ph].

[125] F. Cascioli, P. Maierhofer, and S. Pozzorini, *Scattering Amplitudes with Open Loops*, Phys. Rev. Lett. **108** (2012) 111601, arXiv:1111.5206 [hep-ph].

[126] E. Bothmann et al., *Event Generation with Sherpa 2.2*, SciPost Phys. **7** (2019) 034, arXiv:1905.09127 [hep-ph].

[127] S. Schumann and F. Krauss, *A Parton shower algorithm based on Catani-Seymour dipole factorisation*, JHEP **03** (2008) 038, arXiv:0709.1027 [hep-ph].

[128] S. Hoeche, F. Krauss, M. Schonherr, and F. Siegert, *QCD matrix elements + parton showers: The NLO case*, JHEP **04** (2013) 027, arXiv:1207.5030 [hep-ph].

[129] F. Cascioli, T. Gehrmann, M. Grazzini, S. Kallweit, P. Maierhöfer, A. von Manteuffel, S. Pozzorini, D. Rathlev, L. Tancredi, and E. Weihs, *ZZ production at hadron colliders in NNLO QCD*, Phys. Lett. B **735** (2014) 311–313, arXiv:1405.2219 [hep-ph].

[130] M. Grazzini, S. Kallweit, and D. Rathlev, *ZZ production at the LHC: fiducial cross sections and distributions in NNLO QCD*, Phys. Lett. B **750** (2015) 407–410, arXiv:1507.06257 [hep-ph].

[131] M. Grazzini, S. Kallweit, and M. Wiesemann, *Fully differential NNLO computations with MATRIX*, Eur. Phys. J. C **78** (2018) 537, arXiv:1711.06631 [hep-ph].

[132] S. Kallweit and M. Wiesemann, *ZZ production at the LHC: NNLO predictions for $2\ell 2\nu$ and 4ℓ signatures*, Phys. Lett. B **786** (2018) 382–389, arXiv:1806.05941 [hep-ph].

[133] B. Biedermann, A. Denner, S. Dittmaier, L. Hofer, and B. Jäger, *Electroweak corrections to $pp \to \mu^+\mu^-e^+e^- + X$ at the LHC: a Higgs background study*, Phys. Rev. Lett. **116** (2016) 161803, arXiv:1601.07787 [hep-ph].

[134] B. Biedermann, A. Denner, S. Dittmaier, L. Hofer, and B. Jager, *Next-to-leading-order electroweak corrections to the production of four charged leptons at the LHC*, JHEP **01** (2017) 033, arXiv:1611.05338 [hep-ph].

[135] F. Caola, K. Melnikov, R. Röntsch, and L. Tancredi, *QCD corrections to ZZ production in gluon fusion at the LHC*, Phys. Rev. **D92** (2015) 094028, arXiv:1509.06734 [hep-ph].

[136] F. Caola, M. Dowling, K. Melnikov, R. Röntsch, and L. Tancredi, *QCD corrections to vector boson pair production in gluon fusion including interference effects with off-shell Higgs at the LHC*, JHEP **07** (2016) 087, arXiv:1605.04610 [hep-ph].

[137] K. Melnikov and M. Dowling, *Production of two Z-bosons in gluon fusion in the heavy top quark approximation*, Phys. Lett. **B744** (2015) 43–47, arXiv:1503.01274

[hep-ph].

[138] J. M. Campbell and R. K. Ellis, *An Update on vector boson pair production at hadron colliders*, Phys. Rev. **D60** (1999) 113006, arXiv:hep-ph/9905386 [hep-ph].

[139] S. Frixione, V. Hirschi, D. Pagani, H. S. Shao, and M. Zaro, *Electroweak and QCD corrections to top-pair hadroproduction in association with heavy bosons*, JHEP **06** (2015) 184, arXiv:1504.03446 [hep-ph].

[140] ATLAS Collaboration, *Studies on top-quark Monte Carlo modelling for Top2016*, Tech. Rep. ATL-PHYS-PUB-2016-020, CERN, Geneva, Sep, 2016. URL: https://cds.cern.ch/record/2216168.

[141] ATLAS Collaboration, *Tagging and suppression of pileup jets with the ATLAS detector*, Tech. Rep. ATLAS-CONF-2014-018, CERN, Geneva, May, 2014. URL: https://cds.cern.ch/record/1700870.

[142] ATLAS Collaboration, *Performance of pile-up mitigation techniques for jets in pp collisions at $\sqrt{s} = 8$ TeV using the ATLAS detector*, Eur. Phys. J. **C76** (2016) 581, arXiv:1510.03823 [hep-ex].

[143] ATLAS Collaboration, *Expected performance of the ATLAS b-tagging algorithms in Run-2*, Tech. Rep. ATL-PHYS-PUB-2015-022, CERN, Geneva, Jul, 2015. URL: https://cds.cern.ch/record/2037697.

[144] J. Alwall, M. Herquet, F. Maltoni, O. Mattelaer, and T. Stelzer, *MadGraph 5 : Going Beyond*, JHEP **06** (2011) 128, arXiv:1106.0522 [hep-ph].

[145] W. Buttinger and M. Lefebvre, *Formulae for Estimating Significance*, Tech. Rep. ATL-COM-GEN-2018-026, CERN, Geneva, Oct, 2018. URL: https://cds.cern.ch/record/2643488.

[146] M. Pivk and F. R. Le Diberder, *SPlot: A Statistical tool to unfold data distributions*, Nucl. Instrum. Meth. A **555** (2005) 356–369, arXiv:physics/0402083.

[147] R. J. Barlow, *Extended maximum likelihood*, Nucl. Instrum. Meth. **A297** (1990) 496–506.

[148] ROOT Collaboration, *HistFactory: A tool for creating statistical models for use with RooFit and RooStats*,.

[149] G. Cowan, K. Cranmer, E. Gross, and O. Vitells, *Asymptotic formulae for likelihood-based tests of new physics*, Eur. Phys. J. C **71** (2011) 1554, arXiv:1007.1727 [physics.data-an], [Erratum: Eur.Phys.J.C 73, 2501 (2013)].

[150] A. Wald, *Tests of Statistical Hypotheses Concerning Several Parameters When the Number of Observations is Large*, Transactions of the American Mathematical Society **54** (1943) 426–482, URL: http://www.jstor.org/stable/1990256.

[151] A. L. Read, *Presentation of search results: The CL(s) technique*, J. Phys. G **28** (2002)

2693–2704.

[152] A. Armbruster, *Discovery of a Higgs Boson with the ATLAS Detector*, May, 2013. URL: https://cds.cern.ch/record/1553771. Presented 02 May 2013.

[153] A. statistics forum, *Frequentist Limit Recommendation*, 2011. URL: https://indico.cern.ch/event/126652/contributions/1343592/attachments/80222/115004/Frequentist_Limit_Recommendation.pdf.

[154] W. Verkerke and D. Kirkby, *The RooFit toolkit for data modeling*, 2003.

[155] I. Antcheva et al., *ROOT: A C++ framework for petabyte data storage, statistical analysis and visualization*, Comput. Phys. Commun. **180** (2009) 2499–2512, arXiv:1508.07749 [physics.data-an].

[156] F. James, *Statistical Methods in Experimental Physics (2nd Edition)*. World Scientific Publishing Co. Pte. Ltd., second edition ed., 2006.

[157] N. Berger et al., *Simplified Template Cross Sections - Stage 1.1*, arXiv:1906.02754 [hep-ph].

[158] F. Chollet et al., *Keras*, URL: https://keras.io.

[159] M. Abadi et al., *TensorFlow: Large-Scale Machine Learning on Heterogeneous Systems*, 2015. URL: https://www.tensorflow.org/. Software available from tensorflow.org.

[160] P. Speckmayer, A. Hocker, J. Stelzer, and H. Voss, *The toolkit for multivariate data analysis, TMVA 4*, J. Phys. Conf. Ser. **219** (2010) 032057.

[161] I. Goodfellow, Y. Bengio, and A. Courville, *Deep Learning*. MIT Press, 2016. http://www.deeplearningbook.org.

[162] A. Graves, *Supervised Sequence Labelling with Recurrent Neural Networks*. Studies in Computational Intelligence. Springer, Berlin, 2012. URL: https://cds.cern.ch/record/1503877.

[163] ATLAS Collaboration, *Measurements of Higgs boson production and couplings in the four-lepton channel in pp collisions at center-of-mass energies of* 7 *and* 8 *TeV with the ATLAS detector*, Phys. Rev. D **91** (2015) 012006, arXiv:1408.5191 [hep-ex].

[164] D. Rainwater, R. Szalapski, and D. Zeppenfeld, *Probing color-singlet exchange in Z+2-jet events at the CERN LHC*, Phys. Rev. D **54** (1996) 6680–6689.

[165] I. W. Stewart and F. J. Tackmann, *Theory uncertainties for Higgs mass and other searches using jet bins*, Phys. Rev. D **85** (2012) 034011, URL: https://link.aps.org/doi/10.1103/PhysRevD.85.034011.

[166] J. Andersen et al., *Les Houches 2017: Physics at TeV Colliders Standard Model Working Group Report*, 2018.

[167] A. Bredenstein, A. Denner, S. Dittmaier, and M. Weber, *Radiative corrections to the*

semileptonic and hadronic Higgs-boson decays H —> W W / Z Z —> 4 fermions, JHEP **02** (2007) 080, arXiv:hep-ph/0611234.

[168] S. Boselli, C. M. Carloni Calame, G. Montagna, O. Nicrosini, and F. Piccinini, *Higgs boson decay into four leptons at NLOPS electroweak accuracy*, JHEP **06** (2015) 023, arXiv:1503.07394 [hep-ph].

[169] S. Boselli, C. M. Carloni Calame, G. Montagna, O. Nicrosini, F. Piccinini, and A. Shivaji, *Higgs decay into four charged leptons in the presence of dimension-six operators*, JHEP **01** (2018) 096, arXiv:1703.06667 [hep-ph].

[170] ATLAS Collaboration, *Measurement of inclusive and differential cross sections in the $H \to ZZ^* \to 4\ell$ decay channel in pp collisions at $\sqrt{s} = 13$ TeV with the ATLAS detector*, JHEP **10** (2017) 132, arXiv:1708.02810 [hep-ex].

[171] G. D'Agostini, *A Multidimensional unfolding method based on Bayes' theorem*, Nucl. Instrum. Meth. A **362** (1995) 487–498.

[172] ATLAS Collaboration, *Constraints on the off-shell Higgs boson signal strength in the high-mass ZZ and WW final states with the ATLAS detector*, Eur. Phys. J. C **75** (2015) 335, arXiv:1503.01060 [hep-ex].

[173] ATLAS Collaboration, *Electron efficiency measurements with the ATLAS detector using the 2015 LHC proton–proton collision data*, ATLAS-CONF-2016-024, 2016, URL: https://cds.cern.ch/record/2157687.

[174] ATLAS Collaboration, *Muon reconstruction performance of the ATLAS detector in proton–proton collision data at $\sqrt{s} = 13$ TeV*, Eur. Phys. J. C **76** (2016) 292, arXiv:1603.05598 [hep-ex].

[175] B. Biedermann, A. Denner, S. Dittmaier, L. Hofer, and B. Jager, *Next-to-leading-order electroweak corrections to the production of four charged leptons at the LHC*, JHEP **01** (2017) 033, arXiv:1611.05338 [hep-ph].

[176] ATLAS Collaboration, *Measurements of four-lepton production in pp collisions at $\sqrt{s} = 8$ TeV with the ATLAS detector*, Phys. Lett. B **753** (2016) 552, arXiv:1509.07844 [hep-ex].

[177] ATLAS Collaboration, *Measurement of $W^{\pm}$ and Z-boson production cross sections in pp collisions at $\sqrt{s} = 13$ TeV with the ATLAS detector*, Phys. Lett. B **759** (2016) 601, arXiv:1603.09222 [hep-ex].

[178] CMS Collaboration, *Measurements of the $pp \to ZZ$ production cross section and the $Z \to 4\ell$ branching fraction, and constraints on anomalous triple gauge couplings at $\sqrt{s} = 13$ TeV*, Eur. Phys. J. C **78** (2018) 165, arXiv:1709.08601 [hep-ex].

[179] CMS Collaboration, *Measurement of the WZ production cross section in pp collisions at*

$\sqrt{s} = 7$ *and* 8 *TeV and search for anomalous triple gauge couplings at* $\sqrt{s} = 8$ *TeV*, Eur. Phys. J. C **77** (2017) 236, arXiv:1609.05721 [hep-ex].

[180] ATLAS Collaboration, *Measurements of Four-Lepton Production at the* Z *Resonance in pp Collisions at* $\sqrt{s} = 7$ *and* 8 *TeV with ATLAS*, Phys. Rev. Lett. **112** (2014) 231806, arXiv:1403.5657 [hep-ex].

[181] A. Azatov, C. Grojean, A. Paul, and E. Salvioni, *Taming the off-shell Higgs boson*, Zh. Eksp. Teor. Fiz. **147** (2015) 410–425, arXiv:1406.6338 [hep-ph].

[182] T. Behnke, J. E. Brau, B. Foster, J. Fuster, M. Harrison, J. M. Paterson, M. Peskin, M. Stanitzki, N. Walker, and H. Yamamoto, *The International Linear Collider Technical Design Report - Volume 1: Executive Summary*, arXiv:1306.6327 [physics.acc-ph].

[183] H. Baer et al., *The International Linear Collider Technical Design Report - Volume 2: Physics*, arXiv:1306.6352 [hep-ph].

[184] CLIC, CLICdp Collaboration, P. Roloff, R. Franceschini, U. Schnoor, and A. Wulzer, *The Compact Linear* e^+e^- *Collider (CLIC): Physics Potential*, arXiv:1812.07986 [hep-ex].

[185] C. S. Group, *CEPC Conceptual Design Report: Volume 1 - Accelerator*, arXiv:1809.00285 [physics.acc-ph].

[186] CEPC Study Group Collaboration, C. S. Group, *CEPC Conceptual Design Report: Volume 2 - Physics & Detector*, arXiv:1811.10545 [hep-ex].

[187] F. An et al., *Precision Higgs physics at the CEPC*, Chin. Phys. C **43** (2019) 043002, arXiv:1810.09037 [hep-ex].

[188] ATLAS Collaboration, *Projections for measurements of Higgs boson cross sections, branching ratios, coupling parameters and mass with the ATLAS detector at the HL-LHC*, Tech. Rep. ATL-PHYS-PUB-2018-054, CERN, Geneva, Dec, 2018. URL: http://cds.cern.ch/record/2652762.

[189] T. Kawamoto et al., *New Small Wheel Technical Design Report*, URL: https://cds.cern.ch/record/1552862.

[190] ATLAS ITk Collaboration, H. Hayward and O. B. O. T. A. I. Project, *Overview and developments for the Phase-II upgrade of the inner tracker of the ATLAS experiment*, PoS **EPS-HEP2017** (2017) 499.

[191] ATLAS Collaboration, A. Schwartzman, *A High Granularity Timing Detector for the Phase-2 Upgrade of the ATLAS Experiment: Detector concept, R&D, and first test beam results*, PoS **ICHEP2018** (2019) 085.

[192] P. Gkountoumis, *Electronics design and system integration of the ATLAS New Small*

Wheels, Journal of Instrumentation **12** (2017) C01088–C01088, URL: https://doi.org/10.1088%2F1748-0221%2F12%2F01%2Fc01088.

[193] W. Wu, *FELIX: the New Detector Interface for the ATLAS Experiment*, IEEE Transactions on Nuclear Science **66** (2019) 986–992, URL: http://dx.doi.org/10.1109/TNS.2019.2913617.

[194] R. Collaboration, *JavaScript ROOT*, 2020. URL: http://jsroot.gsi.de.

[195] R. Wang, *sTGC offline data monitoring website*, 2020. URL: http://stgc-wedge-integration.web.cern.ch.

[196] T. pandas development team, *pandas-dev/pandas: Pandas*, Feb., 2020. URL: https://doi.org/10.5281/zenodo.3509134.

Publications

已发表论文

1. Measurement of the four-lepton invariant mass spectrum in 13 TeV proton-proton collisions with the ATLAS detector, JHEP 04 (2019) 048, arXiv:1902.05892
2. Measurement of the Higgs boson coupling properties in the $H \to ZZ^* \to 4\ell$ decay channel at $\sqrt{s}$ = 13 TeV with the ATLAS detector, JHEP 03 (2018) 095, arXiv:1712.02304
3. Search for Higgs boson decays to beyond-the-Standard-Model light bosons in four-lepton events with the ATLAS detector at $\sqrt{s}$=13 TeV, JHEP 06 (2018) 166, arXiv:1802.03388

待发表论文

1. Higgs boson production cross-section measurements and their EFT interpretation in the 4ℓ decay channel at $\sqrt{s}$ = 13 TeV with the ATLAS detector submitted bo EPJC, arXiv:2004.03447

会议报告

1. Measurements of the Higgs boson production, fiducial and differential cross sections in the 4ℓ decay channel at $\sqrt{s}$ = 13 TeV with the ATLAS detector, ATLAS-CONF-2018-018